



Investigation on Multi-Physics Modelling of Fault Tolerant Stator Mounted Permanent Magnet Machines

Mr Petrica Taras

A thesis submitted for the degree of Doctor of Philosophy (PhD)

Department of Electronic and Electrical Engineering,

University of Sheffield, United Kingdom

June 2018

Abstract

This thesis investigates the stator mounted permanent magnet machines from the point of view of fault tolerant capability. The topologies studied are switched flux (and its derivatives C-Core, E-Core and modular), doubly salient and flux reversal permanent magnet machines. The study focuses on fault mode operation of these machines looking at severe conditions like short-circuit and irreversible demagnetization. The temperature dependence of the permanent magnet properties is taken into account. A complex multi-physics model is developed in order to assess the thermal state evolution of the switched flux machine during both healthy and faulty operation modes. This model couples the electro-mechanical domain with the thermal one, thus being able to consider a large range of operating conditions. It also solves issues such as large computational time and resources while still maintaining the accuracy. Experimental results are also provided for each chapter. A hierarchy in terms of fault tolerant capability is established. A good compromise can be reached between performance and fault tolerant capability. The mechanism of the magnet irreversible demagnetization process is explained based on magnetic circuit configuration. It is also found that the studied topology are extremely resilient against the demagnetizing influence of the short-circuit current and the magnet demagnetization is almost only affected by temperature.

Acknowledgements

I am very grateful for the help and support I received during the development of this thesis. I would like to thank my supervisors Dr. Guang-Jin Li and Professor Zi-Qiang Zhu for offering me this opportunity to do research at this level in a prestigious university. I am very grateful for the considerable support and guidance I received from Dr. Guang-Jin Li during these four years.

I would also like to acknowledge the support provided by former and past colleagues in the EMD Group. In particular, I had received valuable help from Dr. Kan Liu who introduced me to the dSpace platform and helped me with advice at the beginning. I thank also Dr. Hanlin Zhan for helping me with various issues related to machine control, dSpace and test equipment. I am grateful to my friends Dr. Chukwuemeka Awah and Dr. Tayfun Gundogdu for their support and willingness to share their knowledge especially when it comes to Maxwell software. I also acknowledge the interesting and helpful discussions with Daniel Fernandez concerning permanent magnets field.

I would like to thank Mr. John Wilkinson for assisting me in building the prototype in the lab but also for the archery lessons I had the privilege to take at the Chantry Bowmen of Rotherham.

Finally, I am grateful for the friends I met while being a member in the EMD Group. I would like to thank Fernando Alvarez-Gonzales, Ahmed Allu, Nickolay (Nick) Nesterov, Shuai (Mark) Xiao, Dr. Francisco (Paco) Vedrano-Santos and Burcu Gundogdu for the many pleasant moments and conversations.

Contents

Abstract	2
Acknowledgements	3
List of Abbreviations	7
Nomenclature	9
Chapter 1. Introduction	15
1.1. Background and Overview	16
1.1.1. Background.....	16
1.1.2. Considered topologies.....	16
1.1.3. Considered type of faults	17
1.1.4. Methods and models used in research	18
1.2. Literature Review.....	19
1.2.1. Features and principle of operation	19
1.2.2. Other available topologies	22
1.2.3. Comparison of SFPMM with other PM machines.....	26
1.2.4. Faults classification.....	28
1.2.5. Fault-tolerant operation strategies	31
1.2.6. Thermal analysis and design.....	33
1.2.6.1 Importance of thermal modelling	33
1.2.6.2 Cooling methodologies.....	34
1.2.6.3 Thermal modelling methods	35
1.3. Research Scope and Contributions	37
1.4. Publications List	39
Chapter 2. Comparative Investigation of Stator Mounted Permanent Magnet Machines under Fault Conditions	41
2.1. Introduction.....	42
2.2. Model Description	43
2.3. Performance During Healthy and Faulty Operation	47
2.3.1. Reluctance and cogging torques	47
2.3.2. Performance in degraded mode	52
2.3.3. Short-circuit current comparison	57

2.4. PM Irreversible Demagnetization at High Speed	62
2.5. Experimental Validation for Short-Circuit Current	66
2.6. Conclusions.....	71
Chapter 3. Comparative Study of Alternative Modular Switched Flux Permanent Magnet Machines	73
3.1. Introduction.....	74
3.2. Features and Topologies of Modular SFPM Machines	74
3.3. Influence of Flux Gaps on Machine Performance	78
3.3.1. Winding factor	79
3.3.2. Open-circuit air-gap flux density	81
3.3.3. Phase back-EMF	84
3.3.4. Electromagnetic torque	90
3.3.5. Copper loss	94
3.4. Experimental Validation	96
3.5. Conclusions.....	102
Chapter 4. Comparative Study of Fault Tolerant Switched Flux Permanent Magnet Machines	104
4.1. Introduction.....	105
4.2. Features of Investigated Machines	106
4.3. Fault Modelling of the SFPMM.....	108
4.3.1. Investigated faults	108
4.3.2. Method of investigation	110
4.3.3. Dynamic model (motoring mode).....	111
4.3.4. Experimental validation of faulty model	114
4.4. Analysis of Conventional SFPMM Demagnetization Withstand Capability	123
4.4.1. Conventional SFPMM - low speed short-circuit	123
4.4.2. Conventional SFPMM - high speed short-circuit	127
4.4.3. Discussion on demagnetization mechanism	127
4.5. Analysis of Modular SFPMM Demagnetization	133
4.5.1. Local over-heating case	133
4.5.2. Global over-heating case	138
4.5.3. Experimental validation of temperature effect on PMs	140
4.6. Conclusions.....	142

Chapter 5. Combined Multi-Physics Model of Switched Flux Permanent Magnet Machines under Fault Operations	144
5.1. Introduction.....	145
5.2. The Co-Simulation Model	147
5.2.1. Investigation methodology	147
5.2.2. Electromechanical model and associated control	150
5.2.3. Thermal model.....	152
5.2.3.1 Airgap heat transfer	153
5.2.3.2 The convection coefficient calculation.....	155
5.3. Thermal Assessment During the Inter-Turn Short-Circuit.....	155
5.3.1. Thermal and electro-mechanical models predictions	155
5.3.2. Demagnetization analysis	164
5.4. Experimental Validation of Thermal Model.....	168
5.5. Conclusions.....	174
Chapter 6. Conclusions and Future Work	175
6.1. Summary of Studied Configurations	176
6.2. Conclusions.....	176
6.3. Future Work.....	178
Appendix	180
A.1. Dynamic Electro-Mechanical Model.....	180
A.2. Control Diagram	182
A.3. Iron Losses and Permanent Magnet Eddy Current Loss.....	183
A.4. Thermal Model.....	185
References	187

List of Abbreviations

Abbreviation	Full meaning
AlNiCo	Aluminium Nickel Cobalt
BLAC	BrushLess Alternating Current
BLDC	BrushLess Direct Current
CFD	Computational Fluid Dynamics
DC	Direct Current
DSPMM	Doubly Salient Permanent Magnet Machine
EMF	ElectroMotive Force
FE	Finite Element
FP	Frozen Permeability
FRPMM	Flux Reversal Permanent Magnet Machine
HCD	Highest Common Divisor
HE-SFPMM	Hybrid Excitation Switched Flux Permanent Magnet Machine
ICE	Internal Combustion Engine
IPM	Interior Permanent Magnet
LP	Lumped Parameter
MMF	Magneto Motive Force
MTPA	Maximum Torque Per Ampere

NdFeB	Neodimium-Iron-Boron
PM	Permanent Magnet
SFPMM	Switched Flux Permanent Magnet Machine
SPM	Surface-mounted Permanent Magnet
TEFC	Totally Enclosed Fan Cooling

Nomenclature

Symbol	Description
α	ratio of the short-circuited turns over the total phase turn number
α_c	convection coefficient
B	magnetic flux density
β	coefficient of cubical expansion
B_{knee}	knee point flux density
B_m	magnetic flux density in the affected PM
B_r	PM remanent flux density
c_p	air specific heat capacity
d	lamination sheet thickness
Δ	flux gap opening (absolute value)
ΔB_{pp}	peak to peak flux density value
ΔT	temperature rise
[e ₀]	phase back-EMF vector
e _h , e _f	back-EMFs in the healthy and faulty components of phase A
E _f	fundamental back-EMF

E_{\max}	Magnitude of the phase back-EMF
ε	surface emissivity (heat exchange through radiation)
f	electric frequency
f (Appendix, equation (A.5))	friction coefficient for linear speed dependent mechanical losses
g	gravitational acceleration constant
γ	mass density
Gr	Grashof number
h	convection coefficient
H	magnetic field intensity
H_c	PM magnetic field coercitivity
$[i]$	phase current vector
i_h, i_f	currents through healthy and faulty components of phase A
i_{total}	resultant current of phase A
I	electric current
I_a, I_b, I_c	phase currents (phase A, B,C)
i_{sc}	short-circuit current
J	moment of inertia
k	thermal conductivity
k_d	distribution factor
k_{eddy}	coefficient for eddy current based iron losses

k_{h1}, k_{h2}	coefficients for determining the hysteresis iron losses
k_p	pitch factor
k_{w1}	fundamental winding factor
L	phase self-inductance
L (Chapter 5)	characteristic length (of a convection surface)
$[L]$	inductance matrix
L_B, L_C	self-inductances for phases B and C
L_f, L_h	self inductances for the faulty and healthy components of phase A,
L_{end}	end-winding self inductance
l_g	air-gap radial thickness
l_{mean}	average end-turn length
M_{xy}	Mutual inductance between x and y coils
μ	air dynamic viscosity
μ_0	vacuum magnetic permeability constant
MMF_1, MMF_2	magneto-motive forces generated by PMs adjacent to the affected one
n_{coils}	number of coils per phase
n_{cond}	number of conductors per coil
v	air velocity
N_{ph}	number of turns per phase

N_r	number of rotor poles
N_s	number of stator teeth
Nu	Nusselt number
p	pole pair
p (Appendix (A.10) and (A.11))	total heat sources (volumic power density)
p_{copper}	copper (Joule) losses
p_{eddy}	eddy current iron losses
p_h	hysteresis iron losses
p_{iron}	total iron losses
p_{PM}	permanent magnet (eddy) losses
p_{out}	heat flux (exchange through a boundary surface)
$[\Phi_0]$	flux linkage vector
Φ_{demag}	demagnetizing flux
Φ_{max}	flux linkage magnitude
Φ_{PM}	flux generated by the affected PM
Φ_{pole1}	fundamental space harmonic value of the flux per pole
Φ_{y1}, Φ_{y2}	yoke magnetic fluxes
Pr	Prandtl number
q	number of coils per phase
R	phase resistance
$[R]$	phase resistance matrix

R_h, R_f	resistances for healthy and faulty components of phase A
R_{ag}, R_{ag1}, R_{ag2}	airgap magnetic reluctances
$R_{contact}$	contact resistance
R_{demag}	affected PM reluctance
R_{fg}	flux gap magnetic reluctance
R_{PM}	adjacent PM magnetic reluctance
R_r	rotor radius
ρ	air density
σ	angle between two phases
σ (Appendix, (A.9))	electric conductivity
σ (Appendix, (A.12))	Stefan Boltzmann constant (heat exchange through radiation)
ω	angular electric frequency
Ω	mechanical speed
T	temperature
T_a	Taylor number
T_{amb}	ambient temperature
T_{cogg}	cogging torque
T_{em}	electromagnetic torque
T_{faulty}	steady state temperature in faulty mode
T_{FLUID}	average ambient temperature
$T_{healthy}$	steady state temperature in faulty mode

T_{init}	initial temperature
T_{LOAD}	load torque
T_{reluct}	reluctance torque
τ_p	pole pitch
τ_s	slot pitch
θ_e	electrical angle
θ_m	mechanical
θ_{mgn}	magnet thickness
[v]	phase voltage vector

Chapter 1. Introduction

This chapter provides the background and summarizes the research scope and contributions brought by the present work. The main topologies studied are introduced and discussed. Their potential for fault tolerant applications is highlighted and their advantages and disadvantages explained. A comparison with classical rotor mounted PM machines is also given. The types of faults approached as well as the methods and models used are also highlighted in this chapter.

1.1. BACKGROUND AND OVERVIEW

1.1.1. BACKGROUND

In recent years, the automotive and aircraft fields have experienced a trend of adopting more and more electrical solutions instead of conventional (mechanical and hydraulic) ones. The public demand for air pollution reduction and high-efficiency has led to hybrid or even fully electrical vehicles in which the internal combustion engine (ICE) is replaced by an electrical drive. Similarly, in the aircraft industry, the established hydraulic actuators are replaced more and more by electric counterparts, leading to “more electric aircraft” [1]. In both cases, especially in the aircraft field, a high degree of robustness and fault-tolerance must be ensured by the electrical devices. This means that the affected components need to provide satisfactory performance even after the fault occurred. In addition, other constraints need to be satisfied as well, e.g. high torque (or force) density which are imposed by the necessity to keep a low volume and weight or a wide speed range. The focus of this research project consists of the study of several promising topologies, i.e. the stator mounted permanent magnet machines with a particular focus on the switched flux permanent magnet machine (SFPMM) and its derivatives. These types of machines have several characteristics which makes them suitable for the aircraft and automotive industries but also for other fields which require fault-tolerant operation. Having permanent magnets in their configuration ensures a high torque density. Moreover, due to the position of armature windings and magnets, which are all on the stator, the cooling can be much easier than other rotor mounted permanent magnet machines. The rotor does not contain any windings or PMs, similar to the rotor of SRMs, making them very robust at higher speeds. Although in their conventional configuration (double layer winding), complete fault-tolerance is not achievable, several derivatives exist which address this issue and will be included in this research. The topologies will be assessed under several types of fault conditions which can occur during operation. The possibility of fault diagnosis and identification for particular fault operations is also considered.

1.1.2. CONSIDERED TOPOLOGIES

The SFPMM is introduced in 1955 [2], having the permanent magnets (PM) and windings located in the stator and being under intensive study in the last decade [3], [4], [5], [6], [7], [8], [9], [10], due to its inherent advantages when compared with the rotor mounted PM machines. Fig. 1.1 shows a typical example of the SFPMM with 12-slot/10-pole, a classic slot/pole number combination that has been widely investigated in both industry and academia.

In its conventional form, this topology exhibit some degree of fault-tolerant capabilities, albeit its

alternatives existing in the same class could perform even better. The conventional SFPMM has a double layer concentrated winding (two sides of adjacent coils located in the same stator slot) which does not allow thermal and electromagnetic separations between two adjacent coils. Better fault-tolerant topologies, which will be studied and compared with the conventional SFPMM, are the single layer SFPMM, C-core and E-core. These machines are used to address some of the above issues while possibly introducing some new ones.

Other topologies of interest include the doubly salient permanent magnet machine (DSPMM) [11] and the flux reversal permanent magnet machine (FRPMM) [12], [13], [14] which have also the PM mounted on the stator. A comparative study, between the SFPMM, DSPMM and FRPMM is relevant, especially from the point of view of irreversible demagnetization, due to the interesting common features these machine share.

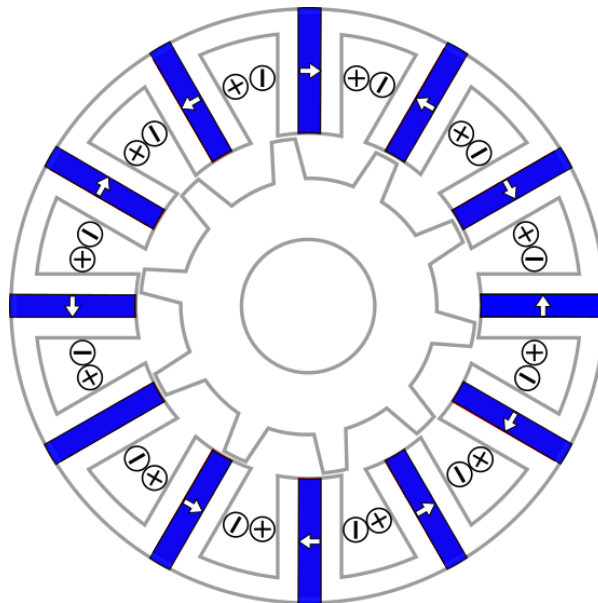


Fig. 1.1 Conventional topology of SFPMM [3].

1.1.3. CONSIDERED TYPE OF FAULTS

The faults of interest in this research project, concerning the topologies from section 1.1.2, are listed below:

- **Inter-turn short-circuit in the armature winding.** This faulty condition is often regarded as the most severe. This is mainly because it affects only several turns, it is limited only by the resistance and inductances (self and mutual) of those particular turns and it is of uttermost interest for study as it is very

severe, could lead to the entire winding destruction. Since the coils are close to the permanent magnets, it can also lead to another type of fault, namely irreversible demagnetization which affects the post-fault performance of the machine. For all these types of short-circuit faults, a post-fault operation must be assessed in terms of severity and possibility of escalation to a standstill of the machine.

- **Irreversible demagnetization of the PMs.** This type of fault can occur due to an escalating short-circuit fault or the flux weakening, or even a poorly designed machine magnetic circuit. The short-circuit based demagnetization [15], [16] will be extensively studied as the PMs are enclosed by the coils for the SFPMM topologies. In case of the short-circuit occurring in one of the coils, the heat produced by the affected coil propagates to the enclosed PM which will affect the magnetic properties of the PM material [17], [18], [19]. In particular, the flux density B_r , coercivity value H_c and knee point value are quantities of interest, which are temperature dependent. This study will consider also various commonly used types of permanent magnets.

Some of the aforementioned faults can be reduced by using more fault tolerant versions of the conventional machines. In this research project, relevant comparisons will be studied between conventional topologies and improved ones. In particular, the single layer version of the SFPMM as well as the C-core and E-core topologies are of interest because they can introduce the additional physical, thermal, electromagnetic separations between the coils which are lacking in the original design.

1.1.4. METHODS AND MODELS USED IN RESEARCH

The research will make use of finite element models, MATLAB/Simulink models and experimental tests. A control strategy is required to keep the machine up and running after the fault occurs in order to achieve fault tolerant operation. The most suitable tool for the study would be a co-simulation model which will allow integration of the control part (done by MATLAB/Simulink) with FE models (done by Flux software). However, the solving time required by co-simulation is very high and a simplified and improved model which does not lose accuracy but is much less time consuming will be proposed later on.

The electromagnetic FE models are used for two purposes:

- parameter extraction – these parameters are used later on in the Simulink models;
- demagnetization assessment – these FE models are using output results from the Simulink ones.

The frozen permeability method is used along with these models to accurately determine inductances while accounting for the PM working point and also to separate the effects of armature currents and

magnets generated magneto-motive force (MMF) on demagnetization.

In order to assess the temperature effects due to various faults, thermal and multi-physics models will be used. The most important scenario to be studied is when a short-circuit with high severity occurs (i.e. inter-turn type with a small number of turns) and the temperature rises in the PM enclosed by the affected coil.

1.2. LITERATURE REVIEW

The SFPMM topology is central to this research because it can be used in many fields, like automotive [4], [20], aircraft, wind turbines [5], etc. due to its robustness and high torque density. Therefore a review of the current state of the field is presented in this chapter, starting with features, principle of operation and so on. For comparison purpose, other stator mounted permanent magnet machines such as the DSPMM and the FRPMM will also be investigated.

1.2.1. FEATURES AND PRINCIPLE OF OPERATION

The first SFPMM topology was proposed in 1955 by Rauch and Johnson [2], as shown in Fig. 1.2 (a). It employs a simple magnet free rotor structure, similar to the switched reluctance machines. However, the PMs are located in the stator, competing for space with the armature windings for a given machine size and split ratio. In the first topology, the PMs are oversized in order to compensate for the low energy density of the magnet material (AlNiCo) available at that time. On the contrary, the modern topology as shown in Fig. 1.2 (b) [3], [8], uses high energy density PMs (NdFeB for example) allowing for an optimal distribution of PMs and armature windings in the stator.

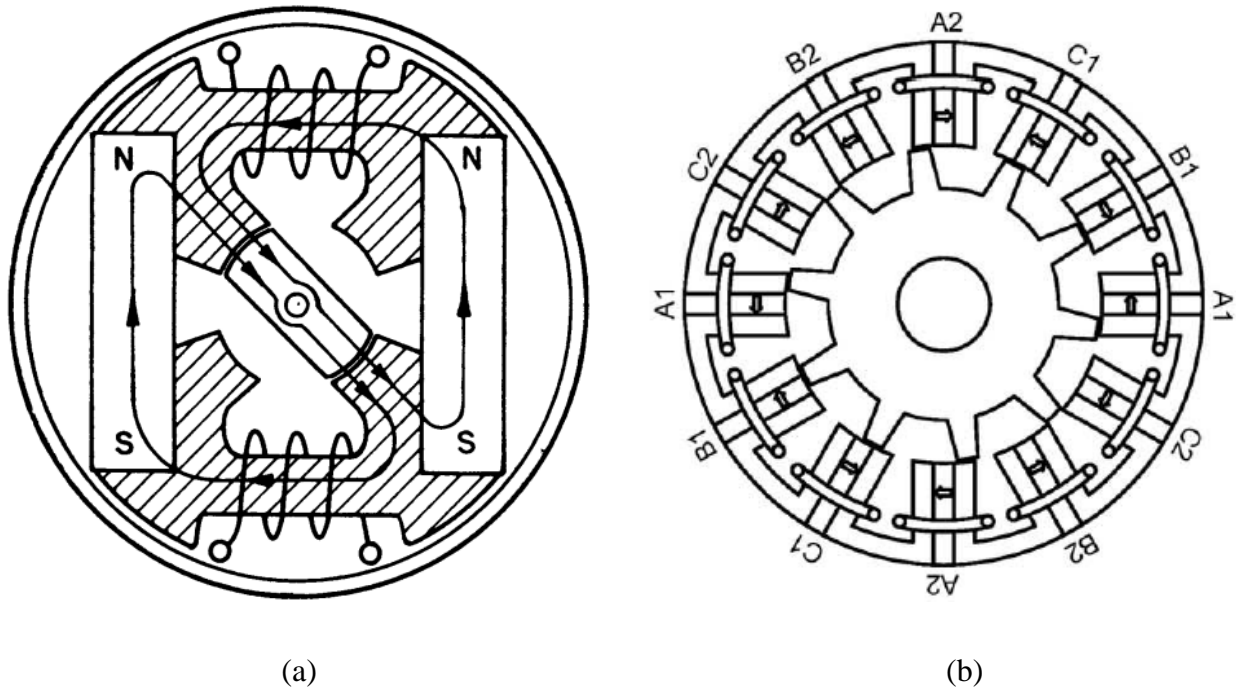


Fig. 1.2 Switched flux topology evolution. (a) first SFPM topology [2], (b) modern SFPM configuration [3].

It can be seen from Fig. 1.2 (b) that the modern configuration has a modular stator structure, and each module comprises of a PM sandwiched between two U-shape iron segments. The PMs are circumferentially magnetized in alternative fashion indicated by the arrows. Since the PMs are located on the stator, they are more accessible for cooling than rotor mounted counterparts because the airgap is a bad thermal conductor. However, this also leads to a complicated manufacturing process. However, the armature windings are made from concentrated coils which have shorter end-winding and hence could lead to lower copper volume and lower copper losses when compared with the distributed windings.

The operation principle of the SFPM is detailed in Fig. 1.3 [21], starting from a single module. The negative and positive d -axis as well as q -axis positions are shown in Fig. 1.3 (a) to (d). When the rotor tooth is aligned with the stator tooth resulting in a maximum flux linkage through that phase with either a negative or a positive sign. Fig. 1.3 (f) shows the flux linkage, back-EMF and current waveforms for a typical SFPM – with the four rotor positions indicated by dashed lines (the negative and positive d -axis and q -axis). If the rotor tooth is aligned with the PM axis or two adjacent rotor teeth are positioned equally with respect to the PM axis then the q -axis position is identified and the flux linkage is zero. It can be seen that between the two d -axis positions, the flux linkage reverses its direction and thus it “switches” direction through the coil, giving the name of this type of machines.

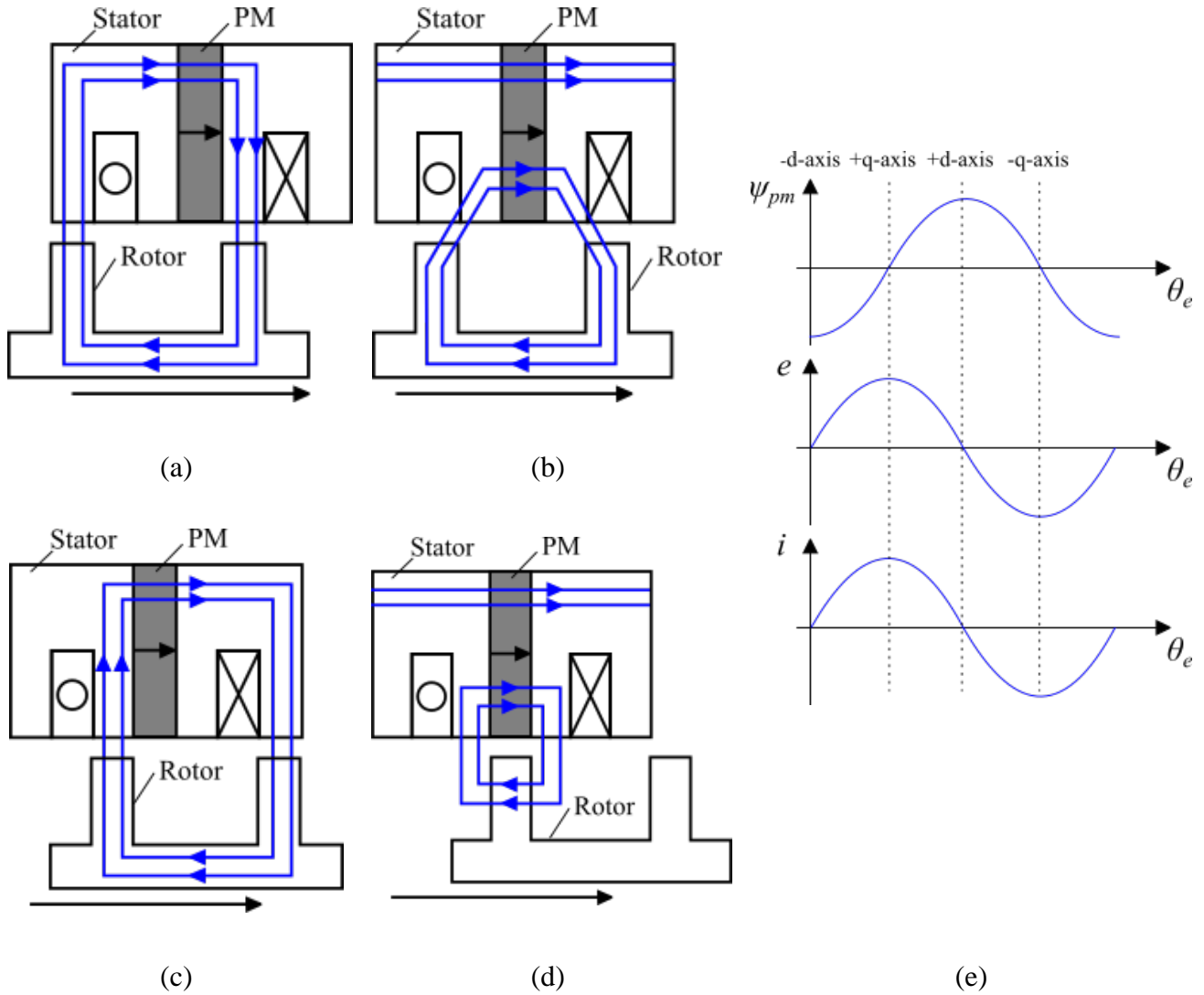


Fig. 1.3 Principle of operation for SFPMM. (a) negative d -axis rotor position, (b) positive q -axis rotor position, (c) positive d -axis rotor position, (d) negative q -axis rotor position, (e) waveforms for the PM flux linkage, back-EMF and armature currents [21].

The back-EMF waveform for the SFPMM is very close to sinewave, as shown in Fig. 1.3 (e), making it suitable for brushless alternating current (BLAC) operation. Moreover, it is worth mentioning that for this particular topology, the number of pole pairs p is actually equal to the number of rotor teeth N_r which makes it different from other PM machines [3], [22]:

$$\theta_e = N_r \cdot \theta_m = p \cdot \theta_m \tag{1.1}$$

where θ_e and θ_m are the electrical and mechanical angle.

The torque results predominantly from the PM excitation as the reluctance torque (difference between

the d - and q -axis inductances) is negligible [3]. The SFPMM has been compared with other PM machines [23], [24], [25], both rotor and stator PM mounted, being found that the SFPMM has a high torque density due to its bipolar flux linkage waveform characteristics [3], [21]. In order to achieve symmetrical back-EMF waveform in 3-phase SFPMM for example, the following relationship between the stator and rotor pole numbers must be satisfied for the double layer winding configuration [22], [26]:

$$\frac{N_s}{HCD(N_s \& N_r)} = 6 \cdot j \quad (j = 1, 2, 3 \dots) \quad (1.2)$$

where N_s is the number of stator teeth, N_r is the number of rotor poles while HCD stands for the Highest Common Divisor. For single layer machines, (1.2) becomes [27]:

$$\frac{N_s}{HCD(N_s \& N_r)} = 12 \cdot j \quad (j = 1, 2, 3 \dots) \quad (1.3)$$

There are several variations of the conventional SFPMM from Fig. 1.2 (b) – these are presented in the next section.

1.2.2. OTHER AVAILABLE TOPOLOGIES

Other SFPMM in the same class exists in the literature [22], each one adding features that are lacking in the conventional one. Fig. 1.4 shows some of them along with the conventional one [Fig. 1.4 (a)] for comparison purposes. The simplest modification which can be brought to the conventional machine is to replace the double layer winding with a single layer configuration [28]. The resulting machine, as shown in Fig. 1.4 (b), has better properties in terms of fault tolerant operation (especially the short-circuit case) and the coils are now thermally, magnetically and electrically isolated. The mutual inductance between coils has decreased, while the self-inductance has increased. As a result, in case of short-circuit, the short-circuit currents will not significantly influence the remaining healthy coils due to limited mutual effect between adjacent coils. In addition, the short-circuit current will be limited due to the high self-inductance. A comparative study between the double layer and single layer SFPMMs is conducted in [28] in terms of fault-tolerance capability. Dual 3-phase machines are used and a symmetrical 3-phase short-circuit is introduced in the 1st 3-phase set, the post-fault operation has been ensured by the 2nd 3-phase (redundant) set. The post-fault operation constraint is that both machines need to have the same average torque as in the healthy mode (4 Nm). It is found that the short-circuit peak current is significantly reduced for the single layer machine. Also, the single layer machine has less torque ripple during the faulty operation and an improved torque transient regime [28]. A drawback of the single layer

configuration is a lower power factor due to higher self-inductances and also the limited overload capability.

The E-core topology [29] [Fig. 1.4 (c)] is derived from the single layer configuration by removing the PMs from the unwound stator teeth and replacing the gap with iron. This new topology has the same characteristics of the single layer machine. Its main feature is the halved PM volume and hence the lower associated material costs. If the magnetless tooth is removed from the E-core machine then the resulting configuration is named C-core, as shown in Fig. 1.4 (d). The C-core topology loses the fault-tolerant capability given by coil separation as now there are two coil sides located in each stator slot, leading to double layer winding structure. In [29] - [30], the torque capabilities of the E-core and C-core configurations are compared with the one given by the conventional SFPMM. It is concluded that although the PM volume is halved, the performance does not necessarily degrade significantly. This is achieved by optimizing the C-core and E-core topologies and also having a different number of rotor poles when compared to the conventional machine. For the E-core topology for example, after optimization, it is shown that the torque is 15% higher when compared with the conventional one [29]. This is regardless of the fact that the PM volume and number are halved in the proposed E-core machine. Along with the C-core, the E-core topology has also better flux weakening properties with respect to the conventional SFPMM. In [31] a comparison in terms of flux weakening capability, torque and highest torque per ampere is conducted between the conventional SFPMM, E-core and C-core machines considering also various slot/pole number combinations. It is found that the conventional SFPMM has limited speed range. However, the E-core and C-core have infinite speed range. The highest average torque per ampere is achieved for the E-core configuration while the C-core achieves the highest torque overall.

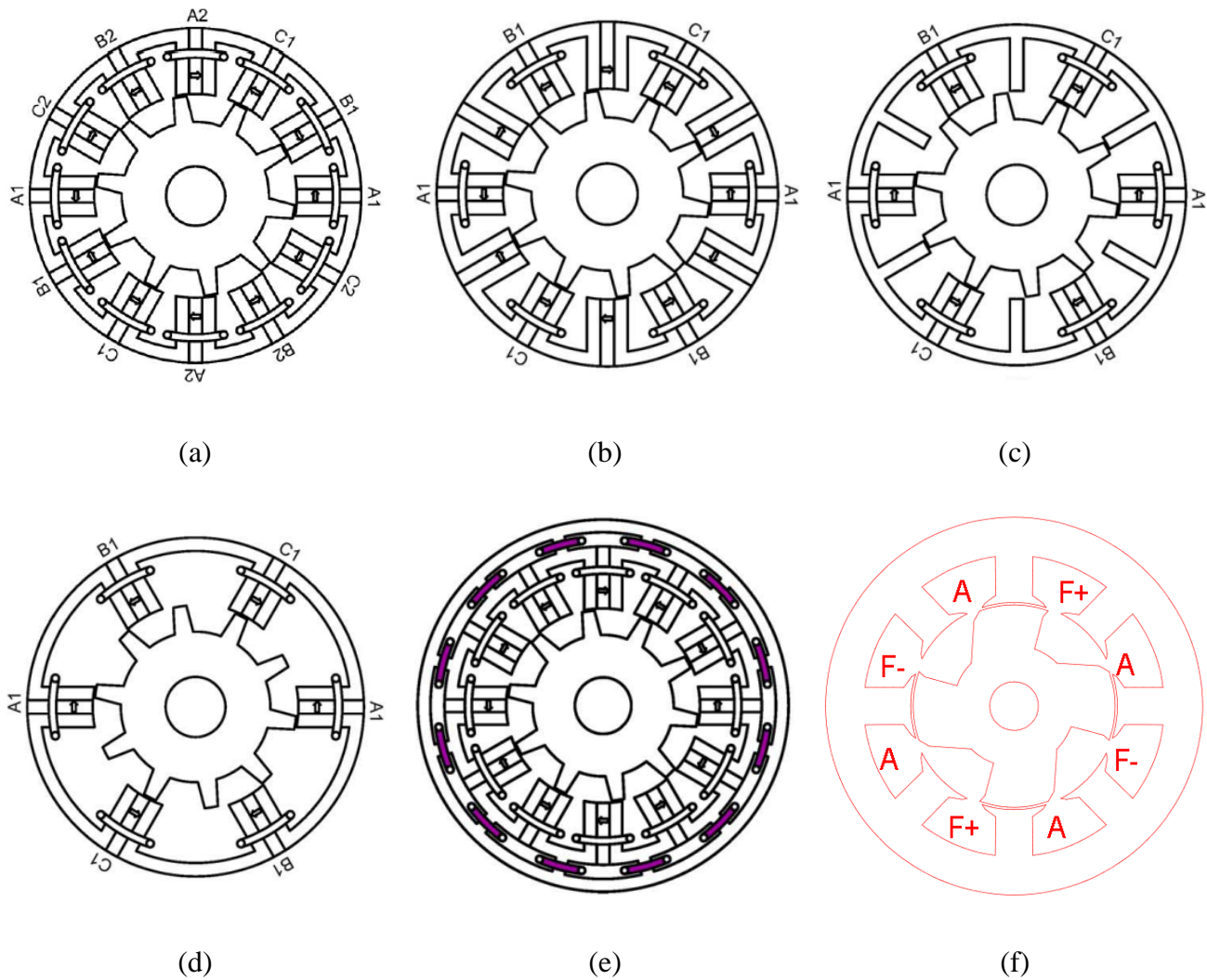


Fig. 1.4 SFPMM variants encountered in literature. (a) conventional double layer, (b) single layer, (c) E-Core, (d) C-Core, (e) hybrid excitation [32], (f) magnetless (DC excited) [33].

As for other PM machines, beyond the base speed, flux weakening operation needs to be implemented. This can be achieved by:

- Control strategy – introducing a negative d -axis current to counteract the PM field at the expense of higher copper losses and with the risk of PM demagnetization [34].
- Adapting an extra DC winding (for flux regulation) to the SFPMM structure. Two possibilities exist in this direction, the HE-SFPMM [HE – hybrid excitation Fig. 1.4 (e)] and the wound field (magnetless) switched flux machines [6], [33] [Fig. 1.4 (f)].

The HE-SFPMM has an extra DC coil which assists flux regulation in order to improve the flux weakening capability of the original SFPMM design [35]. When it comes to the DC coil position, the

PMs of a conventional SFPMM are shortened out [36] to make room for the DC windings (albeit the torque capability is reduced when compared with the conventional SFPM without DC coils). The HE-SFPM topology is so flexible that it is even possible for the DC coil to share the same slots with the armature windings with good flux regulation capability being achieved [37].

The HE-SFPM has applications in the automotive industry or any other field in which a much wider speed range is required. However, specific to HE-SFPM with rare earth PMs is the oversaturation effect in which the increase of the DC current does not necessarily lead to flux strengthening due to local saturation effects in the stator iron [38] - [39]. The magnetless switched flux machines implies the PM replacement with DC windings [6], [33]. This is done at the expense of a lower torque when compared to the PM based machines. However the possibility of having a much lower material cost and removing the risk of magnet demagnetization still makes this topology attractive.

Other topologies exist in literature and they will be mentioned briefly below:

- Various features can be combined in a single machine topology. For instance, the E-core topology can accommodate an extra DC winding, making it an E-core HE-SFPM machine [40] - [41]. The extra DC windings are placed on the magnetless stator teeth.
- A multi-tooth [42] SFPMM can be derived from the C-core topology. The stator tooth surface facing the airgap has small teeth. This topology can produce higher torque at low armature current when compared with the conventional SFPMM. Also, due to the dummy slots created in the stator by the multi-tooth structure, the torque ripple is significantly reduced. However, when compared with the conventional machine for overload conditions, the multi-tooth design delivers less torque due to higher magnetic saturation at high currents.
- A sandwiched SFPMM using V-Shape magnets is proposed in [43]. It is derived also from the C-core topology, except that each tooth carries two PMs instead of just one as in the original geometry. The PM volume in the machine is increased, at the expense of stator slot area available for the coils. The performance is better in terms of generated torque, when compared with the original counterpart. The downsides are an increased cogging torque and hence torque ripple for the V-shape magnets version. Also, due to the high volume of the PM material, the price for the V-shape machine will be higher.
- In [44] a modular rotor SFPMM is introduced. This topology reduces the total iron losses and rotor active mass (hence the inertia moment also). When compared with the conventional version, the total losses (iron, magnet eddy current and copper losses) reduction in the machine is 13% while the rotor active mass is reduced by 11%.

- Other topologies reported in the literature include outer rotor configuration [45], topologies using mechanical adjusters for flux weakening [46], [47] and [48], a SFPMM in which the PMs are located in the rotor [49], [50] (albeit the flux switching operation is retained), axial field versions [51], [52], dual stator (partitioned) machines in which the PMs and windings are separated into two stators [53], etc.

1.2.3. COMPARISON OF SFPMM WITH OTHER PM MACHINES

The SFPMM has been compared with rotor mounted PM machines, being found that it has comparable performances if not better. In [54], [55] and [56], it was compared with an interior permanent magnet (IPM) machine. Both topologies have buried PM inside laminations, making it easy to withstand high demagnetization currents. It is difficult to compare the two machines and several criteria are used in the literature. One criterion for comparison would be to maintain the same average torque between compared machines. However, it is also possible to maintain some of the geometrical dimensions constant (like the stator outer diameter). It is found, for example in [54], that when keeping the reluctance torque component low in the IPM machine (by adopting non-overlapping concentrated windings and having appropriate control strategy) the SFPMM has better flux weakening capabilities and slightly better output torque. Another study [55] has found that the SFPM machine offers a more sinusoidal back-EMF, lower torque ripple, better mechanical integrity due to PM location. But the SFPMM is also characterized by a low magnet utilization ratio and high cost (albeit the study focuses on conventional SFPMM when topologies like E-core addresses this issue). In [57] and [58] a comparison between SFPM and surface mounted permanent magnet (SPM) generator is conducted with an emphasis on high speed operation. It is found that the solution used to retain the PMs at high speed (banding) for the SPM machine is detrimental to performance, leading to the SFPMM as the better choice. In [59], when comparing SFPMM and SPM it is found that SFPMM has better torque capabilities for the same copper loss, due to flux focusing effect which leads to a higher flux density in the airgap.

In [23], [24], [25], [60] the SFPMM was compared with two other stator mounted PM machines, i.e. the doubly salient PM machines (DSPMM) and flux reversal PM machines (FRPMM). The comparison is relevant although their operating principle is different, they share other common features like the close proximity of PMs to the coils and thus to the heat sources, same type of winding (concentrated), same passive iron rotor construction, doubly salient structure, none of them have reluctance torque, etc. By way of example, the two topologies for comparison are given in (Fig. 1.5 (a) and (b)) and they differ by the PMs location. The DSPMM has the PMs mounted in the stator yoke, while the FRPMM has the PMs mounted on the stator teeth surfaces facing the airgap.

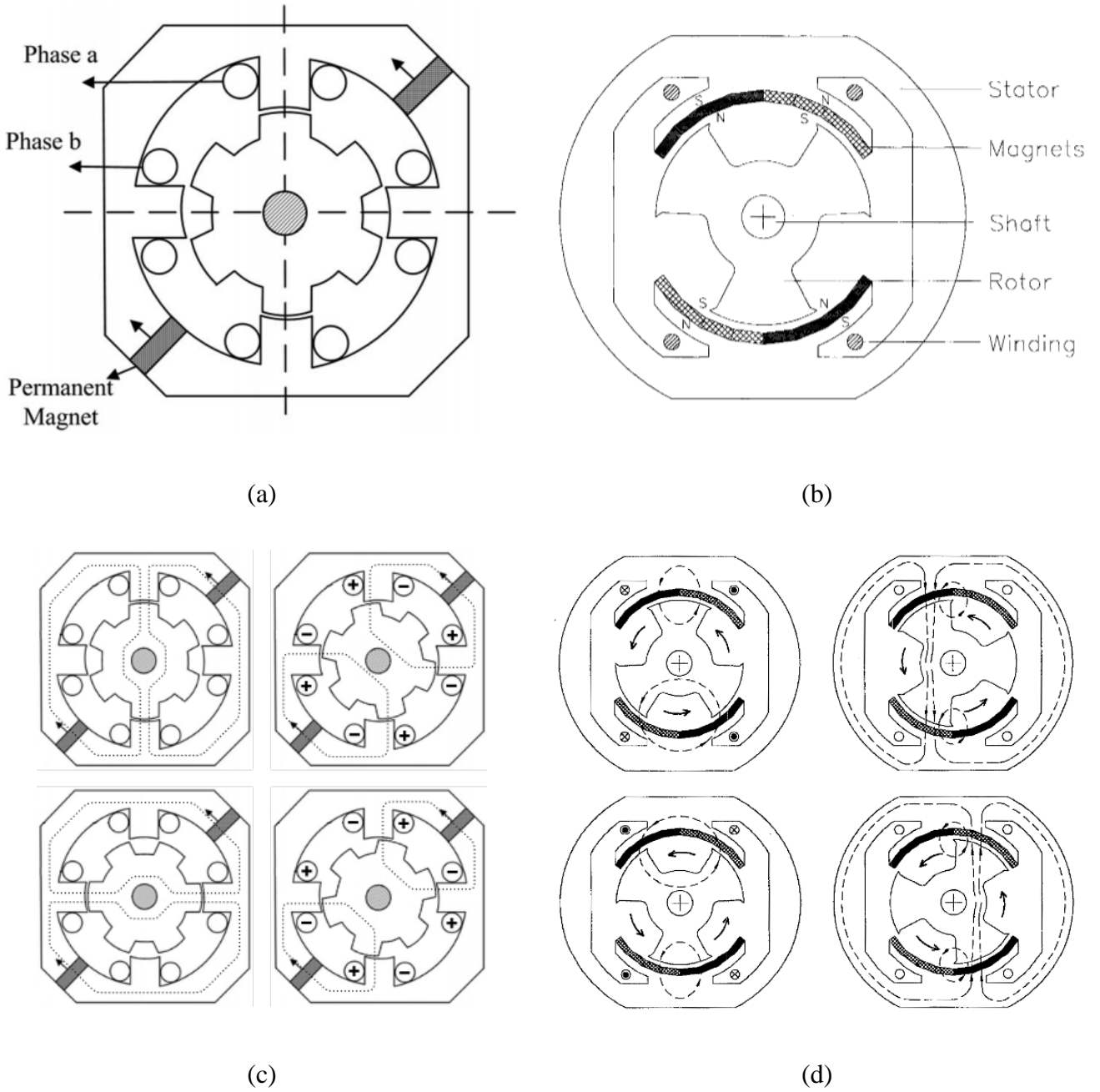


Fig. 1.5 Doubly salient PM machine (DSPMM) and flux reversal PM machine FRPMM. (a) DSPMM [25], (b) FRPMM [12], (c) magnetic flux paths for DSPMM, (d) magnetic flux paths for FRPMM.

The DSPMM has unipolar flux linkage due to its specific structure [24]. This seriously affects its torque density. Whereas, the SFPMM is a superior alternative from this point of view. Also, another difference is that DSPMM presents trapezoidal back-EMF which makes it more suitable for brushless direct current (BLDC) drive. However, with rotor skewing, the back-EMF can be made sinusoidal and BLAC operation can be used. The only drawback of the SFPMM [25] is a very high magnetic saturation

within the stator and rotor teeth due to the flux focussing feature. This might limit their overload capability.

The FRPMM [61] has the PMs in the airgap, being subjected to radial forces and demagnetization risks [62]. The PM thickness is important and constrained by two factors:

- effective thickness of the airgap
- ability to withstand magnet irreversible demagnetization

Based on their flux line distribution, the FRPMM has the weakest demagnetisation withstanding capability. This is because its PMs are positioned in series with the MMF produced by the armature windings and are also very thin. This is not the case for the DSPMM and SFPMM for which the armature reaction flux does not cross through the magnets. Regarding the performance, the FRPMM machine is also a low performer. Despite the fact that it has bidirectional flux linkage it still delivers less torque than the SFPMM topology, presumably due to the lower PM volume and lack of flux concentration effect [25]. Nonetheless the FRPMM is still attractive for this study due to its higher torque per PM volume (when compared with the SFPMM [63]).

The SFPMM, its derivatives (E-Core, C-Core) and other stator mounted PM machines have also been closely associated with the Vernier PM machines and magnetic gears due to the way the airgap flux is modulated by the stator and rotor teeth [64]. This in turn has implication on the electromagnetic torque production mechanism including its working harmonics. A flux-modulation effect exists which allows generation of steady torque for all aforementioned topologies [65]. For the SFPMM, E-Core and C-Core in [66], Wu *et al* have analysed the airgap field harmonic spectra of a SFPMM as well as an E-Core and C-Core alternatives with various stator/rotor pole number combinations. A similarity between the SFPMM machines and magnetic geared types is found based on the discovery that the rotor teeth provides modulation effect for the PM and armature reaction fields just like the iron pieces in a magnetic geared machine.

1.2.4. FAULTS CLASSIFICATION

The PM machines, as other electrical machines, can experience various faults during their operations. These faults can be classified as:

- Mechanical faults such as rotor eccentricity;
- Electromagnetic faults such as short-circuits (inter-turn, entire coil or phase), open-circuit, magnet demagnetization, etc.
- Thermal faults such as winding local overheating.

It is worth mentioning that the different types of faults are often interlinked. For example, the winding short-circuit can generate high short-circuit current, which is an important heat source and can lead to winding overheating. In this research, the electromagnetic faults are of the main research interest and will be investigated in much more detail. All the electromagnetic faults have serious consequences and need various strategies to be dealt with if post-fault operation is envisaged. Amongst all the electromagnetic faults, the most severe one is the short-circuit fault, followed by irreversible demagnetization and open-circuit ones. If fault-tolerant operation is enabled, each of these faults will ultimately lead to temperature rise, especially the short-circuit which can also cause magnet demagnetization. Moreover, the currents in the healthy coils must be increased to compensate the loss of faulty coils, leading to further increase in copper losses and in temperature. In case of the short-circuit fault, the short-circuit current peak value can be very high – the temperature of the affected coil can increase very quickly provoking further damage in the machine. Furthermore, different from open-circuit faults, the short-circuited coil creates a braking torque, which needs to be compensated by the currents in the remaining healthy coils.

The short-circuit current can lead to another type of fault, the irreversible demagnetization of one or more PMs in two ways:

- by increasing the local temperature in the adjacent PMs,
- by generating a large negative d -axis current with demagnetizing effect.

The irreversible demagnetization fault in the PMs leads usually to an armature current increase in order to compensate for resulting torque loss. This leads to further increase in temperature which leads to aggravation of the demagnetization fault, continuing until the machine stalls. The loop of events which can lead to machine stalling due to evolving demagnetization phenomena is presented for example in [67] and illustrated in Fig. 1.6.

The back-EMF amplitude and waveform is changed, as the PM symmetry of the machine is affected (only associated PMs have been demagnetized). The severity of the demagnetization depends on the type of fault which generates it. For instance, if an inter-turn (small number of turns) short-circuit occurs, then the demagnetization effect is not large enough. This is because the flux (or MMF) generated by the short-circuited turns is not high enough to demagnetize the affected PM. However a large number of short-circuited turns will produce a stronger flux which would demagnetize the PMs more easily.

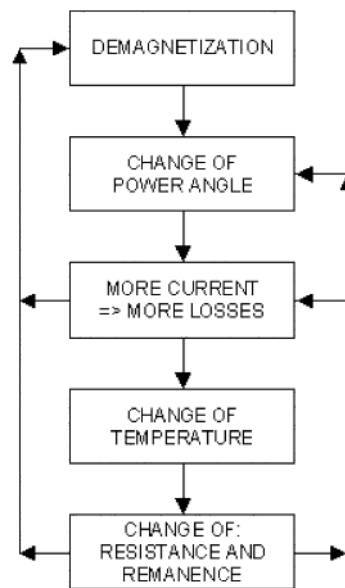


Fig. 1.6 Demagnetization process evolution in PM machines [67].

It is worth mentioning that this is not the only scenario that can lead to demagnetization. In case of high speed applications, flux weakening is used to reduce the terminal voltage (imposed by a limit voltage rating of the inverter). This is done by applying a negative d -axis current to decrease the d -axis flux linkage, thus lowering the working point of the PM. In case of the machines with infinite or large enough speed range, the flux weakening can completely cancel out the PM generated flux, posing a serious risk for magnet irreversible demagnetization.

The methods used to evaluate the demagnetization effect on PM machines range from simple analytical models [68] (for simple topologies), finite element models, up to multi-physics models (coupling electro-mechanical-thermal processes) for complicated topologies with temperature dependent properties [69].

Up to date, the demagnetization possibility in SFPMM is not analysed in the same depth as for other PM machines. A few papers are available, focussing on ferrite and NdFeB based PM machines [70]. In [70] an investigation using magnetic circuits and FEM models has been carried out. It is found that during normal operation (motoring, generating and flux-weakening modes) the SFPM machine does not present the risk of PM demagnetization associated with other types of PM topologies. For example, this is not the case for IPM motor [71]. The analysis of the magnetic flux paths shows that the MMF contributed by the stator windings, in normal operation mode, sums up with the MMF produced by the PMs in order to increase the flux density in the magnets. Furthermore, spatial harmonic analysis carried out on MMFs produced by windings and PMs shows that the harmonic components of the same order are spatially aligned. This analysis however is conducted in healthy mode operation and low temperature, i.e. the

magnets working point is safely above the knee point. In [72], the demagnetization of SFPMM with NdFeB is investigated under healthy mode conditions but over a range of temperatures. It is found that at high temperatures, the PM will eventually demagnetize due to high knee point values.

When it comes to demagnetization due to high current produced by a short-circuit fault, this has not been studied up to date. The short-circuit current leads to temperature increase in the affected winding. The SFPMM has certain characteristics which makes it different from other PM machines. In particular, the PMs are located inside the coil which makes them prone to demagnetization due to temperature increase. This will be investigated in depth in this thesis.

1.2.5. FAULT-TOLERANT OPERATION STRATEGIES

Fault-tolerant operation is of utmost importance in automotive and aircraft industries in order to ensure safety regulations. When it comes to fault occurrence, there are two approaches to limit the damage that might occur [73]:

- through machine design. The objective is to make sure that the fault has either a low probability to occur or it is difficult for it to propagate to other parts of the machine [74], [75], [76], [77], [78];
- through post fault control strategies, [79], [80], [81]. These control strategies will ensure post-fault operation albeit in degraded mode (i.e. with higher copper losses, torque ripple, etc.).

The two approaches are complementary. The motor design solutions were summarized in [73] and they include:

- high phase inductance to limit the short-circuit current peak value. This is also useful to reduce the copper losses and temperature increase. When it comes to the SFPMM, this feature is exhibited by the single layer, C-core and E-core machines;
- phase separation which is necessary to prevent fault propagation between the phases. This includes the thermal, electromagnetic and mechanical separations. Only the single layer and the E-core topologies are suitable from this point of view.
- low mutual inductance which is equivalent with magnetic separation. This is required to prevent the faulty phases from magnetically influencing the remaining healthy phases.
- redundant or multi-phase systems. A higher number of phases (higher than 3) can be used as a solution to provide better post-fault operation. Alternatively a second set of 3-phase (redundant) [74] can be equipped for the armature windings to provide a backup in case of failure in the primary winding set.

The post-fault control strategies are dependent on the type of fault and fault-tolerant objective. The fault must be diagnosed as soon as possible in order to activate the post-fault operation strategy [82] - [83]. The objectives of a post-fault control strategy can include one or several of the following:

- maintain the same average torque [28], [84];
- keep low torque ripples [85] - [86];
- keep low copper losses [87].

Most commonly, the objective of a fault-tolerant strategy is to keep the average torque constant. The presence of a faulty phase means an imbalance in the rotating magnetic field (hence an increase in torque ripples) and a loss of torque. For machines operating under current control [88], the drive will increase the currents in the remaining healthy phases. This is done in order to compensate for the torque loss at the expense of having higher torque ripples and copper losses when compared with the healthy mode. If the machine is designed properly, it can safely operate in faulty mode. This is true for both the open- and short-circuit faults. The open-circuit faults are the easiest to deal with as the affected winding does not heat up and the inverter leg driving the affected phase can be shutdown. The strategy is therefore to modify the current amplitudes and phase angles of the remaining healthy phases.

Most challenging faults are the short-circuit types as there is no control over the short-circuit current. The affected coil is isolated from the control circuits. Moreover, the severity of the short-circuit is determined only by the machine parameters. If the machine topology is designed by default to have fault-tolerant capabilities then the short-circuit current is limited. Moreover in case of redundant or multi-phase machines, if one phase is affected then a controlled short-circuit can be imposed via the inverter [89] - [90]. For example, in case of a dual 3-phase machine, if one of the phases in the primary set is affected then the entire primary set can be short-circuited and the secondary winding set is used. The purpose is to avoid the imbalance resulted from a single short-circuited phase. The three phase short-circuit consequences might be less severe than the single phase one since the short-circuit current amplitude and resulting torque ripple can be lower. The condition that the mutual inductance between the primary and the secondary sets needs to be low is very important.

In [71] for instance, it is found that by carefully controlling the d - and q -axes currents, the irreversible demagnetization fault can be avoided for IPM machines having the PMs made of either ferrite or NdFeB. In [91] a short-circuit fault mitigation technique is proposed called magnet flux nulling for three phase IPM machine. In [92] this technique is extended to an n -phase machine based on instantaneous power balance theory. The technique consists of imposing the flux linkage through the affected coil to be constant. The induced back-EMF and hence the short-circuit current will be zero. The currents supplying

the remaining phases should be adjusted (both amplitude and phase angle) based on relevant objectives like minimum torque ripple, etc. In [93] a general control strategy is given for both the short-circuit and open-circuit faults which reduces torque ripples and copper losses. The current and voltage constraints are considered. Moreover, the strategy is valid in both constant power and constant torque modes. The method consists of determining the amplitudes and phase angles of the healthy coil currents based on minimizing a cost function given by the total flux linkage in the machine.

1.2.6. THERMAL ANALYSIS AND DESIGN

1.2.6.1 IMPORTANCE OF THERMAL MODELLING

The commonality to all PM machines is the risk of demagnetization due to temperature rise caused by short-circuit, overload operation or other abnormal operations. Such operation conditions can be thermally very challenging to electrical machines because the supply current might have a much higher value than the rated one, causing significant overheating (local or global). The effects of temperature on various materials in the motor depends on its value and also operation time. In particular, the insulation and the permanent magnets are the most sensitive to temperature rise. For insulation, surpassing its temperature class limit will lead to accelerated ageing. As a result, the motor lifetime will be reduced significantly. The permanent magnets, depending on their grades and materials, have the ability to withstand a certain level of temperature. However, the temperature effects on the magnets can be irreversible, which might lead to a permanent drop in their performance. This is more stringent in highly dynamic fields like automotive and aircraft where there are restrictions on volume and weight. For the SFPMM and other stator mounted PM machines, the thermal analysis might be even more important as the PMs are located closer to the source of heat, i.e. the coils.

In general, the size of the machine is also dictated by its ability to remove heat. An optimum thermal design translates into a reduced machine footprint and hence possible lower costs and higher torque/power density. This can be achieved by using superior materials, more effective cooling technologies, etc. For example, better steel grade for laminations can be used to reduce the core loss. For an optimal design, several characters of electrical machines need to be considered:

- during operation, the highest temperature (hotspots) often occurs in the stator armature windings;
- there is an anisotropy in terms of heat removal when it comes to the laminations (radial direction). This is due to the stacked laminations structure (to reduce iron losses). Furthermore, there is a thin insulation material (lamination coatings) between lamination sheets to prevent eddy currents in axial direction. However, this layer also greatly reduces the heat flow in the axial direction;

- windings anisotropy– the heat flow has also a preferred direction (axial) due to the fact that inside the stator slots, the copper wires are oriented in the axial direction. In the radial direction the heat flow is poor because the combination of copper wire, insulation and impregnation varnish results in poor thermal conductivity. This results in a large temperature gradient between the middle of the slot and slot wall.
- the slot liner also has a poor thermal conductivity, which might increase even more the stator slot temperature.

For an accurate design or analysis, these factors must be considered. In addition, due to the existing of two preferred heat flow directions, the model needs to take into account 3D effects as well.

1.2.6.2 COOLING METHODOLOGIES

In order to keep the temperature rise within the normal limits, a cooling system might need to be employed. The cooling solution can be forced cooling (air, water or oil) or natural cooling based [94]. Depending on the cooling method employed, the heat removal can be in radial and/or axial direction and there are various types of motors depending on these features.

Axial cooling involves a fan (centrifugal or axial type) mounted on the rotor shaft. The fan operates by creating a large difference in pressure allowing the fluid (air) to circulate and cool down the motor surfaces through forced convection process. The fan can be mounted outside the machine (TEFC – Totally Enclosed Fan Cooling solution [95]) or inside the machine (with a strong inflow which may contain also dust, debris, etc.), as shown in Fig. 1.7. The latter requires ducts or vents in the front and back plates or channels in the motor's housing in order to allow the external air to be circulated inside the machine. Adopting one solution or another depends on the industry safety requirements as well as motor lifetime specifications.

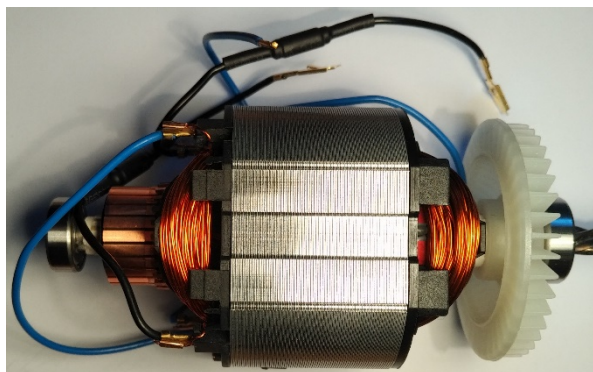


Fig. 1.7 Example of axial cooled motor (electric power tools application).

A fan cooling solution is suitable for high speed applications as the airflow will increase with speed. However the ventilation losses and generated noise will also increase significantly with speed. In particular the ventilation losses depend on cube of speed [96]. There are however, additional limitations at lower speed operations which might not generate enough airflow to effectively cool the motor. Therefore a more suitable solution would be to use radial cooling. These can be either passive using a housing with fins or using water jackets (Fig. 1.8) or copper pipes circulating the cooling fluid inside stator slots. More complicated cooling solutions (for special applications) include techniques like spray cooling [94] or hybrid cooling (involving both axial and radial methods, water jacket outside and rotor mounted fan inside the machine housing) in order to achieve the maximum compactness possible. For spray cooling method a nozzle sprays the cooling liquid onto end-windings. Upon contact with the hot surfaces it partially evaporates being recovered later by using a condenser. The condenser will drain the liquid out in a reservoir which will also collect the unevaporated liquid. This kind of cooling is very effective, because the change of phase for coolant can achieve a convection coefficient of around 500 – 50000 W/k/m² while it can only be around 200 – 25000 W/k/m² for the forced water cooling.

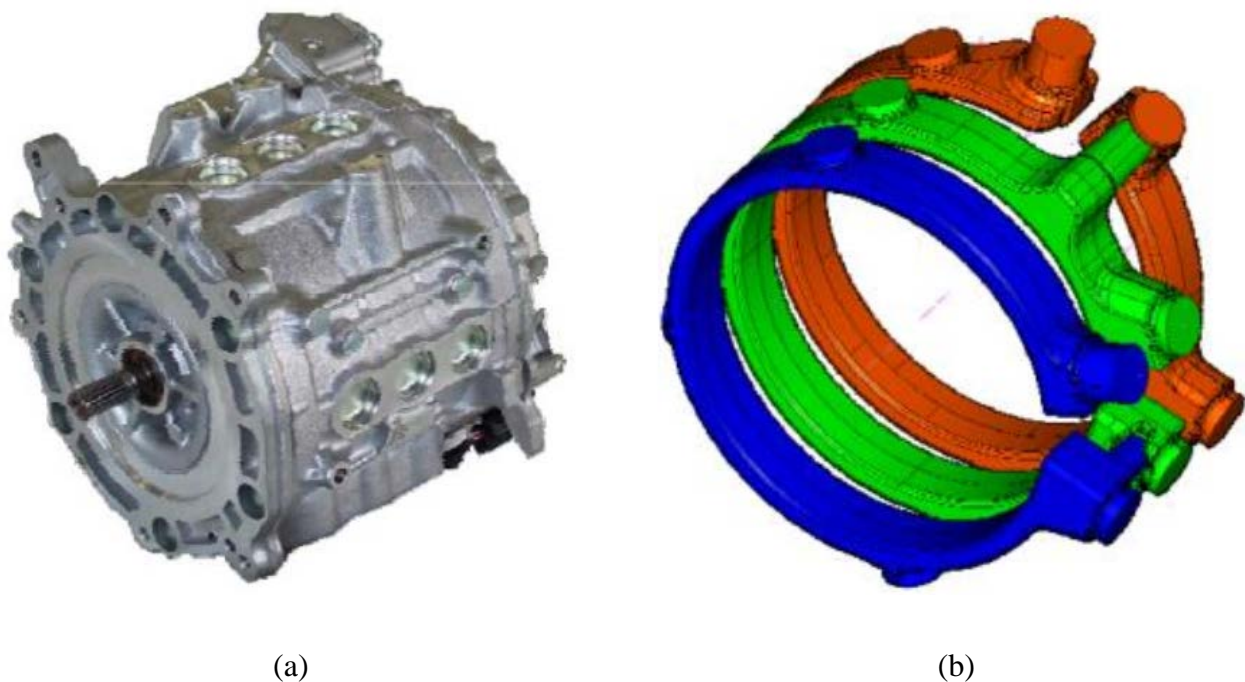


Fig. 1.8 Nissan Leaf electric motor using radial cooling [94]. (a) the motor, (b) channels in the water jacket.

1.2.6.3 THERMAL MODELLING METHODS

The most basic approach for thermal analysis is based on lumped parameter circuit models which are

used as early as in 1931 [97] for their simplicity. MotorCAD developed by Motor Design Ltd [98] is a well-known thermal analysis package based on lumped parameter (LP) thermal circuits which simplifies the design and allows a very fast solving process. In a LP thermal circuit model (Fig. 1.9), the heat flow is equivalent with current and temperature with voltage (based on analogy with DC electric circuits). It is an entirely passive circuit with the thermal capacitor being responsible for imposing the temperature evolution and its value depends on the volumetric heat capacity of the material considered. The resistors are used to model various heat flow paths in the machine.

The LP thermal circuit is a flexible modelling tool which can be extended to account for other conditions for example the airflow through the machine. Jokinen in [99] shows that by adding heat flow controlled sources (corresponding to current controlled sources in electrical circuits) the coolant flow can also be considered. This is important because often the thermal analysis needs to consider the various cooling systems and conditions. In this respect, one of the more challenging parts consists in properly imposing a certain type of boundary conditions on heat exchange surfaces called the convection coefficients. These parameters describe the ability of that surface to exchange heat with surrounding area using the convection phenomena. They depend on a range of other quantities like the speed of airflow or the surface temperature. In order to accurately estimate these coefficient values, fluid dynamics can be employed [94]. Previous works in literature have established simple analytical formulas suitable for a large number of commonly encountered cases. However there are lots of complex motor topologies which require estimation of convection coefficients using computational fluid dynamics (CFD), which is also one type of finite element (FE) modelling.

When it comes to FE models for thermal analysis, different from electromagnetic analysis, most machines need a 3D geometry. The reason is that the end-winding component cannot be ignored anymore. There is a strong heat flow in the axial direction (parallel with the rotor axis) in the windings of the electrical machines. The heat is carried out towards the end-winding where it is exchanged with the environment through the convection process.

More complicated multi-physics models in which the electromechanical domain is coupled with the thermal one can also be employed to accurately predict temperature distributions within electrical machines [100]. These can be as simple as a magnetic circuit LP model coupled with a thermal LP model of the electric motor or as complex as coupled 3D FE models (both non-linear electromechanical and thermal). Most FE software packages nowadays will include a thermal module and/or the possibility to couple it with a FE electromechanical module. Challenges in using these complex models include the added complexity in building accurate CAD geometries as well as the increased requirements for

computational resources.

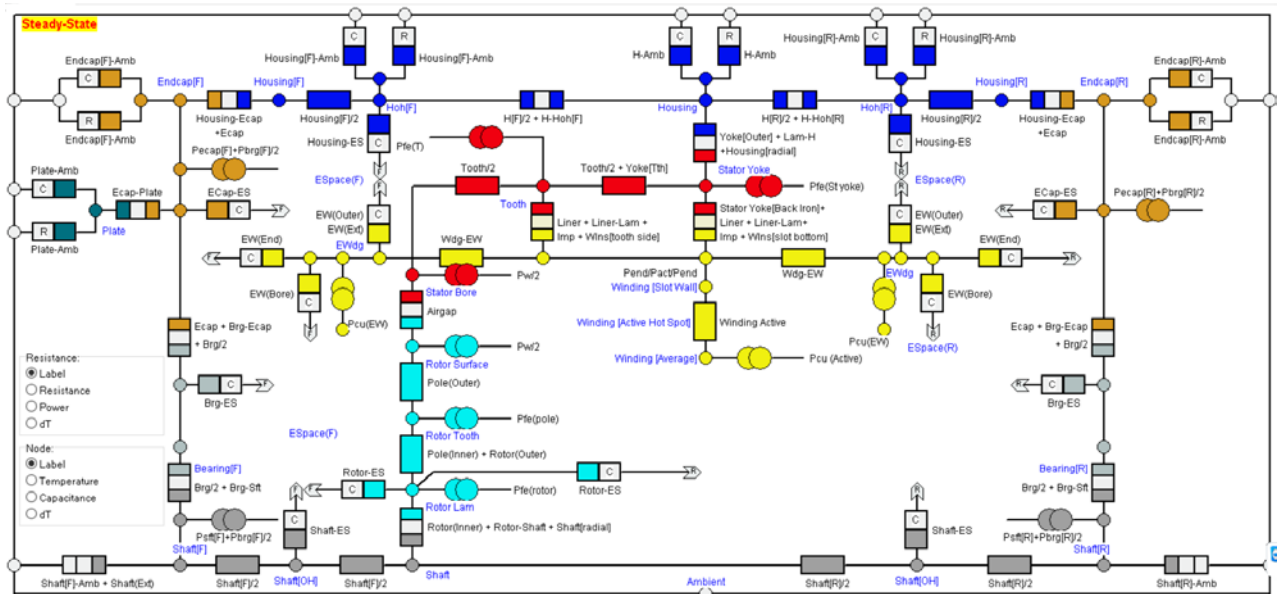


Fig. 1.9 Details of the LP modelling in MotorCAD package [98].

1.3. RESEARCH SCOPE AND CONTRIBUTIONS

In this section, the research scope of this thesis is defined. It revolves around stator mounted PM machines studied under fault conditions. The studied topologies of interest are the SFPMM (and its derivatives the C-Core, E-Core and modular machines), the DSPMM and the FRPMM. These are studied under short-circuit and PM demagnetization conditions. The hybrid excitation as well as multiphase versions of these machines have been left out due to the limited time for this PhD study. However, it is worth mentioning that the hybrid excitation machines, due to the presence of their DC windings, allow an extra degree of control during the short-circuit conditions thus potentially improving the post-fault performance. The multiphase machines distribute their MMF on multiple phases, thus reducing the severity of faults in one single phase. These aspects will be part of our future works. The C-Core, E-Core and modular machines are added into the study due to two reasons. Firstly, they can introduce some degree of electromagnetic and thermal separations between the phases, particularly the E-core and modular topologies, which is not present in the conventional SFPMM. Secondly, they require less PM material and their connection to the conventional SFPMM can help to understand the conventional SFPMM better.

This thesis consists of 6 chapters as follows:

Chapter 1 introduces the topics approached in the present study. A literature review is provided in order to put in context the subject of this thesis. The topologies investigated in the thesis are introduced and compared with other PM machines and their advantages and disadvantages are discussed. The research scope and a brief description of each chapter are also provided.

Chapter 2 compares the double layer SFPMM, DSPMM and FRPMM machines under faulty modes. Both the short-circuit and demagnetization faults are studied. It introduces the models and methods used in the following chapters as well. Experimental results at low speed are also provided for the SFPMM.

Chapter 3 focuses on the investigation about the conventional SFPMM and its derivatives. It establishes a link between the SFPMM, C-Core, E-Core and modular machines via a dimensional parameter called flux-gap. The influence of rotor poles is also considered. All the models in this chapter concerns healthy mode only. The performance is investigated and experimental results in terms of cogging and static toques, back-EMF and inductance are compared with the predicted ones.

Chapter 4 compares the demagnetization and short-circuit features of the SFPMM and its derivatives for both low and high speed short-circuit faults. The temperature dependence of the PM characteristics is also considered. The effects of the temperature and short-circuit current on demagnetization process are separated and discussed. The irreversible demagnetization mechanism for the SFPMM and its derivatives is analysed. Using the outcome of this chapter, a hierarchy of these machines based on their fault tolerant capabilities is established.

Chapter 5 proposes an effective and accurate multi-physics model to determine the thermal distribution in critical parts of the machine like PMs and windings. Both faulty and healthy operation modes are analysed. This chapter builds on previous ones by coupling the electromechanical model developed there with a 3D transient thermal finite element model. The result is a flexible multi-physics model which reduces considerably the computational time for the solving process while still providing accurate results. Experimental results concerning temperature variation before and after short-circuit have been obtained to validate the predictions.

Chapter 6 gives a general conclusion of this thesis and also provides some meaningful research directions for future works.

The contributions of this thesis are from a few different aspects about fault tolerant electrical machines used in both industry and academia, and a list is shown as following:

- 1) Establishing a hierarchy in terms of fault tolerant features as well as the performance/cost for stator mounted PM machines (SFPMM, DSPMM and FRPMM – Chapter2). The PM properties are

considered temperature dependent. This chapter also concludes that for these topologies, the irreversible demagnetization occurs mainly due to temperature rise within the PM. The demagnetizing effect of the MMF generated by the short-circuit current is negligible due to the particular magnetic circuit structure for these topologies.

- 2) Unify the SFPMM derived topologies using the flux-gap parameter (Chapter 3). Extensive coverage of these topologies is provided for 10, 11, 13 and 14 rotor poles identifying the best candidates from performance point of view.
- 3) A study of the SFPMM and C-Core and E-Core machines highlighting their response to fault behaviour. The irreversible demagnetization process is explained based on the particular magnetic circuit configuration of the SFPMM (and its derivatives - Chapter 4).
- 4) A multi-physics thermal model suitable for accurately accounting for both the short-circuit and the over-heating. The model is further used to analyze the effect of the fault conditions for a conventional double layer SFPMM. It also validates the assumptions done in previous chapters which are using much simpler models. It provides the means to assess the demagnetization more precisely by looking at temperature distribution in the PM. It has found that the irreversible demagnetization occurs due to temperature increase and this was already established in previous chapters. However, it is found out that when the short-circuit occurs, it will take a few minutes to reach the demagnetization temperature threshold. This leaves enough time to detect the fault which can be achieved in several electrical cycles, thus allowing corrective measures to be put in place.

1.4. PUBLICATIONS LIST

Based on the above contributions, throughout this PhD study, 4 IEEE/IET journal papers and one international conference papers have been published. A list of these publications is given as following:

1. P. Taras, G. J. Li and Z. Q. Zhu, "Comparative study of alternative modular switched flux permanent magnet machines," *2015 IEEE International Conference on Industrial Technology (ICIT)*, Seville, pp. 658-663, 17-19 Mar. 2015.

2. G. J. Li, P. Taras, Z. Q. Zhu, J. Ojeda and M. Gabsi, "Investigation of irreversible demagnetisation in switched flux permanent magnet machines under short-circuit conditions," in *IET Elec. Power Appl.*, vol. 11, no. 4, pp. 595-602, Apr. 2017.

3. P. Taras, G. J. Li and Z. Q. Zhu, "Comparative study of fault-tolerant switched-flux permanent-magnet machines," in *IEEE Trans. Ind. Electron.*, vol. 64, no. 3, pp. 1939-1948, Mar. 2017.

4. P. Taras, G. J. Li, Z. Q. Zhu, M. P. Foster, and D. A. Stone, "Comparative investigation of stator

mounted permanent magnet machines under fault conditions,” in *IET The Journal of Engineering*, July 2018.

5. P. Taras, G. J. Li, Z. Q. Zhu, M. P. Foster, and D. A. Stone, “Combined Multi-Physics Model of Switched Flux PM Machines under Fault Operations,” accepted for publication in *IEEE Trans. Ind. Electron.*, Nov. 2018.

Chapter 2. Comparative Investigation of Stator Mounted Permanent Magnet Machines under Fault Conditions

In this chapter, machines having permanent magnets (PM) mounted in the stator are compared during fault operations such as armature winding short-circuits. The magnet potential irreversible demagnetization is also investigated due to the fact that the permanent magnets are placed close to the armature coils (heat sources), and hence are prone to temperature related demagnetizations. It is found that the doubly salient and flux reversal machines have inherently higher fault tolerant capabilities when compared with the switched-flux one. From the point of view of demagnetization withstand capability, the doubly salient topology stands out as the most robust one, while the switched flux is the weakest one.

2.1. INTRODUCTION

The topologies considered in this chapter, as shown in Fig. 2.1 (a)-(c), are the switched-flux permanent magnet machine (SFPMM) [101], the doubly salient permanent magnet machine (DSPMM) [11] and the flux reversal permanent magnet machine (FRPMM) [12]. In such machines, both windings and PMs are located in the stator and therefore are stationary. The three topologies differ amongst them by the PM locations in the stator magnetic circuit. For the SFPMM, the magnets are sandwiched between two iron segments in the middle of the stator teeth. The DSPMM has the magnets in the back-iron while the FRPMM contains them at the surface of the stator teeth adjacent to the airgap. Each of these machines possess challenges, for example SFPMM topology can easily saturate the adjacent iron segments while the FRPMM PM volume is limited due to effective airgap constraints.

The rotor is a salient piece of iron, making the entire structure very robust at high speeds. Since both the windings and the PMs are located on the stator, making their cooling much easier compared to the traditional stator mounted permanent magnet machines or rotor wound field synchronous machines. Potential applications of these topologies are in the automotive [102] and aircraft industries as with appropriate cooling, their volume can be reduced to competitive levels.

It has been established in literature [25], [59] and [60] that compared to the SFPMM, the DSPMM and the FRPMM have performance limitations due to the location of PMs and their magnetization directions. For the DSPMM, its flux linkage is unipolar, leading to limited induced phase back-EMF. For the FRPMM, having the PM located in the airgap is problematic, which exposes them to the demagnetization issues due to generally small PM thickness. The SFPMM on the other hand, has been favourably compared with established topologies like the surface mounted and interior permanent magnet machines [59], [103].

However, having the PMs located closer to the windings (heat sources) in the stator-mounted PM machines raises the issue of potential magnet irreversible demagnetization [70], [104] and [105]. This can be even more serious under fault operation such as inter-turn short-circuit which can lead to significant local temperature increase. Moreover, the fault tolerant capabilities under inter-turn short-circuit fault for the SFPMM, the DSPMM and the FRPMM have not been compared in literature. To fill in this gap, a comparison from the point of view of irreversible demagnetization is essential for all three considered topologies and will be carried out in this chapter.

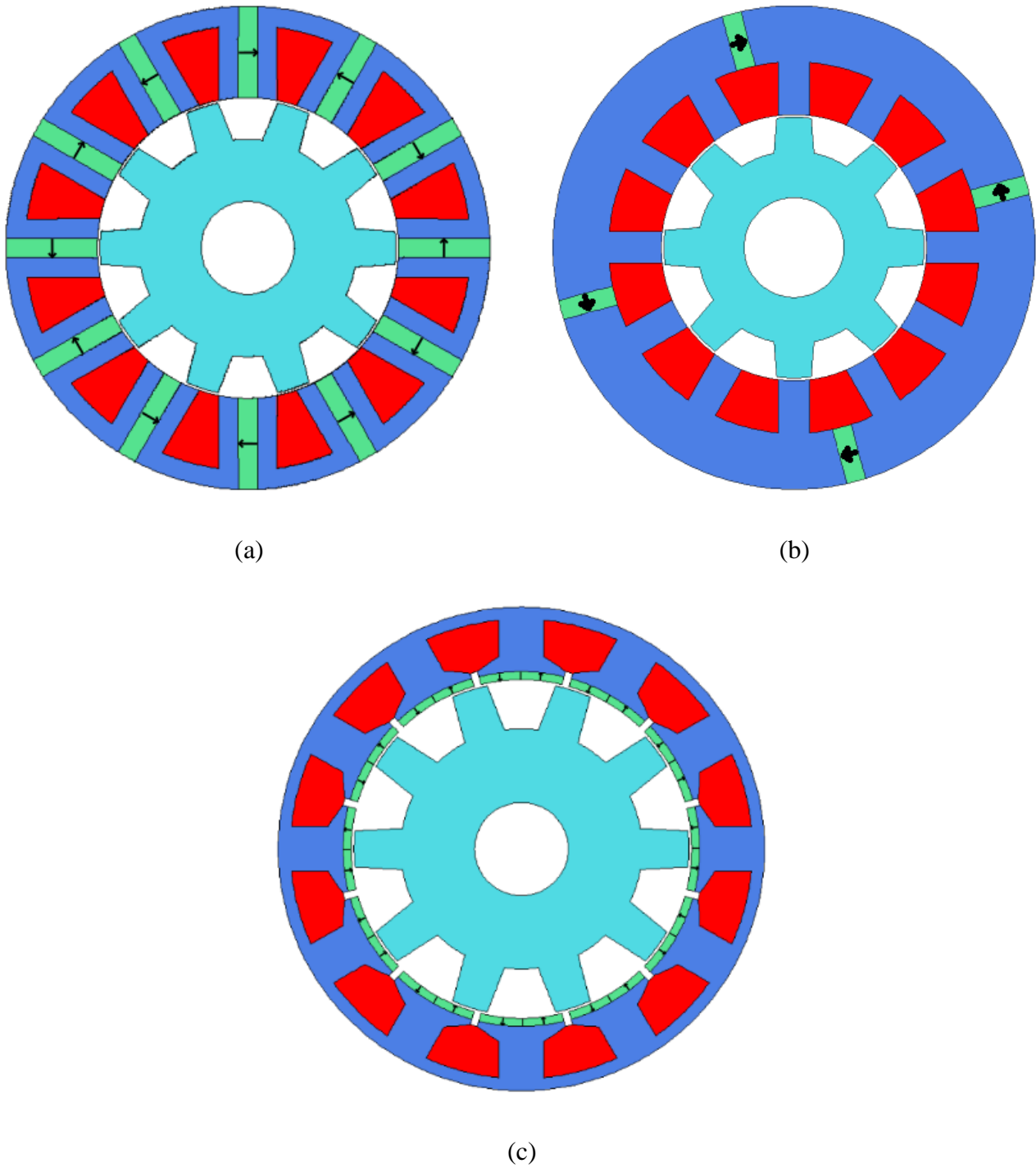


Fig. 2.1. Cross-sections of stator mounted PM machines investigated in this chapter. (a) SFPMM, (b) DSPMM, (c) FRPMM.

2.2. MODEL DESCRIPTION

The specifications of the investigated machines are given in Table 2.2. In order to make a fair and simple comparison, the outer diameter and active length, the winding cross-section area, the number of turns, slot

fill factor and the rated current are the same for all machine topologies. This in turn ensures that the copper losses, an important source of heat, are kept the same. In addition, for all topologies, the windings are double layer type. However, the machines have been optimized to achieve the highest possible average torque while respecting the above constraints.

The optimization procedures modifies the following parameters

- Split ratio
- Stator tooth tip arc length
- Rotor tooth tip arc length
- PM thickness

Initial optimization process started from the volume and split ratio defined for [3] which were applied for all initial geometries. Then the optimization process was applied to all topologies, leading to the following results:

TABLE 2.1

SPECIFICATION OF INVESTIGATED MACHINES (SFPMM/DSPMM/FRPMM)

Machine	Initial torque [Nm]	Optimised torque [Nm]
SFPMM	2.27	2.64
DSPM	0.90	1.01
FRPMM	1.08	1.56

It is found that the SFPMM can produce much higher torque than the other two machines with the DSPMM being the lowest one. However, the DSPMM and the FRPMM require a much smaller PM volume than SFPMM (see Table 2.2), making them more attractive from the cost point of view. The permanent magnet grade, for all topologies, is N35H [106].

TABLE 2.2

SPECIFICATION OF INVESTIGATED MACHINES (SFPMM/DSPMM/FRPMM)

Stator slot number	12	RMS rated armature current [A]	11
Rotor pole number	10/8/10	Average torque [Nm]	2.6/1.0/1.6
Stator outer radius [mm]	45	PM volume [mm ³]	18360/3750/5460
Split ratio	0.62/0.55/0.70	PM thickness [mm]	3.6/3.6/1.2
		Torque/PM volume [mNm/mm ³]	0.14/0.267/0.275

In this chapter, there will be three stages in the investigations:

- (1) 2D FE models parameters extraction;
- (2) Matlab/Simulink models of healthy and faulty operations;
- (3) 2D FE models using an accurate PM model (but also more time consuming to solve) to assess demagnetization occurrence.

Firstly, the 2D FE models of the aforementioned machine topologies are developed to extract characteristics such as the cogging torque, the self- and mutual-inductances and the back-EMF which are both rotor position and temperature dependent. The thermal characteristics are obtained by considering the PM material working at the assumed temperatures.

Secondly, these results are stored in look-up tables and used in the Matlab/Simulink models that implement the voltage and torque equations (A.1) and (A.2) from the Appendix. The control diagram from Fig. A.2 in the Appendix is also used to maintain the torque and speed references during both healthy and faulty conditions. The used strategy is the Maximum Torque Per Ampere (MTPA).

This model is able to consider both the healthy and the faulty conditions. The faulty condition assumes that a single coil out of 4 is short-circuited (fault severity is 25%) and that the adjacent PM works at a higher temperature due to the inter-turn short-circuit, Fig. 2.2. The cases with different numbers of turns short-circuited can also be investigated using similar approaches.

For simplicity, the rest of the PMs are assumed to work at 25°C. This assumption might be questionable and to be more accurate, the thermal modelling of the entire machine before and after the short-circuit is needed. However, this is out of the scope of this chapter and will be investigated in detail in chapter 5.

Thirdly, the finite element models are used again to assess the PM irreversible demagnetization. They rely on output from the previous Matlab/Simulink models, namely the rotor position and current waveform variations in time. In order to accurately account for the demagnetization, a special PM material model, as shown in Fig. 2.3, is used. This can recalculate the local map of remanent flux density within the affected PM if the local flux density drops below the knee point, which also means that the magnet is irreversibly demagnetized. The PM operation point, w , is compared with the knee point magnetic field H_k at each time step. If the local magnetic field has dropped below the knee point value, say the point d , the new PM operation point w' is established along a recoil line given by point d and B_r' . In this manner, performance degradation due to demagnetization can be considered.

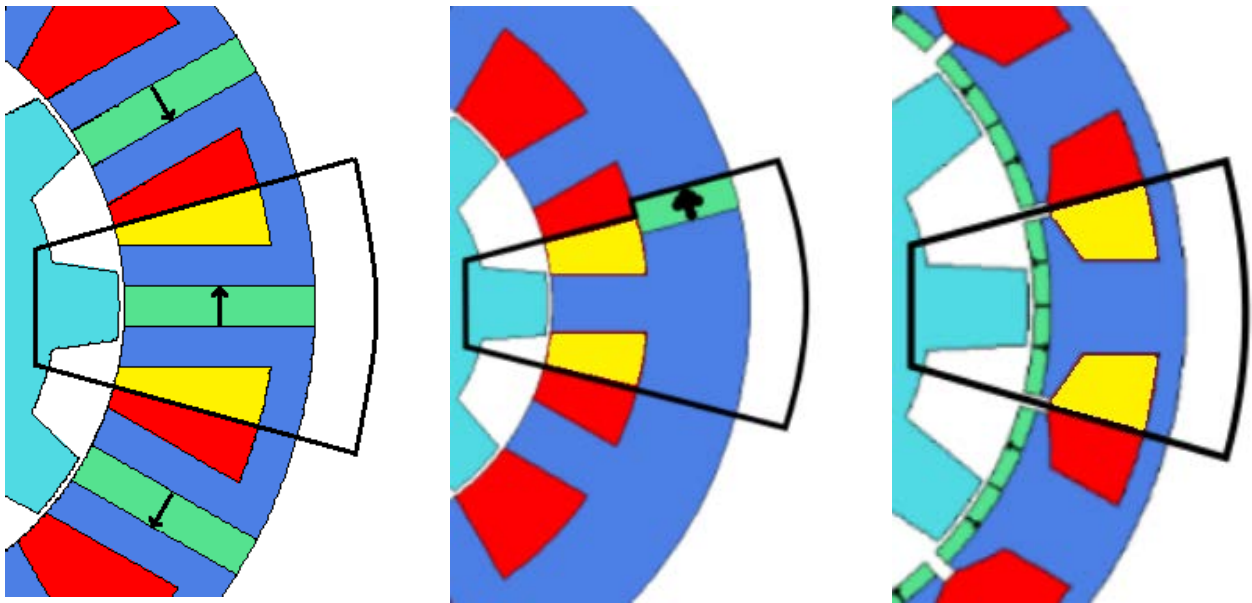


Fig. 2.2 Inter-turn short-circuit coil and PM locations.

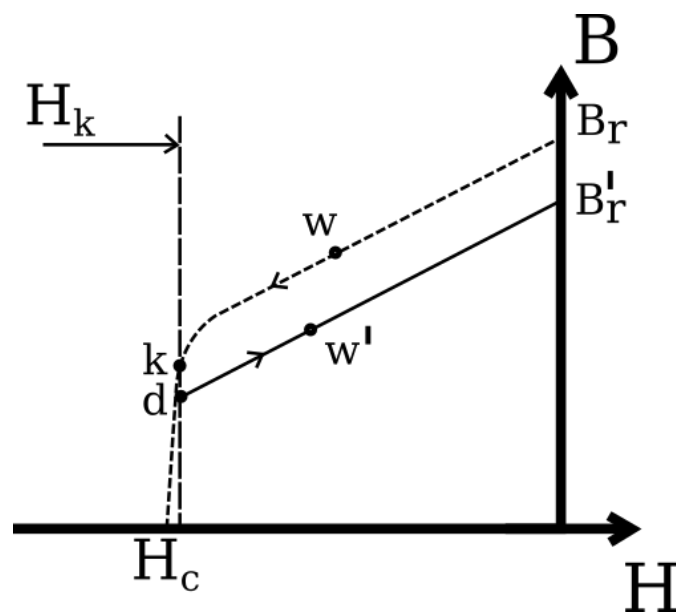
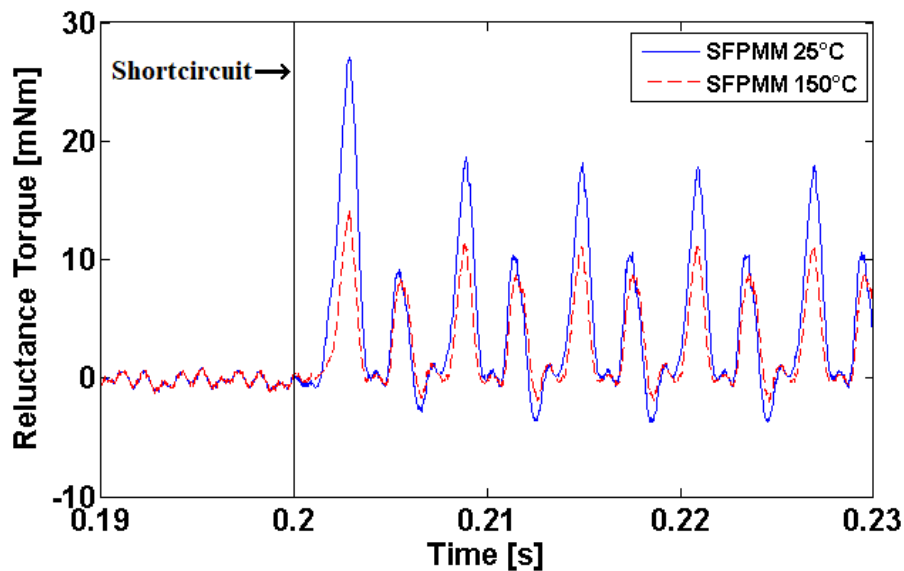


Fig. 2.3 The PM model used to assess the irreversible demagnetization.

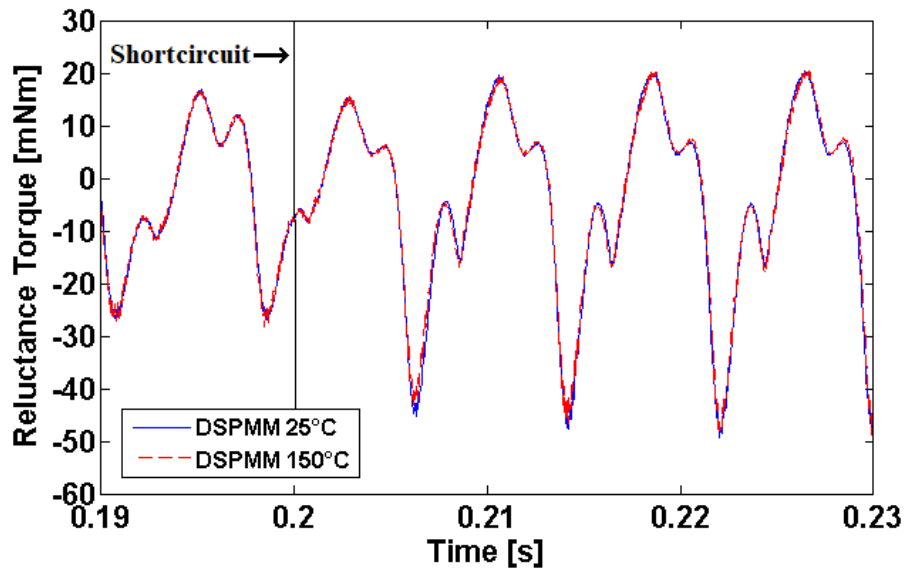
2.3. PERFORMANCE DURING HEALTHY AND FAULTY OPERATION

2.3.1. RELUCTANCE AND COGGING TORQUES

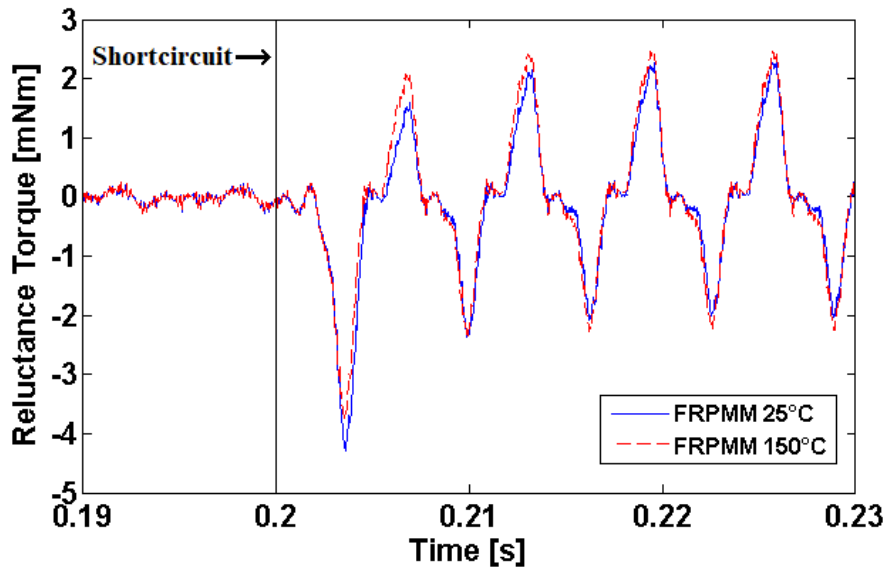
As shown in equation (A.5) in Appendix, these quantities are affecting the torque balance in the mechanical equation. The temperature rise will affect them. For example, the cogging torque will be changed due to PM property variation with the temperature and the reluctance torque will be changed due to the unbalance introduced by the short-circuit current. The next set of results concerning the reluctance torque were obtained using Matlab/Simulink models. The reluctance torque requires the inductance variation with the rotor position and the current variations and its expression was given in Appendix (equation A.7). The inductance variation with rotor position is computed in the first stage using FE models then used in look-up tables in the Simulink model. The reluctance torque variation before and after the short-circuit (0.2 s) is shown in the following figures for the three investigated machines:



(a)



(b)



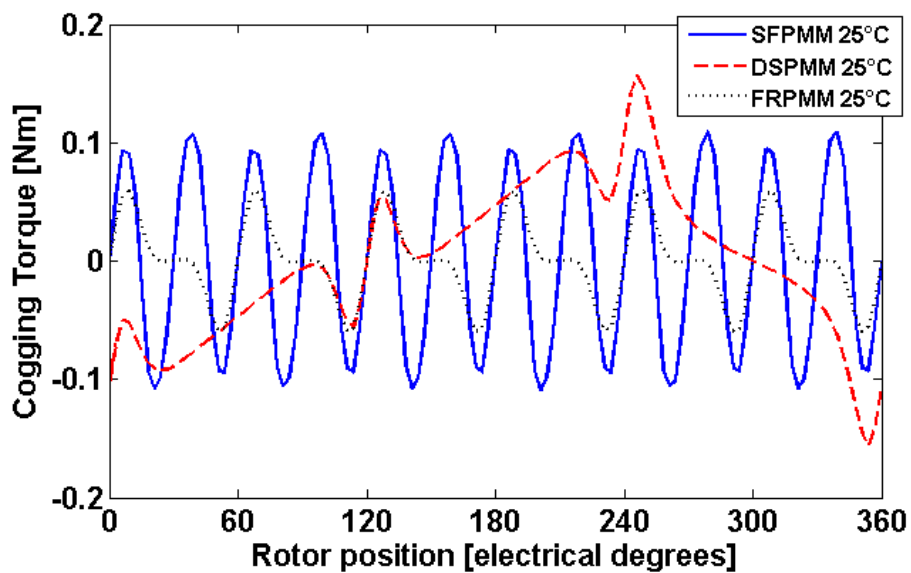
(c)

Fig. 2.4 Reluctance torque for low and high temperatures during both healthy and short-circuit operation. The fault is introduced around 0.2s mark. (a) SFPMM, (b) DSPMM, (c) FRPMM.

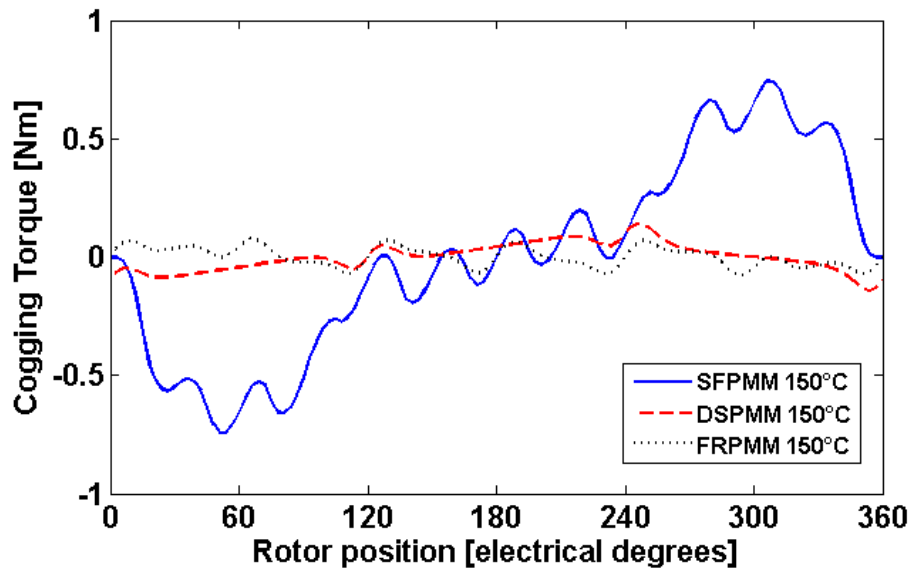
It can be noticed that during healthy conditions, the reluctance torque is negligible, a result which agrees with the findings in literature. An increase in the reluctance torque (both average and peak-to-peak values) after the short-circuit can be observed for the SFPMM. Moreover, this topology also

displays a difference between the short-circuit at low and high temperatures. Despite the fact that the short-circuit increases the peak to peak value for the reluctance torque, the average value for this torque component however is extremely small ($< 5\text{mNm}$).

When it comes to the cogging torque, its influence is non negligible, especially if temperature is considered. Due to the fact that all three machines have a salient structure, the resultant cogging torque is important, producing noticeable ripples in the on-load torque waveforms. The cogging torque waveforms are computed for various temperatures using 2D FE models then stored in look-up tables and will be used further in the Matlab/Simulink models. Fig. 2.5 (a) and (b) show the cogging torque variations of the three investigated machines for low and high temperatures.



(a)



(b)

Fig. 2.5 Cogging torque comparison. (a) 25 °C, (b) 150 °C.

Fig. 2.5 shows that at low temperature the FRPMM has the smallest cogging torque while the DSPMM has the highest. However, when it comes to the on-load torque at rated condition, the DSPMM will have the highest torque ripple reported to the rated torque value (1 Nm - Table 2.2). It has also been found that increasing the temperature of one PM will increase the peak to peak cogging torque for the SFPMM and the FRPMM and slightly decrease it for the DSPMM as shown in Table 2.3.

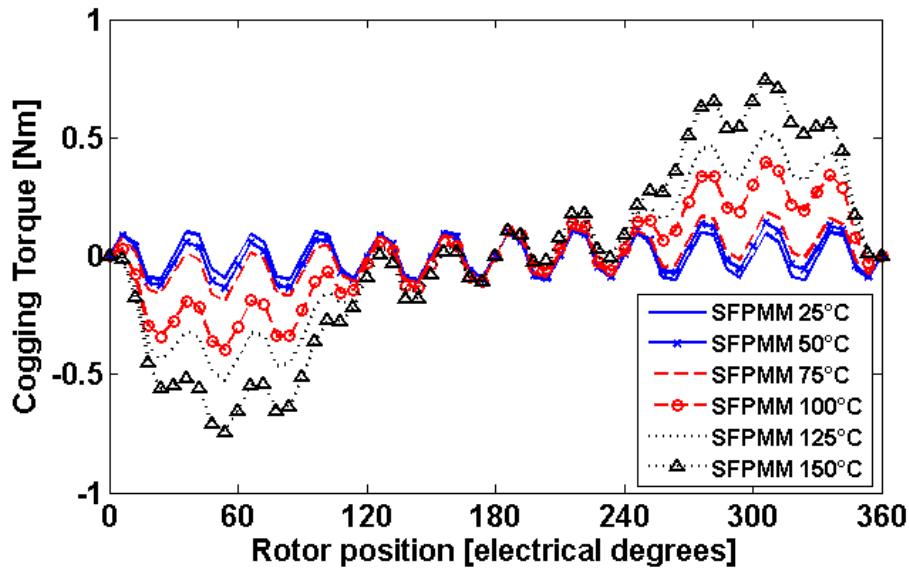
TABLE 2.3

COMPARISON OF PEAK-TO-PEAK COGGING TORQUE [NM]

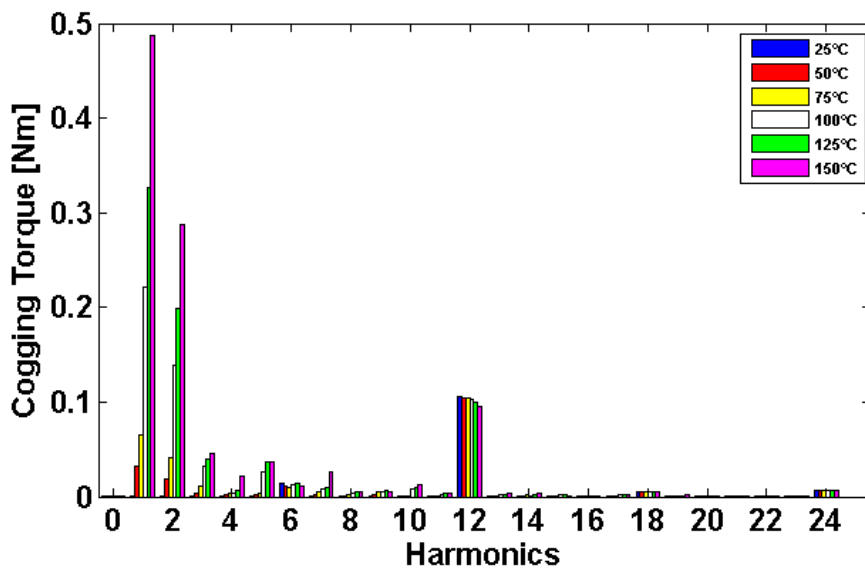
	SFPMM	DSPMM	FRPMM
25 °C	0.217	0.312	0.119
150 °C	1.487	0.286	0.158

In particular, the variation of the cogging torque with temperature for SFPMM is investigated further as it is the most important one when compared with the DSPMM and FRPMM. The position 0 electrical degrees in Fig. 2.6 corresponds with the affected PM axis (the central line in radial direction of the affected PM, as shown in Fig. 2.2). It can be seen how the first and second harmonics become more and more important with temperature rise, breaking the initial symmetry and accentuating the imbalance around 0° position. At the same time, the main harmonic (12th) under healthy conditions decreases slightly with

temperature. These considerations, along with the fact that the cogging torque leads to important torque ripples (which needs to be compensated by control strategy), requires that the cogging torque must be considered in the Matlab/Simulink models for more accurate predictions.



(a)

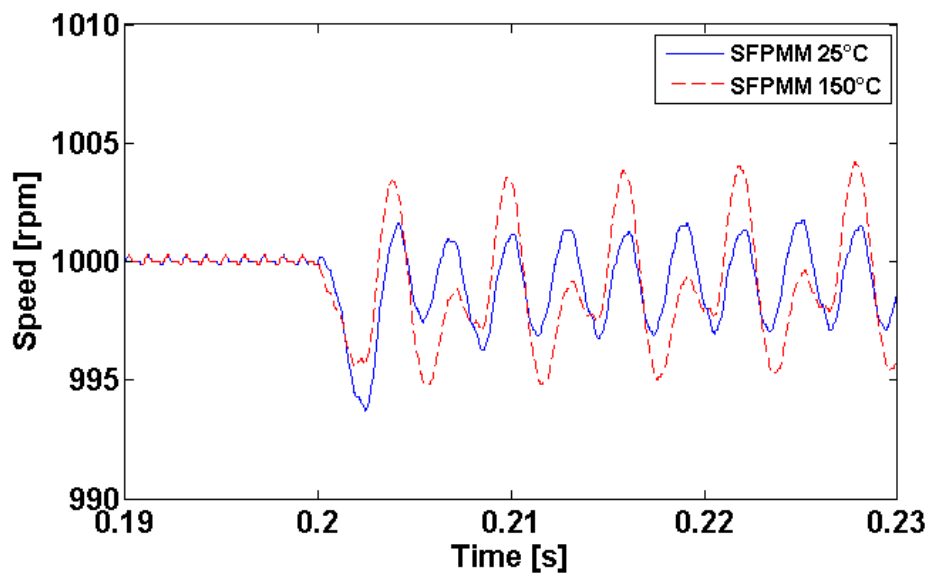


(b)

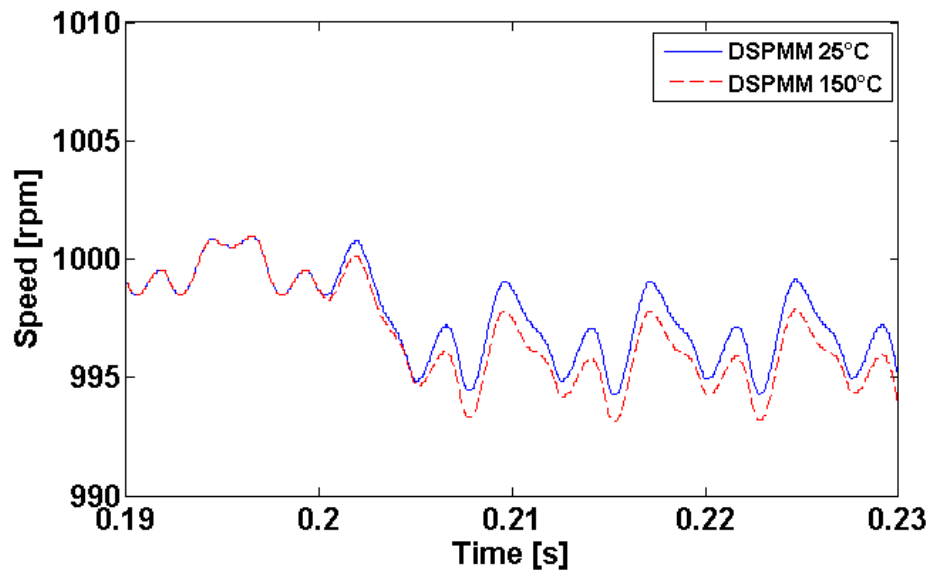
Fig. 2.6 Cogging torque variation with temperature (SFPMM). (a) waveforms, (b) spectra. In this figure, only one magnet is affected, and the temperature of other magnets are assumed to be constant (25°C).

2.3.2. PERFORMANCE IN DEGRADED MODE

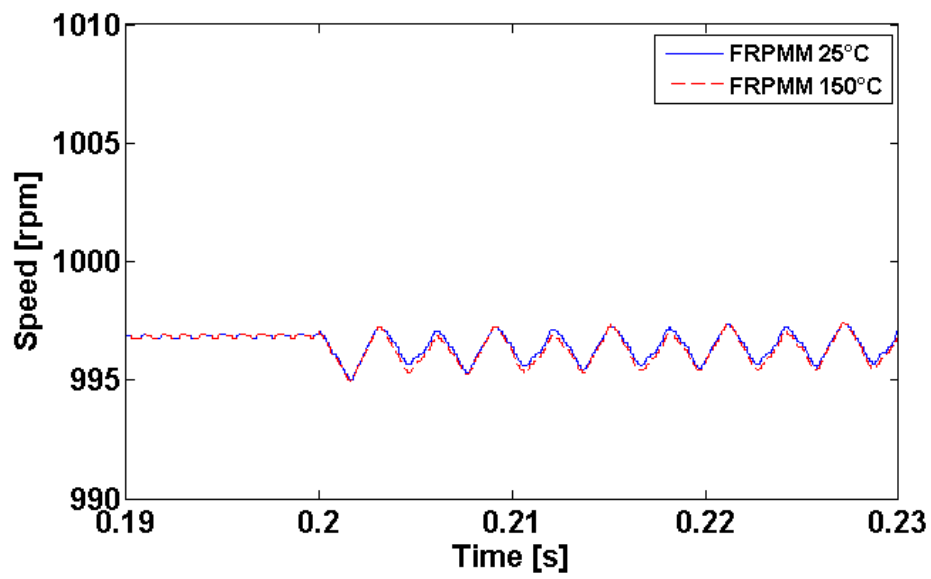
In this section, parameters related to dynamic performance like the torque and speed are investigated for all machines at both low and high temperatures. It is worth noting that the affected coil is generating a so called drag torque. This torque is acting as a braking torque opposing the useful torque generated by the unaffected parts of the motor, leading to a significant drop in the resultant torque, which needs to be compensated by control strategy. The speed responses will be different for each machine, as the control parameters vary from topology to topology. The SFPMM topology exhibits noticeable increase in speed and torque ripple with temperature which has not been observed for the DSPMM and FRPMM.



(a)

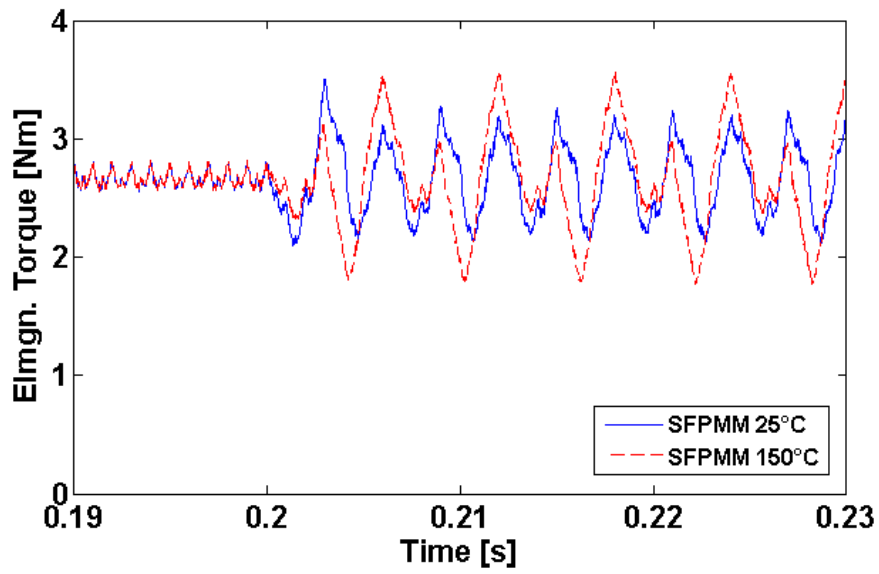


(b)

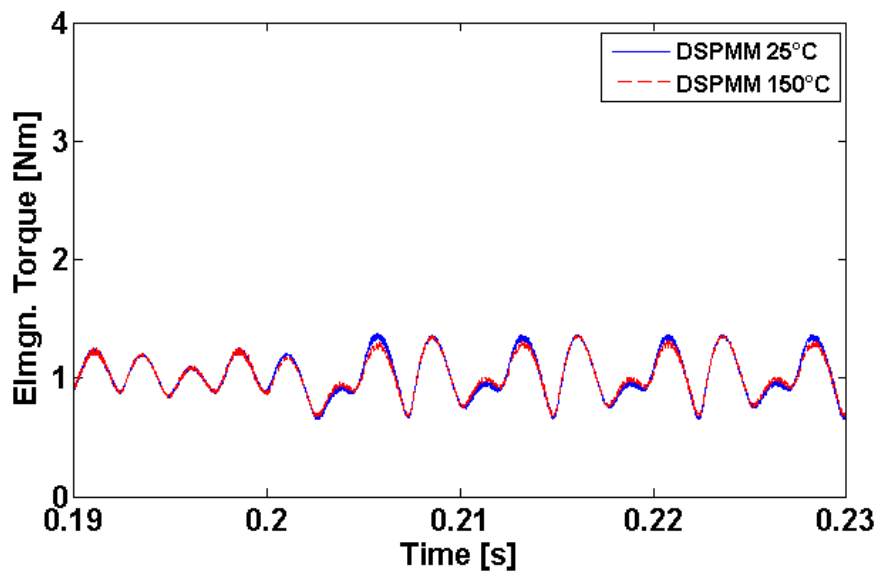


(c)

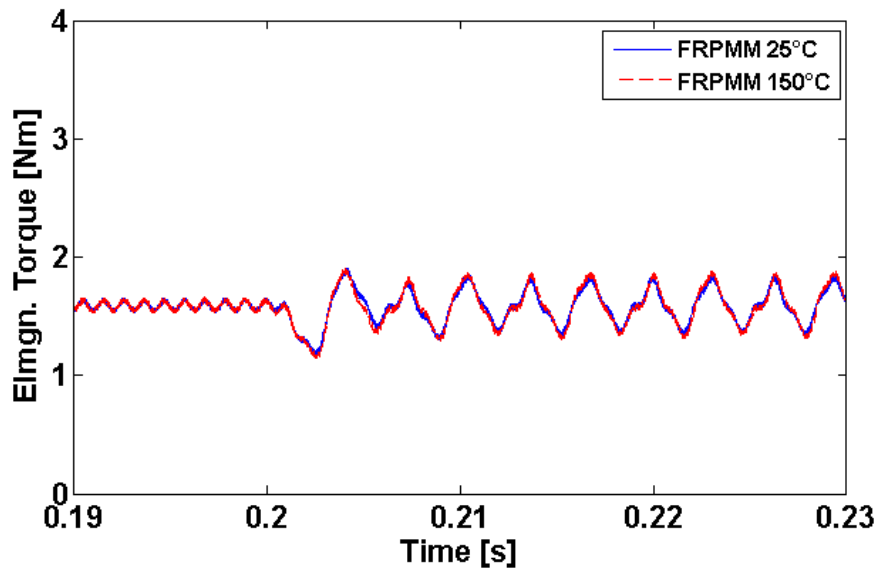
Fig. 2.7 The speed waveforms comparison for different temperatures. The short-circuit occurs at 0.2 s. (a) SFPMM, (b) DSPMM, (c) FRPMM.



(a)



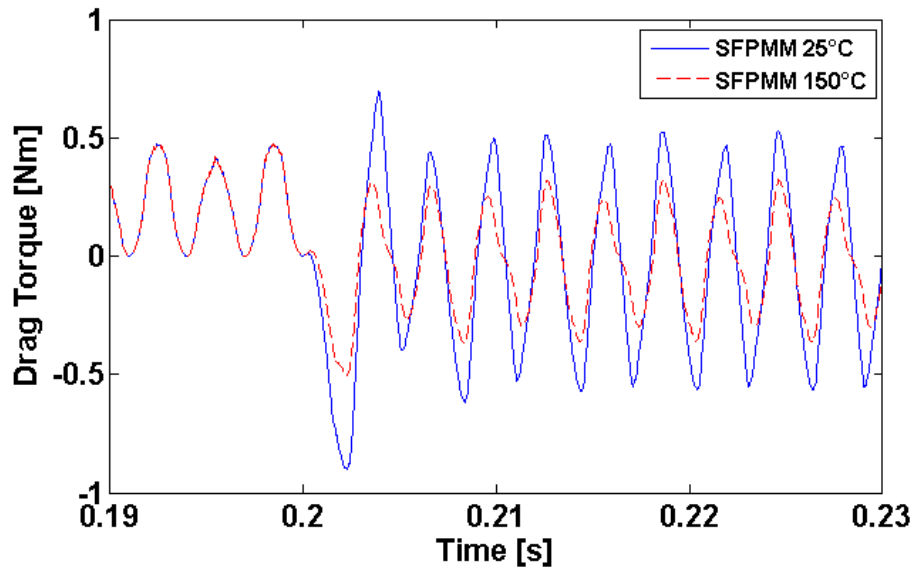
(b)



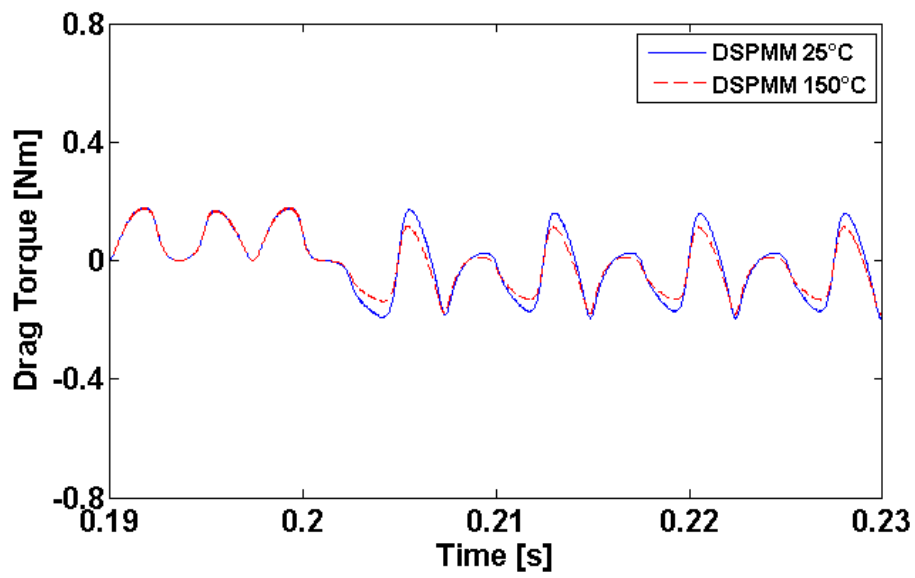
(c)

Fig. 2.8 Torque waveforms comparison for different temperatures. The short-circuit occurs at 0.2 s. (a) SFPMM, (b) DSPMM, (c) FRPMM.

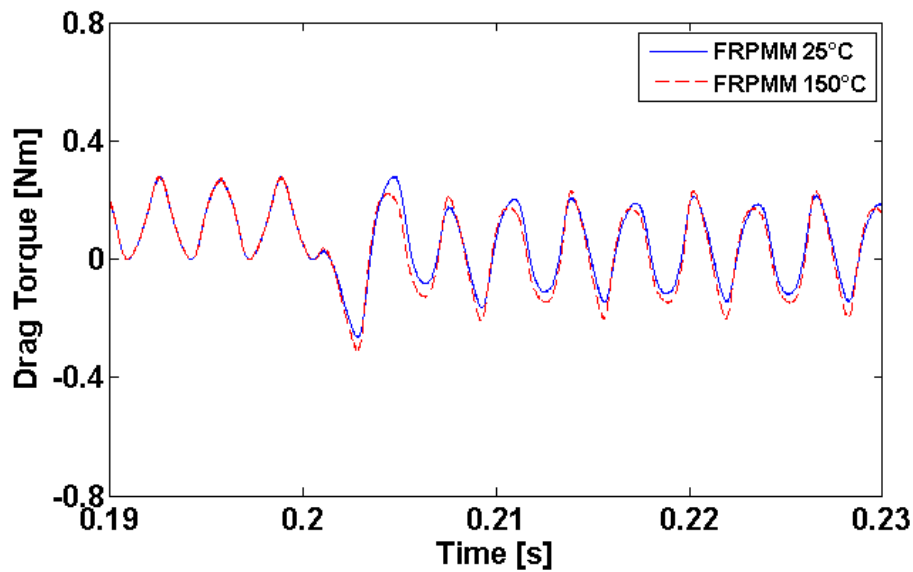
The drag torque has also been calculated using the Matlab/Simulink model, as shown in Fig. 2.9 (a)-(c). Before the short-circuit, i.e. healthy conditions, the torque is a healthy component produced by one coil and it is always positive. After the short-circuit, since the short-circuit current is in opposite direction against the healthy one (in the rest of the phase) and also the induced back-EMF in the affected coil, the affected coil will generate negative torque and lead to an overall reduction of the resultant torque if the control strategy does not kick in. Again, the overall results show that the torque and speed responses during short-circuit conditions are not significantly affected by the high temperature in the affected magnet for the DSPMM and FRPMM.



(a)



(b)



(c)

Fig. 2.9 Drag torque waveforms comparison for different temperatures. The short-circuit occurs at 0.2 s. (a) SFPMM, (b) DSPMM, (c) FRPMM.

2.3.3. SHORT-CIRCUIT CURRENT COMPARISON

In Fig. 2.10, a comparison between the current waveforms for both the healthy and faulty conditions is shown for low and high temperatures (25°C and 150°C, only for the affected PM, and other PMs are working at the operating temperature of 25°C). The machines operate under healthy conditions then the aforementioned short-circuit is introduced at around 0.2s. The reference speed is 1000 rpm and the reference torque is imposed to rated values given in Table 2.2 which ensures all the machines operate at the same rated current before the short-circuit occurs. The 1000 rpm value is chosen in order to ensure that the fault effects due to short-circuit can be observed during the investigations. At this value, the short-circuit current will be quite high, generating both important copper losses and a demagnetizing magnetic field.

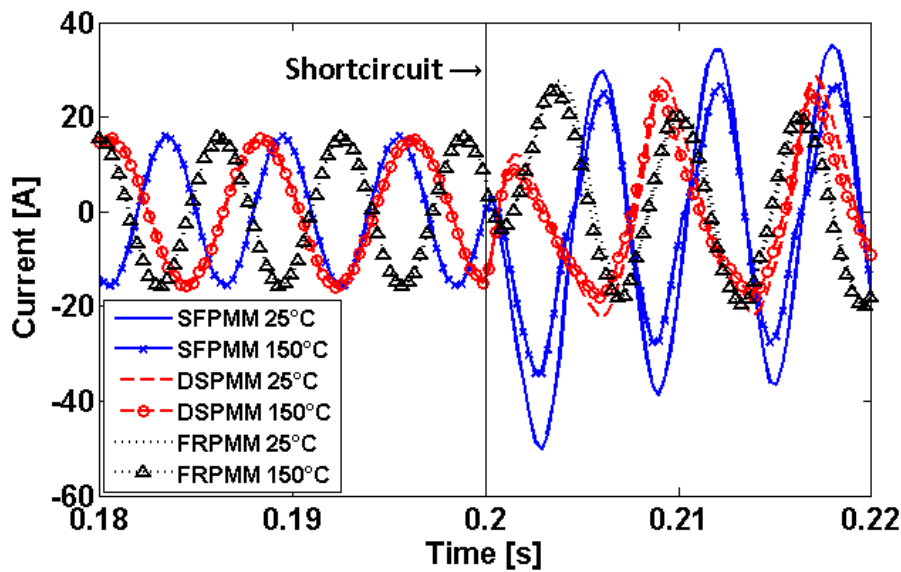


Fig. 2.10 Short-circuit current comparison for all topologies during fault conditions at 1000 rpm, low (25°C) and high (150°C) temperatures.

As expected, the low temperature case yields the highest short-circuit currents for all the investigated machines. This is because the phase resistance in the affected coil increases with temperature rise while the back-EMF decreases. The highest short-circuit current is reached by the SFPMM. However, when it comes to temperature effects on the short-circuit current value, it can be noticed for the DSPMM and the FRPMM that increasing the temperature barely affects their short-circuit currents. This can be explained by using (2.1), which is an analytical approximation of the short-circuit current i_{sc} :

$$i_{sc} \approx \frac{\alpha \cdot E_{max}}{\sqrt{(\alpha \cdot R)^2 + (\alpha^2 \cdot \omega \cdot L)^2}} \quad (2.1)$$

where α is the ratio of the short-circuited turns over the total phase turn number, R and L are the phase resistance and self-inductance, E_{max} is the magnitude of the phase back-EMF while ω is the angular electric frequency. The short-circuit current is directly proportional to the back-EMF which would explain the differences between the SFPMM, DSPMM and FRPMM, as shown in Fig. 2.11. The back-EMF waveforms show that the temperature increase has the most significant impact on the SFPMM topology. However, since only one PM is affected, the study is going to focus further on the back-EMF

generated in the coil surrounding that PM alone. By doing so, it reveals further a significant property degradation with temperature rise for that particular PM. This will be detailed in section 2.4.

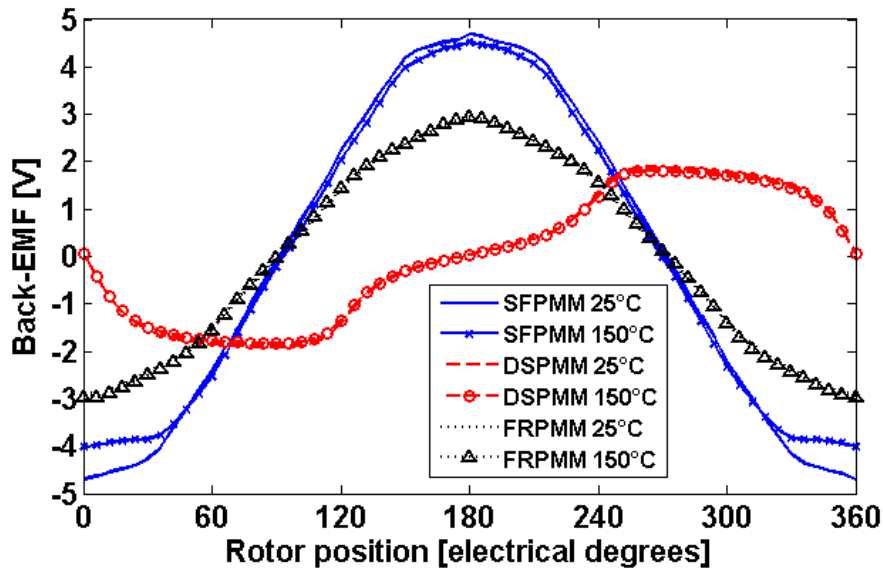
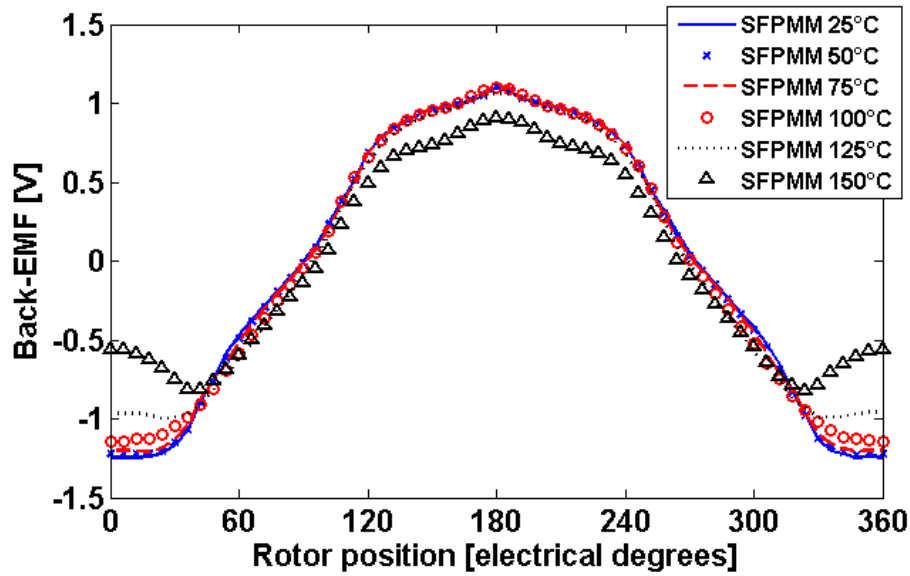
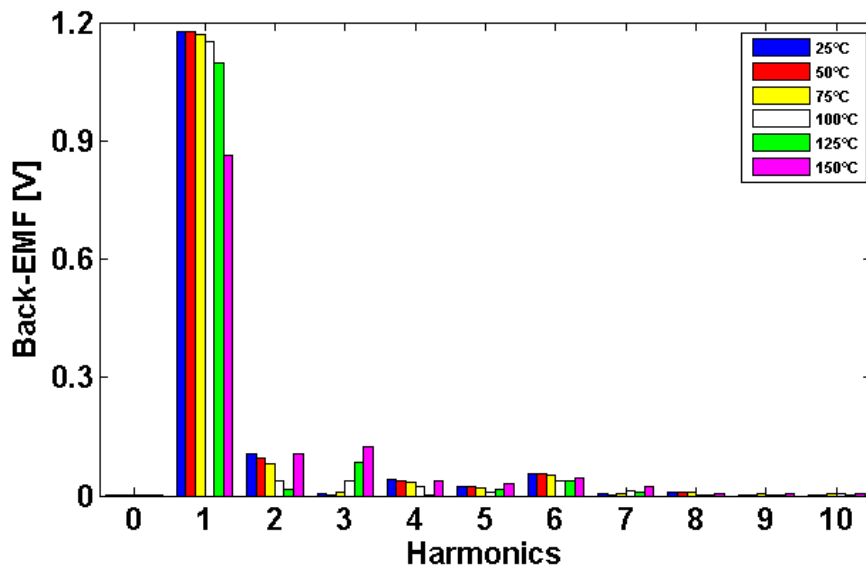


Fig. 2.11 Phase back-EMF comparison for all topologies at low (25°C) and high (150°C) temperatures.

The back-EMF dependence on temperature is investigated further for the SFPMM since it exhibits the largest variation with temperature rise. The study focuses on a single coil, e.g. the affected coil. This shows a much clearer picture of the performance drop when compared with the results shown in Fig. 2.11 mainly because the back-EMF induced in a single coil will have harmonics which are cancelled when the coil is series connected with the other 3 coils of the same phase. In Fig. 2.12, it can be seen that the main harmonics, 1st and 2nd suffer a strong reduction with the temperature rise, with noticeable effects starting from 100°C.



(a)

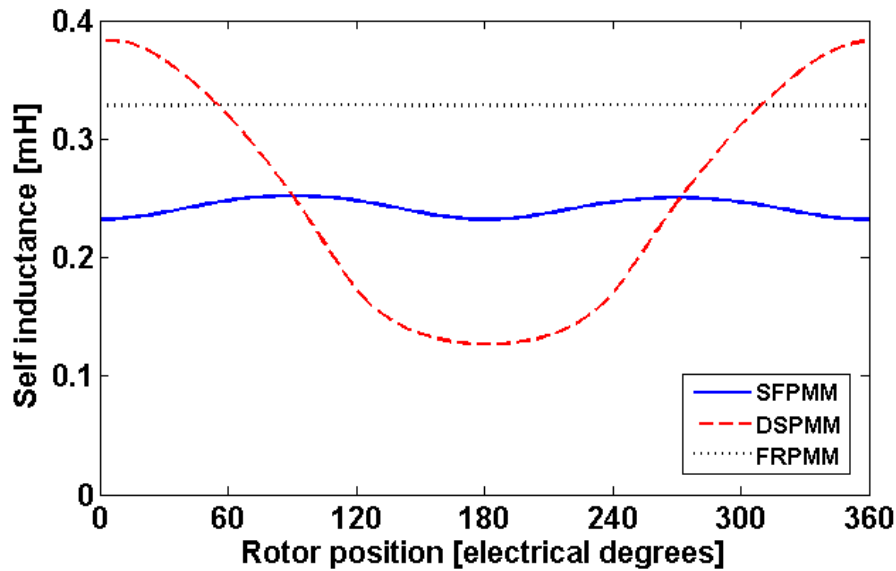


(b)

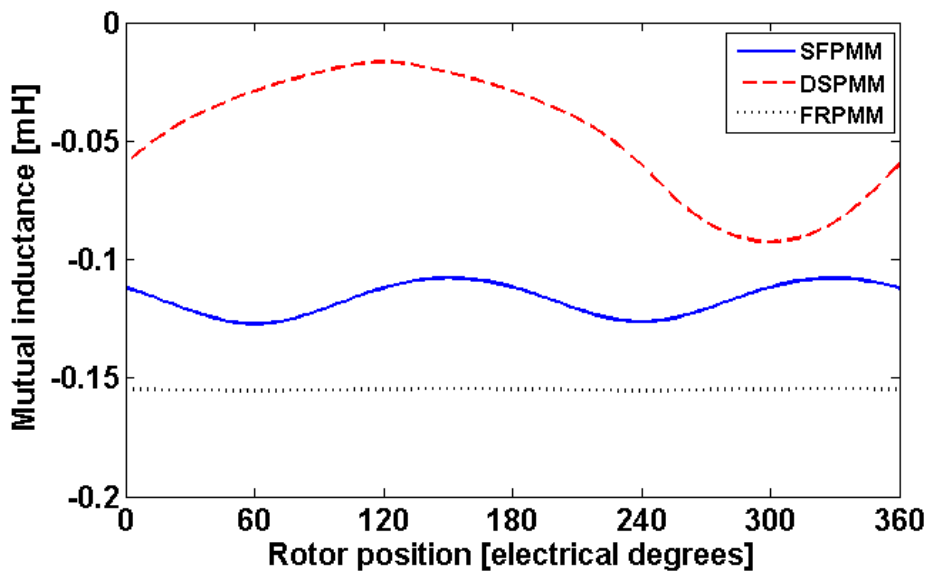
Fig. 2.12 Coil back-EMF variation with temperature rise of the SFPMM. The rotor speed is 400 rpm. (a) waveforms, (b) spectra.

The self and mutual inductance variations with rotor position for all topologies are given in Fig. 2.13. It is noted that the self and mutual inductances of the FRPMM topology are almost constant. This is due to the shape of the stator teeth and the large effective airgap length. The average values for inductance are summarized in Table 2.4. The FRPMM has the highest self-inductance, which is useful in limiting the

short-circuit current. Therefore, when considering the phase self-inductance variation with rotor position together with the back-EMF result from Fig. 2.11, it would explain why the FRPMM topology is subjected to the smallest short-circuit current.



(a)



(b)

Fig. 2.13 Inductance variations with rotor position for all topologies. (a) self-inductances; (b) mutual-inductances.

Based on the mutual-inductance results, one can conclude that the DSPMM topology has the strongest magnetic separation between the phases while the FRPMM is the worst. However, since all topologies considered are double layer, there is no thermal or physical separation at all between adjacent coils. To address this issue, the single layer winding structure could be employed.

TABLE 2.4

AVERAGE SELF AND MUTUAL INDUCTANCES FOR ALL TOPOLOGIES

	SFPMM	DSPMM	FRPMM
Self [mH]	0.242	0.249	0.329
Mutual[mH]	-0.117	-0.048	-0.155

2.4. PM IRREVERSIBLE DEMAGNETIZATION AT HIGH SPEED

The PM irreversible demagnetization is studied under the aforementioned fault conditions for three temperatures: 25°C, 100°C and 150°C, and all are at high speed (1000 rpm). To reiterate the assumptions made in section 2.2, only one PM is assumed to be affected by the fault (due to its proximity to the short-circuit location). This affected PM is working at the higher temperature mentioned above while the remaining ones are working at 25°C. The flux densities within the affected PM are studied next and compared with the knee point values (-0.08, 0.28 and 0.5 T for the three considered temperatures, respectively). At 25°C all topologies are safe from demagnetization, therefore the results are not shown here. However, for higher temperature (150°C), almost the whole affected magnet will be demagnetized regardless of the machine topologies and this will be investigated first.

The flux density colour maps within the affected magnet under faulty conditions and at 150°C are given in Fig. 2.14. It is worth mentioning that the simulations with PMs as the only magnetic source were also carried out. This can be achieved by removing the armature field (produced by both the healthy and faulty coils) using the frozen permeability method [107]. The purpose of such simulations is to investigate the influence of the magnetic circuit on the PM working point at relatively higher temperature. Based on obtained results under fault conditions, it was found that for all topologies there is very little difference in flux density with or without armature field. Therefore, one can conclude that the short-circuit current only contributes to increase the local temperature of the affected magnet but the demagnetization process occurs mainly due to the influence of the rest of the magnetic circuit.

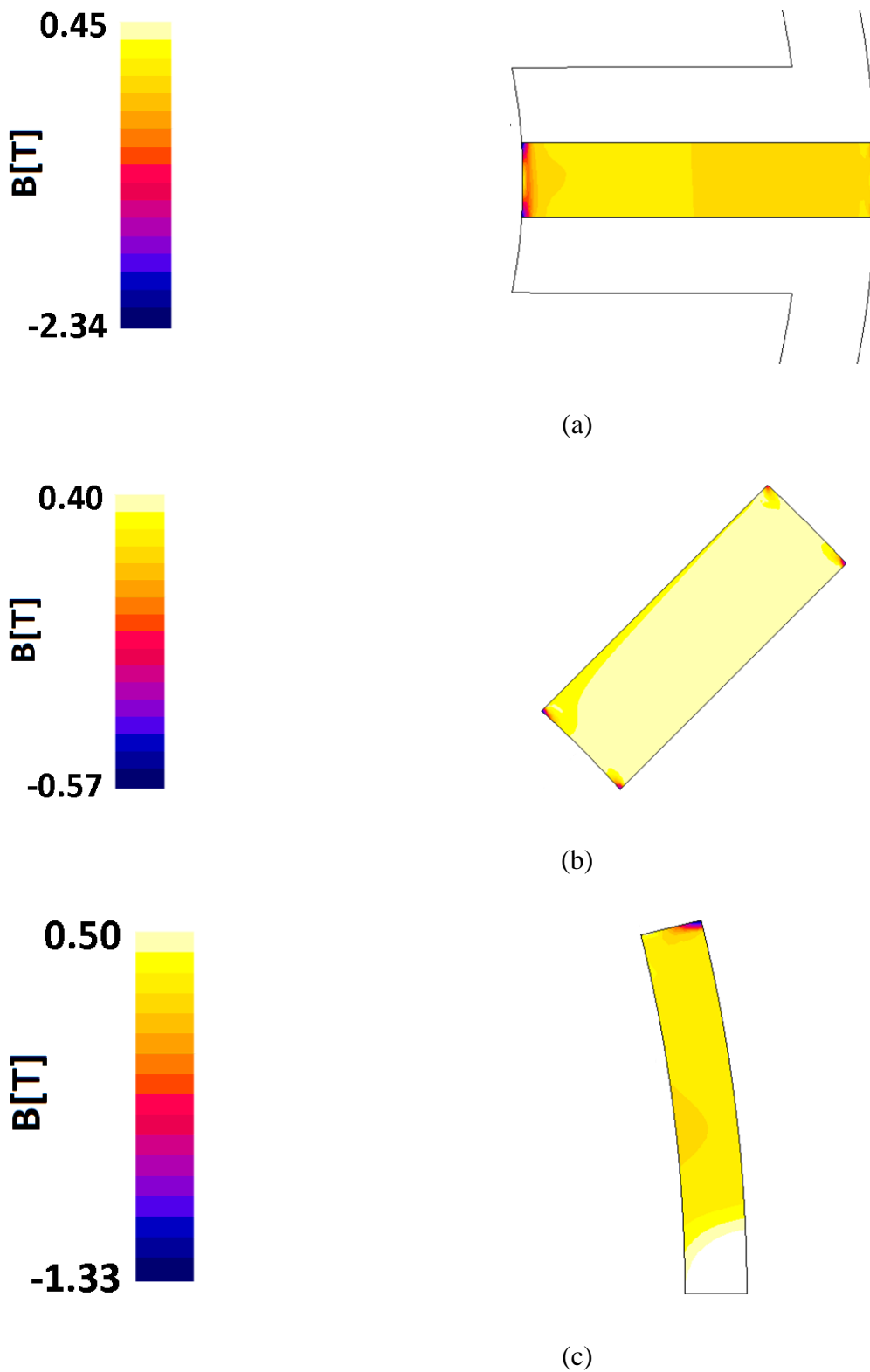


Fig. 2.14 Flux density colour maps for all topologies at 150°C. Any coloured regions (< 0.5 T) value indicate irreversible demagnetization (a) SFPMM; (b) DSPMM; (c) FRPMM.

The maps in Fig. 2.14 show that all topologies will experience severe irreversible demagnetization at higher temperature. However, the PM of the FRPMM has a small area in which the flux density does not drop below the knee point value. When investigated further, as shown in Fig. 2.15, it was found that this is because of a local phenomenon caused by the close vicinity of the opposite sign PM. The neighbouring PM will enhance the local magnetic field thus ensure that the flux density is well above the knee point value, avoiding irreversible demagnetization.

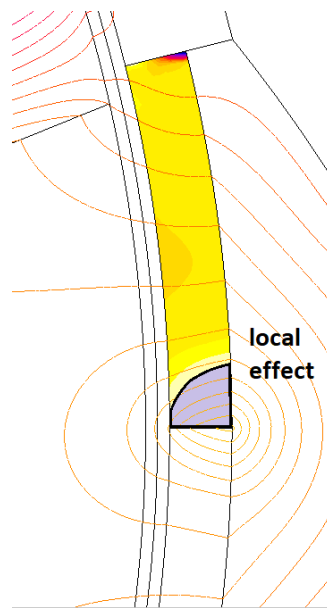


Fig. 2.15 Flux lines showcasing local phenomenon for FRPMM.

The results concerning the 100°C case are also given, as shown in Fig. 2.16. It can be seen that the most affected topology is the SFPMM which gets completely demagnetized, followed by the FRPMM which is only partially affected. The DSPMM topology however does not demagnetize, thus being the most reliable when it comes to demagnetization withstand capabilities.

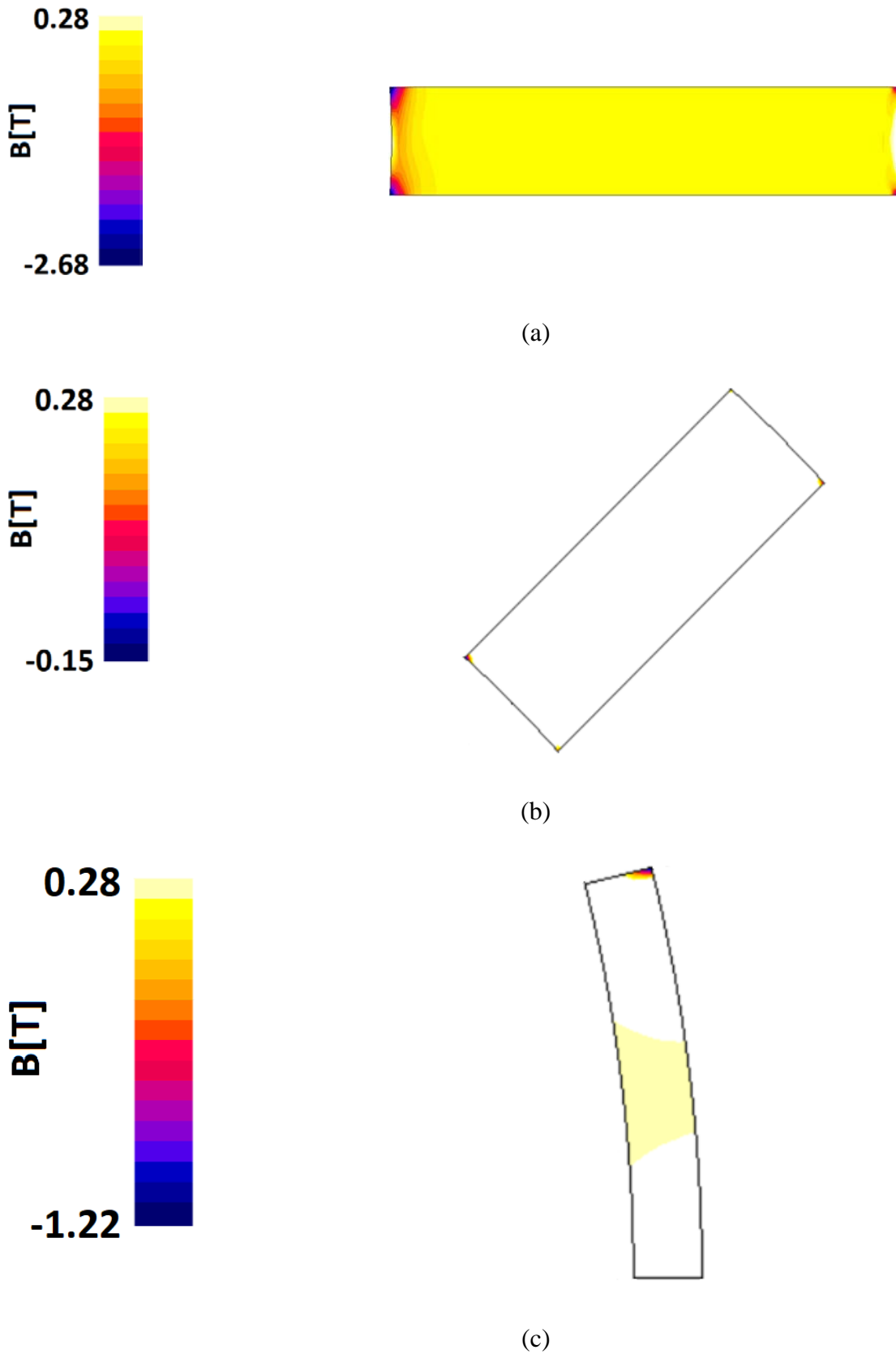


Fig. 2.16 Flux density colour maps for all topologies at 100°C. Any coloured regions (< 0.28 T) indicate irreversible demagnetization. (a) SFPMM; (b) DSPMM; (c) FRPMM.

The SFPMM demagnetization process for 100°C case was detailed in [108] and will also be explained in chapter 4 so only the FRPMM is investigated further in this chapter. The current sources are removed and only the PMs are kept in the model as the magnetic field source using the previously mentioned frozen permeability method. The results are shown in Fig. 2.17 and it can be seen that the demagnetization process is mainly due to the magnetic circuit lowering the operating point of the PM on the B(H) curve and not due to the demagnetizing magnetic field produced by the short-circuit current.

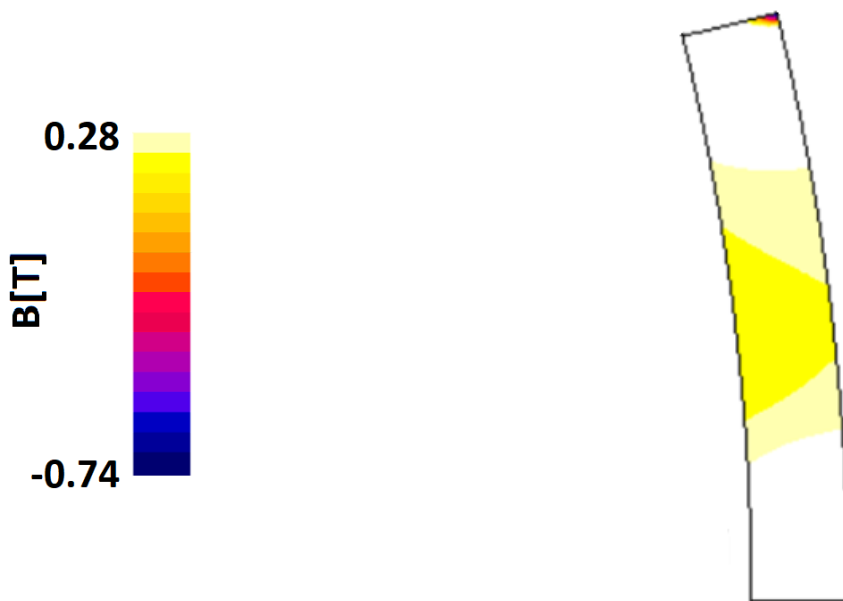


Fig. 2.17 Flux density colour maps at 100°C for FRPMM without considering armature field. Any coloured regions (<0.28 T) indicate irreversible demagnetization.

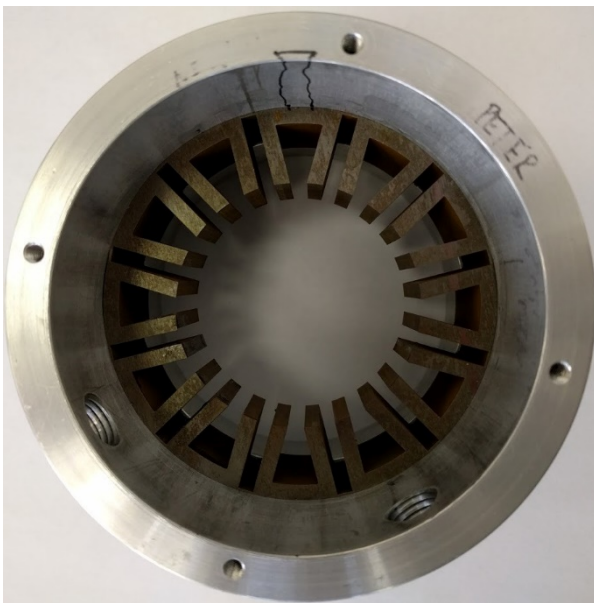
2.5. EXPERIMENTAL VALIDATION FOR SHORT-CIRCUIT CURRENT

In order to validate the FE and Simulink models, a SFPMM prototype is built and tested according to methodologies used in [108] and [84]. The dSPACE framework was used to implement the control strategies.

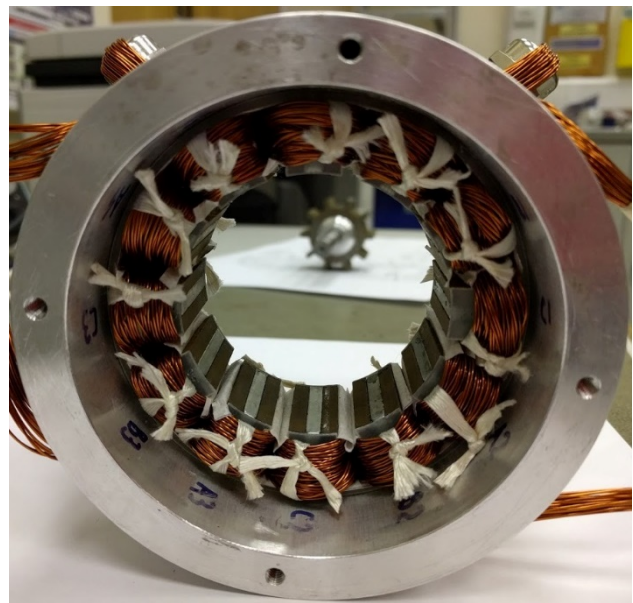
The dimensions of the conventional machine are given in Table 3.1, while the E-core machine has the same parameters as in [109] and therefore not reproduced here. It should be mentioned that although the stator diameter and copper losses are the same, the split ratio is different between the two prototypes. However, the E-core prototype has the same rated current, the same number of turns per phase, the same slot area as the conventional one and hence the resulting short-circuit currents can be compared between

the two machines.

The conventional SFPMM stack lamination for stator is shown in Fig. 2.18 (a). The stator is a single structure since the stator U-segments are connected by a narrow bridge (0.5 mm) at the back-iron level. Additionally, the entire stator structure is glued inside the aluminum housing. This avoids issues with precise positioning of the segments and allows adding and gluing the PMs without having to resort to a special fixture. At this stage, terminals for each of the 12 coils are wired separately to allow flexibility and different connections during experiments.



(a)



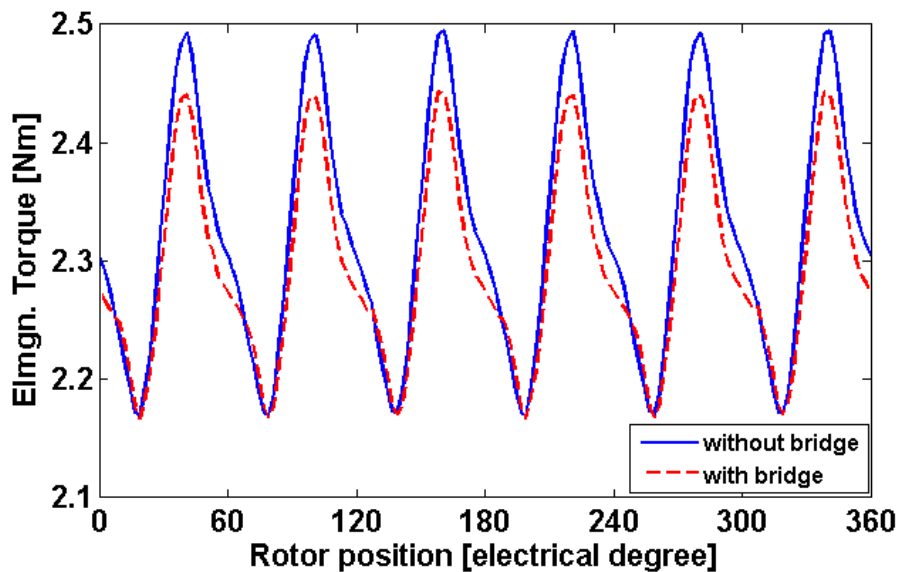
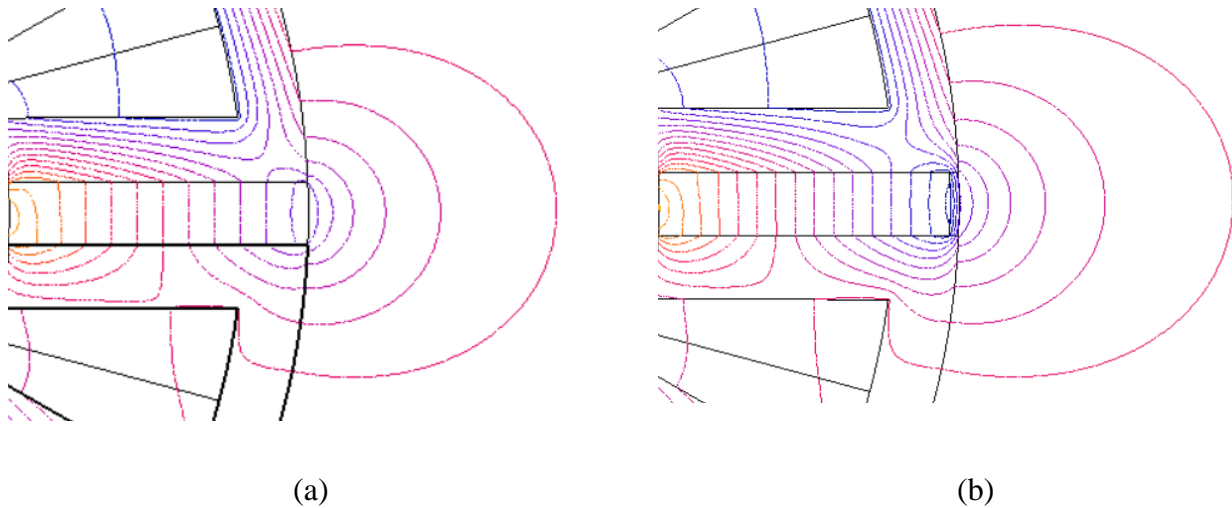
(b)



(c)

Fig. 2.18. Prototype of conventional SFPMMs with 12-slot/10-pole. (a) stator laminations (b) conventional stator with PM and windings added, (c) 10 pole rotor.

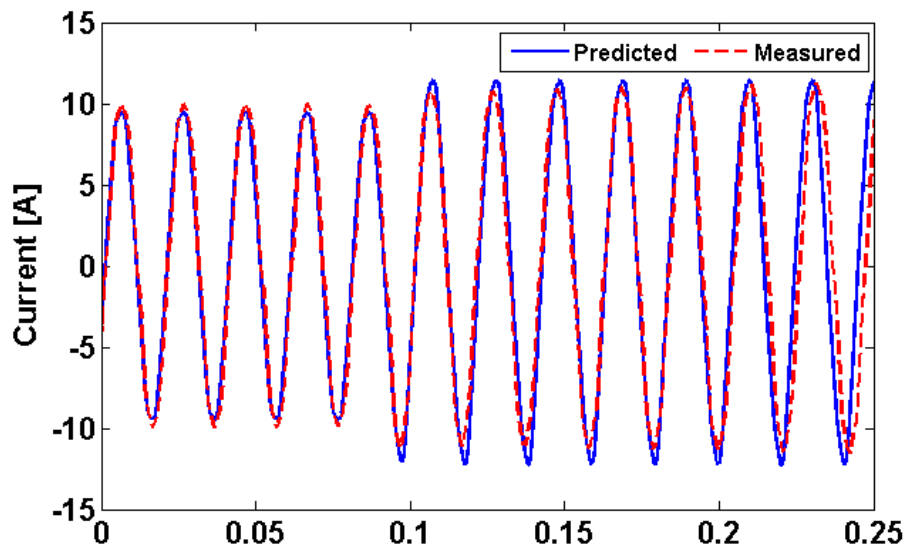
In order to build the prototype, a compromise was adopted. The individual stator U-segments are connected together using a 0.5 mm bridge at the edge of the stator. This solution avoids the difficulty of gluing the PMs and the stator segments together since the stator is one continuous structure now. The drop in performance is less than 1% as shown in Fig. 2.19 (c). The narrow bridge becomes saturated quickly, therefore locally the flux lines distribution does not differ too much (Fig. 2.19 (a) and (b)).



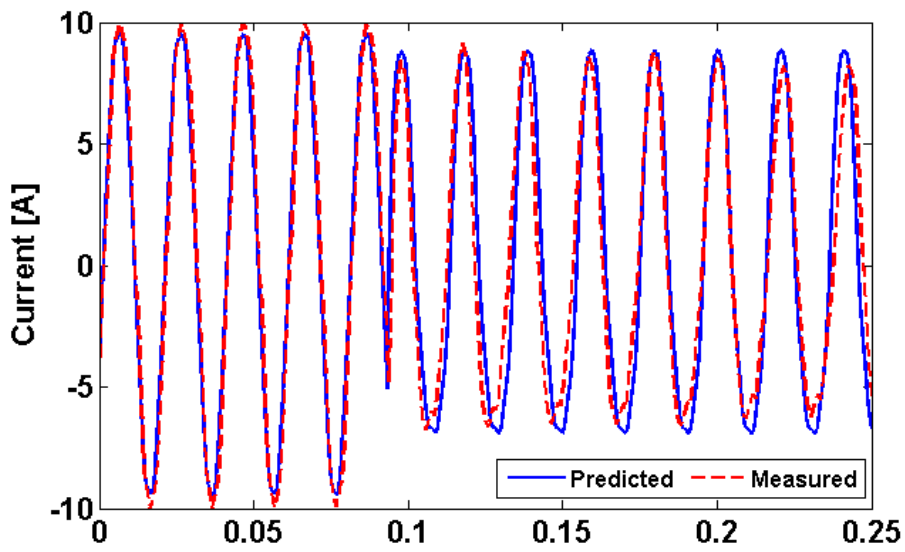
(c)

Fig. 2.19 The influence of adding the narrow bridge. (a) flux lines distribution, no bridge, (b) flux lines distribution, with bridge, (c) performance comparison (torque) between bridge and no bridge versions.

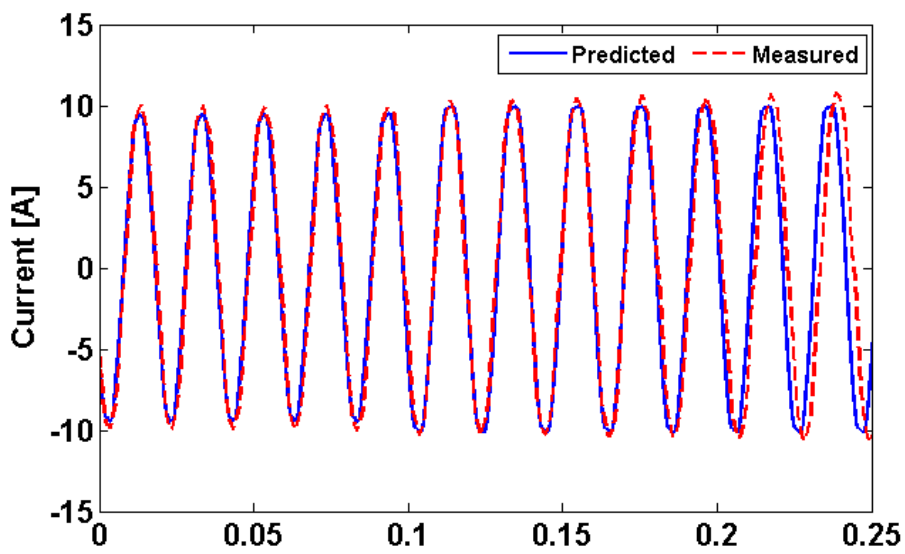
The comparison between the predicted and measured results is given in Fig. 2.20. The experimental validation is carried out for low temperature and moderate speed (25 °C & 300 rpm). A load torque of 1.44 Nm is introduced. Also, a low fault severity of 25% is considered to prevent damaging the machine during tests. The short-circuit is introduced at around 0.1 s. It can be observed that the predicted currents match well with the measured ones, as shown in Fig. 2.20 (a)-(c), so do the speeds, as shown in Fig. 2.20 (d). This validates the adopted FE and Simulink models.



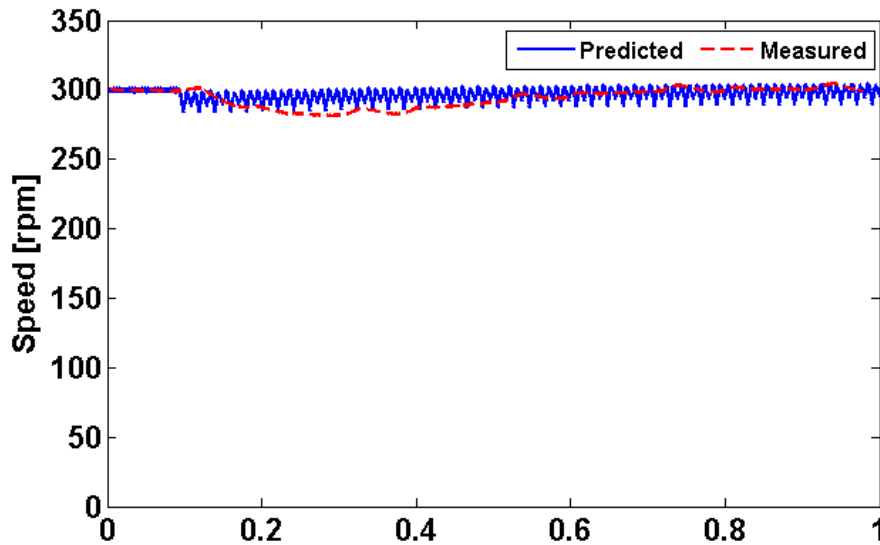
(a)



(b)



(c)



(d)

Fig. 2.20. Comparison between measured and predicted results (25% fault severity – 1 out of 4 coils short-circuited). (a) i_h healthy current, (b) i_f short-circuit current, (c) i_b phase current, (d) Speed.

2.6. CONCLUSIONS

Three stator mounted PM machines, namely the SFPMM, DSPMM and FRPMM topologies have been investigated from the point of view of fault tolerance to inter-turn short-circuit and irreversible demagnetization. Their properties are summarized in Table 2.5. Due to their different magnetic circuit configurations, the DSPMM and FRPMM present large self-inductance and smaller back-EMF, which allow them to restrain the short-circuit current to reasonable values, closer to the rated current. The DSPMM is the most resilient to demagnetization. Combining its excellent cost/performance makes it an interesting candidate for cost effective applications. The FRPMM shows good capabilities in limiting the short-circuit current. Despite this, it was discovered that the demagnetization process can still happen due to temperature effect alone. It is possible that increasing the thickness of the PMs for FRPMM will improve the demagnetization withstand capability at the expense of overall performance. This will be investigated in future works.

TABLE 2.5

SUMMARY OF INVESTIGATED MACHINES (SFPMM/DSPMM/FRPMM)

	SFPMM	DSPMM	FRPMM
Torque/PM [mN/mm^3]	0.14	0.267	0.275
Peak short-circuit current [A] at 1000 rpm	46.1	28.1	27.8
Demagnetization withstand capability	poor	good	poor

Finally the DSPMM and FRPMM show excellent torque/PM capabilities. However, it would be relevant to investigate other versions of SFPMM which might also have a good performance/cost ratio. For this reason, in the next chapter an study is conducted concerning SFPMM versions which require half of the PM volume.

Chapter 3. Comparative Study of Alternative Modular Switched Flux Permanent Magnet Machines

The electromagnetic performance of alternative single layer modular switched flux permanent magnet (SFPM) machines, i.e. conventional, C-core, E-core and modular, is compared by finite element analysis in this chapter. The comparison includes winding factor, open-circuit flux density, back-EMF and electromagnetic torque, together with the influence of four slot/pole number combinations (12s/10p, 12s/11p, 12s/13p and 12s/14p). It is found that with flux gaps the electromagnetic performance of modular SFPMs does not necessarily degrade. The flux focusing and defocusing effects are observed in the C-core and some of the E-core machines. However, the flux defocusing effect occurs in all modular machines with large flux gap openings. Since the flux gap opening affects the slot area, the copper loss will be changed as well. Hence, the variation of copper loss against flux gap opening for the same current or the same torque has also been investigated.

3.1. INTRODUCTION

The conventional SFPMM [7] with its double layer winding configuration is not suitable for fault tolerant applications since there is no physical and magnetic separation between the phases. This can be improved by adopting a single layer winding, in which only alternate stator poles are wound. This results in a single layer solution [110], [22], also known as the alternate poles wound SFPMM. Moreover, by also removing some of the PMs on the stator, a modular structure can be obtained to achieve even better fault-tolerant capability since the self-inductance increases whilst the mutual-inductance decreases [110]. Furthermore, the stator structure is simplified and the PM volume is reduced. It also provides the possibility of assembling the machine on-site, which is particularly useful for large PM machines.

Several versions of single layer SFPMMs have been proposed in recent years. They are all based on the modification of the unwound stator teeth. The C-core topology [22] completely removes the unwound teeth whilst the E-core [109] replaces the PMs from the unwound teeth with the same iron material as the stator iron core. Each of these machine topologies has its own strengths and weaknesses. It is worth noting that although the PMs are the main contributors in the torque production [3], the reduction by half of the available PM volume in the stator, forming a modular structure, does not necessarily mean that the average torque decreases by half as well [110]. This characteristic will be further investigated in this chapter. Although the conventional, C-core, E-core and modular machines have been individually investigated in literature, the systematic comparative study of the single layer C-core, E-core and modular machines with flux gaps has rarely been carried out. Thus, this chapter will comprehensively investigate the influence of the flux gap opening on the machine performances.

This chapter is organized as follows. In section 3.2, the main characteristics of three single layer SFPMM topologies (C-core, E-core and modular) derived from a conventional 12-slot/10-pole single layer SFPMM are introduced. In section 3.3, the performances of these single layer machines in terms of electromagnetic torque, back-EMF, and copper loss, as well as the flux focusing/defocusing effect are calculated and compared against their conventional counterparts. Experimental validation for conventional SFPMM machine is provided in section 3.4 and conclusions in section 3.5.

3.2. FEATURES AND TOPOLOGIES OF MODULAR SFPM MACHINES

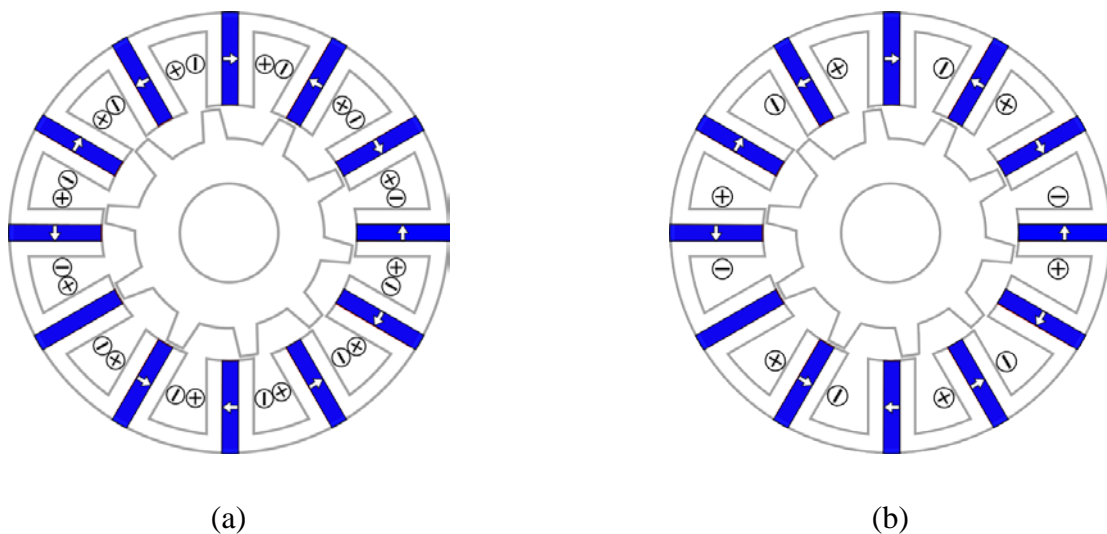
The cross sections of both the conventional and modular machines (12s/10p only) are shown in Fig. 3.1, and the main parameters are given in Table 3.1. The rotor has a very simple mechanical structure,

since all the active parts (windings and PMs) are located on the stator. Compared with the conventional one, the modular topology has its PM volume reduced by half and some of the PM magnetization directions changed in order to maintain an alternating polarity across the stator circumference. Giving the different magnet magnetization directions for the modular structure, the coil connections must also be changed, Fig. 3.1 (b). Moreover, the unwound stator teeth are modified by either inserting a flux gap or replacing the magnet material with iron while the wound teeth containing the PM have the same geometry as those in the conventional machines. All studied machines have 3-phase windings with two coils per phase.

TABLE 3.1

PARAMETERS OF THE INVESTIGATED MACHINES

Stator slot number	12	Stator yoke height (mm)	3.6
Rotor pole number	10/11/13/14	Stack length (mm)	25
Rated speed (rpm)	400	Air-gap length (mm)	0.5
Rated current (A)	11	Rotor outer radius (mm)	27.5
Rated torque (Nm)	2.3/2.6/2.8/2.7	Magnet thickness (mm)	3.6
Stator outer radius (mm)	45	Magnet remanence NdFeB (T)	1.2
Stator inner radius (mm)	28	Number of turns/phase	72



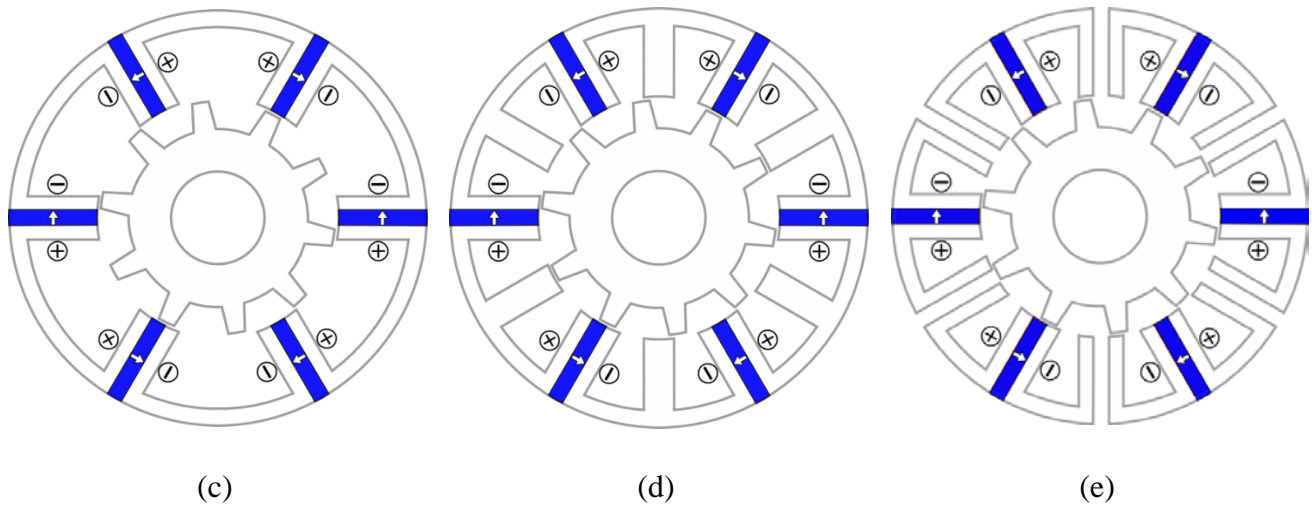
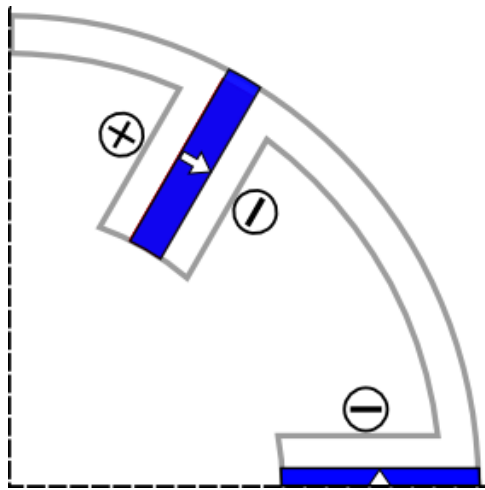


Fig. 3.1 Cross-sections of SFPM machines with 12s/10p. (a) Conventional double layer, (b) Conventional Single Layer, (c) C-core, (d) E-core, (e) Modular.

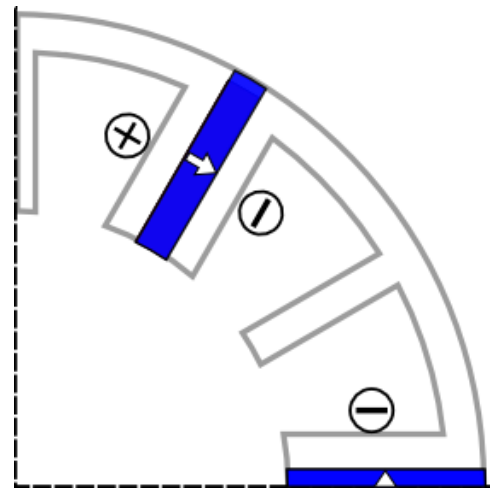
When the magnets in the unwound stator teeth are removed, a flux gap opening is 7.5 mech. deg., Fig. 3.2 (e), and will be used as the baseline for the following analysis. The flux gap opening can be increased or reduced, leading to enlargement or reduction of the inserted flux gap, as shown in Fig. 3.2. For simplicity, during this process, other machine dimensions are maintained constant. However, at some point during the reduction process, as shown in Fig. 3.2 (d), the tooth sides adjacent to flux gaps will overlap, leading to the disappearance of the flux gap. At this point, the SFPM becomes an E-core machine with a zero flux gap opening. Continuing the reduction of the flux gap opening will result in the reduction of the unwound stator tooth thickness until the lower negative limit (-15 degrees), for which the tooth disappears, transforming the E-core topology to a C-core one. Therefore, the flux gap width ranges from -15 mech. deg. to 20.625 mech. deg., with the lower limit being given by the unwound tooth disappearance while the higher limit is imposed by the feasibility of the windings. At a 7.5 deg. flux gap opening, the copper area is the same for both modular and conventional single layer machines as shown in Fig. 3.1 (b) and (e). In such a way, a link between the three types of SFPM topologies under investigation is defined with the help of the flux gap parameter and the structural changes which affect the unwound teeth, such as:

- Modular machines with actual flux gaps inserted – the flux gap range is given by the interval (0, 20.625) mech. deg. and the resulting stator is segmented.

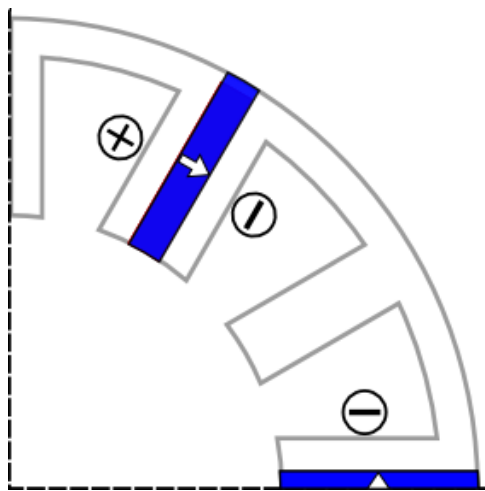
- E-core machines with a variable cross-section of the unwound tooth – the flux gap interval is $(-15, 0)$ mech. deg.
- C-core machine, obtained from the E-core machines at the flux gap opening of -15 mech. deg. However, for some large negative values of the flux gap opening, the E-core topology will be equivalent to a C-core one as the narrow unwound teeth will be heavily saturated and will not be able to properly direct the flux into the airgap.



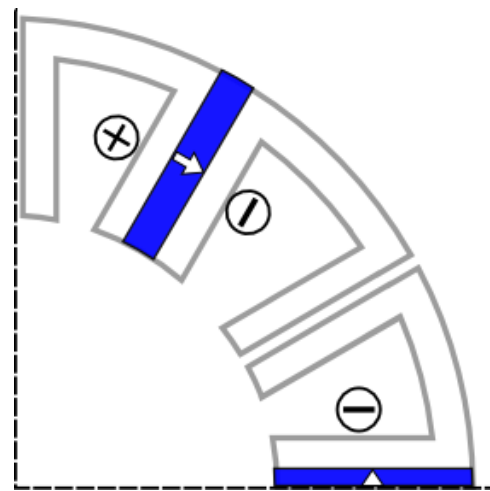
(a)



(b)



(c)



(d)

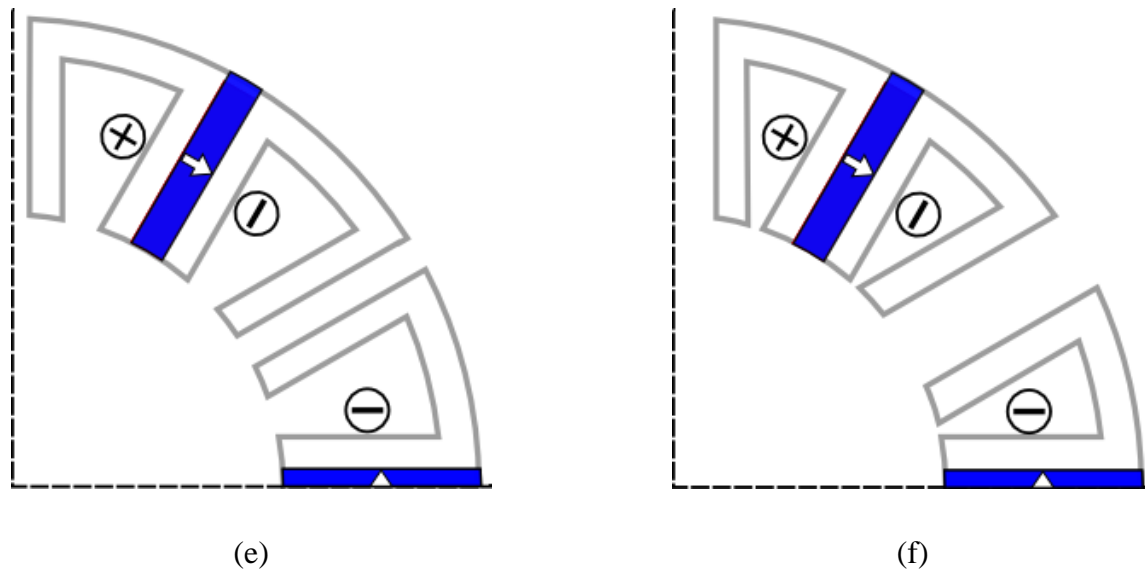


Fig. 3.2 Flux gap opening variation. (a) -15 degrees, (b) -7.5 degrees, (c) 0 degrees, (d) 3.75 degrees, (e) 7.5 degrees, (f) 20.625 degrees.

The removal of half of the magnets creates the possibility for a better separation between the phases, with respect to the conventional single layer machine. However, it is worth mentioning that from this point of view, the C-core topology is equivalent to the double layer SFPMM in terms of separation between the phases, while the modular machines with large flux openings provide the best decoupling between phases magnetically, electrically and thermally. However, flux gap openings will inevitably change the copper area and the copper loss, as will be detailed in section 3.3.5.

3.3. INFLUENCE OF FLUX GAPS ON MACHINE PERFORMANCE

The modification of the unwound stator tooth geometry affects the winding factor, the open-circuit air-gap flux density, the flux per pole, the back-EMF and also the electromagnetic torque [111]. All the aforementioned parameters are important for the machine performance and will be studied in the following subsections.

3.3.1. WINDING FACTOR

For all single layer machines, the fundamental winding factor k_w can be determined as the product between the pitch factor k_p and the distribution factor k_d . Using the same method for other types of PM machines with fractional slot concentrated windings [112], [113] the winding factors are determined to be 0.97 for 12s/10p and 12/14p machines and 0.99 for 12s/11p and 12s/13p conventional single layer machines.

The classic definition of the winding factor cannot be applied directly to the modular machine structure, due to the insertion of flux gaps which in turn affects the pitch factor. The distribution factor is given by the expression [114]:

$$k_d = \frac{\sin(q \cdot \sigma/2)}{q \cdot \sin(\sigma/2)} \quad (3.1)$$

where q is the number of coils per phase and σ is the angle between two phases (in electric radians). While the distribution factor is constant across the flux gap range, the pitch factor changes and the method proposed in [114] are used instead for modular machines:

$$k_p = \sin\left(\frac{\pi}{2} \cdot \frac{\tau_s - 0.5 \cdot (\Delta - \theta_{mgn})}{\tau_p}\right) \quad (3.2)$$

where Δ is equal to the flux gap opening (absolute value), $\tau_s = 2\pi/N_s$ is the slot pitch, N_s is the number of stator slots, $\tau_p = 2\pi/N_r$ is the pole pitch with N_r being the number of rotor poles which is also equivalent, for the SFPMM, with the number of pole pairs. θ_{mgn} is the magnet thickness and is introduced in order to correctly account for the winding factor which must be equal for both the conventional and modular machines with a 7.5 deg. flux gap. The expression $\tau_s - 0.5(\Delta - \theta_{mgn})$ is a correction of the slot pitch due to the presence of flux gaps. According to this expression, for a flux gap opening smaller than 7.5 deg., the slot area and hence the corrected slot pitch increases while for values of the flux gap higher than 7.5 deg., the slot pitch is reduced.

Using (3.1) and (3.2), the winding factor variation across the flux gap range for all studied slot/pole

number combinations is calculated, as shown in Fig. 3.3.

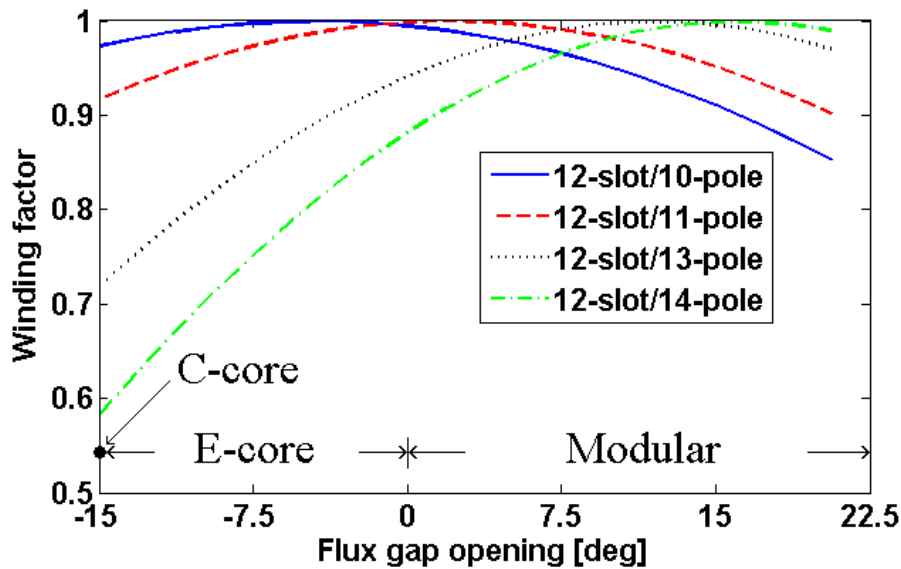


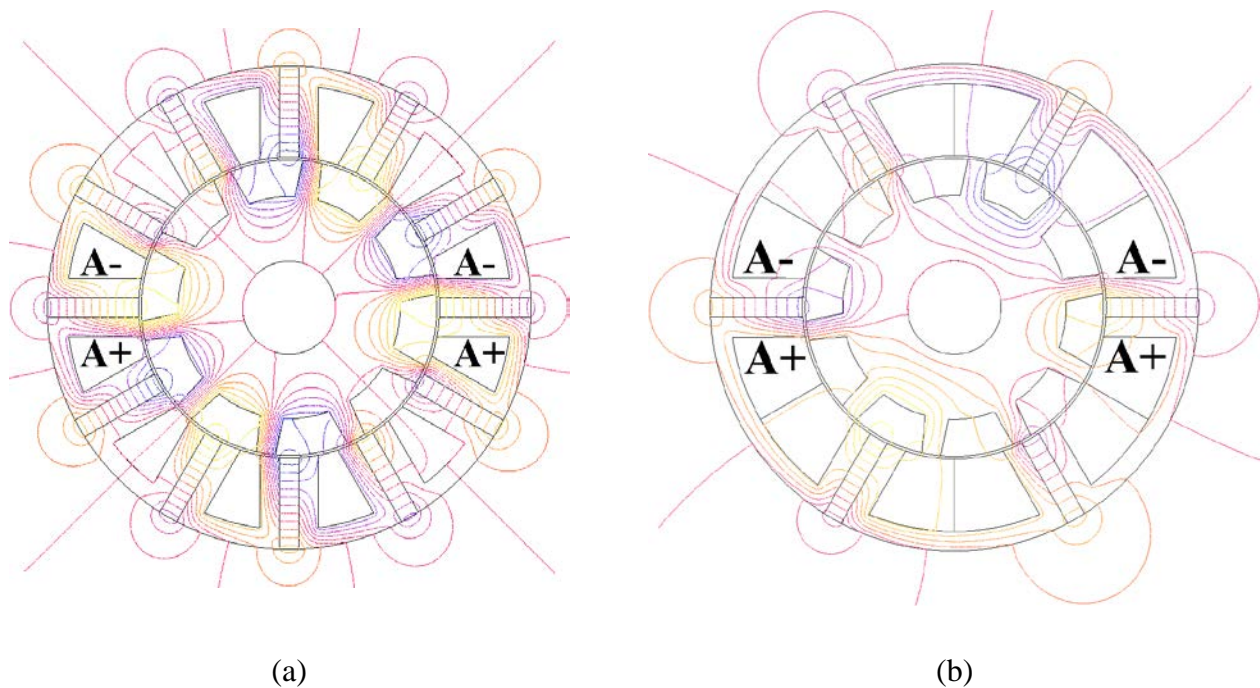
Fig. 3.3 Winding factor variation for modular machines.

For the number of poles less than the number of slots such as the 12s/10p and 12s/11p, the slot pitch is smaller than the pole pitch for the conventional machine. The modification of the stator structure modifies the slot pitch so that the winding factor value decreases for flux gaps higher than 7.5 deg. While reaching its maximum for a flux gap smaller than 7.5 deg. However, for the number of poles higher than the number of slots such as the 12s/13p and 12s/14p conventional machines, the slot pitch is higher than the pole pitch. Adding flux gaps to the stator will change the winding factor so that the maximum will be reached for the modular topology (flux gap openings > 7.5). For flux gap values lower than 7.5, the winding factor decreases continuously for these particular slot/pole number combinations.

Based on these results, the flux gap value must be carefully chosen depending on the slot/pole number combination. This is because for different slot/pole number combination, the flux gap openings to achieve the maximum winding factor are different, e.g. for the 12s/10p, the E-core configuration gives the maximum winding factor while for the rest of the slot/pole number combinations, the modular topologies gives the maximum winding factor. However, the winding factor is not the only quantity affecting the final output torque and the next sections will study the influence of other important parameters such as open-circuit air-gap flux density and phase back-EMF.

3.3.2. OPEN-CIRCUIT AIR-GAP FLUX DENSITY

The open-circuit flux distributions for various values of the flux gaps are shown in Fig. 3.4, and are also compared with the conventional machine. Only the results for the 12s/10p configuration are shown because other slot/pole number combinations have similar results. It can be noted that the conventional machine will generate larger leakage flux outside the machine. This is due to its larger number of permanent magnets (12 magnets against only six for the modular machines) which also doubles the PM volume. Within the limited volume of the stator, the PMs are much closer to each other for the conventional machine. There is no magnetic separation between phases and the permanent magnets are influencing each other, pushing some of the flux lines outside the machine and thus increasing the leakage flux. In contrast, for the E-core and modular machines there is noticeable magnetic separation between phases. For the modular machines, this is provided naturally due to the flux gaps that act as flux barriers. However, for the E-core, the magnetless stator tooth diverts the PM flux thus ensuring the magnetic separation between phases. When it comes to the C-Core, it has a similar structure as the double layer machine. Two coil sides of two different phases are located in the same stator slot. As it can be seen in Fig. 3.4 (b), adjacent PMs still influence each other, in a similar way with the double layer conventional machine shown in Fig. 3.4 (a). Therefore, no actual magnetic separation occurs for the C-Core machine either. C-Core can be regarded as an unoptimized version of the double layer conventional machine but with larger difference between the stator and rotor teeth number.



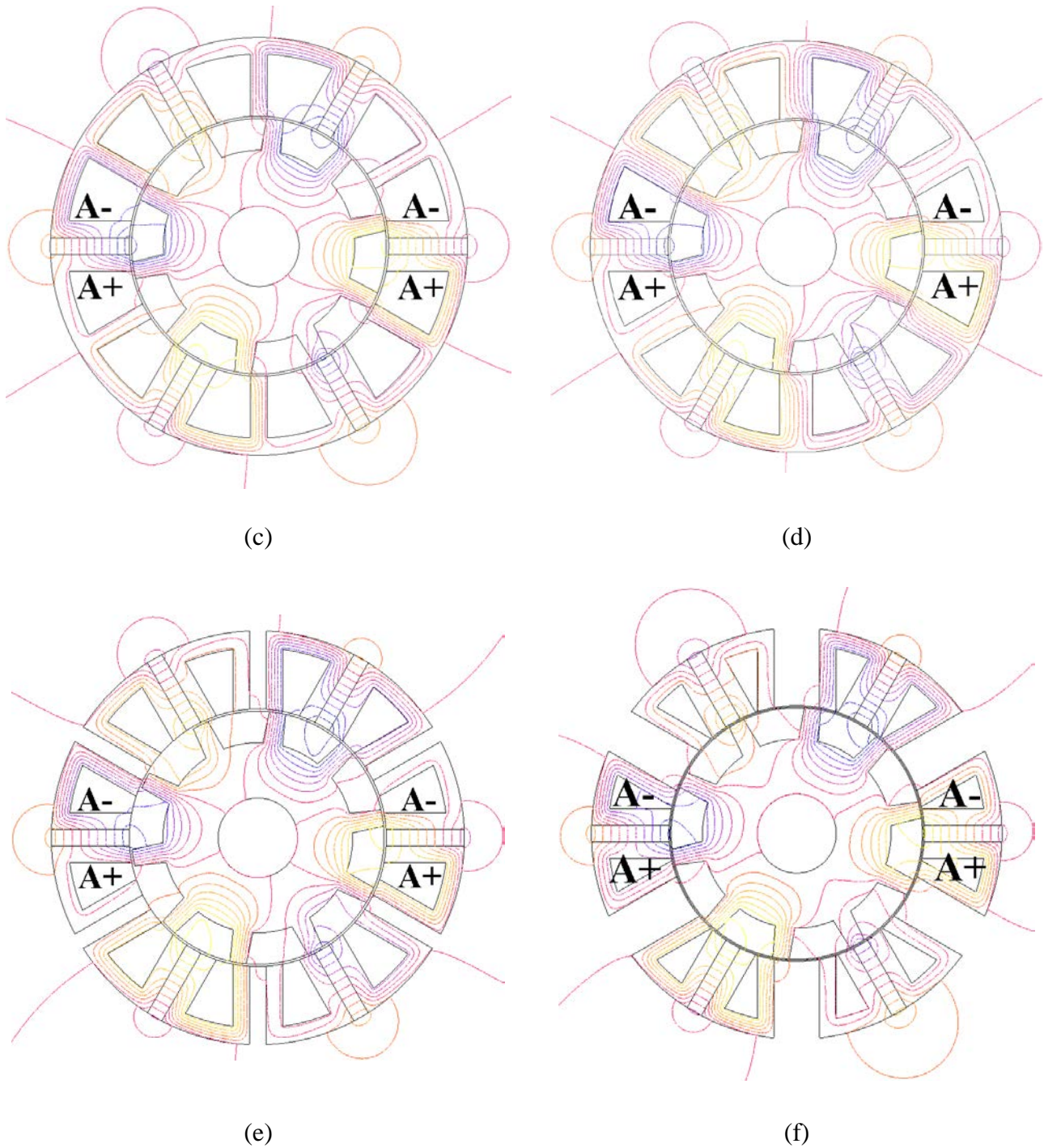
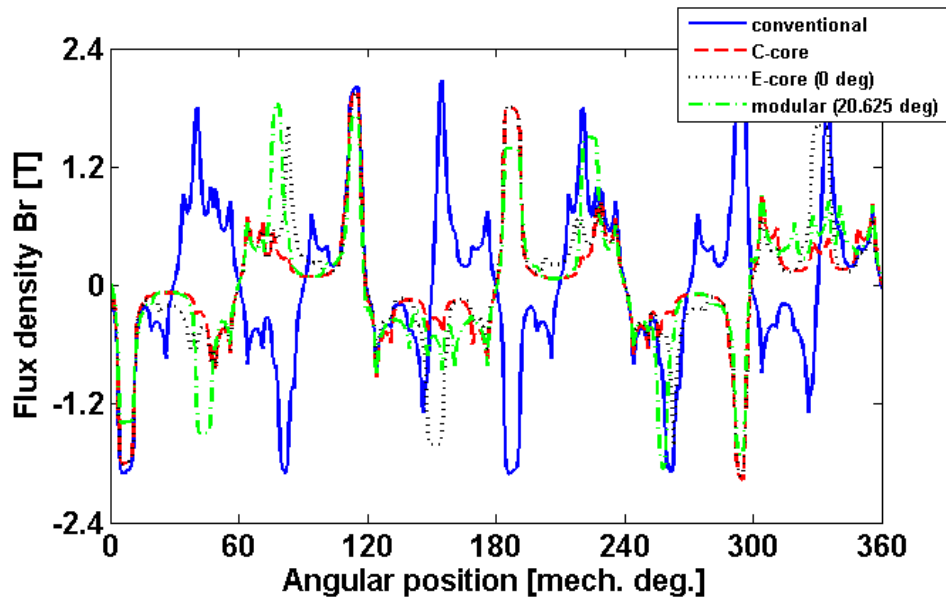


Fig. 3.4 Open circuit flux distributions. (a) conventional, (b) -15 degrees, (c) -7.5 degrees, (d) 0 degrees, (e) 7.5 degrees, (f) 20.625 degrees.

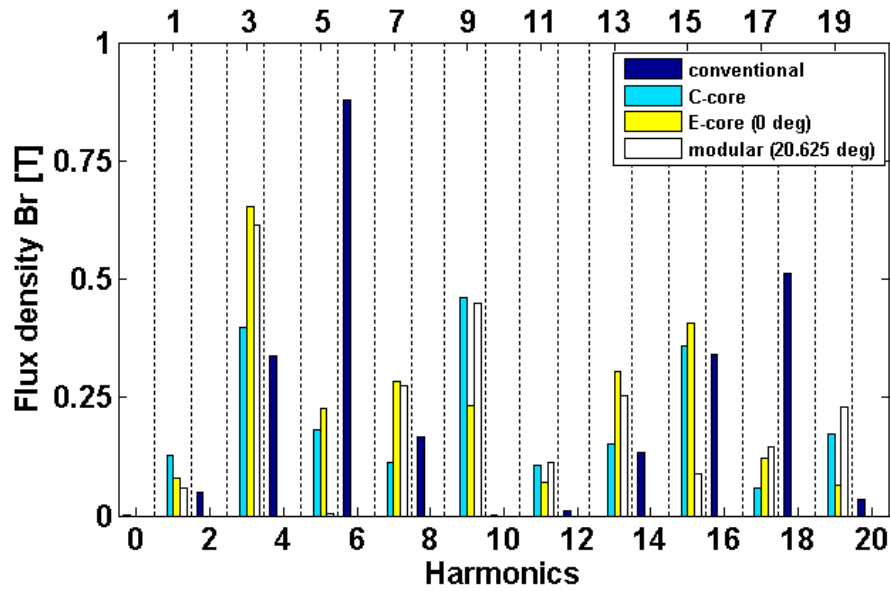
The radial components of the airgap flux density due to PMs are given in Fig. 3.5 (a) for the conventional, C-core, E-core [with the highest width of the unwound tooth as shown in Fig. 3.4 (d)] and modular topologies. The radial component of the airgap flux density is non-sinusoidal with high peaks

due to the doubly salient nature of the SFPMMs.

The spectra of the radial open circuit airgap flux densities are shown in Fig. 3.5. The conventional machine stands out with respect to the modular ones by having only even order harmonics. The removal of half of the magnets leads, in case of the modular machines, to a complete change in the harmonic spectrum. The modular machines are still able to deliver output torque since the coil electrical connections are modified in order for the armature winding to produce only odd order harmonics, similar with the ones produced by the PMs. As a result, the armature field harmonics can interact with the harmonics in the open-circuit airgap field in order to generate output torque.



(a)

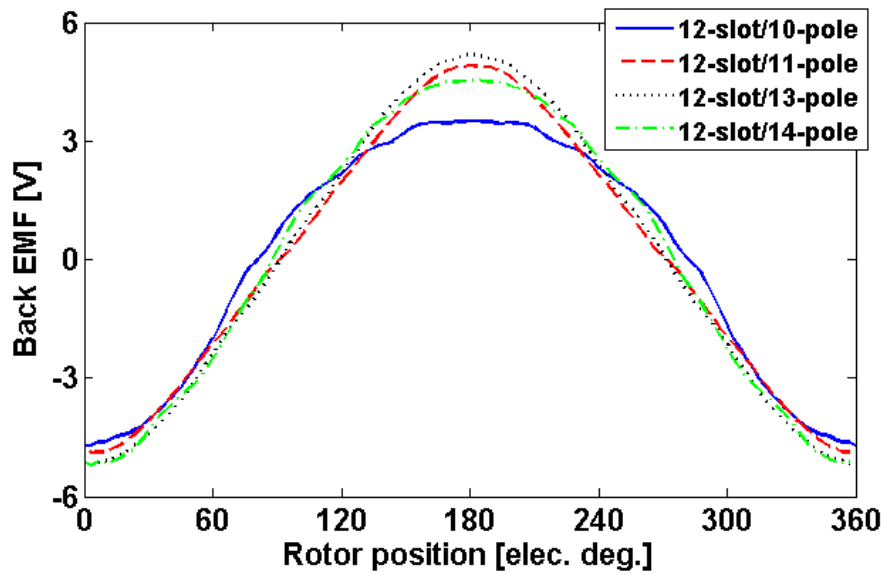


(b)

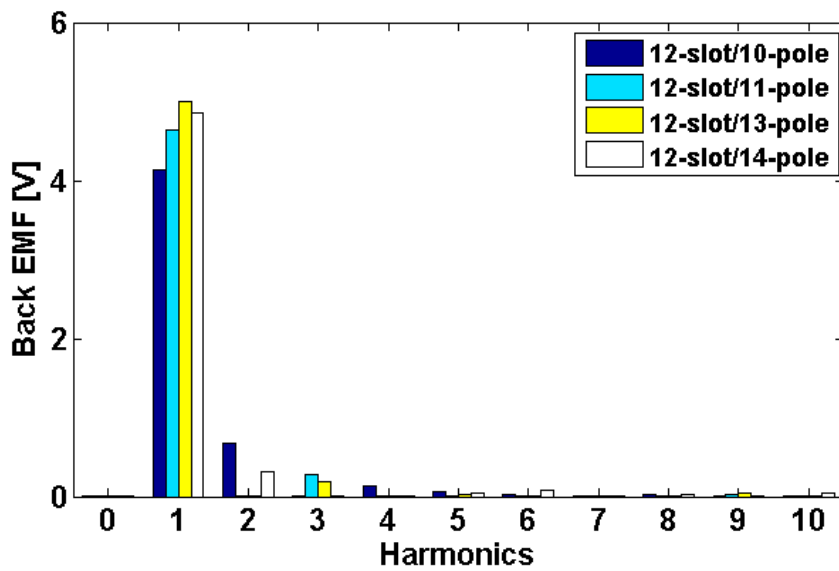
Fig. 3.5 Radial component of open circuit airgap flux density (12s/10p). (a) variation with angular position (400 rpm), (b) spatial harmonics spectrum.

3.3.3. PHASE BACK-EMF

The back-EMF variation of the phase A against rotor position is shown in Fig. 3.6 for conventional machines with different slot/pole number combinations (speed is 400 rpm). For a number of rotor poles closer to the slot number (11p and 13p), the waveform is closer to an ideal sinewave, while the 12s/10p and 12s/14p combinations exhibit an asymmetric waveform and a slightly increased number of harmonic contents [110], as shown in Fig. 3.6.



(a)



(b)

Fig. 3.6 Phase back-EMF for conventional machine (all slot/poles combinations). (a) variation with rotor position (400 rpm), (b) harmonic spectrum.

The fundamental phase back-EMFs of the modular machines with different flux gap openings are shown in Fig. 3.7. For some values of the flux gap opening, it can be noticed that the values are within

10% difference of the conventional ones for the same slot/pole number combination, as shown in Table 3.2.

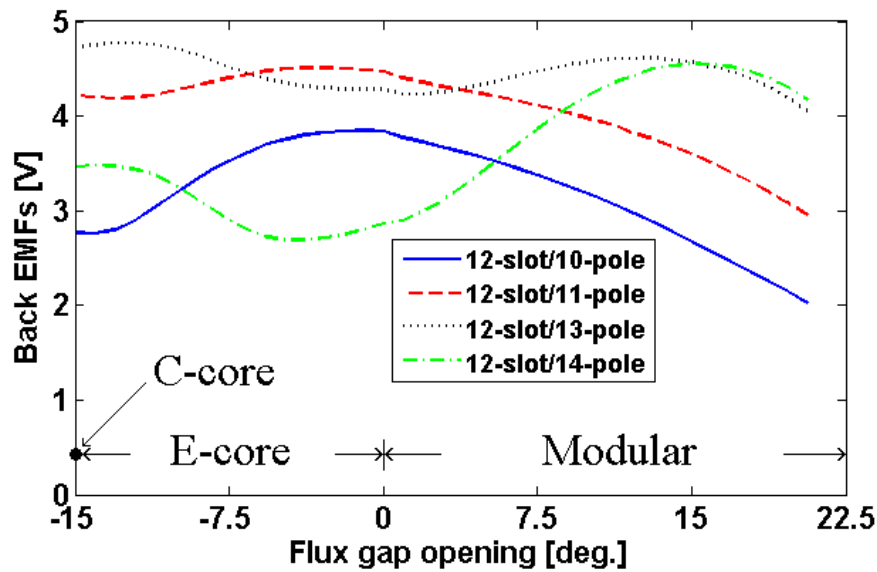


Fig. 3.7 Fundamental back-EMF variation against flux gap opening.

TABLE 3.2

BACK EMFs FUNDAMENTALS COMPARISON

Slot/Pole	Conventional	Modular	Flux gap [deg.]
	[V]	[V]	
12s/10p	4.14	3.85 (-7%)	-0.938 (E-core)
12s/11p	4.63	4.51 (-3%)	-2.81 (E-core)
12s/13p	5.01	4.77 (-5%)	-12.19 (E-core)
12s/14p	4.85	4.54 (-6%)	15.939 (Modular)

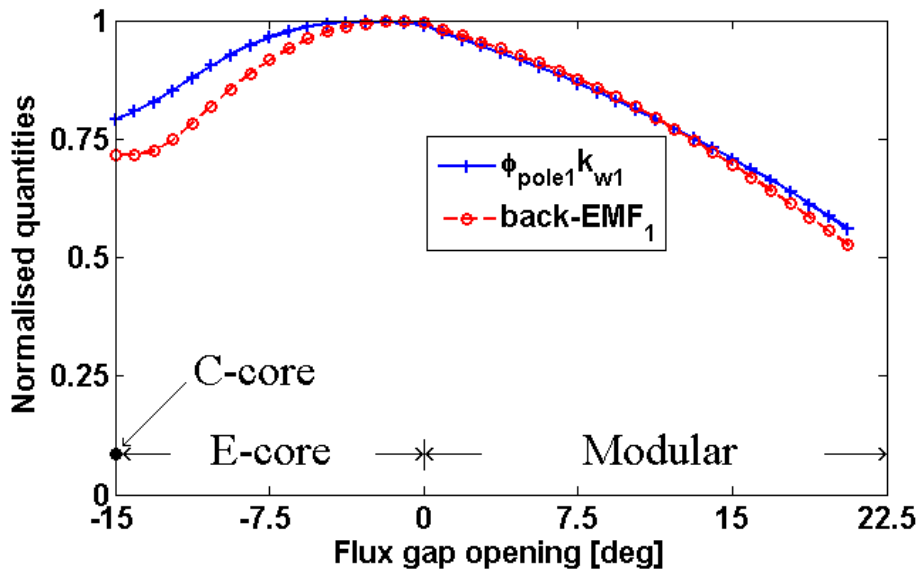
The back-EMF variation within the flux gap range shows that each slot/pole number combination can perform better for a particular topology. For example, the 12s/10p and 12s/11p machines reach their highest back-EMF value for the E-core topology as predicted by the winding factor variation. The

12s/13p and 12s/14p machines achieve higher back-EMF for their modular versions, again as predicted by the winding factor. However, in case of the 12s/13p, the C-core topology provides the absolute maximum and this cannot be explained by the influence of the winding factor alone. Overall, the 12s/13p C-core topology is the best option in terms of the generated back-EMF for all considered modular topologies and slot/pole number combinations. It is worth mentioning that the 12s/14p C-core topology represents an improvement over its E-core topology, in terms of generated back-EMF.

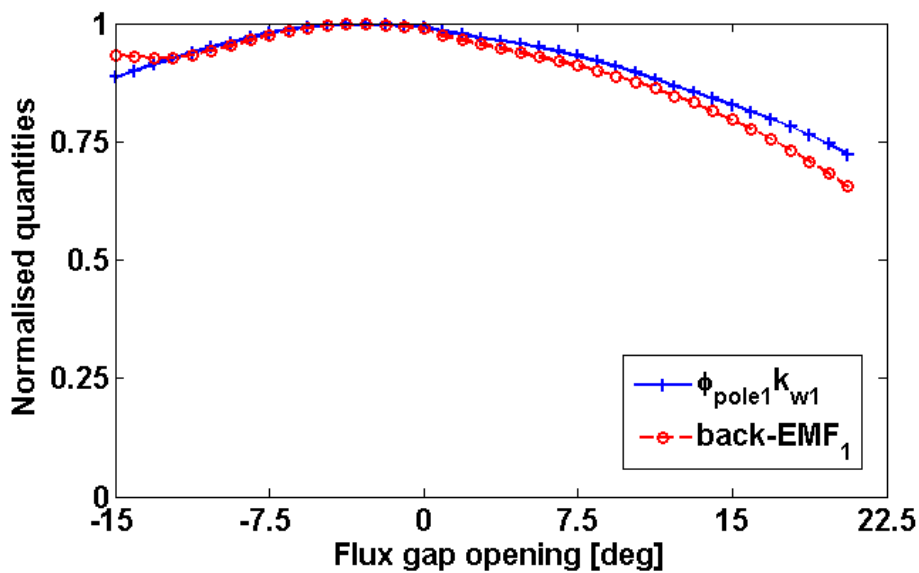
As shown in Fig. 3.3 and Fig. 3.7, the fundamental EMF variation against the flux gap opening is slightly different from that of the winding factor. This is mainly due to the fact that the EMF, apart from winding factor, also involves another factor, i.e. flux/pole as described by [115]:

$$E_f = \frac{2 \cdot \pi}{\sqrt{2}} \cdot f \cdot N_{ph} \cdot k_{w1} \cdot \phi_{pole1} \quad (3.3)$$

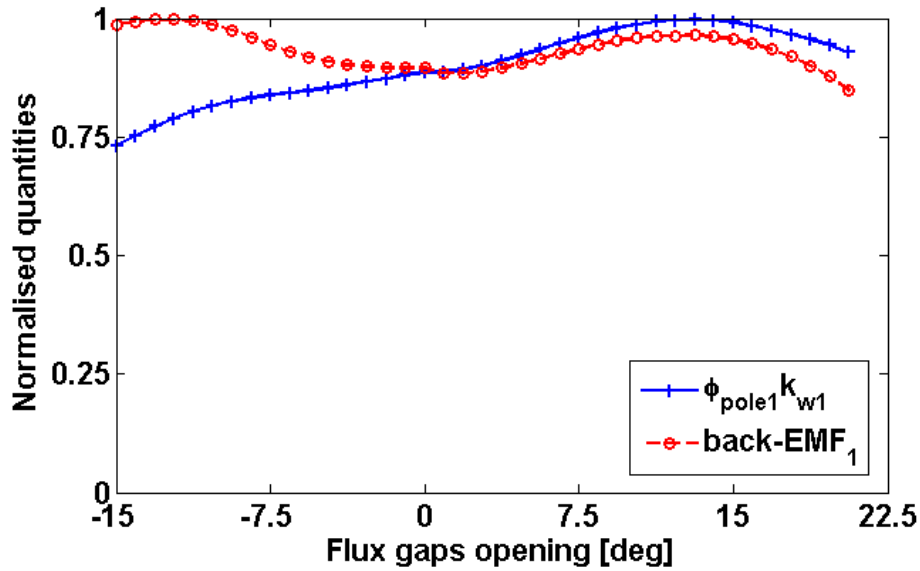
where k_{w1} is the fundamental harmonic winding factor and ϕ_{pole1} is the fundamental space harmonic value of the flux per pole. N_{ph} is the number of turns per phase while f is the electrical frequency. It should be noted that the study in this chapter assumes that all the machines operate at rated speed (400 rpm). Due to the fact that the study considers a different number of rotor poles, the frequency will increase with the number of poles, thus the generated back-EMF will also increase. Next, a comparison is made between the fundamental back-EMF values and the $k_{w1} \times \phi_{pole1}$ product for all slot/pole number combinations, as shown in Fig. 3.8.



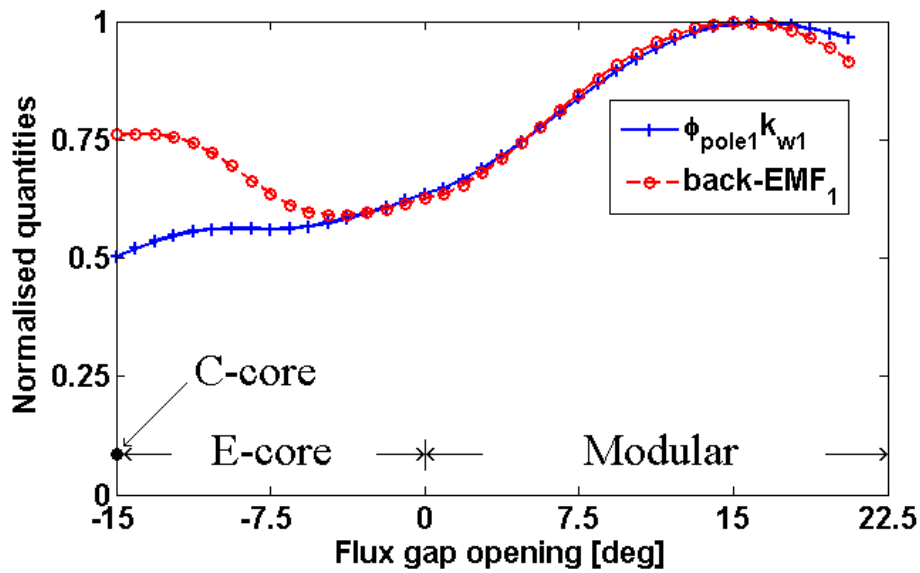
(a)



(b)



(c)



(d)

Fig. 3.8 Normalised back-EMF and $k_{w1}\Phi_{pole1}$ product variation against flux gap opening. (a) 12s/10p, (b) 12s/11p, (c) 12s/13p, (d) 12s/14p.

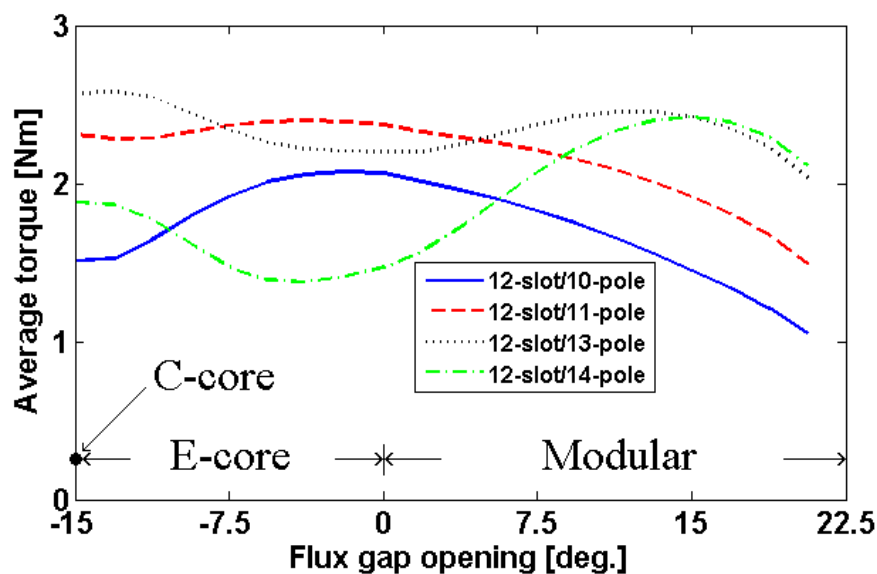
The differences between the back-EMF and the $k_w \times \Phi_{pole}$ product for the C-core and some of the E-core topologies can be explained by the presence of a flux focusing/defocusing effect. The C-core topology and some of the E-core topologies with a narrow tooth width experience a flux focusing effect

for the number of rotor poles higher than the number of stator slots while having a flux defocusing effect for lower number of rotor poles.

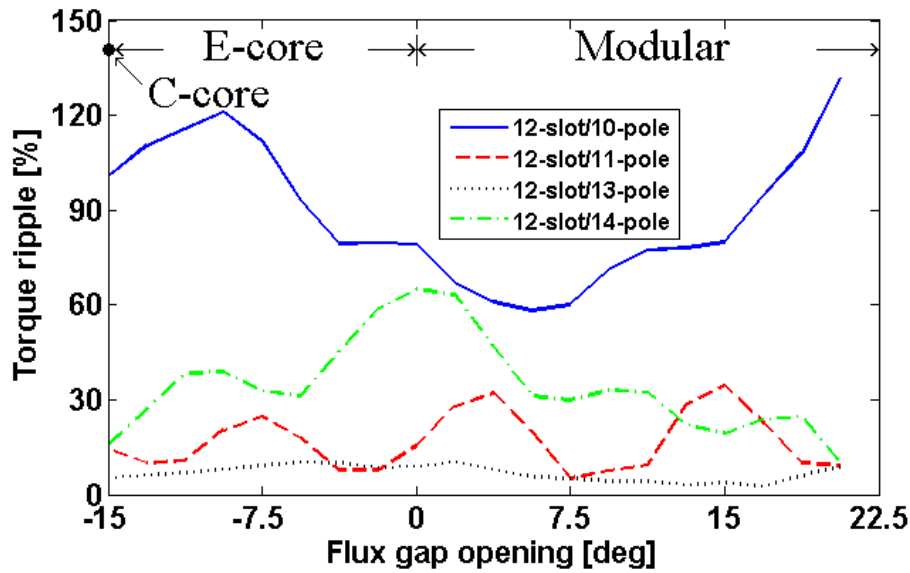
3.3.4. ELECTROMAGNETIC TORQUE

For modular machines, the average torque variation with flux gap opening, at the rated phase current is given in Fig. 3.9 (a). Depending on the slot/pole number combination and flux gap opening, the average torque value will significantly vary, which is similar to that shown in Fig. 3.7. However, for the current geometrical dimensions, they will never surpass the average torques produced by the conventional counterparts (<10 % difference). Knowing that only half of PMs are used for the modular machines it still makes them very attractive when compared to their conventional counterparts. The torque ripple variation has also been calculated, as shown in Fig. 3.9 (b). This is similar to that of the conventional machines, i.e. the closer the pole number to the slot number, the lower the torque ripple. Moreover, by properly choosing the flux gap opening, the torque ripple can be further minimized.

When compared to the relevant conventional counterpart (they have the same winding factor), it can be seen, as shown in Fig. 3.9 (a) and Table 3.3, that the modular machine with 7.5 deg. flux gap opening can generate comparable average torque. This is particularly the case for machines with pole number close to the slot number, i. e. 12s/11p and 12s/13p. However, for each slot/pole number combination, there is a specific flux gap opening, for which the modular machine can generate a torque even closer to the conventional machine, as shown in the Table 3.4.



(a)



(b)

Fig. 3.9 Average torque and torque ripple variations against flux gap opening. (a) average torque, (b) torque ripple.

TABLE 3.3

 AVERAGE TORQUE COMPARISON (SAME K_w AND FLUX GAP)

Slot/Pole	Conventional	Modular [Nm]
	[Nm]	
12s/10p	2.27	1.82 (-20%)
12s/11p	2.56	2.21 (-12%)
12s/13p	2.76	2.37 (-14%)
12s/14p	2.65	2.07(-22%)

Overall, based on Table 3.3 and Table 3.4 it can be noticed that no matter the choice of modular topology (E-Core, C-Core, Modular) there is always going to be a torque/volume penalty due to reduction of the PM volume with respect to the conventional machine. E-core topology is a good compromise with less than 10% performance penalty when compared with conventional one (Table 3.4) for 10, 11 and 13 poles version. E-core machine magnetless tooth will saturate depending on its thickness and number of rotor poles which in turn shows that there is an optimum flux gap for which the E-core machine achieves

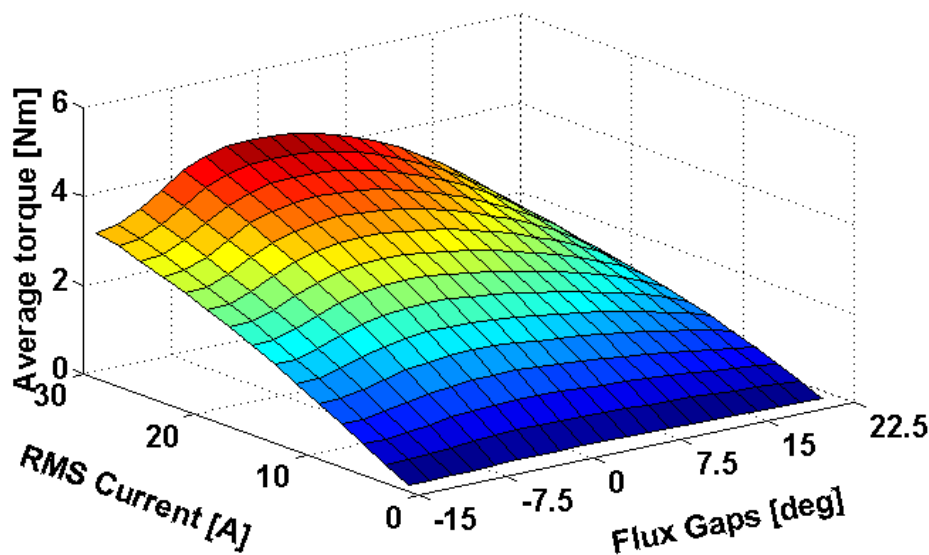
its maximum performance (Table 3.4).

TABLE 3.4

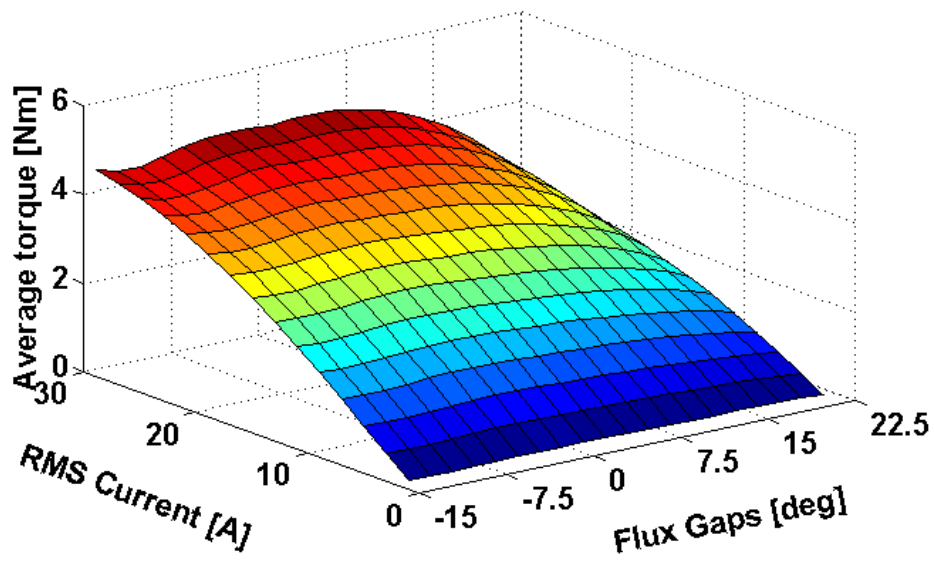
AVERAGE TORQUE COMPARISON (BEST VALUE)

Slot/Pole	Conventional [Nm]	Modular [Nm]	Flux gap [deg.]
12s/10p	2.27	2.07 (-9%)	-1.875 (E-core)
12s/11p	2.56	2.39 (-7%)	-3.75 (E-core)
12s/13p	2.76	2.58 (-7%)	-13.13 (E-core)
12s/14p	2.65	2.42 (-9%)	15 (Modular)

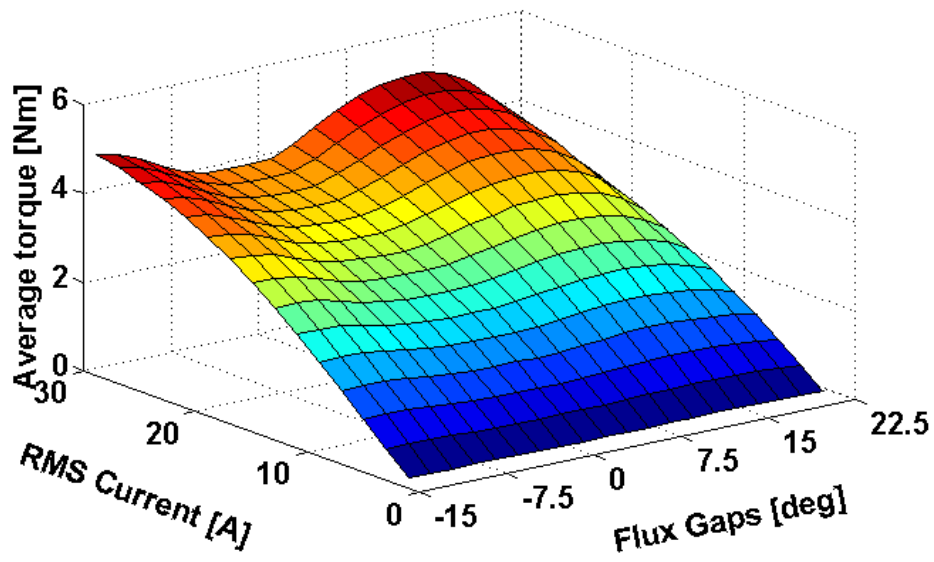
For a range of phase RMS currents between 1 and 29 A, the average torque variation for modular machines has been calculated, as shown in Fig. 3.10. It is interesting to note that some topologies perform better at overload conditions for a given number of poles albeit no general rule can be derived to explain it. For example, the E-core topology appears to be a good solution (maximum average torque > 4.5 Nm) at overload condition if a 12s/10p or 12s/11p configuration is chosen [Fig. 3.10 (a) and (b)]. However for the 13p and 14p it appears that the modular topology has better overload capability. For the C-core, reasonable results at overload condition, i.e. maximum average torque > 5 Nm, can be obtained for the 11p and 13p configurations.



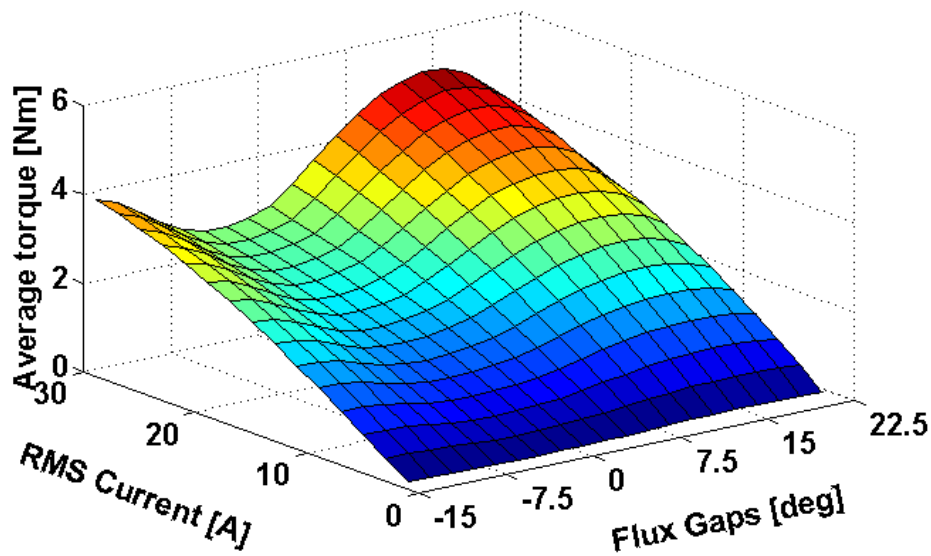
(a)



(b)



(c)



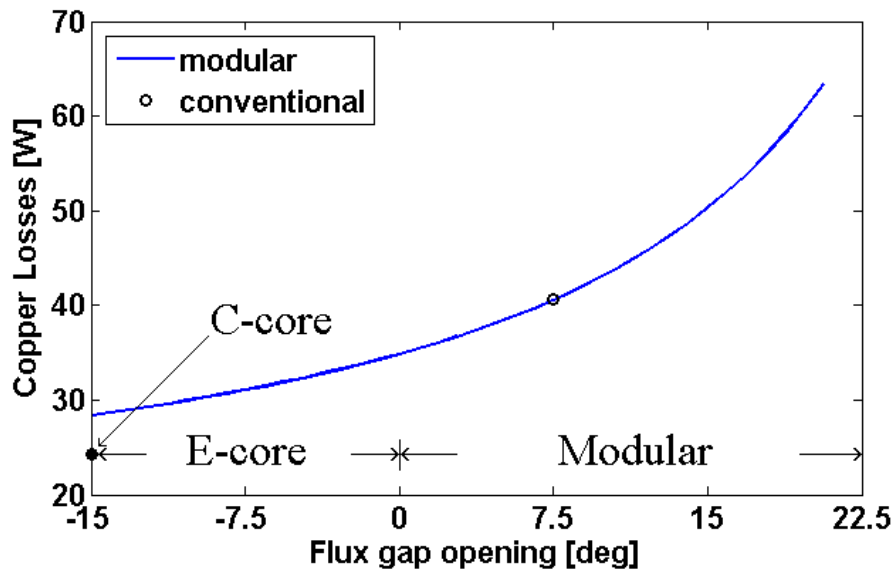
(d)

Fig. 3.10 Average torque variation against phase RMS current and flux gap opening for modular machines. (a) 12s/10p, (b) 12s/11p, (c) 12s/13p, (d) 12s/14p.

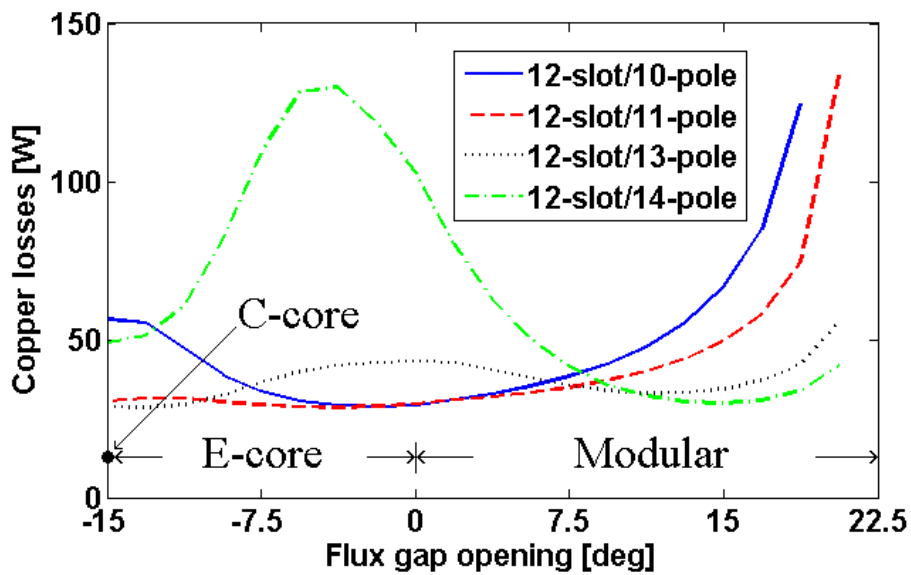
3.3.5. COPPER LOSS

The copper loss needs to be investigated for a fairer comparison. This is because the slot area allocated to windings varies while the flux gap changes. Since the number of turns is kept constant and the same rated current is applied for the whole flux gap range, the current density and thus the copper loss will be changed. The copper loss variation with the flux gap opening for the same rated current is given in Fig. 3.11 (a). The lack of the unwound tooth in the case of the C-core topology makes additional room for the windings which results in maximum possible area and thus have the lowest copper loss. For the maximum value of the flux gap opening, the copper loss increases roughly twice when compared to the C-core version.

In Fig. 3.11 (b) the copper loss is calculated when the torque is kept constant for different flux gap openings (the highest torque for each slot/pole combination). For some slot/pole number combinations and flux gap values, the phase current must be increased significantly to achieve the target torque which in turn explains the high value of the copper losses. However, for all the modular machines, it is possible to minimize the copper loss by properly choosing the flux gap opening.



(a)



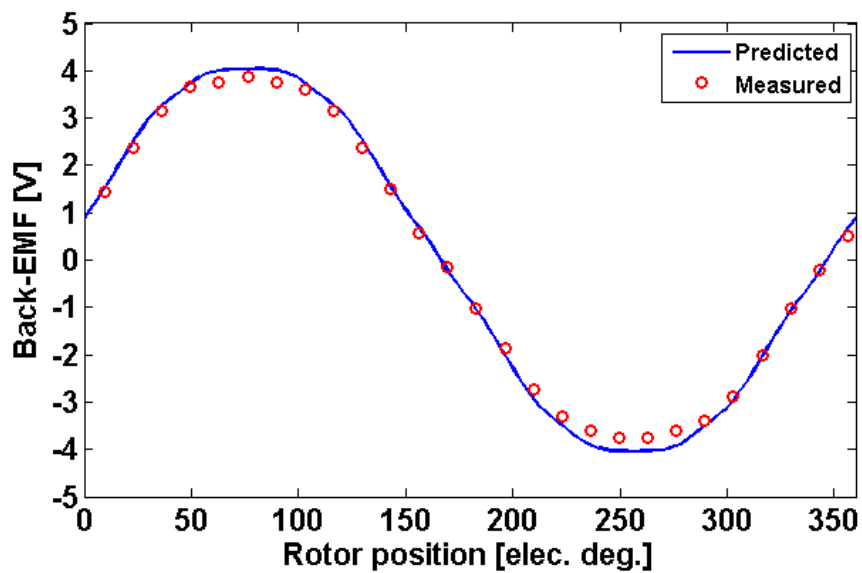
(b)

Fig. 3.11 Copper loss. (a) constant rated current, (b) constant targeted average torque (best value for each slot/pole number combination).

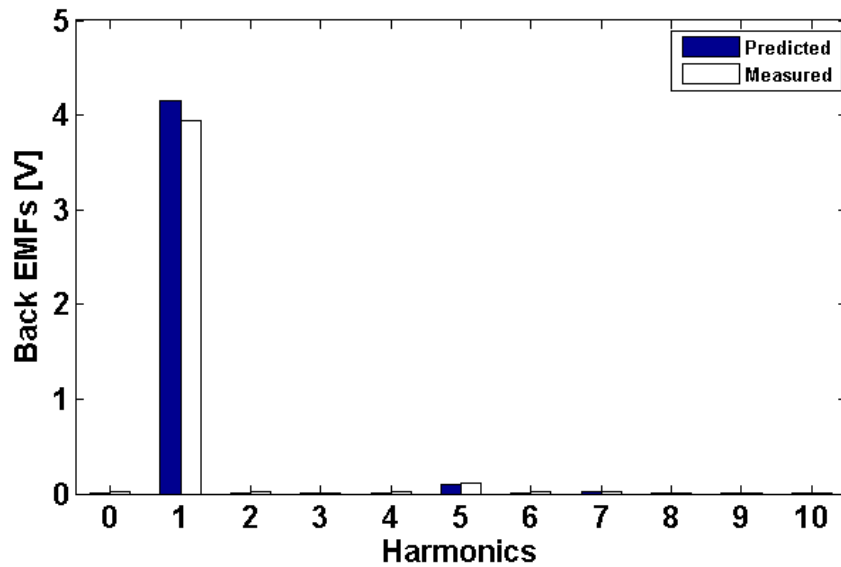
3.4. EXPERIMENTAL VALIDATION

In order to experimentally verify the results obtained in this chapter, the prototype for the conventional double layer machine presented in section 2.5 was used.

The tests in terms of phase back-EMF, cogging torque, static torque, and self- and mutual-inductances have been carried out. The first compared parameter is the phase back-EMF, as shown in Fig. 3.12. The FE results match very well with the measured ones.



(a)



(b)

Fig. 3.12 Predicted and measured phase back Back-EMFs. (a) waveforms, (b) spectra.

For cogging torque (Fig. 3.14) and static torque (Fig. 3.16) measurements, the method introduced in [116] was used. Both types of experiments are using a lathe which secures the prototype and also allows precise, measurable rotation of the motor shaft. A mechanical arm is connected to the motor shaft, transforming the motor output torque into a linear force measured by a digital scale. When it comes to the cogging torque, the motor has an open circuit connection, without any type of power supply connected.

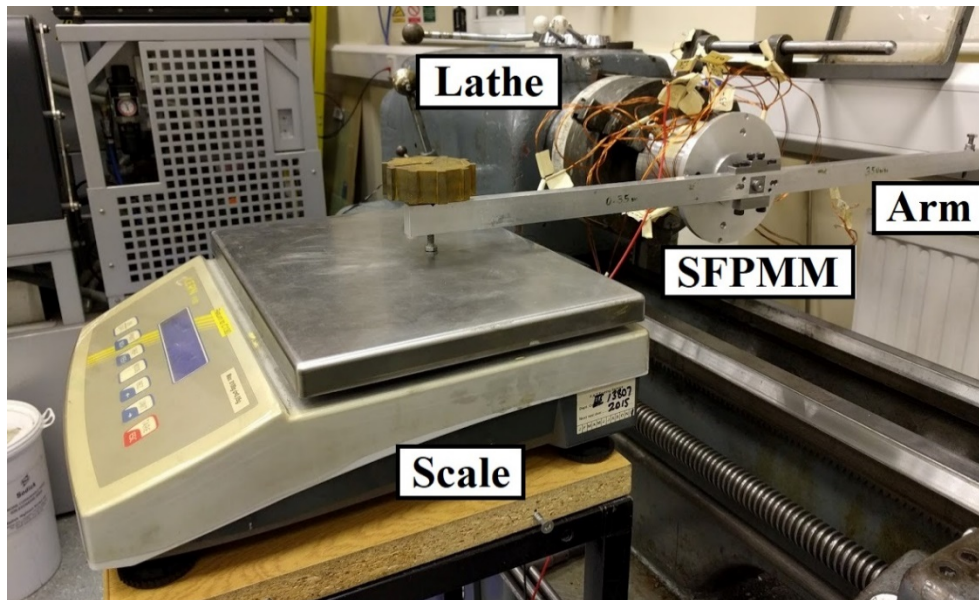


Fig. 3.13 Experimental setup for cogging and static torque.

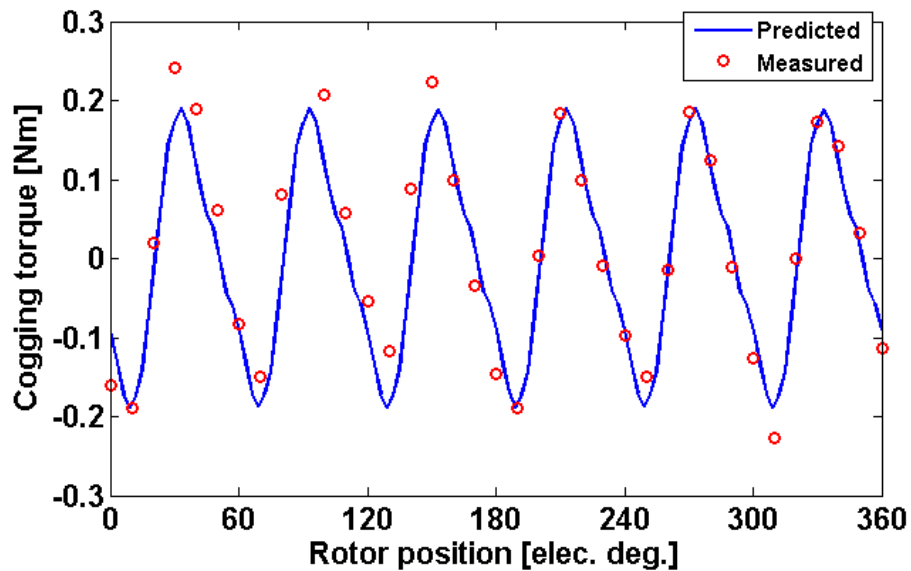


Fig. 3.14 Cogging torque waveform.

The static torques for different currents I ranging from 5A to 15A are obtained next. The phases are connected to a DC supply in such a manner that $I_a=I$ and $I_b=I_c=-I/2$, Fig. 3.15. Then the torque can be measured for different rotor positions. In such a way, the torque vs phase advance angle can be simulated. It is worth noting that in Fig. 3.16, the waveform of static torque is not smooth. This is mainly due to the

existence of torque ripple.

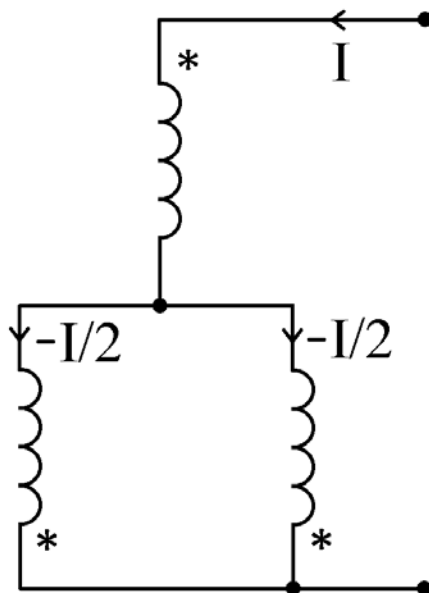
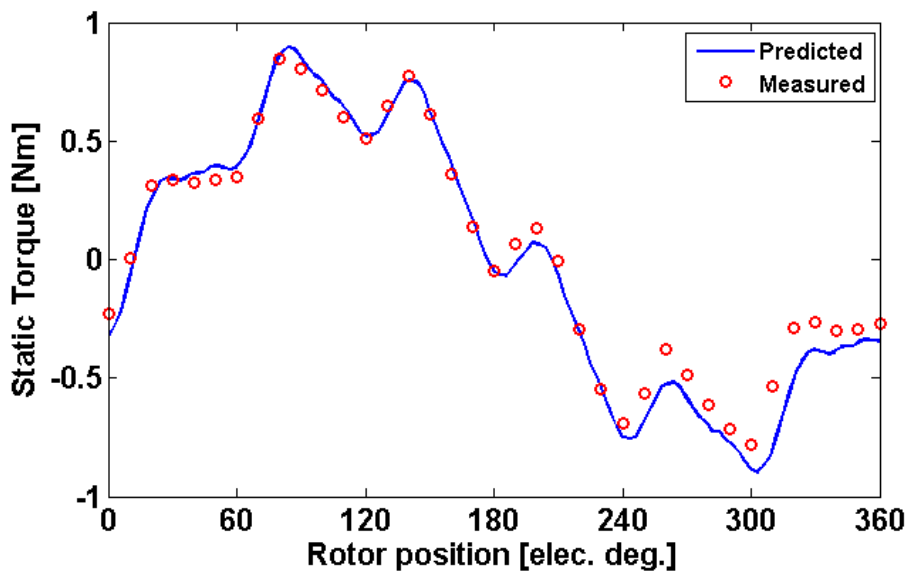
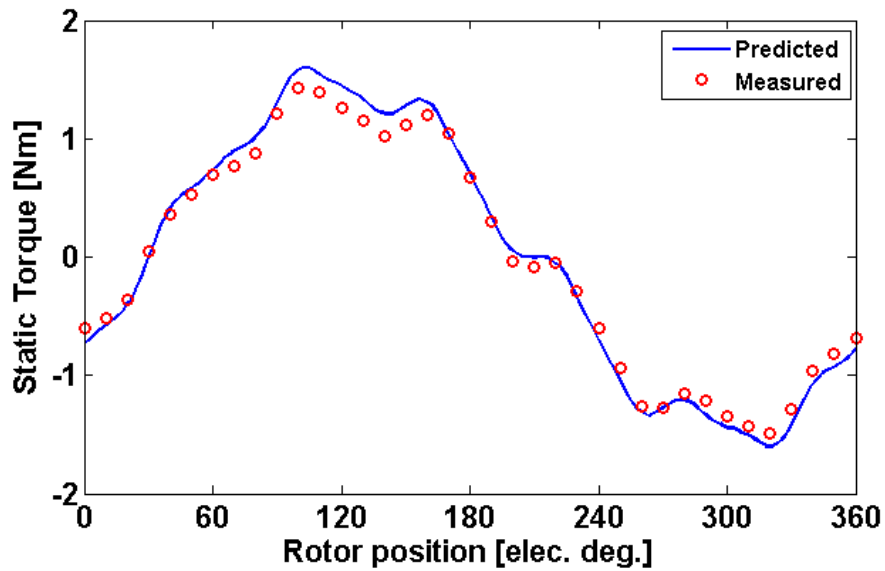


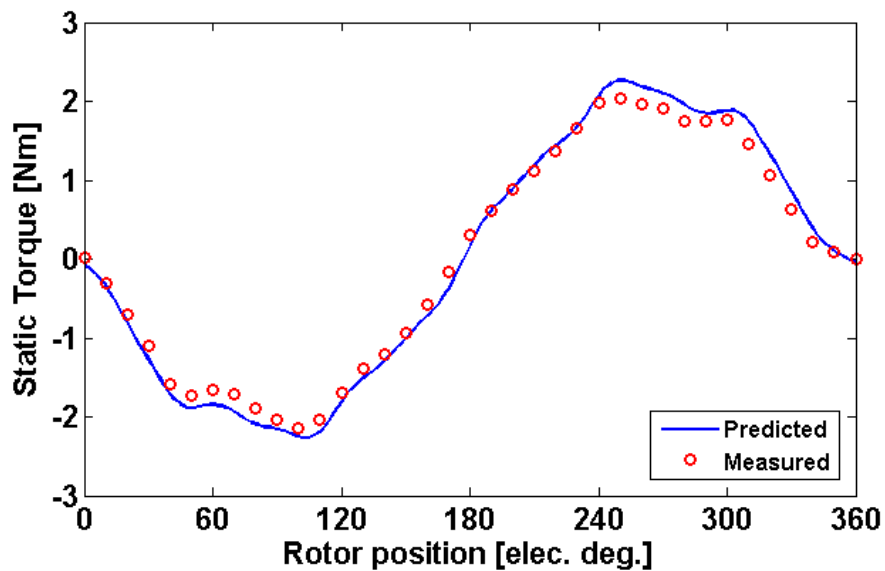
Fig. 3.15 Phase connection for measuring the static torque.



(a)



(b)



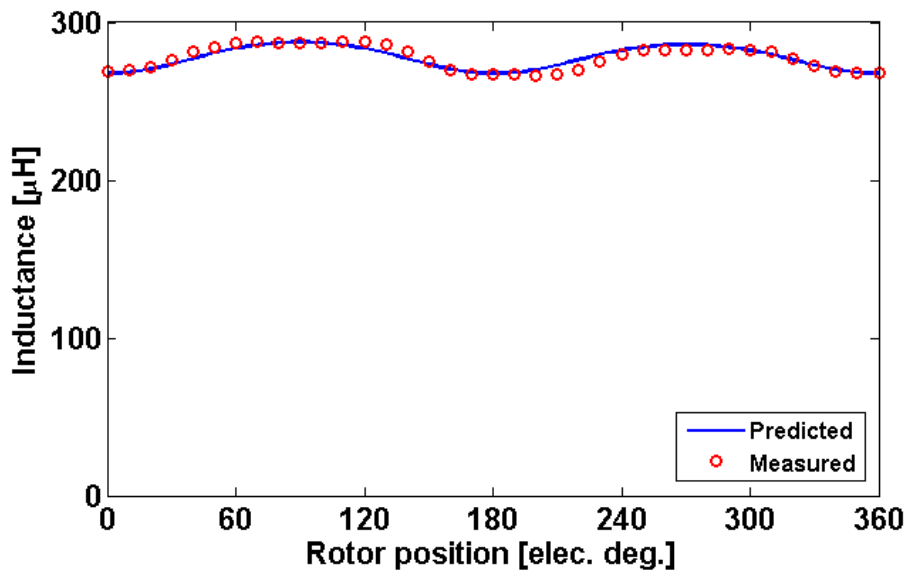
(c)

Fig. 3.16 Static torque experimental validation. (a) $I = 5A$, (b) $I = 10A$, (c) $I = 15A$.

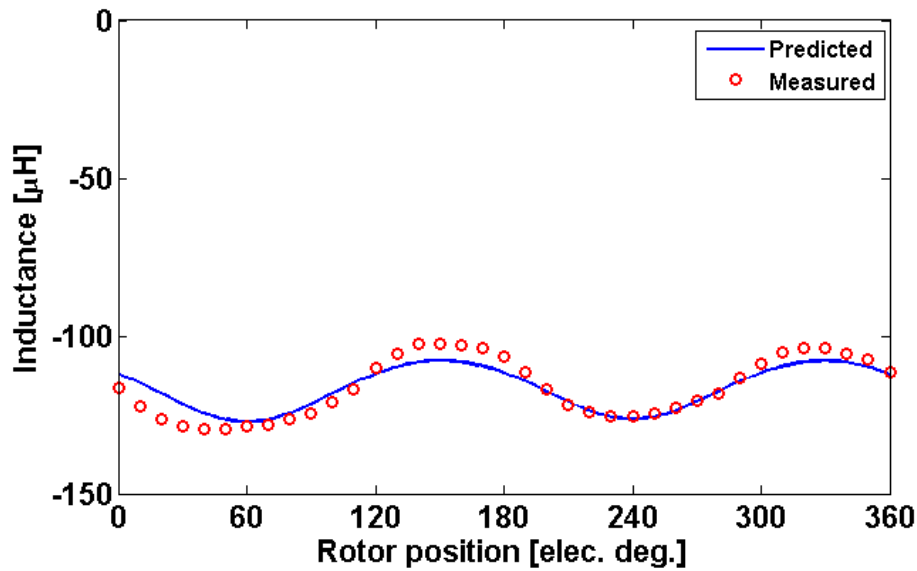
The self- and mutual-inductance are measured with a RLC-meter using a 4-wire probe. The rotor position is varied for an electric cycle. The measured results are further compared with 2D FEM results – the end winding inductance is used to compensate for 3D effects and it is calculated using the following expression [117]:

$$L_{end} = n_{coils} \cdot n_{cond}^2 \cdot K_{W1}^2 \cdot (2 \cdot l_{mean}) \cdot 1.2 \cdot \mu_0 \quad (3.4)$$

where n_{coils} represents the number of coils per phase, n_{cond} is the number of turns per coil, K_{w1} is the fundamental winding factor, l_{mean} is the average end-turn length and μ_0 is the vacuum magnetic permeability constant.



(a)



(b)

Fig. 3.17 Inductance variation with rotor position. (a) self-inductance, (b) mutual-inductance.

The mean values of the inductances are further compared in Table 3.5. Overall, there is a good agreement between the predicted and measured results.

TABLE 3.5

MEAN VALUES OF PHASE INDUCTANCES

	Self-inductance (μH)	Mutual-inductance (μH)
Predicted	277.61	-116.75
Measured	277.50	-116.30

3.5. CONCLUSIONS

The electromagnetic performance of alternative single layer modular switched flux permanent magnet (SFPM) machines, i.e. conventional, C-core, E-core and modular, was compared by finite element analysis in this chapter. The comparison includes winding factor, open-circuit flux density, back-EMF and electromagnetic torque, together with the influence of four slot/pole number combinations (12s/10p,

12s/11p, 12s/13p and 12s/14p). It is found that with flux gaps, the electromagnetic performance of the modular SFPMMs does not necessarily degrade. The flux focusing and defocusing effects are observed in the C-core and some of the E-core machines. However, the flux defocusing effect occurs in all modular machines with large flux gap openings. Since the flux gap opening affects the slot area, the copper loss will be changed as well. Hence, the variation of copper loss against flux gap opening for the same current or the same torque has also been investigated.

A unified way of approaching the study was proposed by using the flux gap parameter associated with the magnetless teeth. Using the flux gap parameter, the modular topologies can be naturally derived from each other. The reduction of the PM volume affects the resulting modular machine in terms of the magnetic phase coupling, phase back-EMF and electromagnetic torque. As a result, the phase back-EMF and the average torque for the modular machines, the PM volume of which has been halved, are smaller when compared to their conventional counterparts. However, for each slot/pole combination, a value of the flux gap can be chosen in order to keep the torque value within a 10% difference from the conventional one while maintaining an acceptable level of copper loss. Therefore the results in this chapter can be used to select an optimal slot/pole number based on resulting torque, torque ripple and copper loss. The accuracy of the predicted results were fully validated by a series of tests using a conventional double layer machine.

The study in this chapter focuses mostly on performance analysis during normal operating conditions (healthy mode). However, given the potential of these topologies for fault tolerant application, their performance during fault conditions is also relevant for investigation. Therefore, their resilience to faults is going to be investigated in the next chapter.

Chapter 4. Comparative Study of Fault Tolerant Switched Flux Permanent Magnet Machines

The fault tolerant capabilities are compared in this chapter for the conventional double layer switched flux permanent magnet machine and its single layer counterparts, i.e. C-core, E-core and modular. The comparison includes the inter-turn short-circuit and irreversible demagnetization faults. The temperature effects on permanent magnet material are taken into account and the influence of short-circuit current over demagnetization is evaluated. Various fault scenarios are investigated, including high speeds and high fault severity. A combination of Simulink and finite element models is used in the study. Based on the predictions, it is found that the modular topology produces the lowest short-circuit current and also has the best demagnetization withstand capability while the conventional one produces the highest short-circuit current and has the worst demagnetization withstand capability. The frozen permeability method is employed to separate the flux produced by armature current and magnets, and the results showed that, besides the influence of short-circuit current, the available magnet volume and magnetic circuit configuration play an important role in the demagnetization process. The mechanism of demagnetization is revealed and found out to be mainly due to temperature rise and poor PM materials utilization. It is also found that removing half of the magnets, such as using C-core, E-core and modular topologies, generally improves the demagnetization withstand capability and also increases the torque per magnet volume. Measured results are also presented to validate the short-circuit current predictions and magnet demagnetization.

4.1. INTRODUCTION

Drawbacks of the conventional SFPMM [3] include the double layer winding configuration hence making it unsuitable for fault tolerant applications in its conventional form. The reason is that there is no thermal, physical and magnetic separation between phases. This can be improved by using a single layer winding in which only alternate stator poles are wound [22], [110], [28], [47]. The single layer machines magnetic configuration can be derived from the conventional one based on the modification of the unwound stator teeth. As a result, topologies like C-core [22], E-core and modular [110] can be obtained. These topologies have been detailed and studied in the previous chapter from a performance point of view mainly. They do improve on the conventional SFPMM by achieving better fault-tolerant capability though design as well as cost reductions due to using less PM material.

However, an important issue of all the SFPMMs is the PM location, which is inside the concentrated armature coils, making them potentially vulnerable to demagnetization due to high temperatures and demagnetizing fields during flux weakening or short-circuit operation [68], [67], [70]. This would be a problem for instance in the aforementioned aircraft applications where the machines often need to operate at high temperatures at around 150°C, which can irreversibly demagnetize the PMs. Although important, the issue of demagnetization in the SFPMMs has been brought under investigation only recently. The available literature shows that the machine can withstand demagnetization under generating and motoring operations, given that the PM temperature is kept low [18], [70], [72], [105]. The armature MMF is found to be always parallel to the PM MMF and hence will not demagnetize the magnets. In [18], an analysis of a SFPMM using ferrite as PM shows that local demagnetization occurs in the corners of the PM adjacent to the airgap leading to deteriorated machine performance. This occurs in both generating and motoring modes. In [72] a study considering PM dependence with temperature is carried out, showing the possibility of irreversible demagnetization at high temperatures. Finally, in [105] the demagnetization is assessed for a SFPMM having hybrid ferrite and NdFeB PMs at different temperatures.

However, in the available literature, most studies are concerned with healthy conditions and also conventional SFPMM topology. Moreover, the fault-tolerant topologies such as C-core, E-core and modular machines have been compared only from the point of view of electromagnetic performance and static characteristics but have not been studied under faulty operations, particularly under the inter-turn short-circuit conditions. Due to the specific topology of the SFPMM (PMs are surrounded by armature coils), the inter-turn short-circuit could have a dramatic effect on the affected PM. Therefore, to fill in this gap, in this chapter the potential irreversible PM demagnetization due to inter-turn short-circuit of four SFPMM machines, i.e. conventional double layer, single layer C-core, E-core and modular

machines, is investigated. Since the short-circuit fault can quickly lead to significant temperature rise, the temperature dependent properties of PM material are also considered in the study.

In section 4.2 the investigated topologies are detailed and their performance, fault tolerance and magnetic phase separation summarized based on self and mutual inductance. They do build upon the previous chapter study with the difference that only a few topologies have been selected from each class. For example, the E-core will correspond to a 0 deg. fluxgap. In section 4.3 the models involved and the faults studied are given. Also, this section contains the experimental validation. The results in this section are important for the next one, section 4.4 where the irreversible demagnetization process is studied. In 4.5 a more in detail study of the demagnetization is carried out with a focus on the temperature and magnetic circuit configuration. Finally, in section 4.6, the conclusions of the chapter are drawn.

4.2. FEATURES OF INVESTIGATED MACHINES

The cross sections of the conventional and modular machines were introduced in previous chapter while their main parameters were given in Table 3.1. Compared with the conventional one, the C-core, E-core and modular topologies have the PM volume reduced by half and some of the PM magnetization directions changed in order to maintain an alternating polarity across the stator circumference. Giving the different magnet magnetization directions for the C-core, E-core and modular structures, the coil connections must also be changed. Moreover, in case of the E-core and modular machines, the unwound stator teeth are modified by either removing the magnets or replacing the magnets with iron while the wound teeth containing the PM have the same geometries as those in the conventional machines. All machines have 3-phase winding, and all studied fault tolerant machines (C-core, E-core and modular) have two coils per phase while the conventional one has four coils per phase. However, to maintain similar phase back-EMF level, the number of turns per phase is the same for all investigated machines. The PM material used in all machines is NdFeB (N35H grade) [106].

As shown in Chapter 3 and [118], a link can be established between these topologies based on a geometrical parameter named “flux gap” which quantifies the variation of the unwounded stator tooth width. In this way, the C-core, E-core and modular machines can be studied and compared in a unified way by varying the flux gap opening. However in this chapter only representative topologies from each class are investigated.

A performance comparison of the investigated machines, Fig. 4.1, shows that the E-core topology produces the highest average torque. Although the E-core machine produces 10% lower average torque

than its double layer conventional counterpart (Table 4.1), it is still acceptable, given the fact that the PM volume is halved in the former. This also means that the E-core SFPMM makes better use of the available PMs. It is interesting to note that with the increasing flux gap opening, the performance of the E-core topology improves while for the modular topology the performance deteriorates. It can be concluded that the auxiliary unwound tooth, without flux-gaps, is important in retaining as much performance as possible when compared with the conventional double layer SFPMM. This also explains the choice of that particular E-Core topology with the widest tooth in the study.

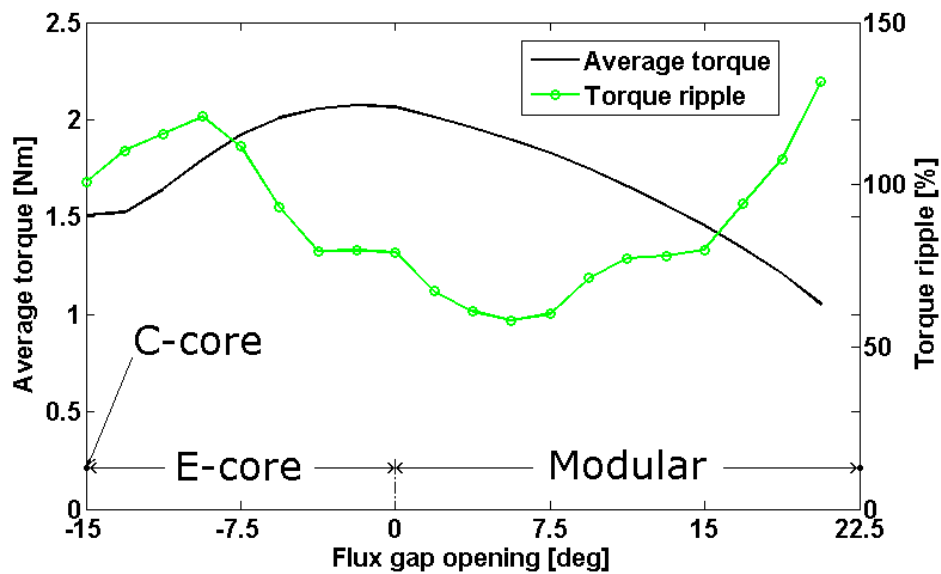


Fig. 4.1. Average torque and torque ripple variations against flux gap.

TABLE 4.1

PERFORMANCE COMPARISON

	Average torque [Nm]	Torque ripple [%]
Conventional	2.2	17
C-core	1.5	101
E-core	2.0	79
Modular (7.5 deg.)	1.8	60

TABLE 4.2

AVERAGE SELF- AND MUTUAL INDUCTANCES

	Self inductance [mH]	Mutual inductance [mH]
Conventional	0.24	-0.12
C-core	0.47	0.09
E-core	0.57	0.05
Modular(7.5 deg.)	0.53	0.04

In addition, the separation between phases and hence the fault tolerant capability can also be linked with the flux-gap parameter, e.g. higher flux-gap opening means stronger separation between phases. It is worth mentioning that the C-core topology (a highly un-optimized double layer machine from the point of view of slot/pole number combination) has similar features as the double layer conventional SFPMM, i.e. both have a strong mutual coupling between phases. This can be proven by the results shown in Table 4.3 in which the C-core topology has a comparable mutual inductance between phases with the conventional one (0.09 mH vs 0.12 mH). However, the modular machines with large flux gap openings have the lowest mutual inductance and provide the best magnetic, thermal and electrical decoupling between phases. The influence of flux gaps on mutual coupling between phases will have a profound influence on short-circuit current and the resulted magnet irreversible demagnetization as will be investigated in the following sections.

4.3. FAULT MODELLING OF THE SFPMM

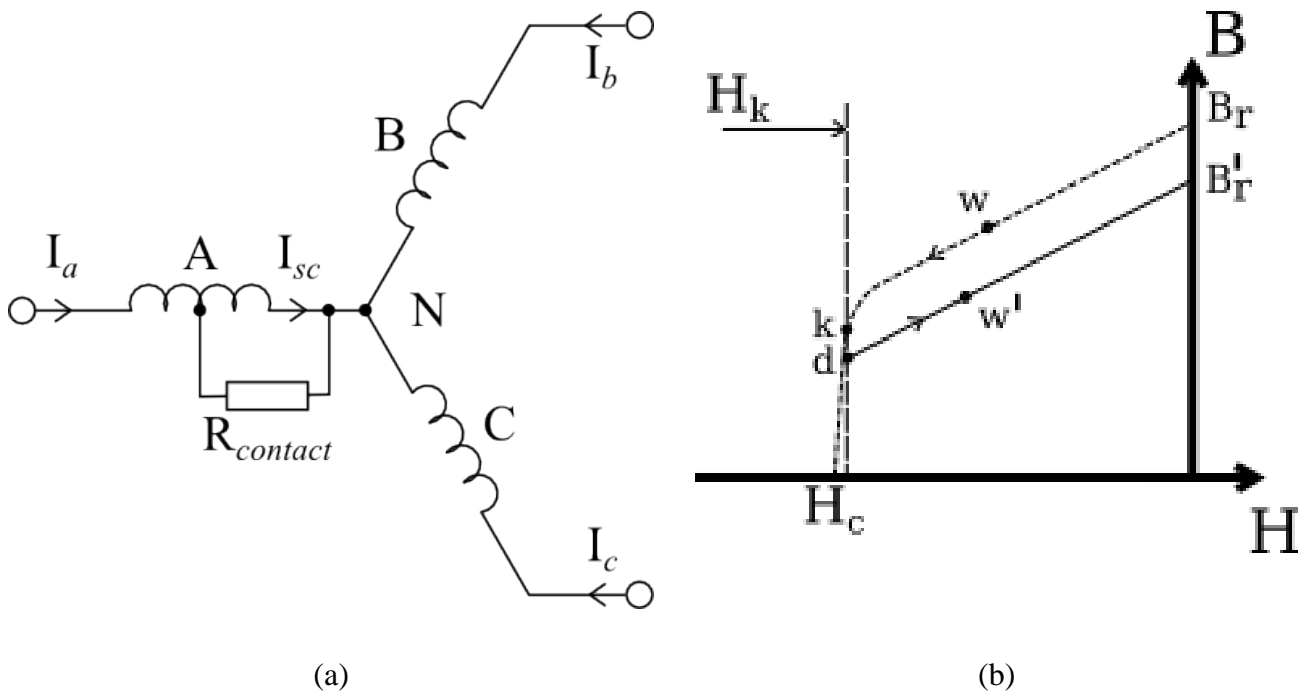
4.3.1. INVESTIGATED FAULTS

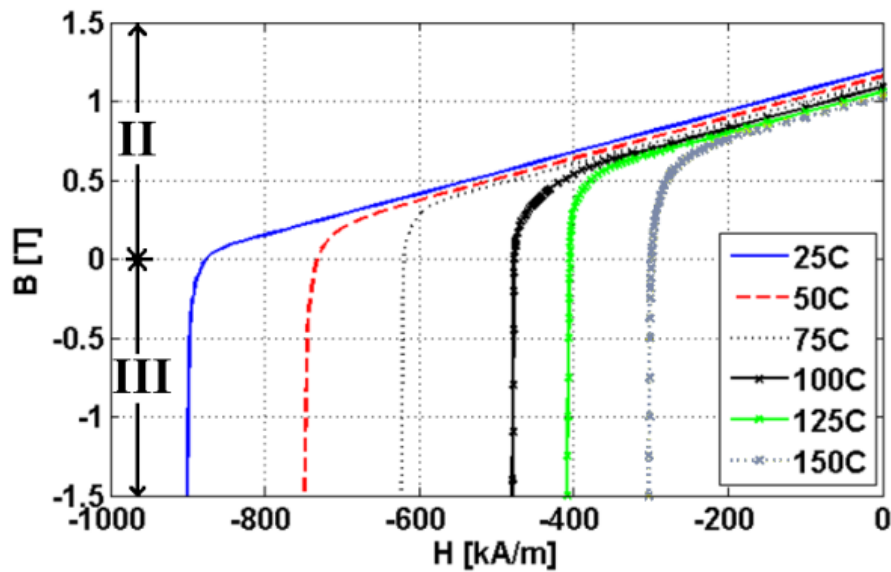
The PM irreversible demagnetization fault under inter-turn short-circuit conditions is investigated in this chapter. The inter-turn short-circuit fault is a severe condition [119], [120], [121] which affects the machine operation and can lead to the destruction of the entire winding. High inter-turn short-circuit currents will lead to local overheating which can propagate further to the PMs placed inside the affected coils of the SFPMMs due to their specific stator topologies. As a result, the irreversible demagnetization fault could occur, lowering the PM remanent flux density (B_r) and hence the overall machine performance. By way of example, the short-circuit is introduced in phase A, as shown in Fig. 4.2 (a).

Furthermore, the fault severity is defined as the ratio of short-circuited number of turns over the total number of turns per phase. For example, if only one coil per phase is short-circuited, then for conventional machine the fault severity is 25% while for C-core, E-core and modular machines, it is 50%. Subsequent studies concerning the demagnetization will be focused on the PM inside the affected coil.

The PM material defined in finite element model has to account for changes in B_r due to irreversible demagnetization especially at higher temperatures [122], [16], [69], [123]. The PM model will update the B_r locally inside each mesh element if the magnetic field strength H drops below the knee point value H_k , as shown in Fig. 4.2 (b). The update algorithm is the following:

- 1) initially the PM working point is defined by the point w which has a remanence of B_r ;
- 2) assuming the new working point is d and $H_d < H_k$, B_r will be updated to B_r' ;
- 3) if the demagnetizing MMF is reduced, the new working point is w' along a recoil line defined by B_r' .





(c)

Fig. 4.2. The faults investigated. (a) schematic representation of the inter-turn short-circuit fault, (b) the PM irreversible demagnetization model, (c) PM demagnetization characteristics for various temperatures.

In addition, the PM demagnetization is strongly dependent on operating temperature, Fig. 4.2 (c). The PM operation point can work in the second and third quadrants of the B(H) curve, depending on the operating conditions and temperatures. This has also been accounted for in the study.

TABLE 4.3

CHARACTERISTICS OF PM MATERIAL

Temperature [°C]	25	50	75	100	125	150
B_r [T]	1.20	1.16	1.13	1.09	1.06	1.03
B_{knee} [T]	-0.08	0.03	0.20	0.28	0.40	0.50

4.3.2. METHOD OF INVESTIGATION

The investigation method adopted in this chapter is based on a combination of FE (Altair/Flux2D) and MATLAB/Simulink models. Firstly, FE models are used to obtain the inductances, back-EMF and cogging torque waveforms which are temperature and rotor position dependent. These will be used later

in phase variable models implemented in Simulink, which will then generate the armature currents under the inter-turn short-circuit conditions. Finally, these currents are introduced in the magneto-static FE models to assess the aforementioned demagnetization. It is worth noting that the solution of using FE and MATLAB/Simulink models is much faster than the co-simulation models while providing satisfactory accuracy.

4.3.3. DYNAMIC MODEL (MOTORING MODE)

The dynamic operation model [28], [84], [124], [125], [126], [127] that can be used for both healthy and faulty operations is based on Matlab/Simulink models and it was discussed in the Appendix. The SFPMM model can be implemented using the voltage and torque equations in the Appendix. The Maximum Torque per Ampere (MTPA) control strategy is used. The conditions imposed for all machines are the same rated current (11 Arms) and the same speed during healthy conditions. Initially, the machine operates under healthy conditions and then the inter-turn short-circuit is introduced in the phase A. The temperature rise effects are considered during the faulty operation for the short-circuited coil and the affected PM.

Using this model, the short-circuit current can be calculated. The peak values during steady state for different temperatures are given in Table 4.4. It can be noticed that short-circuit current decreases with temperature. This is due to two reasons. First, the resistance of the affected coil increases with temperature. Second, the remanence of the affected magnet and its contribution to the phase back-EMF decrease with temperature. Moreover, it is also found that the C-core, E-core and modular machines are characterized by a smaller short-circuit current as expected due to their higher self-inductance.

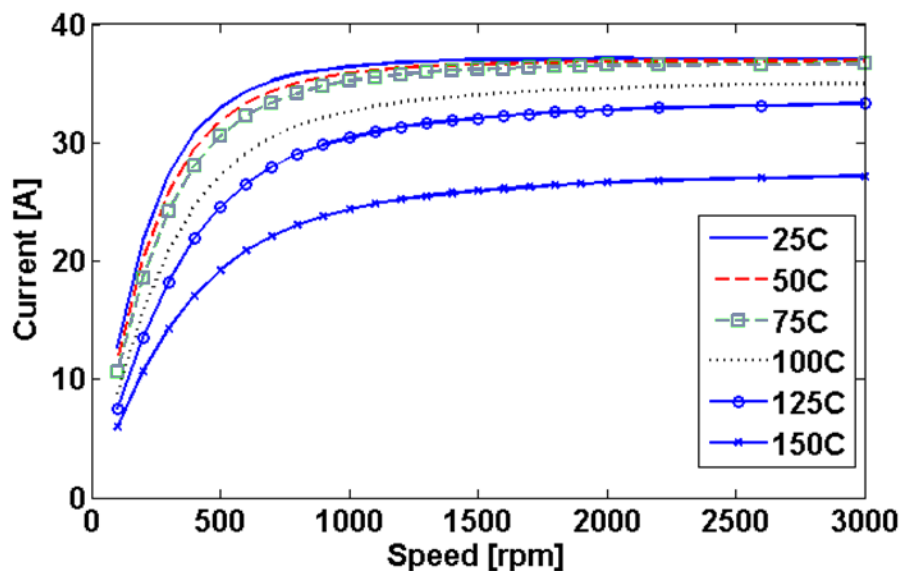
It should be noted that although the short-circuit current is much smaller for C-core, E-core and modular machines, the resulting demagnetizing MMF produced by the short-circuited coil will still be close to that of the conventional machine. This is due to the fact that the short-circuited coil contains a doubled number of turns for the C-core, E-core and modular machines when compared with the conventional counterpart.

TABLE 4.4

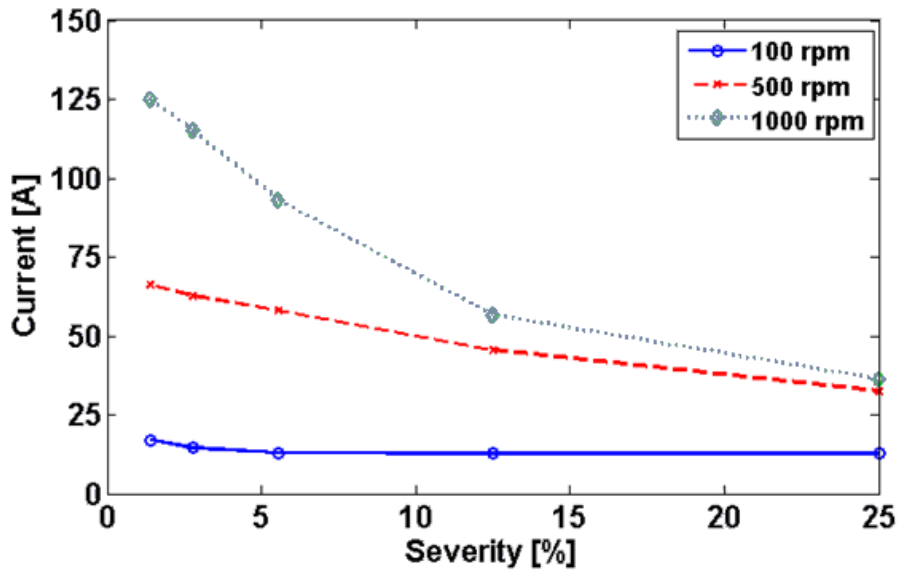
STEADY-STATE PEAK VALUES OF SHORT-CIRCUIT CURRENT 2000 RPM

Machines	25°C	50°C	75°C	100°C	125°C	150°C
Conventional	36.4	35.9	35.2	32.7	30.4	24.4
C-core	20.0	19.9	19.6	17.8	15.9	11.7
E-core	18.9	18.9	18.8	18.5	18.0	15.9
Modular	15.2	15.0	14.8	14.3	13.6	11.1

It is worth looking in more depth at the conventional double layer machine which exhibits the largest short-circuit current. Using the model for this machine, the peak short-circuit current as a function of speed is obtained, as shown in Fig. 4.3 (a), which is also for various temperatures. It is verified that the highest short-circuit current is achieved when the temperature is the lowest. In addition, the short-circuit currents do not change significantly for low temperature cases such as from 25°C to 75°C. Previously it was mentioned that the back-EMF decreases while the resistance increases with temperature, thus limiting the short-circuit current at high temperatures. However, at higher temperature there is an additional phenomena which also helps to reduce the short-circuit current, as will be detailed in section 4.4.3.



(a)



(b)

Fig. 4.3. Conventional SFPMM peak short-circuit current variation (a) vs speed and temperature (25% fault severity – 1 out of 4 coils short-circuited), (b) Peak short-circuit current vs fault severity at 25°C.

The influence of fault severity on short-circuit current was also investigated for the conventional SFPMM, using the same Simulink model, as shown in Fig. 4.3 (b). The short-circuit fault severity varies from 1.4% to 25%, corresponding to a short-circuit of 1 to 18 out of 72 turns per phase. The entire fault severity study concerns only one coil out of four, for three different speeds. Beyond 1000 rpm, the short-circuit current can be regarded as independent of rotor speed as shown in Fig. 4.3 (a). Furthermore, the study is conducted at a low temperature (25°C) in order to obtain the highest short-circuit currents.

It is found in Fig. 4.3 (b) that for different speeds, the one turn short-circuit is the worst scenario as the current will reach a significantly high value, e.g. 125A for 1000 rpm, which is around 10 times the rated current (11A). The short-circuit current variation with fault severity can be explained using (4.1) which gives the approximate short-circuit current peak value (by neglecting mutual coupling with the other phases as well as the contact resistance at the short-circuit point):

$$i_{sc} \approx \frac{\alpha \cdot E_{max}}{\sqrt{(\alpha \cdot R)^2 + (\alpha^2 \cdot \omega \cdot L)^2}} \approx \frac{\omega \cdot \Phi_{max}}{\sqrt{R^2 + (\alpha \cdot \omega \cdot L)^2}} \quad (4.1)$$

where R and L are the phase resistance and self inductance, E_{\max} and Φ_{\max} are the peak values of the back-EMF and phase flux linkage while ω is the angular electric speed. Since the winding is concentrated, the flux due to PMs through the affected coil will be constant for all fault severities. The only term in (4.1) varying with the fault severity α parameter is $\alpha^2\omega L$ (reactance), which is negligible compared to R^2 at low speed while becoming important at high speed. Therefore, at low speed the current does not vary significantly with the fault severity as it is mainly determined by the constant ratio $\omega\Phi_{\max}/R$. However, at high speed both the back-EMF and the reactance term are increasing, cancelling the influence of R . The contribution of α is much more pronounced now as it will reduce the reactance term, thus increasing the short-circuit current, as shown in Fig. 4.3 (b).

The previous analysis can be repeated in order to compare the conventional machine with the modular ones, yielding the results below:

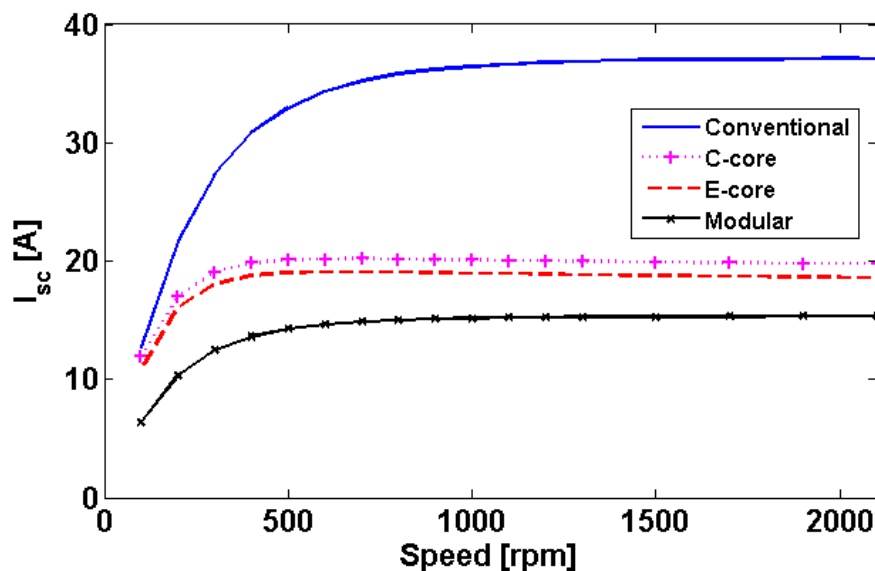


Fig. 4.4. Peak short-circuit current vs speed at 25°C.

4.3.4. EXPERIMENTAL VALIDATION OF FAULTY MODEL

Two prototypes (conventional and E-core machines) are used during experimental validation. Both machines have the 12-slot and 10-pole configuration. The dimensions of the conventional machine are given in Table 3.1 while the prototype itself was introduced in section 2.5. The E-core machine, Fig. 4.5, has the same parameters as in [109] and therefore not reproduced here. It should be mentioned that although the stator diameter and copper losses are the same, the split ratio is different between the two

prototypes. However, the E-core prototype has the same rated current, the same number of turns per phase, the same slot area as the conventional one and hence the resulting short-circuit currents can be compared between the two machines.

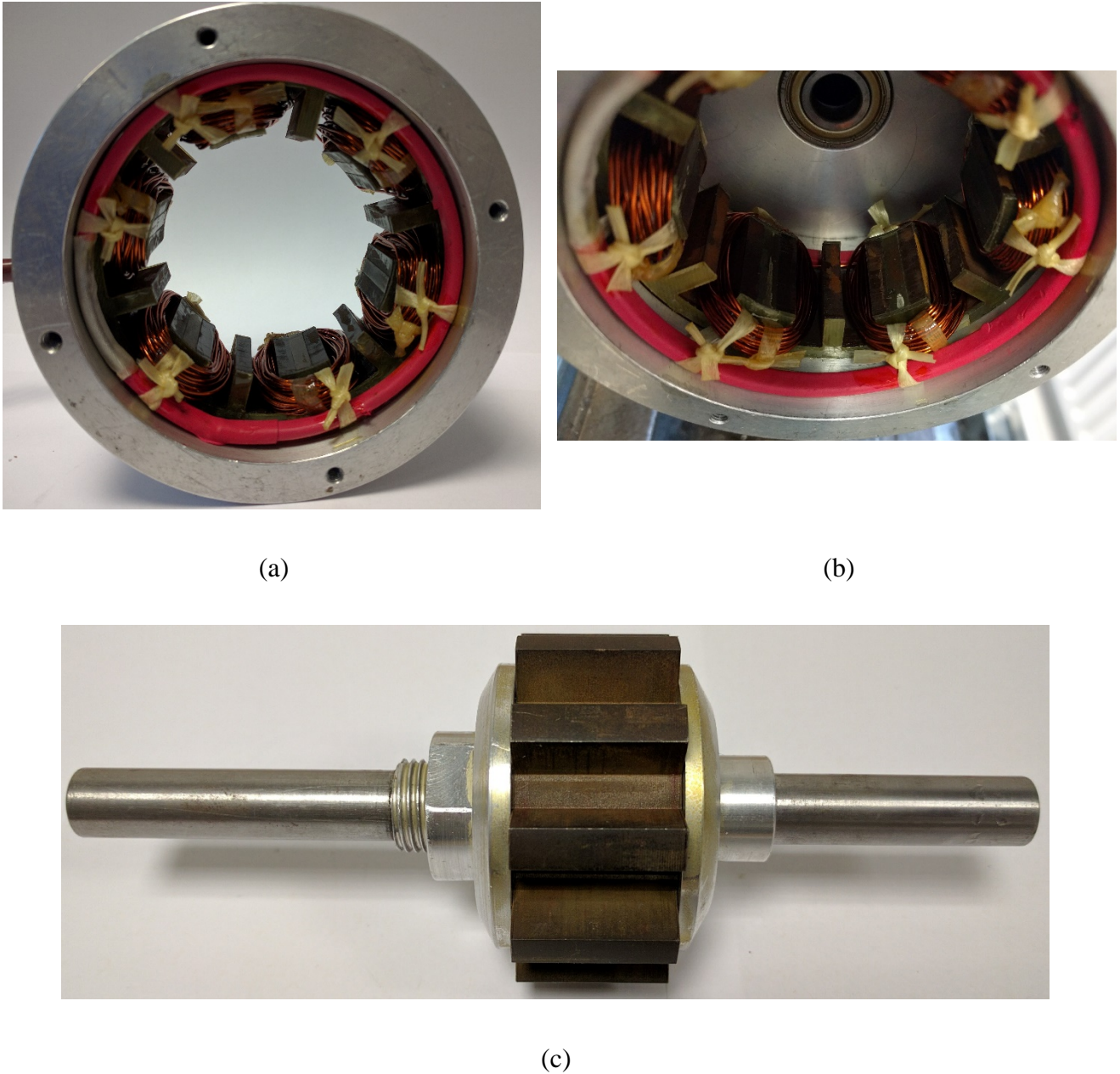


Fig. 4.5. Prototype of E-core SFPMM with 12-slot/10-pole. (a) E-core stator, (b) E-core stator detail, (c) E-core 10 pole rotor.

Two sets of tests have been carried out. In the first set of tests, the SFPMM machines are mounted on a test bench and working in generator mode, being the load of a DC motor. For the conventional machine, three types of short-circuit are investigated, e.g. one coil, one phase and three phase short-circuit, and the relevant peak short-circuit current for speeds up to 600 rpm are obtained, as shown in Fig. 4.6.

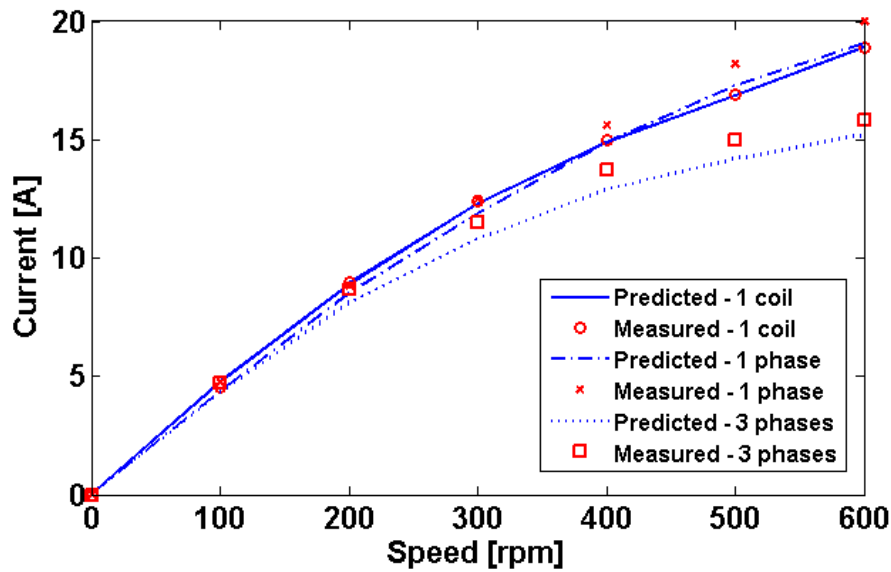
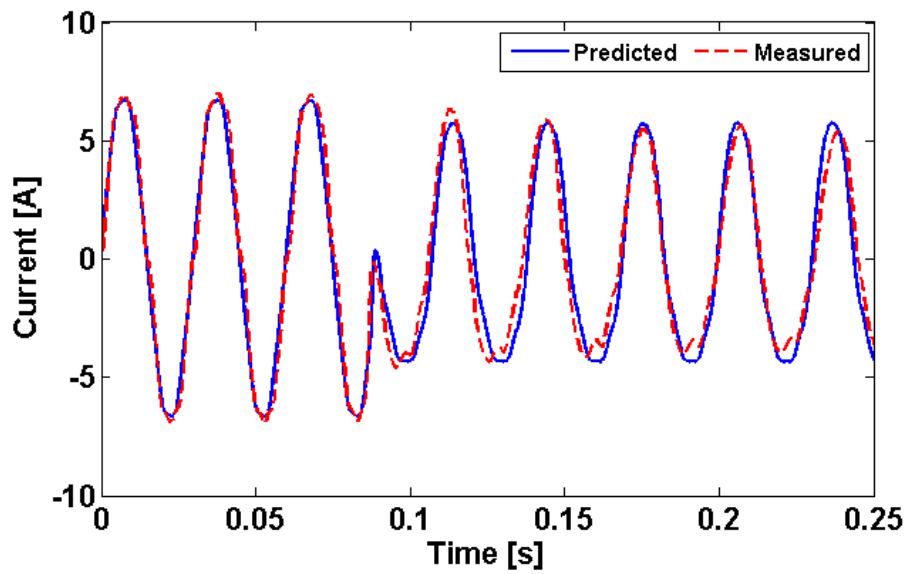


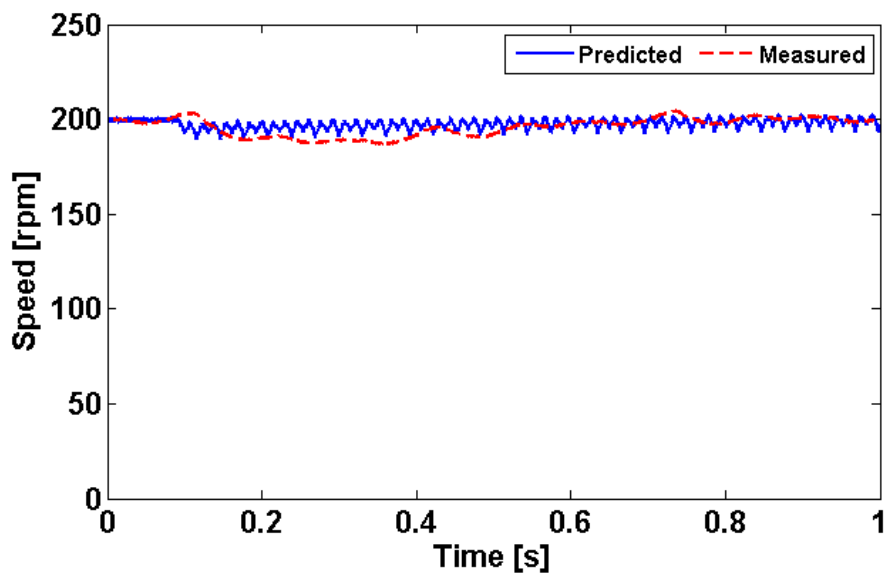
Fig. 4.6. Peak short-circuit current vs rotor speed for one coil, one phase and three phases short-circuits.

A good match can be observed between the predicted and measured results with errors lower than 5%. The value of the currents obtained in experiments are much smaller than that shown in Fig. 4.4. The reason is that the experimental setup introduces additional resistances which are reducing the short-circuit current amplitudes and have to be accounted for in the FE models but.

Secondly, dynamic tests have been carried out in motoring mode for both machines under the MTPA control strategy mentioned previously. The dynamic model discussed in the previous section is implemented using a dSPACE platform [28], an inverter and a DC machine as mechanical load. The speed and torque are maintained at the same values during both healthy and faulty modes. During the healthy operation, the short-circuit fault is introduced using a switch. First experiments concern the conventional machine, at low speed conditions but various fault severities. Phase A is affected with one, two and three coils short-circuited (out of a total of 4) corresponding to the fault severities of 25%, 50% and 75%. The predicted and measured short-circuit current and speed waveforms before and after the inter-turn short-circuits are recorded in Fig. 4.7, Fig. 4.8 and Fig. 4.9. It is shown that at a modest rotor speed, the short-circuit current is lower than the healthy current. However, with the increase in rotor speed, the short-circuit current can be significantly increased, as shown in Fig. 4.3, and can be much higher than the rated current.

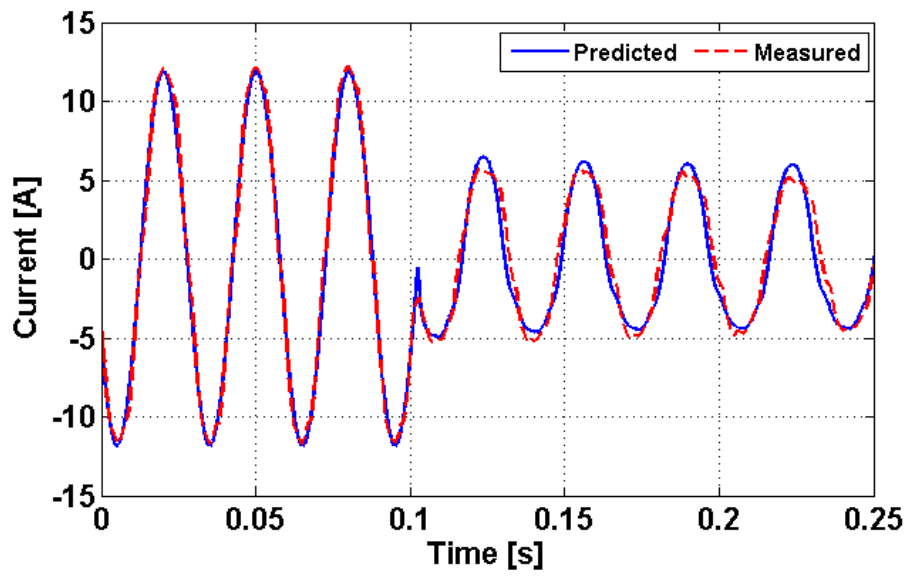


(a)

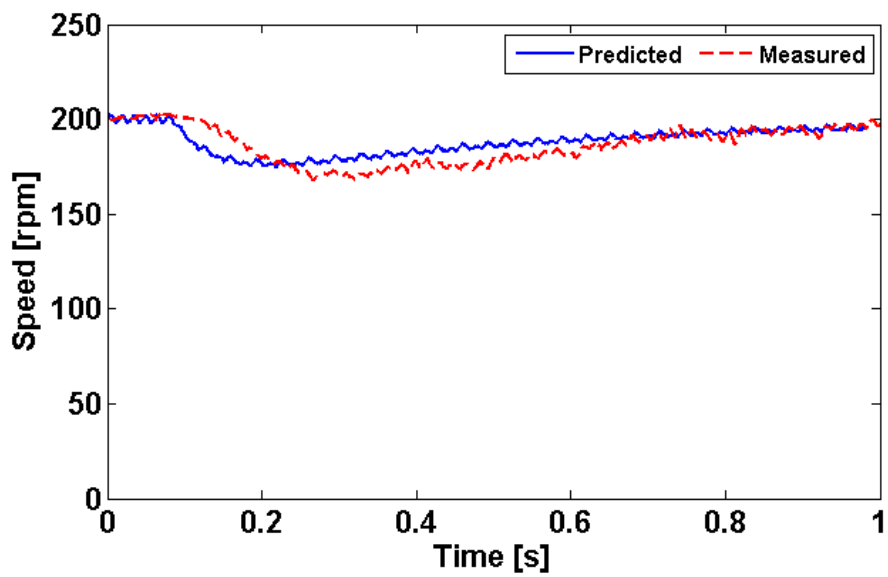


(b)

Fig. 4.7. Predicted and measured short-circuit currents and speeds at 25% fault severity. (a) current, (b) speed

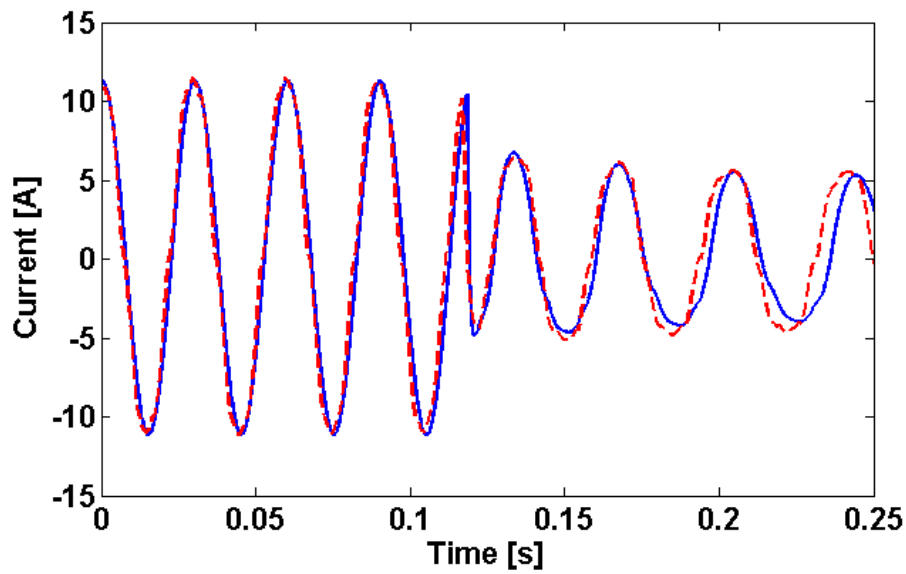


(a)

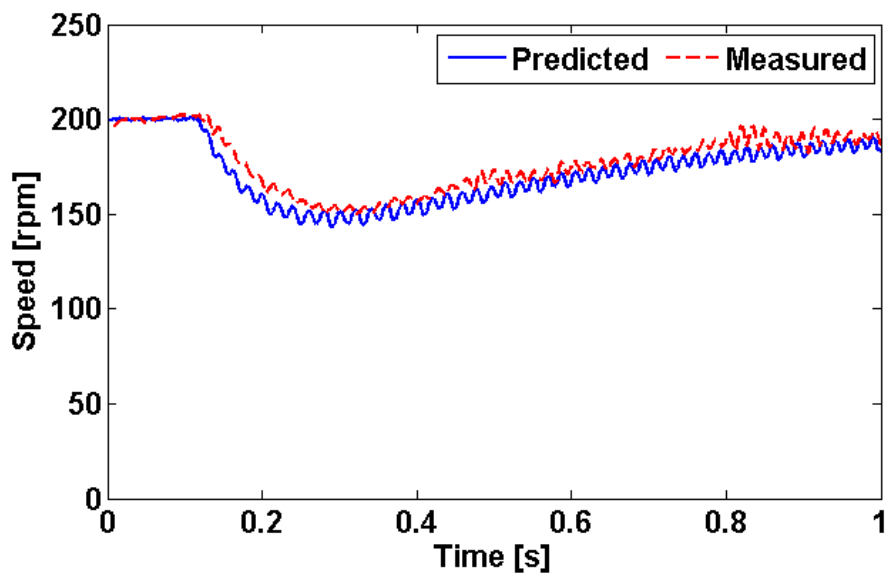


(b)

Fig. 4.8. Predicted and measured short-circuit currents and speeds at 50% fault severity. (a) current, (b) speed



(a)



(b)

Fig. 4.9. Predicted and measured short-circuit currents and speeds at 75% fault severity. (a) current, (b) speed

The next set of experimental results concern high speed tests involving both the conventional and the E-Core machine at high speed. Only one fault severity is tested - phase A is affected and has one coil short-circuited (out of a total of 4) corresponding to a fault severity of 25%. For the E-core machine the

50% case is considered which also corresponds to one coil affected (out of 2 per phase). In both cases, the steady state peak to peak short-circuit current variation with speed is shown in Fig. 4.10. A good match can be observed between the predicted and measured results with errors less than 5%.

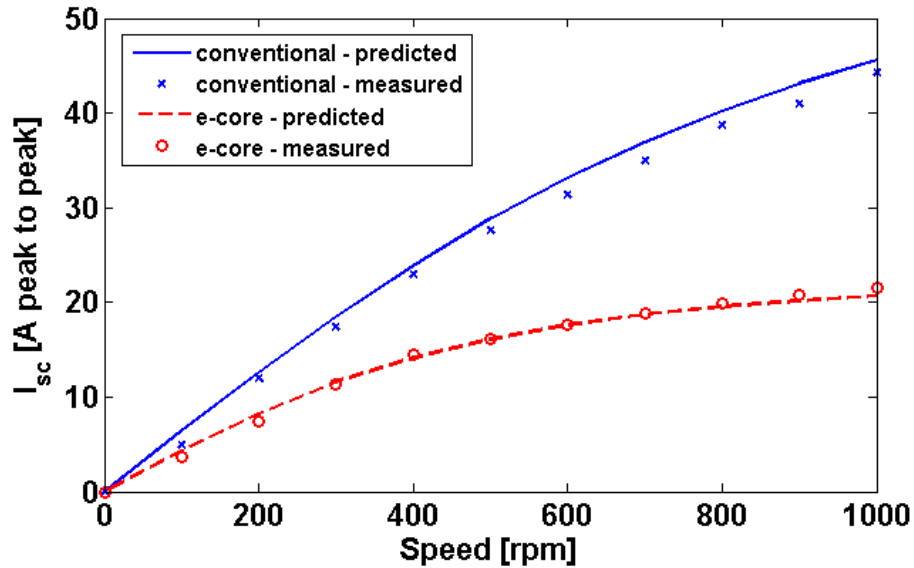
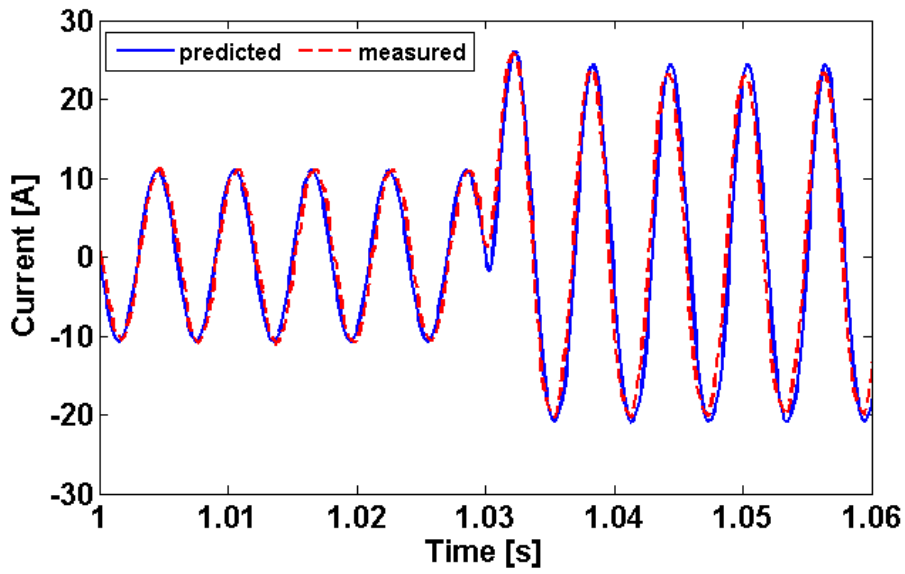
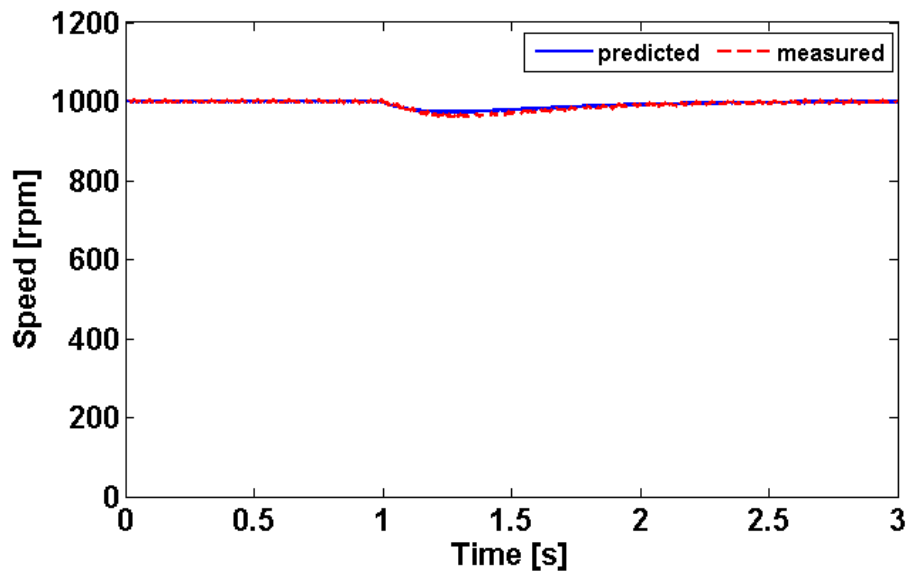


Fig. 4.10. Steady state peak to peak short-circuit current vs rotor speed for conventional/one coil and E-core/one coil short-circuit operation in motoring mode.

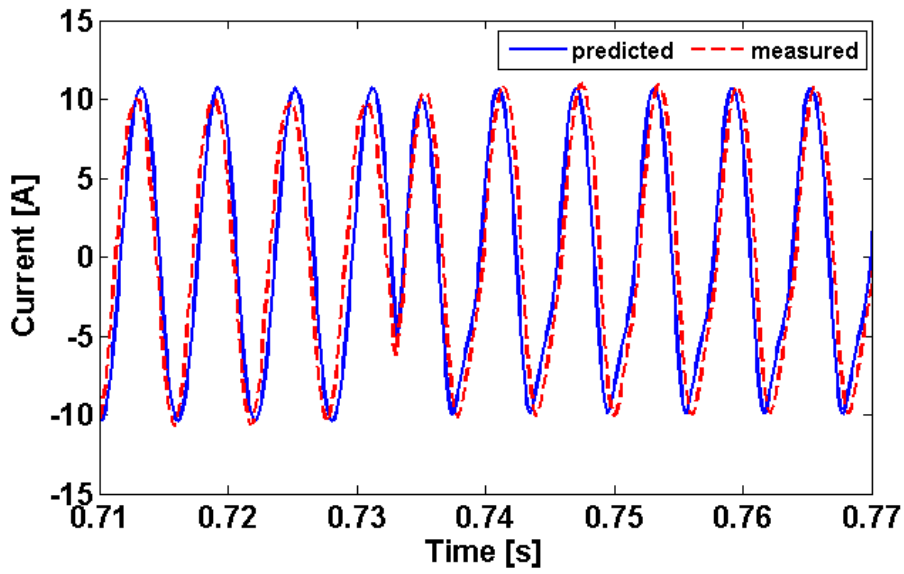
The predicted and measured currents in the affected coils, as well as speed waveforms before and after the inter-turn short-circuit, are shown in Fig. 4.11 for a speed of 1000 rpm.



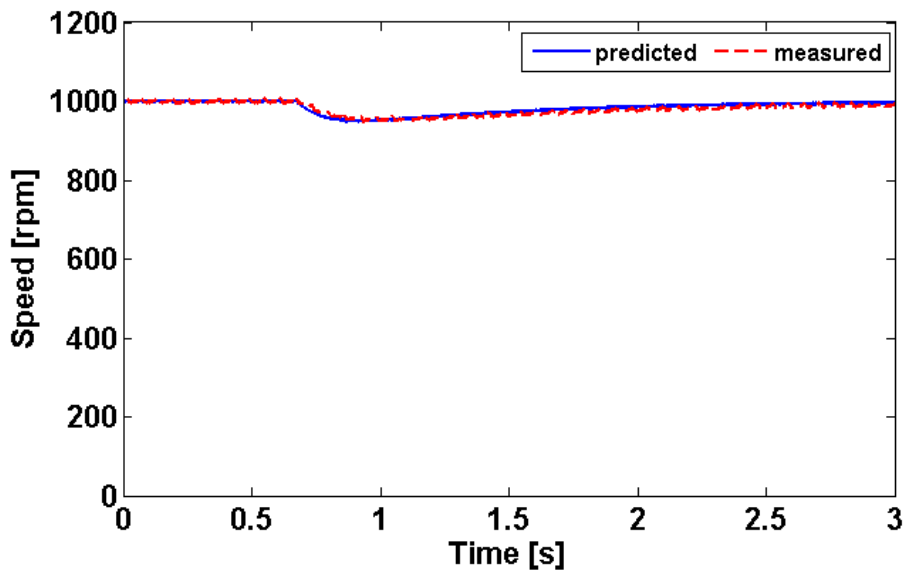
(a)



(b)



(c)



(d)

Fig. 4.11. Predicted and measured currents in the affected coil and speeds. (a) conventional - current, (b) conventional - speed, (c) E-core – current, (d) E-core - speed.

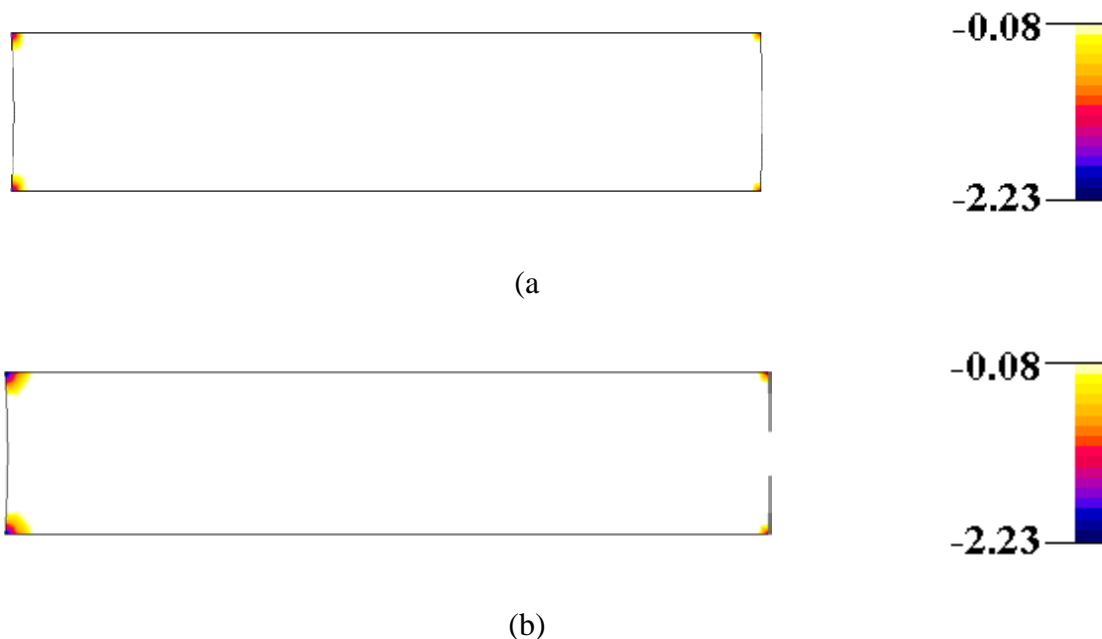
4.4. ANALYSIS OF CONVENTIONAL SFPMM DEMAGNETIZATION WITHSTAND CAPABILITY

First the conventional SFPMM demagnetization process is investigated as it has a higher PM volume than the rest of the machines in the study. Next, the demagnetization effects on modular machines are added to the study.

4.4.1. CONVENTIONAL SFPMM - LOW SPEED SHORT-CIRCUIT

At first, using the aforementioned faulty model, the short-circuit operation is investigated at low fault severity (25% turns short-circuited) and low speed (100 rpm) for SFPMM. Therefore the short-circuit current is kept low. This can establish a baseline to analyse temperature dependent demagnetization because the influence of short-circuit current could be negligible.

Fig. 4.12 shows the demagnetized areas in the affected PM [the coil around this PM is short-circuited, as shown in Fig. 4.2 (a)] for two selected temperatures (25°C and 150°C). As in the previous chapters, it is assumed that the affected PM temperature can change, however the remaining PMs will work at 25°C. Only the positive d -axis (27° mech.) and negative q -axis (0° mech.) positions are shown. At low temperatures, as shown in Fig. 4.12 (a) and (b), the demagnetization occurs only locally, due to end effects. However, at 150°C, as shown in Fig. 4.12 (c) and (d) the entire PM area is demagnetized regardless of rotor position.



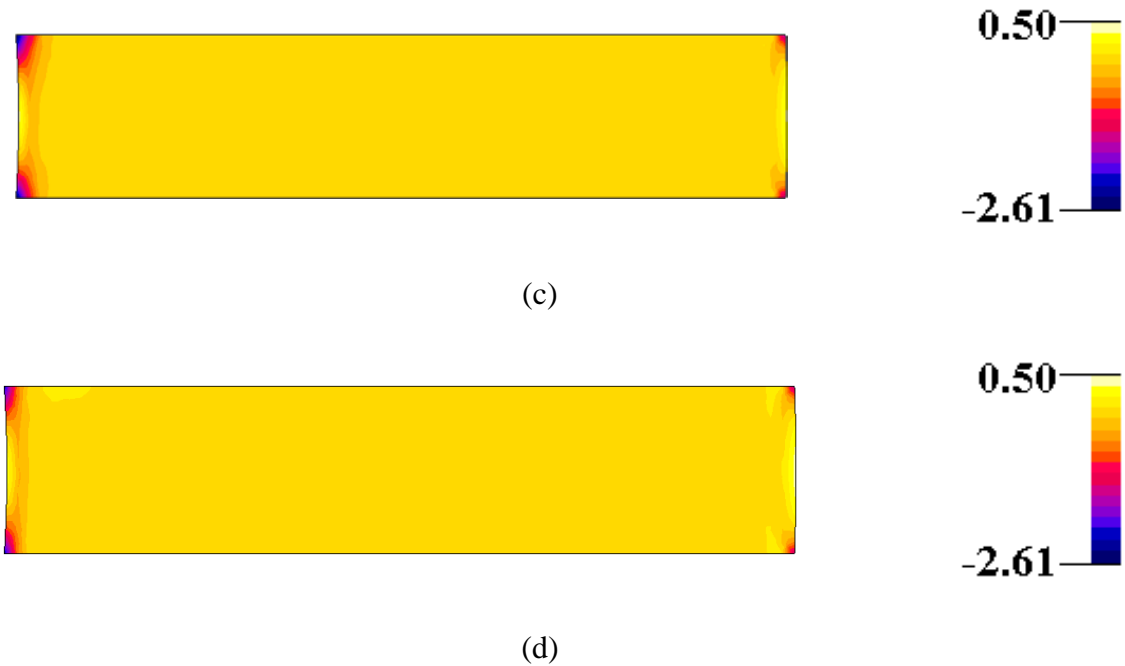
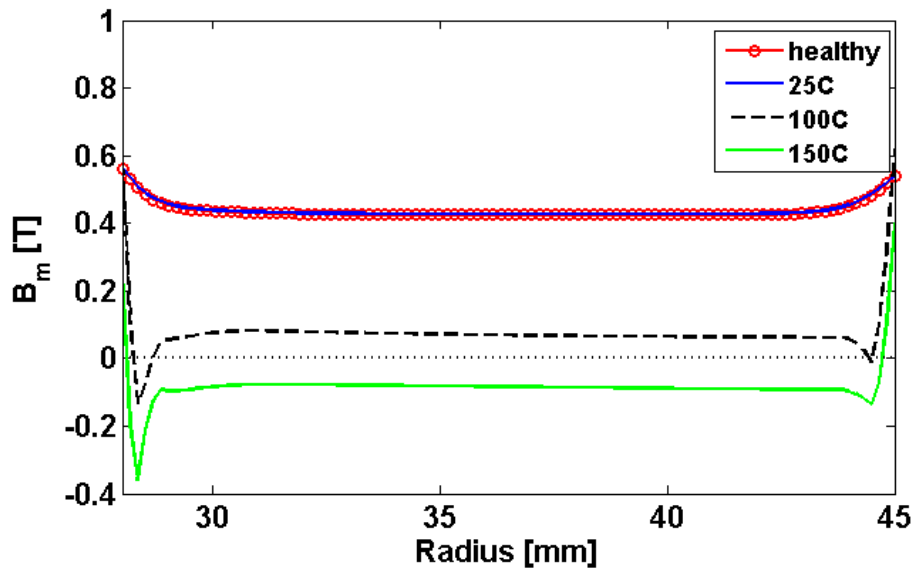


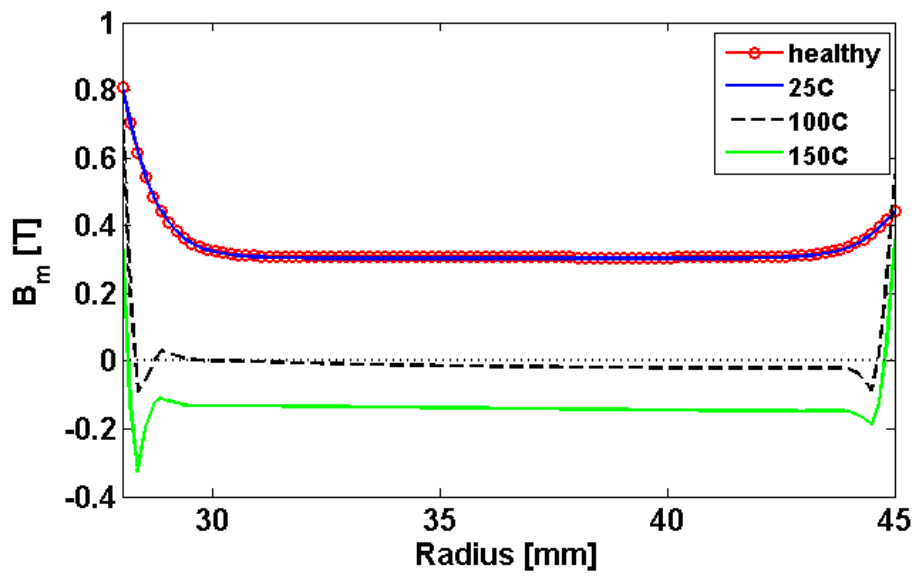
Fig. 4.12. Demagnetization flux density colour maps (white – not demagnetized, coloured – demagnetized) with 25% short-circuit at 100 rpm. Left-hand side is adjacent to the airgap. (a) Positive d-axis 25° C, (b) Negative q-axis 25° C, (c) Positive d-axis 150° C, (d) Negative q-axis 150° C.

In order to better compare various temperature cases, the nodal flux densities (circumferential components) along the central line of the affected PM are shown in Fig. 4.13 (d). For completeness, the results of a healthy case are also included. The cross-coupling effect between armature current and PM lowers the working point of the PMs for the healthy and short-circuit cases. However, the demagnetization due to the cross-coupling is weak and therefore is not detailed here.

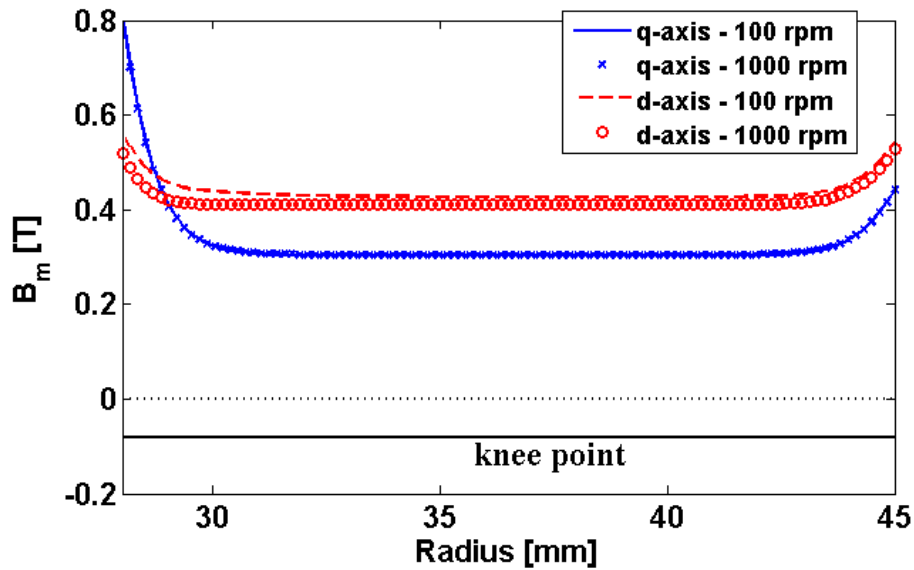
The working point for all temperature cases in Fig. 4.13 are already much lower than the relevant remanence (B_r) from Table 4.3 even for the healthy case. This is mainly due to the influence of the magnetic circuit. However, the influence of temperature is much more significant, which lowers the working point even further. The lowest working point (<0.4 T) for all cases, is achieved in q -axis, as shown in Fig. 4.13 (b). For high temperature cases, e.g. 150°C, the local flux density) in the affected PM can have reversed polarity (thus working in the third quadrant) with respect to the PM magnetization direction, as shown in Fig. 4.13, and hence be heavily demagnetized. This will be investigated in more depth in section 4.3.4.



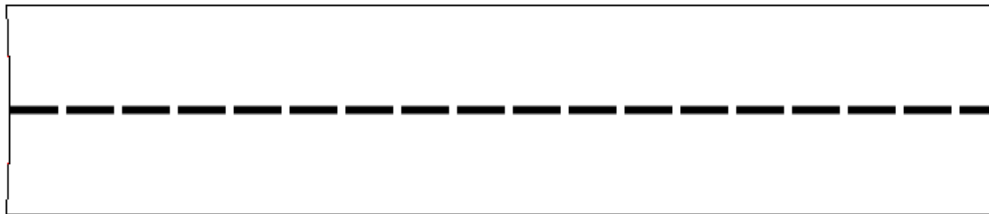
(a)



(b)



(c)



(d)

Fig. 4.13. Flux densities (circumferential components) along the central line affected PM. (a) Positive d-axis (27° mech.), (25% short-circuit at 100 rpm), (b) Negative q-axis (0° mech.), (25% short-circuit at 100 rpm), (c) Positive d-axis (27° mech.) and negative q-axis (0° mech.), (25°C & 25% fault severity) (d) The path (dashed line) through the middle of the PM on which the B_m is represented.

For the conventional SFPMM, the irreversible demagnetization phenomena occurs when the operating temperatures are high enough, e.g. $\geq 100^\circ\text{C}$. Under all aforementioned conditions, the peak short-circuit current is lower than the rated current due to low speed used, as shown in Fig. 4.3 (b). Therefore, the demagnetization of the affected PM could only be due to the influence of the adjacent PMs and temperature rise. However, it is possible that higher speeds can result in higher demagnetizing short-circuit currents, which would aggravate the magnet irreversible demagnetization. This will be investigated in the following section.

A summary of irreversible demagnetization of the studied cases at low speed is given in Table 4.5.

TABLE 4.5

DEMAGNETIZATION SUMMARY: 25% SHORT-CIRCUIT AT 100 RPM

Temperature [°C]	25	50	75	100	125	150
	no	no	no	yes	yes	yes

'yes' or 'no' means irreversible demagnetization in a large area of magnet has occurred or not

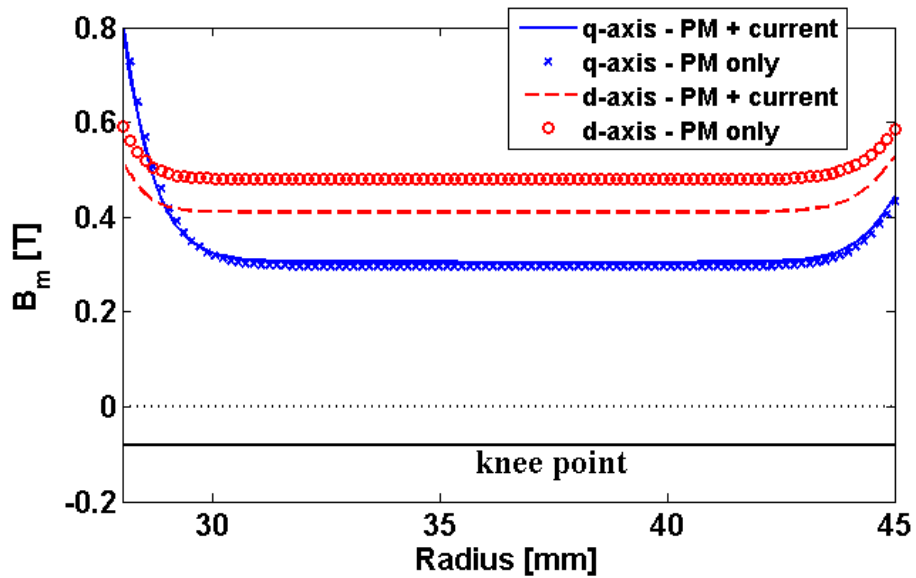
4.4.2. CONVENTIONAL SFPMM - HIGH SPEED SHORT-CIRCUIT

The 25°C, 100 rpm or 1000 rpm with 25% short-circuit case is used in order to assess the magnet irreversible demagnetization, as shown in Fig. 4.13 (c). All PMs are working at the same 25°C temperature. The low temperature is chosen as the short-circuit current could be maximum, based on results shown in Fig. 4.3 (b). This can also eliminate the influence of temperature on magnet demagnetization so that the investigation in this section can be focused on the influence of the short-circuit current. For the selected speed (1000 rpm), the resulting current is within 95% of the maximum achievable short-circuit current (for this fault severity). It is found that in the q -axis the armature winding flux does not influence the working point of the PMs, as shown in Fig. 4.13 (c). However, regarding the positive d -axis the increase in the short-circuit current (from 6.3 to 36 A) has only a slight demagnetizing effect. Similar results were obtained for higher fault severities and therefore are not presented to avoid duplication. One can then draw a conclusion that the SFPMM is robust against magnet demagnetization at low temperature, even under short-circuit conditions.

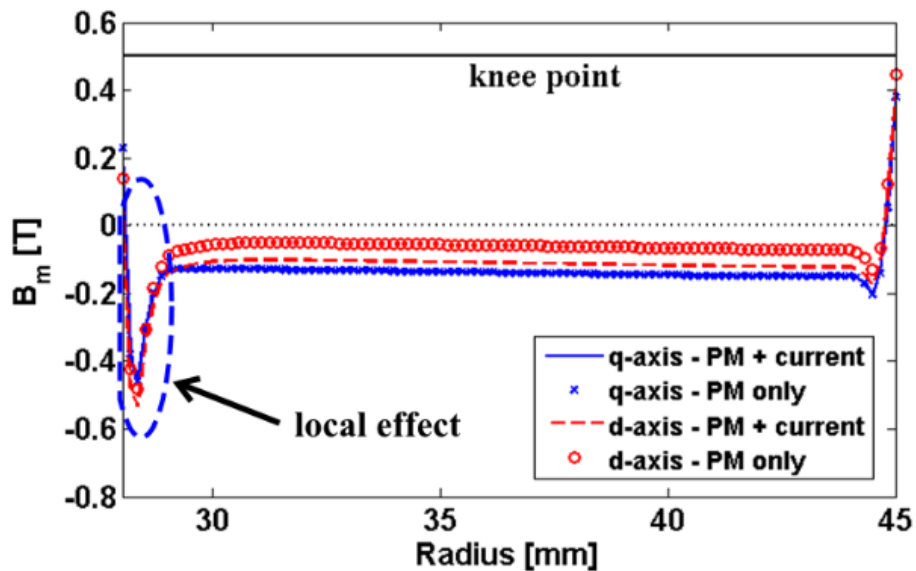
4.4.3. DISCUSSION ON DEMAGNETIZATION MECHANISM

In order to analyse the previously observed magnet demagnetization due to short-circuit and temperature, the influences of the armature MMF and PM field on demagnetization are separated using the well-established frozen permeability (FP) method [107], which has been validated before using it in this thesis. Since the FP method based on the finite element model is only a tool for analysis, its principle will not be repeated. The short-circuits investigated in this section concerns two cases, i.e. low temperature (25°C) and high temperature (150°C), both are at high speed (1000 rpm) and 25% fault severity. This will give an insight into the demagnetization process evolving from lower to higher temperatures. Other temperatures achieve similar results. Therefore, they are not shown here. Fig. 4.14

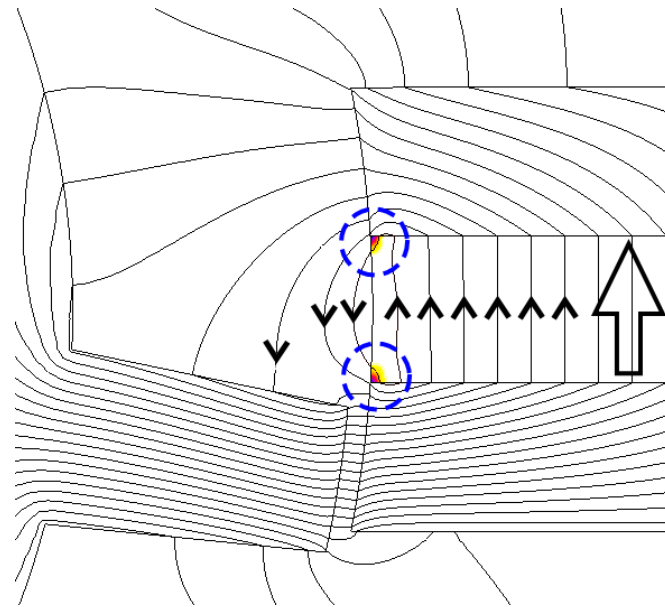
shows the nodal circumferential flux densities (B_m) along the central line of the affected PM obtained from two static FE models. The first FE model contains the influence of both PM and current sources. However, in the second FE model, the PMs are the only sources of magnetic field, while saturation level of the magnetic circuit is kept unchanged using the FP method. Two rotor positions (positive d - and negative q -axes) are considered for each temperature.



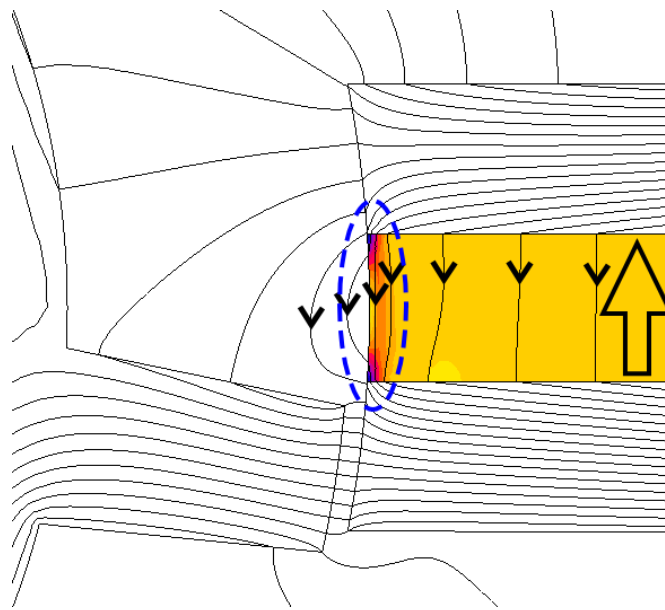
(a)



(b)



(c)



(d)

Fig. 4.14. The circumferential flux density component through affected PM at 1000 rpm & 25% fault severity and local phenomena detailing. The remaining non-affected PM are working at 25°C only. (a) Negative q-axis (0° mech.) and positive d-axis (27° mech.) at 25°C, (b) Negative q-axis (0° mech.) and positive d-axis (27° mech.) at 150°C, (c) Positive d-axis (27° mech.) at 25°C local demagnetization phenomena detailing, (d) Positive d-axis (27° mech.) at 150°C local demagnetization phenomena detailing.

Based on Fig. 4.14 it can be seen that adding the current sources only contributes to a reduction of the magnet working point in the d -axis. This is the case for all studied temperatures. The reduction is due to the short-circuit current, which is equivalent to a demagnetizing d -axis current. However, for all temperatures, the PM flux densities in q -axis are lower than that in d -axis, resulting in more severe demagnetization. It is also found that at low temperature, as shown in Fig. 4.14 (a), the PM flux densities are higher than its knee point, and hence has not been irreversibly demagnetized. Moreover, the PM flux densities along the central line of the affected PM first reduce and increase thereafter with the increasing radius (from 28.5mm to 45mm). This is the case for both d - and q -axes. However, for high temperature as shown in Fig. 4.14 (b), the PM flux densities are lower than its knee point, resulting in severe irreversible demagnetization in both axes. Moreover, there are some local effects at both ends of the affected PM due to magnetic circuit configuration which can enhance local flux lines or reduce them, depending on the PM working temperature. This is explained further in Fig. 4.14 (c) and (d) which shows both the local flux lines as well as the PM demagnetized areas (colour map). The natural PM magnetization is represented with a big hollow arrow while the direction of the local flux lines is given by small arrows superimposed over them. At low temperature the demagnetization has occurred only at the corners of the affected PM adjacent to the airgap, a local effect which was noticed in [22] as well. However at 150°C, general demagnetization occurs in the affected PM with a much worse local phenomena close to the PM edge, Fig. 4.14 (d). Upon closer inspection, this high temperature local effect is the outcome of the evolution of the initial demagnetized areas from low temperature (before short-circuit). These initial areas are expanded at each time steps (FE model) until they merge forming a bridge, as shown in Fig. 4.14 (d), between the PM corners from Fig. 4.14 (c). This is due to a stronger local reduction of the B_r at each time step when compared to the rest of the PM. Therefore at high temperature the enhanced local demagnetization effect at the PM edge is facilitating more the crossing of demagnetizing flux than in the rest of the affected PM. The consideration of this effect is possible only due to the fact that the FE model can update the PM remanent flux density at each time step – this phenomena will not be noticeable with classic linear PM models.

In order to explain the previously observed phenomena in Fig. 4.14 (a) and (b), the following analysis has been carried out. Since the demagnetization contributions of both PMs and armature currents can be separated accurately using the FP method, their influence on magnet demagnetization can be analysed separately. Fig. 4.15 allows a comparison between the PM fluxes at low and high temperatures. At low temperature, the PM is unaffected even though it is under the influence of high short-circuit current. At high temperature, the flux paths change significantly, in particular the flux (Φ_{PM}) generated by the affected PM can be reduced or even eliminated. This can be explained using superimposed, simplified

flux paths over the existing flux lines, which helps to identify and compare the influence of adjacent PMs on the affected one.

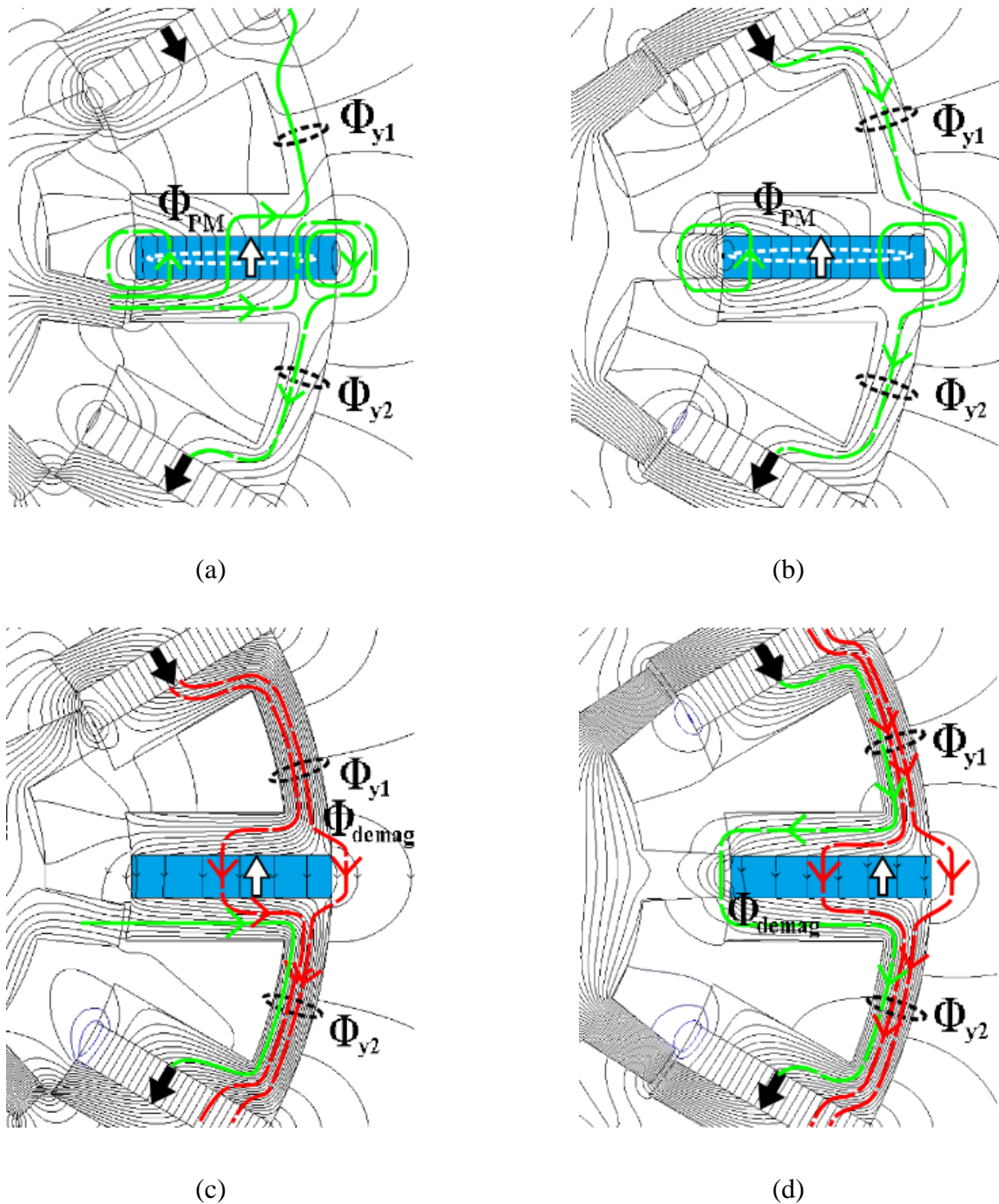


Fig. 4.15. Flux line distributions due to PM sources only at 1000 rpm & 25% fault severity, which is separated from flux due to armature current using FP method and their associated simplified flux diagrams. The remaining non-affected PM (not represented) are working at 25°C only. (a) Positive d-axis (27° mech) 25° C, (b) Negative q-axis (0° mech.) 25° C, (c) Positive d-axis (27° mech) 150° C, (d) Negative q-axis (0° mech.) 150° C.

The flux line distributions at low temperature (25°C), are shown in Fig. 4.15 (a) and (b). Three flux components can be identified in the area surrounding the affected PM. These are the yoke fluxes Φ_{y1} , Φ_{y2} and the PM flux Φ_{PM} generated by the affected PM. For low temperature, it can be seen that the yoke fluxes (Φ_{y1} and Φ_{y2}) are equal regardless of the rotor position. When it comes to high temperature (150°C), as shown in Fig. 4.15 (c) and (d), there can be an extra flux component, the demagnetization flux Φ_{demag} , crossing the affected PM in an opposite direction to its magnetization.

The demagnetizing component Φ_{demag} depends strongly on the yoke fluxes generated by the two adjacent PMs. By way of example, based on Fig. 4.15 (c), it can be seen that for the d -axis the yoke fluxes are not equal with one of them being higher than the other ($\Phi_{y1} < \Phi_{y2}$). Some of the yoke fluxes are diverted from the affected PM due to rotor tooth alignment with the stator tooth, which lowers or cancels the Φ_{demag} component. As a result, the irreversible demagnetization at d -axis is not so severe, as shown in Fig. 4.13 and Fig. 4.14. However, when it comes to the q -axis in Fig. 4.15 (d), the yoke fluxes are equal and contributing in the same manner to Φ_{demag} . Therefore, for this rotor position, the influence of adjacent PMs on the affected one is the same. The demagnetizing flux flows from the upper adjacent PM, crosses the affected PM and enters into the lower adjacent PM without being diverted into other parts of the machine and results in the highest demagnetization.

Despite that the simplified flux lines in Fig. 4.15 are for the 25°C and 150°C cases, the analysis can be extended to other temperatures. For example, for short-circuit at 75°C, the demagnetization phenomena will not occur as the knee point is low enough. Therefore, the Φ_{demag} component does not exist similar to the case at 25°C. Also, this type of analysis can be extended to analyse the influence of current sources on magnet demagnetization. In this case, only the d -axes need to be investigated with the armature flux enhancing (positive d -axis) or decreasing (negative d -axis) Φ_{demag} .

It is worth highlighting that in section 4.3.3 it was found that the short-circuit current decreases as the temperature increases, as shown in Fig. 4.3. This is due to the phase back-EMF and resistance combined effect. However, for temperatures $\geq 100^\circ\text{C}$ the short-circuit current decreases at a much faster pace. At lower temperatures ($\leq 75^\circ\text{C}$), the back-EMF drop (hence short-circuit reduction) is due to reduction in the remanent flux density only. When it comes to higher temperatures, the irreversible demagnetization occurs in a significant (or even entire) volume of the affected PM. This would lead to a further decrease in the remanent flux density. As a result, since the PM working point is located on a lower recoil line, the resulting back-EMF in the short-circuit coil drops even further.

4.5. ANALYSIS OF MODULAR SFPMM DEMAGNETIZATION

As a direct consequence of the short-circuit current, a demagnetizing MMF is developed, which could cause irreversible magnet demagnetization, especially since the coil surrounding the affected PM has an increased number of turns for modular machines. Therefore, a comparison is carried out in terms of demagnetization withstand capability for the conventional, C-core, E-core and modular SFPMMs under the aforementioned short-circuit conditions. Two cases are considered – the first one concerns local over-heating of the affected PM and short-circuited coil while other coils and magnets working at normal operating temperature. The second one assumes fault operation under short-circuit while all the magnets and coils are working at the same temperature, e.g. 100°C – global over-heating. For both cases, only one coil of phase A is short-circuited.

4.5.1. LOCAL OVER-HEATING CASE

In this subsection, it is assumed that the affected PM (the one inside the short-circuited coil) can work at a higher temperature while the remaining ones are operating at 25°C. The color maps of the flux density component parallel with the magnetization direction in the affected PM are shown in Fig. 4.16 for low and high temperature cases. The color map scale is upper limited by the knee point value of the affected magnet to show only the irreversibly demagnetized areas. The negative q -axis rotor position (rotor tooth is aligned with the affected PM) is chosen as being representative, since the PM working point is the lowest in this position. Only the conventional and E-core cases are represented as the C-core and modular topologies yield results similar to the E-core one. It can be seen at low temperature (25°C) that the demagnetization effect is local and confined at the bottom corners of the PMs. This effect was noticed during healthy conditions as well for SFPMM using ferrite magnets [18]. However, at high temperature (100°C), total PM demagnetization occurs for the conventional machine as shown in Fig. 4.16 (c), while for the E-core the demagnetization is limited to only half of the PM, Fig. 4.16 (d). This is due to PM material high knee point (0.28 T for 100°C). For 150°C, the knee point value is even higher (0.5 T), and irreversible demagnetization occurs throughout the entire affected PM for all studied topologies.

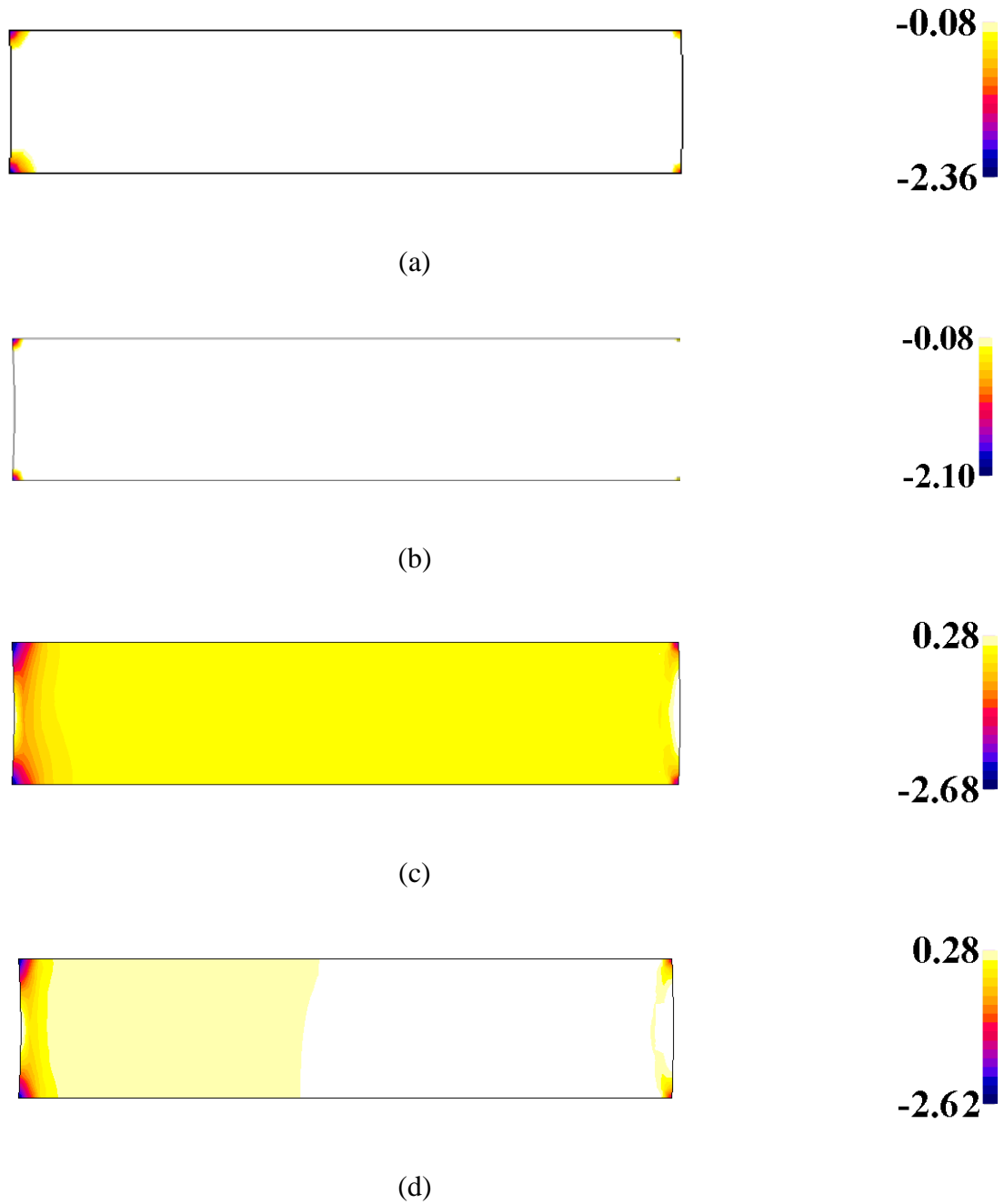
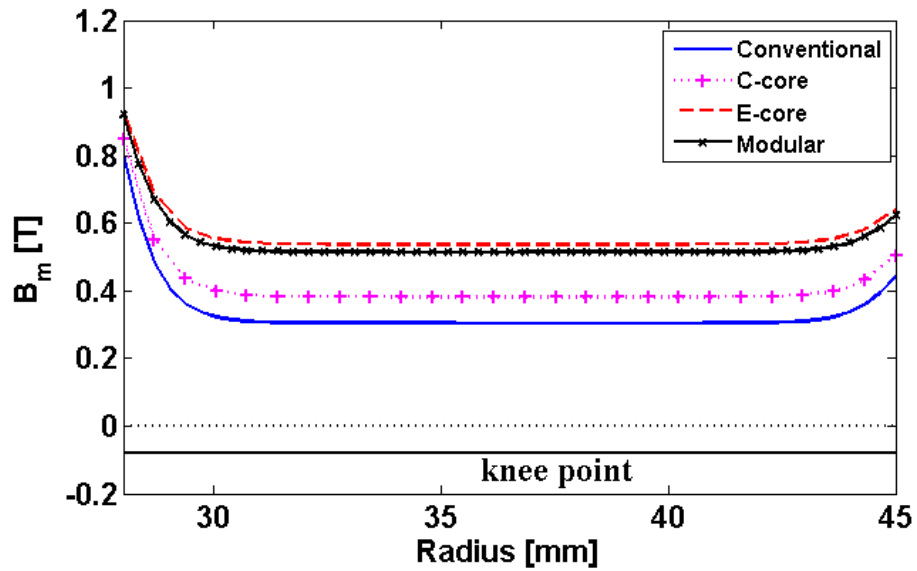


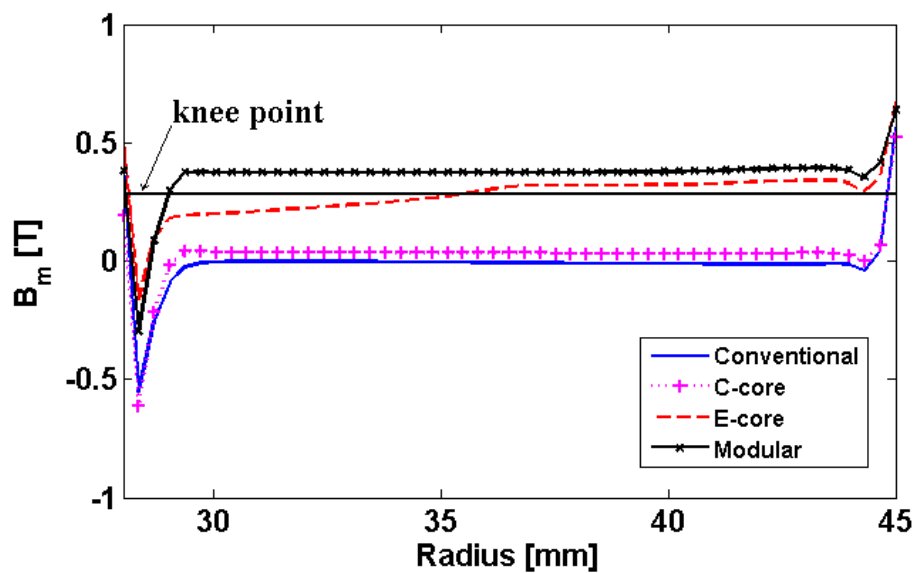
Fig. 4.16. Demagnetization flux density colour maps (white – not demagnetized, coloured – demagnetized) with short-circuit fault at 1000 rpm. (a) conventional 25° C, (b) E-core 25° C, (c) conventional 100° C, (d) E-core 100° C.

The flux density colour maps in Fig. 4.16 only show the irreversibly demagnetized areas, but they cannot easily quantify the severity of the demagnetization. In order to do so, the flux density (circumferential component) along the central line of the affected PM is used. The results for low temperature (25°C) are shown in Fig. 4.17 (a). The knee point value is also given so that the plots can be

compared against it in order to indicate if the irreversible demagnetization has occurred or not. Although none of the topologies is irreversibly demagnetized at this low temperature, the conventional and C-core topologies have lower magnet working points when compared with others, leading to narrower margin to the irreversible demagnetization.



(a)



(b)

Fig. 4.17. Flux densities (circumferential components) along the central line of the affected PM. (a) 25°C, (b) 100°C.

The results for 100°C are shown in Fig. 4.17 (b). Similar to the previous results, the PM working points of the E-core and modular machines are higher than the conventional and C-core counterparts. Most importantly, for the modular machine, most part of the affected PM is not irreversibly demagnetized except for the edge effect at the bottom of the PM. The results for 150°C have also been obtained, which have similar trend as for 100°C, but the affected PM for all topologies has been irreversibly demagnetized although the demagnetization levels for E-core and modular machines are lower than the C-core and conventional machines. It is also found that the modular machine can withstand at least a temperature of 25°C higher than the conventional and C-core machines as shown in Table 4.6 which summarizes the demagnetization occurrence over a wide range of operating temperatures from 25°C to 150°C for the studied topologies:

TABLE 4.6

IRREVERSIBLE DEMAGNETIZATION VS. TEMPERATURE

	conventional	C-core	E-core	modular
25 °C	no	no	no	no
50 °C	no	no	no	no
75 °C	no	no	no	no
100 °C	yes	yes	yes	no
125 °C	yes	yes	yes	yes
150 °C	yes	yes	yes	yes

*yes means irreversible demagnetization has occurred in more than 50% of the area of affected PM.

In order to explain why different machine topologies have different irreversible demagnetization withstand capabilities, the FP method is employed again. Using the FP method, the affected PM can be artificially removed from the FE model without affecting the working point of PMs and the saturation level of stator and rotor iron cores. In such a way, the influence of mutual coupling between adjacent phases and PMs on the affected magnet can be accurately investigated. Fig. 4.18 shows the flux produced by healthy PMs along with all the current sources (healthy and short-circuited). The conclusion is that the rest of the magnetic circuit has a demagnetizing effect over the affected PM since the flux lines are crossing through the affected PM on the opposite direction to its magnetization.

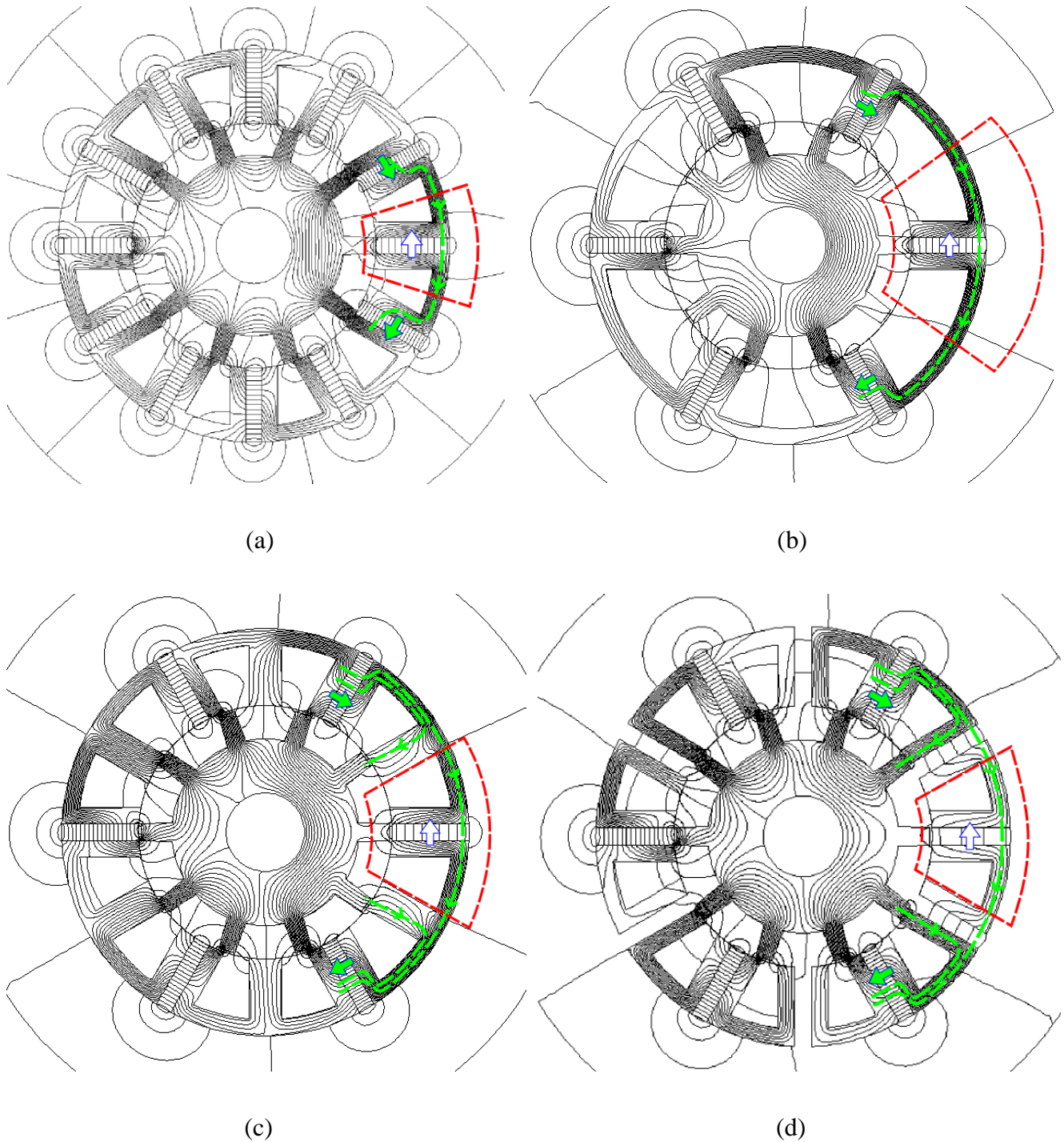


Fig. 4.18. Flux lines produced by PMs & armature currents after removing the affected magnet at 25°C. (a) Conventional, (b) C-core, (c) E-core, (d) Modular.

Looking at the local flux patterns circled by the dashed, fan-shaped curve from Fig. 4.18, it can be seen that the conventional and C-core topologies are quite similar. The demagnetizing flux produced by the rest of the magnetic circuit is flowing freely through the affected PM. This explains in turn why they

both present the worst demagnetization withstand capability. The E-core machine, however, diverts some of the demagnetizing flux through its magnetless tooth, leading to improved demagnetization withstand capability. The modular topology appears to be the best solution amongst all the investigated topologies, with the demagnetizing flux being both diverted but also reduced due to the presence of unwound teeth with flux gaps (increased reluctance). It is worth noting that the previous analysis was carried out at low temperature and short-circuit conditions. However, the results can be extended to higher temperatures under both healthy and short-circuit conditions.

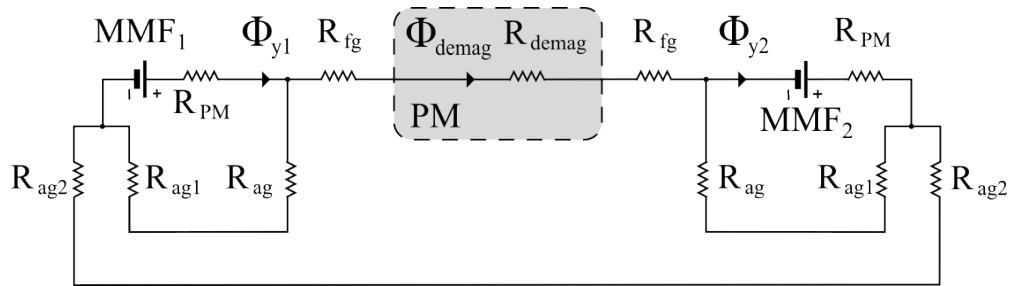


Fig. 4.19. Simplified lumped parameter magnetic circuit for the modular topologies.

A lumped parameter magnetic circuit can also be employed, Fig. 4.19, to explain the previous results. By way of example, only the modular topology is detailed. However, the circuit in Fig. 4.19 can be adopted for the rest of studied machines with appropriate modification. The adjacent PMs are represented by the MMF_1 and MMF_2 which produce flux Φ_{y1} and Φ_{y2} . Φ_{demag} represents the demagnetizing flux through the affected PM. R_{demag} and R_{PM} are reluctances characterizing the affected and adjacent PMs. R_{ag} , R_{ag1} and R_{ag2} are reluctances determined by airgap and different overlapping sections between the stator and rotor teeth. R_{ag} in particular is the airgap reluctance defined between the magnetless stator tooth and the rotor tooth. The flux-gap reluctance is represented by R_{fg} . For modular and E-core topologies part of potentially demagnetizing fluxes Φ_{y1} and Φ_{y2} can be diverted through R_{ag} circuit branch and also reduced by the extra R_{fg} thus minimizing the Φ_{demag} component. Therefore, a modular topology will limit the demagnetizing influence of the rest of the magnetic circuit by either diverting the flux from the concerned area (through R_{ag}) or reducing it (through flux-gap).

4.5.2. GLOBAL OVER-HEATING CASE

In this section it is assumed that the entire machine is exposed to the same high temperature while working under one coil short-circuited condition. By way of example, 100°C is chosen as the working temperature for all PMs and windings. As investigated in previous sections, it is the threshold temperature, beyond which the modular machine starts to be irreversibly demagnetized.

The short-circuit currents obtained for the new case are compared with previous results (only one PM is working at 100°C), as shown in Table 4.7. In this case, it is found that the short-circuit currents are all higher than the local over-heating case.

TABLE 4.7

SHORT-CIRCUIT CURRENT COMPARISON

	conventional	C-core	E-core	modular
one PM	32.7	17.7	18.5	14.3
all PMs	35.2	20.6	18.8	14.6

From Fig. 4.20 it can be noticed that the working point of the PMs is generally higher for all PMs at 100°C case than the previous case where only the affected magnet is working at 100°C. Moreover, the E-core and modular topologies can both safely withstand demagnetization although the edge adjacent to the airgap is still irreversibly demagnetized. This is mainly due to the fact that the adjacent PMs are much weaker in this case, generating smaller demagnetizing MMF.

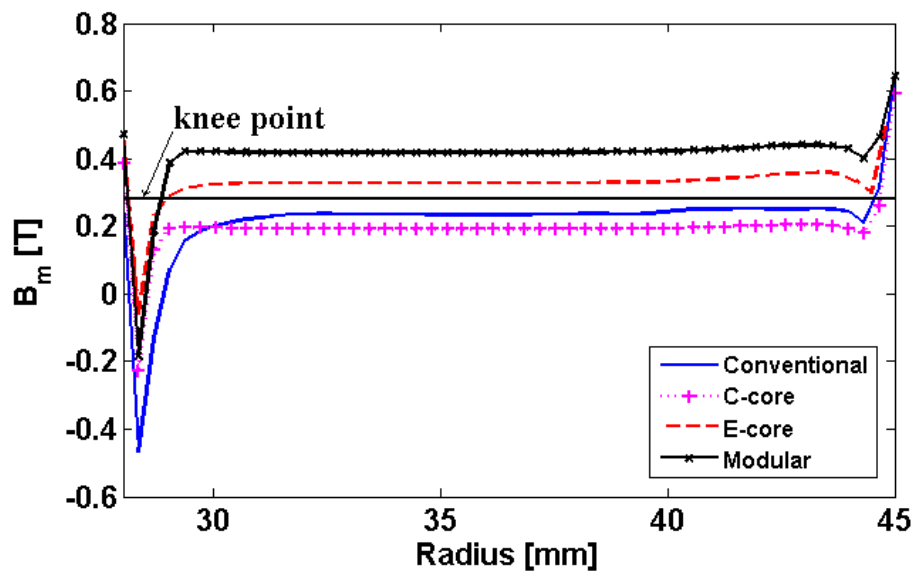


Fig. 4.20. Flux densities (circumferential components) along the central line of the affected PM (all PMs at 100°C).

4.5.3. EXPERIMENTAL VALIDATION OF TEMPERATURE EFFECT ON PMs

In this section, experimental results concerning the variation of PM working point with temperature (and hence indirect validation of reversible demagnetization) are presented for the conventional double layer prototype. This is done by using four type-K thermocouples mounted on two adjacent PMs and the corresponding coils, as shown in Fig. 4.21. The thermocouples for measuring winding temperatures are buried deep in the stator slots while the PM ones are located at the lateral end of the PMs.

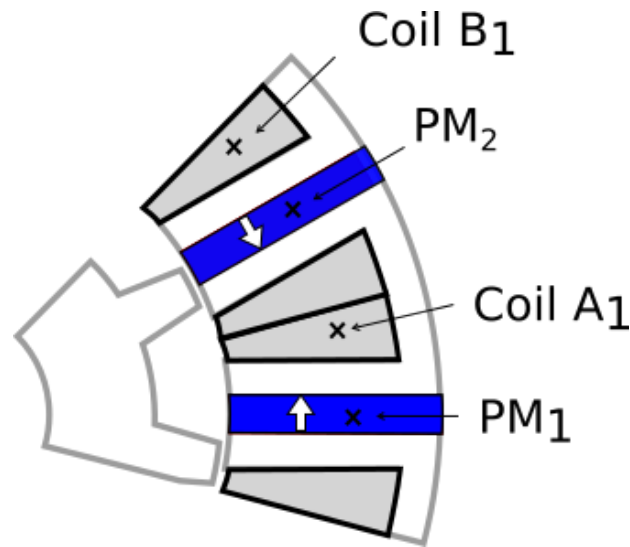


Fig. 4.21. Thermocouples location in slots and PMs

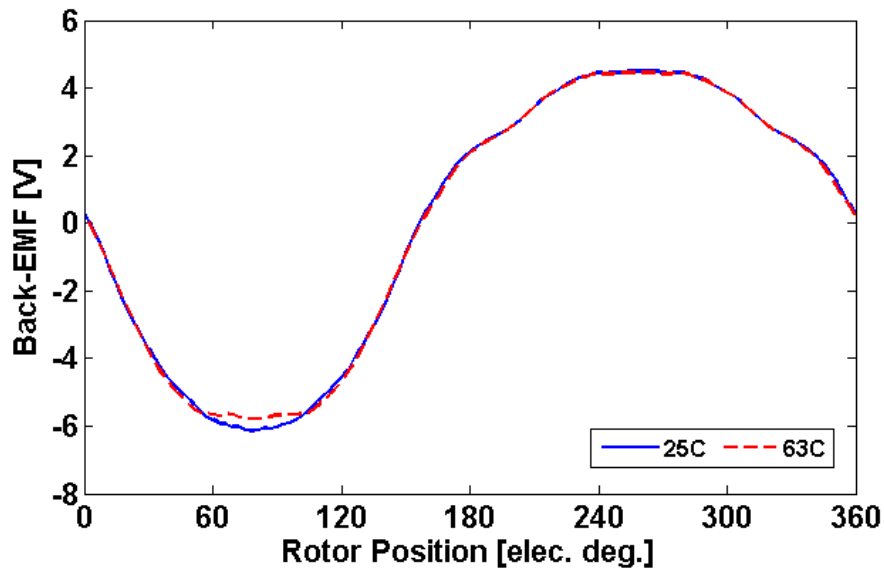
TABLE 4.8

FINAL LOCAL TEMPERATURES

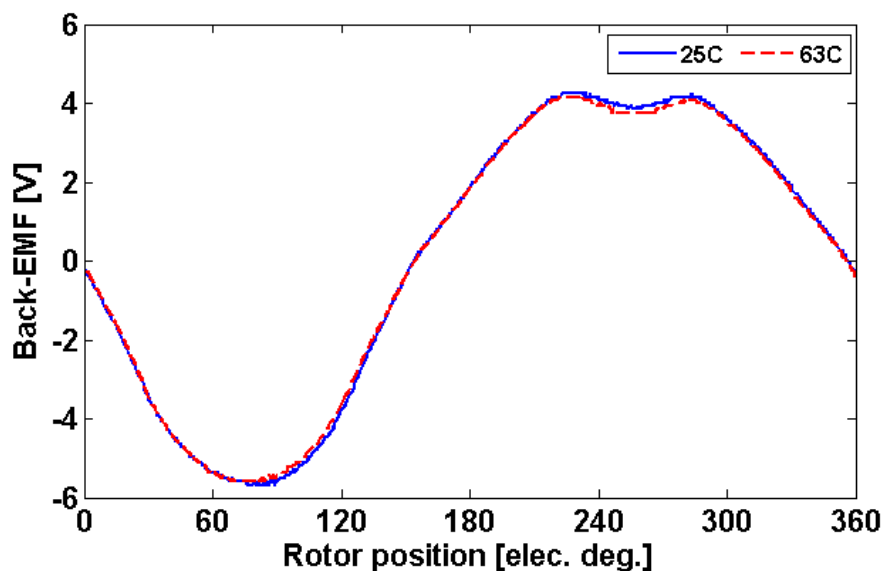
	PM ₁	Coil A ₁	Coil B ₁	PM ₂
Temperature [°C]	63	106	66	51

The purpose of the experiment is to show the back-EMF variation due to temperature increase in the affected PM. The experiment is conducted in open-circuit generator mode since it is found that the magnet demagnetization is mainly due to adjacent magnets rather than armature currents (healthy and short-circuit). The methodology is as follows. First, back-EMF of the coil A₁ is measured at low temperature (25°C). Next, the coil A₁ is short-circuited, while the rotor speed is very high (2000 rpm) in order to produce a high-short-circuit current that will increase the temperature of PM₁ (63°C), as shown in Table 4.8. The PM₁ temperature of 63°C corresponds to 106°C in the coil A₁. After the desirable temperature has been reached on the affected PM (PM₁), the short-circuit is removed and the back-EMF

of the coil A_1 is measured again. A drop of 3% in the back-EMF confirms the expected outcome that the magnet is reversibly demagnetized due to the temperature rise, as shown in Fig. 4.22. The threshold PM temperature (100°C) for irreversible demagnetization has not been reached in order to protect the machine because it will be used for future investigations.



(a)



(b)

Fig. 4.22. Coil A_1 back-EMF. Waveforms for 25°C and 63°C . (a) predicted, (b) measured.

4.6. CONCLUSIONS

Three modular single layer SFPMMs are investigated and compared with their conventional double layer counterparts in terms of machine performance, short-circuit current and demagnetization withstand capability. Table 4.9 summarizes the main features of each topology.

TABLE 4.9
SUMMARY OF THE STUDIED TOPOLOGIES

	Conventional	C-core	E-core	Modular
Av. Torque [Nm]	2.2	1.5	2.0	1.8
Torque/PM vol. [Nm/m ³]	1.44e6	1.96e6	2.61e6	2.35e6
I _{sc} at 25°C [A]	36.4	20	18.9	15.2
DWC	poor	poor	good	best

* DWC: demagnetization withstanding capability

It was found that the conventional SFPMM is extremely resilient to magnet demagnetization in d -axis and at low temperature although the short-circuit current is the highest in this condition. The main factor which contributes to the SFPMM robustness against demagnetization is the magnetic circuit configuration. The affected PM is shielded by two U-shaped iron segments which divert the demagnetizing fluxes from the affected PM, and preventing it from being demagnetized. Therefore, the short-circuit current and adjacent PMs have slight influence on the affected PM. At higher temperature, the short-circuit current is lower due to increased phase resistance, reduced magnet remanence and hence reduced phase back-EMF. However, the knee point is higher and the PM material has much lower coercivity which enables the adjacent PMs to easily demagnetize the affected one. Due to magnetic circuit alignment the highest irreversible demagnetization occurs in the q -axis, which can simplify the post-demagnetization analysis as only these particular positions need to be investigated.

The reduction of the PM volume affects both performance and demagnetization withstand capabilities. There is a performance penalty in adopting fault tolerant solutions such as E-core and modular topologies (for instance a drop in the torque capability and lower power factor due to increased phase self-inductance). However, their demagnetization withstand capability improves compared with conventional and C-core machines. This is mainly due to the fact that the magnetless stator teeth of the E-core and modular machines divert some of the demagnetizing flux produced by the remaining healthy parts of the

magnetic circuit, protecting the affected PM against the irreversible demagnetization. As a result, better phase magnetic separation and also better demagnetization withstand capability can be achieved. It can be concluded that a good compromise between performance (average torque and torque ripple) and fault-tolerant capability would be using a modular topology with a small flux gaps which leads to an average torque drop slightly higher than 10% while being able to withstand a temperature of around 25°C higher than its conventional counterparts. The modular machine can be developed further so the flux gaps can be used for cooling, allowing the machine to work at higher phase currents and to improve the torque/mass ratio. Therefore, the thermal aspect will be developed further in future studies. The resulting high performance, fault tolerant capability and reduced price will make the modular topology well suitable for aerospace and electric and hybrid electric vehicles applications.

The models investigated in this section make some assumptions about the working temperature of PMs and windings. These assumptions allow the development of relatively simple models with fast solving process times. However the models do not provide any information about the temperature evolution in the machine. Therefore, a multi-physics model is developed in the next chapter to evaluate the temperature rise in the machine during fault conditions.

Chapter 5. Combined Multi-Physics Model of Switched Flux Permanent Magnet Machines under Fault Operations

In this chapter, the transient thermal response of a conventional double layer switched flux permanent magnet machine is studied for both healthy and fault conditions such as inter-turn short-circuit. A highly optimized and accurate co-simulation model for different operating conditions is developed, which requires low computation and time resources. The electro-mechanical models for both healthy and faulty operation are implemented in Matlab/Simulink while the thermal model is implemented using 3D FEM software, both of them are coupled and able to predict the influence of temperature rise on the electromagnetic performance and vice versa. Operation under various conditions are investigated and it is found that the temperature rise under fault conditions and high speed can lead to irreversible demagnetization of the permanent magnets. The superposition principle is used to accurately estimate the influence of the short-circuit current over the temperature rise. A series of dynamic tests are carried out to validate the predicted transient thermal responses during both the healthy and fault conditions.

5.1. INTRODUCTION

THE thermal design is crucial in developing new products with a high power to mass (or volume) ratio constraint like the electrical machines used in the aircraft or automotive industries. Traditionally covered using analytical models or lumped parameter circuits, the thermal aspect is being considered more and more [128], [96], [129], [130], [131], [132] due to factors like increased computation power, available software packages as well as the drive from dynamic industries like the ones previously mentioned to develop more compact and lighter solutions. The thermal aspect can be investigated separately or in conjunction with an electro-mechanical finite element simulation package leading to a multiphysics solution. The means of investigation can vary from basic analytical models, lumped parameter circuit networks [133], (MotorCAD, Matlab/Simulink's SimScape toolbox) to more sophisticated full finite element solutions including bidirectional multiphysics couplings (Ansys, Flux, Infolytica, Opera). The goals range from assessing the temperature hotspots in a machine to design iterations in order to improve the heat removal either axially (using fan cooling) or radially (using water jackets). In particular the increase in temperature can accelerate the machine insulation ageing as well as increase the losses and degrade the overall performance.

This has allowed the uprising of several technologies, targeted at both improving the heat flow from the machine to its exterior as well as taking the toil from the insulation, one of the weakest points when it comes to heat. A non-exhaustive list of technologies include:

- Better winding machines or preformed coils to achieve a higher slot filling factor which will lead to a more compact winding with a better heat transfer. This is achieved both using a high accuracy when positioning the conductor in the slot as well as controlling the tension in the wire. In the case of preformed coils, a small compromise might be necessary in the form of a segmented lamination to allow the coil insertion in the stator slot;
- Concepts like rectangular and self-bonding wire which also lead to more compact and thermally efficient windings;
- Glued laminations where each sheet of lamination is glued to the next one (instead of being mechanically stitched or interlocked). This improves the heat removal properties in the axial direction since the air layer introduced by traditional methods of stamping the laminations is replaced by glue which has a higher thermal conductivity;
- varnish and epoxy resin with high thermal conductivity for impregnating or potting the windings, powder coating insulation [134] as alternative for paper or polyester film based slot liner. The ScotchCastTM range of products (3M) provide increased thermal conductivity which gives the

designer higher flexibility. The resins can also be used as an adhesive with good thermal properties.

The challenges in achieving a suitable solution with thermal design are multiple and sometimes exclusive. Some materials have good performance but no optimal thermal capabilities. For example, permanent magnets (PMs) are well-known to achieve a high power density. However, their performance and operational status largely depend on temperature rise. At high speeds, both the eddy current loss within the PMs and the iron losses in the adjacent laminated iron core are high, leading to potential temperature rise with disastrous consequences like irreversible demagnetization. Another demanding requirement is capability of functioning for a limited time interval in a so called degraded mode, i.e. with reduced torque and/or speed, increased torque ripple, etc. This is essential for safety-critical applications but the presence of a fault, e.g. inter-turn short-circuit in one of the windings, can push the working temperature of the machine to a dangerous level. To avoid this, thermal analysis often needs to be carried out during the design phase [95] focusing on topics such as additional cooling, structure optimization, material choice and also proper topology selection.

The SFPMM topology has the PM located inside the concentrated coils which be problematic because this makes the PM prone to temperature related demagnetization due to copper losses in the armature windings [68], [67]. Previous studies in [70], [72], [105], [108], [135] have shown remarkable resilience of the SFPMM against irreversible demagnetization at low and medium temperature ranges due to the way in which the PMs are positioned on the flux paths. Further increasing the PM temperature however will still result in irreversible demagnetization for the SFPMM. Although important, the issue of thermal analysis in the SFPMMs has been brought under investigation only recently and most of previous investigations are focused on the electromagnetic finite element (FE) models [70], [72], [105]. In these models, the PM material is assumed working at an imposed temperature while the machine operates in healthy mode. While this approach has the advantage of using simpler models, it does not give full information about the thermal response of the machine or its behaviour under fault conditions. Some recent papers [108], [135] expand the same approach for a faulty operation mode (under various severity of short-circuit conditions) assuming temperatures up to 150°C. However, without thorough thermal analysis, it cannot show if those values of temperature can be reached. Only in [136] and [137] a transient thermal analysis is conducted for SFPMM working under healthy conditions and generator mode. These are assuming constant copper and iron losses, thus offering limited insight into machine operation. In [138] a coupled model is implemented for healthy conditions, based on improved 2D FE models.

Although the authors suggest a faster simulation time, they limit the study to steady-state thermal performance assessment. Finally, in [139] a multi-physics (thermal-electromagnetic-faulty) model is investigated for the SFPMM. The electro-mechanical part is implemented in Matlab/Simulink while the thermal part is a 3D FE model or alternatively based on lumped parameter networks. However, the multi-physics model is not fully coupled. The heating sources are generated in the magnetic model and carried over into the thermal one. The calculated temperatures in the thermal model are not fed back to the magnetic model. It can be seen, thus, that the most of the literature focus only on either the thermal/magnetic phenomena or limits the study to a single operating point.

In this chapter, a Matlab/Simulink – 3D FE coupled model is described, which is suitable for simulating various operating conditions and characteristics thereby addressing some of the limitations previously described. The proposed model combines the fast simulation times of Matlab/Simulink solvers with the accuracy of a 3D model. It will allow the study of both the healthy and faulty operations as well as the influence of various parameters (like speed) on the temperature rise and vice versa. Moreover, the control strategy effect can also be taken into account.

In section 5.2 the multiphysics model is introduced with all the assumptions required, including for the thermal domain. Section 5.3 uses this model to generate the temperature variation during both healthy and faulty mode. Next, experimental validation is carried out (section 5.4) and the last section 5.5 contains the conclusions.

5.2. THE CO-SIMULATION MODEL

5.2.1. INVESTIGATION METHODOLOGY

The 3D view of the modeled SFPMM is shown in Fig. 5.1 while the main parameters are given in Table 5.1. The employed PM material is NdFeB (N35H grade [106]). This SFPMM is the same as the conventional double layer studied in the previous chapters as also shown by Table 5.1. However, for thermal purposes modelling, its case needs to be included along with appropriate boundary conditions as it will be detailed further in section 5.2.3.

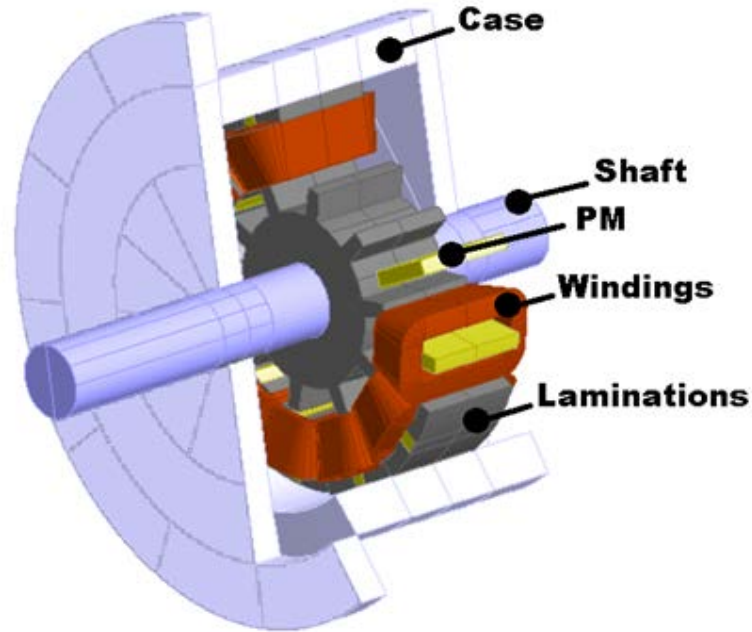


Fig. 5.1. 3D view of the considered SFPMM.

TABLE 5.1

PARAMETERS OF THE INVESTIGATED MACHINE

Stator slot number	12	Stator yoke height (mm)	3.6
Rotor pole number	10	Stack length (mm)	25
Rated speed (rpm)	400	Air-gap length (mm)	0.5
Rated rms current (A)	11	Rotor outer radius (mm)	27.5
Rated torque (Nm)	2.2	Magnet thickness (mm)	3.6
Stator outer radius (mm)	45	Remanence (NdFeB) (T)	1.2
Stator inner radius (mm)	28	Number of turns/phase	72

The proposed co-simulation model combines a Matlab/Simulink (electro-mechanical) component with a 3D FE thermal one [140], as shown in Fig. 5.2. Two dimensions FE magnetic models are used to compute data such as back-EMF, cogging torque, etc. which will be stored in look-up tables. This data is used further in the electro-mechanical model as will be detailed later on. The reason of using 2D FE magnetic model is mainly because it can achieve a reasonable level of accuracy with significantly less computation time and resources than a 3D FE magnetic model. Since the proposed model relies on pre-determined look-up tables, the electro-mechanical model can accurately consider rotor position

dependence. The look-up table data features temperature dependent relationships. This is achieved by including the temperature PM demagnetization curve within the 2D FE magnetic models. Furthermore, the influence of the temperature on the phase resistance is also considered. When it comes to the thermal model, due to the end-windings, their surrounding air cavity and also the end plates, a 3D modelling is necessary. The two physics sub-models (electromechanical and thermal) exchange data (heating sources such as power losses and temperatures) in a bidirectional manner.

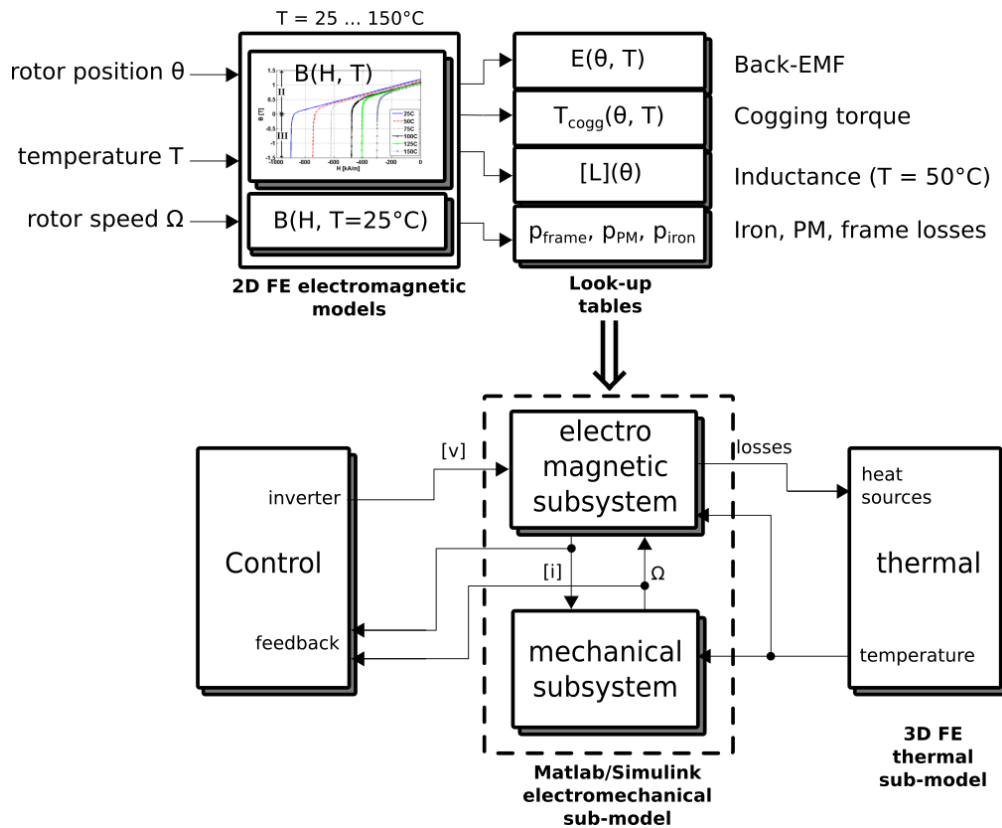


Fig. 5.2. The combined multi-physics model for healthy and faulty operations.

The main challenge in building a general model capable of accounting for the coupled electromagnetic-faulty-thermal phenomena is the difference in time constants between the various models. For example, in electromagnetic model, the time constant is at the level of ms. However, for the thermal model, this might be closer to hours. This is mainly due to the necessity of using a small time step (~ms) in the electrical model in order to achieve acceptable accuracy. However a much larger time constant (~hours) is required for the thermal modelling. Moreover, the simulated operation time of the multi-physics model is determined by its thermal model at a small time step imposed by the electrical model. This is very computationally demanding and requires particular attention.

5.2.2. ELECTROMECHANICAL MODEL AND ASSOCIATED CONTROL

The aforementioned SFPMM works under the classic speed control strategy, as detailed in section A.2 in the Appendix. The Matlab/Simulink model is based on the voltage and torque equations (A.1) and (A.2) in the Appendix. The control strategy used is the Maximum Torque Per Ampere and the control diagram is given in Appendix (Fig. A.2).

Fig. 5.3 shows a faulty operating condition where for the phase A one coil (A1) out of a total of four coils is affected by a short-circuit, i.e. 25% fault severity.

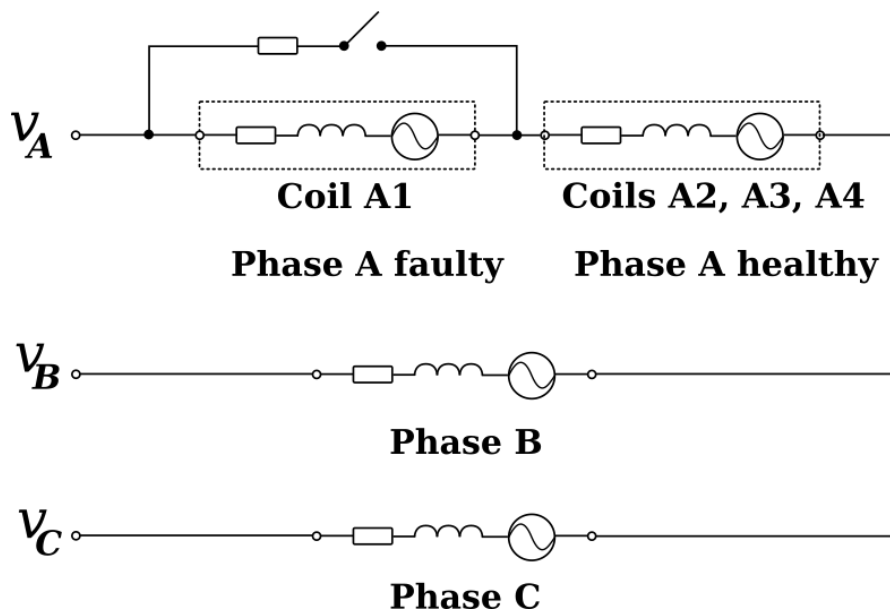


Fig. 5.3. The inter-turn short-circuit fault schematic.

The electro-mechanical model computes the heat sources (copper loss, iron losses and PM eddy current loss) which are going to be used later in the thermal model. The iron losses (calculated using the method introduced in [141]), the PM and frame losses are implemented in look-up tables. The PM eddy losses are assumed to be independent of the temperature variation and only dependent on the speed, as shown in Fig. 5.4. This is to reduce the model complexity. The FE results have shown that the PM losses at 150°C decrease by only 9% when compared with the 25°C case, which justifies the above simplification. However, the copper losses depend on the computed current and the phase resistance, and the latter is temperature dependent.

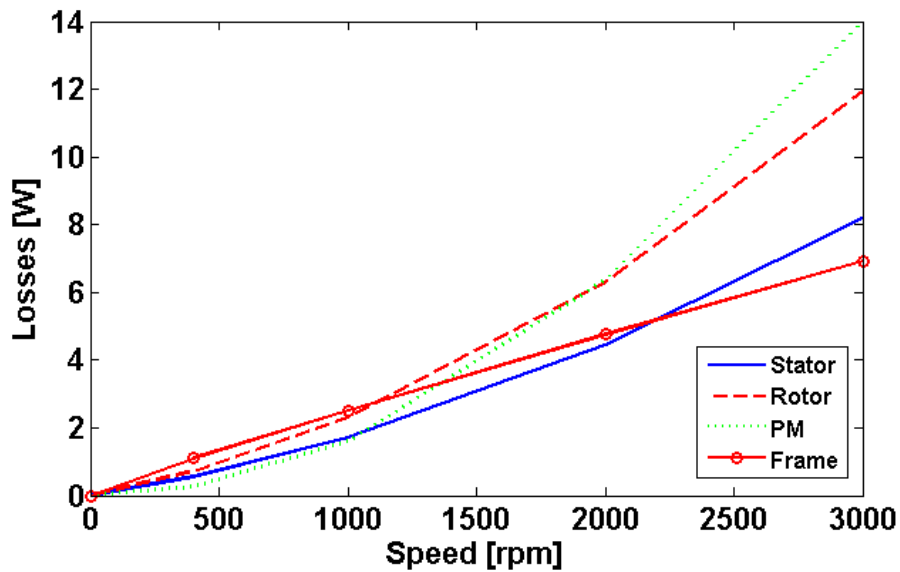


Fig. 5.4. Stator and rotor iron losses, PM and Frame eddy current losses vs rotor speed.

It is worth mentioning that the data exchange between the thermal and electromechanical models is driven by the thermal time step. However, the impact on accuracy is negligible since the electrical quantities vary very slowly with temperature. When sending the copper losses (heat sources) as input into the thermal model, because they were determined for each electrical time step (0.2 ms), they need to be averaged over the thermal time step. The thermal time step is not constant and it is imposed by the user in advance to vary between 25 and 1000s. Its variation accounts for the thermal process evolution which has a fast transient and lengthy steady state processes. This is necessary in order to reduce the simulation time. To better illustrate this point a representative thermal time step distribution across the interval of study is given below, along with a resulting temperature variation in time. It can be seen that at the beginning of the study as well as at the beginning of the degraded mode operation, the thermal process evolution is faster thus needing more time steps for accuracy. The model solving speed is tuned in this way by making use of an optimum time step distribution (variable time step between 25 to 1000s). However, in order to establish the time step distribution (and variation limits for the time step), an initial thermal FE model can be run (with constant fixed time step) or, if available, decisions can be made based on experimental temperature data. This initial assessment is valid as long as the heating sources or operating conditions do not change because otherwise the thermal response of the machine will be different. For subsequent model solving process runs, the initially determined time step distribution will be imposed in advance.

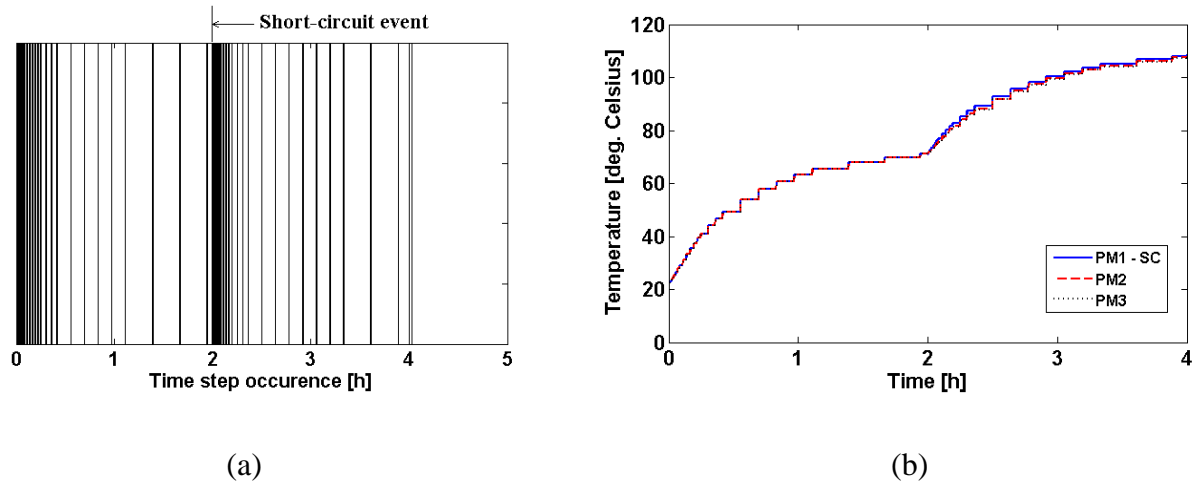


Fig. 5.5 Time step distribution over the interval of study (4 hours). (a) time step distribution, (b) example of temperature output with a zero order hold local variation to highlight the time steps distribution.

5.2.3. THERMAL MODEL

A 3D FE thermal model is used in order to account for the effects of the end-winding and end plates as shown in Fig. 5.6. It is also worth mentioning that the inter-turn short-circuit is studied, which is an asymmetric fault, meaning that the model cannot be reduced based on the available physical symmetries of the machine and the FE model of the whole machine is necessary.

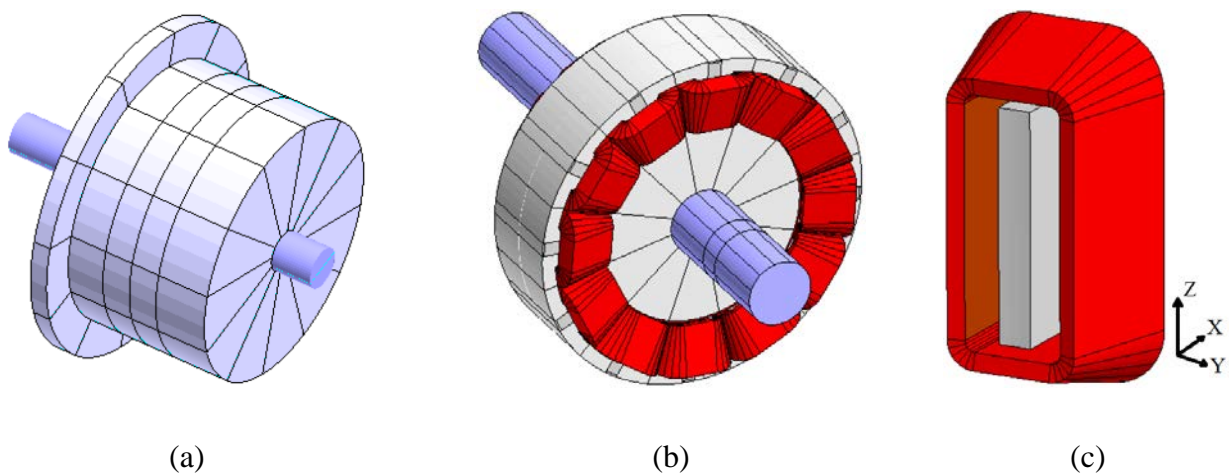


Fig. 5.6. The thermal model. (a) Full motor, including end plate, (b) stator and rotor cores, PMs, coils and shaft, (c) single coil surrounding PM.

The thermal properties of the materials used in the model are given in Table 5.2. Concerning the windings, an anisotropic thermal conductivity was considered due to the fact that there is a much stronger heat transfer by conduction in the Z-axis (axial direction) towards the end-windings and not so much in the radial direction, i.e. XY plane, Fig. 5.6 (c). In the axial direction the thermal conductivity is the same as that of copper since the wires are oriented axially. In the radial direction the thermal conductivity is determined by various factors like the slot fill factor, impregnation varnish characteristics, etc. The radial thermal conductivity was calculated using the method introduced in [142] considering the fact that the fill factor is 0.4 and the winding is not impregnated. The housing is made of aluminium with a polished surface (with an assumed emissivity of 0.09 [143]). The stator lamination material also has an anisotropic variation – this is considered due to the presence of a small layer of coating between the lamination sheets.

TABLE 5.2

THERMAL PROPERTIES OF THE INVESTIGATED MACHINE

Region	Thermal conductivity [W/m/K]	Volumetric Heat Capacity [J/K]
Windings [142]	0.07/0.07/385	1000000
Stator [142]	28/28/0.5	3519000
Rotor	20*	3519000
Frame + Rig	168	2324070
Air [144]	0.0263	1231.1
Shaft	52	3588000

* Equivalent value calculated using the method introduced in [145].

5.2.3.1 AIRGAP HEAT TRANSFER

The airgap heat transfer as well as the convection coefficients in the next sections are introduced using concepts and analytical models from the fluid dynamics field. Concerning the airgap heat transfer between the stator and rotor, the methodology is to determine first the type of flow (laminar, vortex or turbulent). This is given by Taylor’s dimensionless number [146] which was computed for smooth

concentric rotating cylinders. However, it was established that with slight modifications this can be applied successfully to the slotted rotors and stators for relatively low speed applications, which is the case for this study. Motorcad LP thermal models [98] for example, simplifies the air gap structure for salient motors (for both stator and rotor) by considering a single thermal resistance for the heat transfer between stator and rotor. Another example is given in [145] in which a method to simplify a salient airgap structure for a SFPMM to a “smooth rotor” is proposed. The method uses LP thermal resistor networks which are reduced to a much simpler configuration. The end result is a simplified equivalent LP thermal circuit which models the rotor using a single resistor. Furthermore, a finite element model is generated in which the rotor is modelled as smooth with an equivalent thermal conductivity value based on the single thermal resistor value. In particular, the resulting “smooth rotor” allows further for Taylor’s number and associated methods to be calculated. Therefore it was decided to treat the salient rotor structure as a constant airgap structure, as shown in Fig. 5.6 (b), in which the equivalent thermal conductivity of the rotor material was determined using the method introduced in [145]. These simplifications are acceptable as they provide an analytical alternative to more complicated CFD (computational fluid dynamics) models. The Taylor number Ta is:

$$Ta = \rho \cdot l_g \cdot \frac{v}{\mu} \cdot \sqrt{\frac{l_g}{R_r}} \quad (5.1)$$

where ρ is the air density, l_g is the air-gap radial thickness, R_r is the rotor radius, μ is the air dynamic viscosity and v is the air velocity. For the maximum speed considered (3000 rpm), the Ta value is 38.88 which would still allow one to consider the airgap as having a laminar flow. Secondly, based on the Ta value, the Nusselt number Nu is equal to 2 and allows the determinations of the convection coefficient:

$$h = Nu \cdot \frac{k}{L} \quad (5.2)$$

where k is the air thermal conductivity and L is the characteristic length ($L = 2 \cdot l_g$ for airgap region).

Once the convection coefficient h is calculated, an equivalent thermal conductivity can be obtained in the airgap region, facilitating the 3D FE thermal model. For simplicity, this approach was also expanded to the end-space regions.

5.2.3.2 THE CONVECTION COEFFICIENT CALCULATION

The machine housing is cylindrical and is cooled via natural convection. In order to determine the convection coefficient [146], the Grashof and Prandtl dimensionless numbers are determined first. The Grashof number (Gr) is defined as:

$$Gr = \beta \cdot g \cdot \Delta T \cdot \rho^2 \cdot L^3 / \mu^2 \quad (5.3)$$

where β is the coefficient of cubical expansion $\beta=1/(273+T_{FLUID})$. The T_{FLUID} is the average ambient temperature. ΔT is the difference between the housing external surface temperature and T_{FLUID} . ρ is the air mass density. g is the gravitational acceleration and μ is the air dynamic viscosity. The characteristic length L is equal to the machine housing diameter.

The Prandtl number (Pr) is given by:

$$Pr = c_p \cdot \mu / k \quad (5.4)$$

where c_p is the air specific heat capacity.

Next the Nusselt number is determined using a correlation for cylindrical objects:

$$Nu = 0.525 \cdot (Gr \cdot Pr)^{0.25} \quad (5.5)$$

Finally, using the Nusselt number the surface convection coefficients can be determined from (5.2). The convection coefficient is considered as temperature dependent [147] – more specifically it depends on the surface temperature as illustrated by the Grashof number in (5.3). It is found that a higher temperature achieved at the external housing surface will lead to a higher convection heat flux exchange.

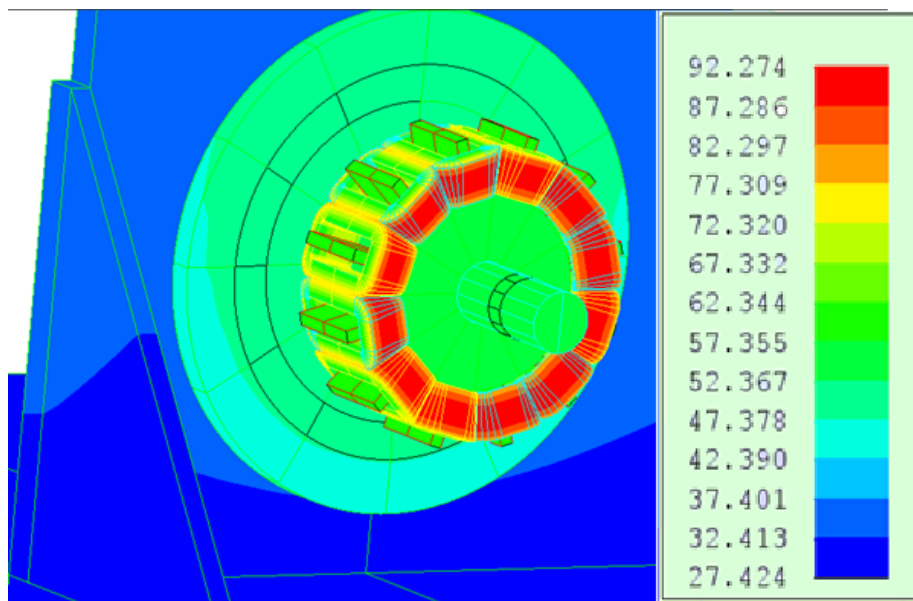
5.3. THERMAL ASSESSMENT DURING THE INTER-TURN SHORT-CIRCUIT

5.3.1. THERMAL AND ELECTRO-MECHANICAL MODELS PREDICTIONS

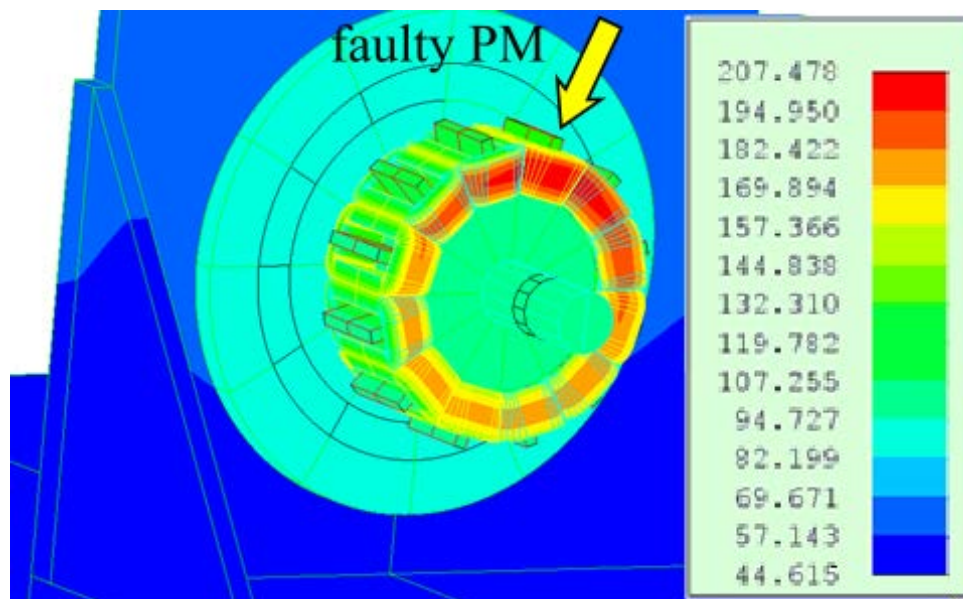
The thermal transient response is studied for two cases – 400 rpm and 1000 rpm at rated torque and under inter-turn short-circuit condition. The ultimate goal is to estimate the overall temperature rise during the fault operation and to predict if the PMs are in danger of being irreversibly demagnetized. It is worth mentioning that at 400 rpm, the short-circuit current is low (8.5A, peak value) and there is no significant increase in temperature. Therefore, these results were not shown here. However, at 1000 rpm, the potential short-circuit current is high (19.9A, peak value). The considered faulty scenario is such that the machine operates for one hour under healthy conditions, then the short-circuit fault is introduced and

the degraded mode maintained by using the control shown in section A.2 (Appendix) for the next 1.5 hours. Under these conditions, the solving process of the entire coupled model takes 7 hours on a 2.6 GHz quad core i7 processor computer with 16 Gb RAM and SSD storage. The majority of the time is spent in the electromechanical model due to its small time step.

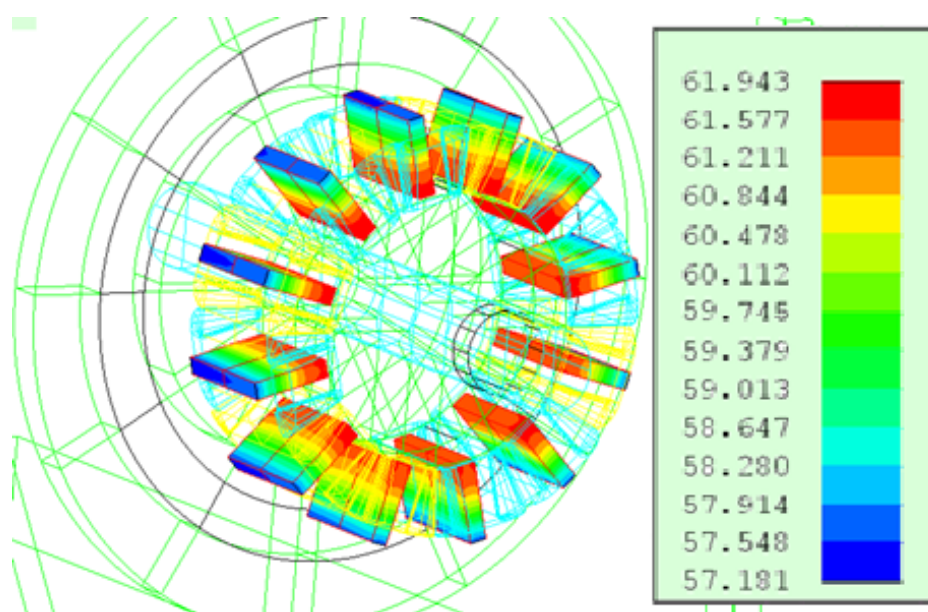
The following results are presented for the machine working at 1000 rpm and rated torque (no flux weakening: $I_d = 0A$). The temperature distributions within the machine are shown in Fig. 5.7. It can be noticed that due to the existing fault there is an imbalance in the temperature distribution for both windings and the surrounded PMs. The affected winding and PM have a temperature rise of $30^{\circ}C$, higher than the rest of the coils and PMs, respectively, contributing to an extra heat source for them. The overall temperature has increased to levels that cause irreversible demagnetization of all PMs ($> 100^{\circ}C$). The windings are also subject to temperatures higher than $120^{\circ}C$ while reaching a peak of $207^{\circ}C$ in the affected coil. This might cause thermal destruction of most of the commercially available insulation materials.



(a)



(b)



(c)

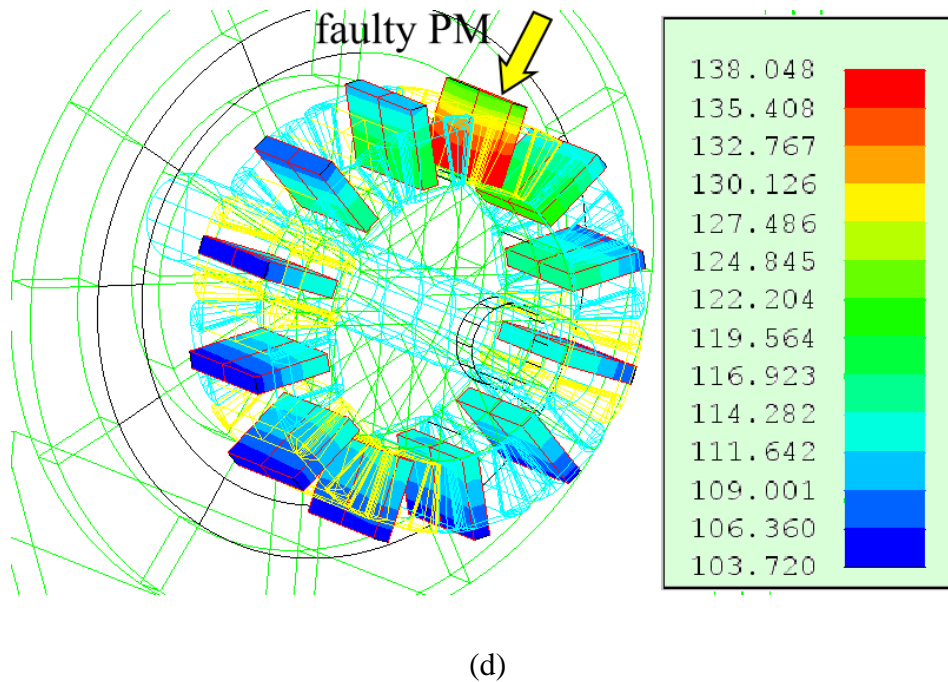
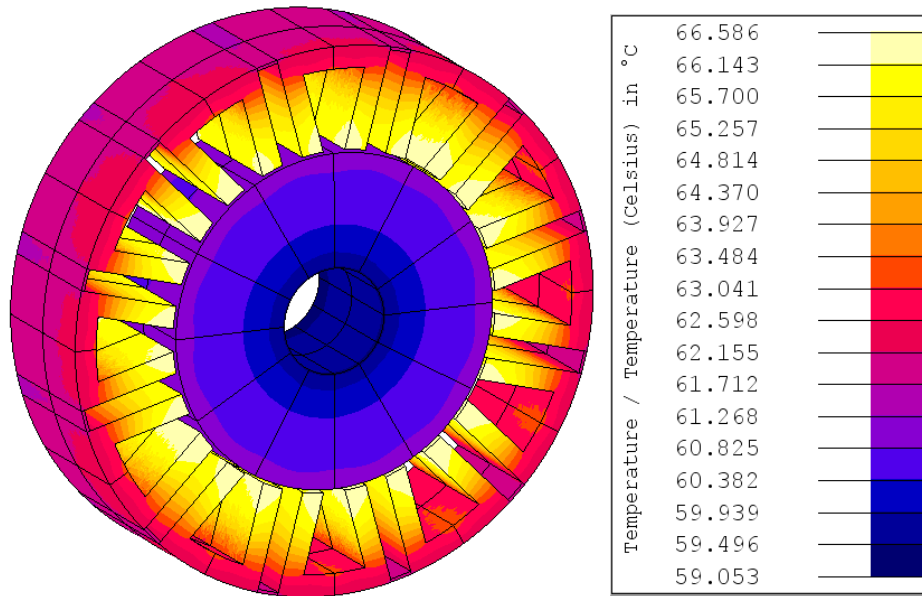
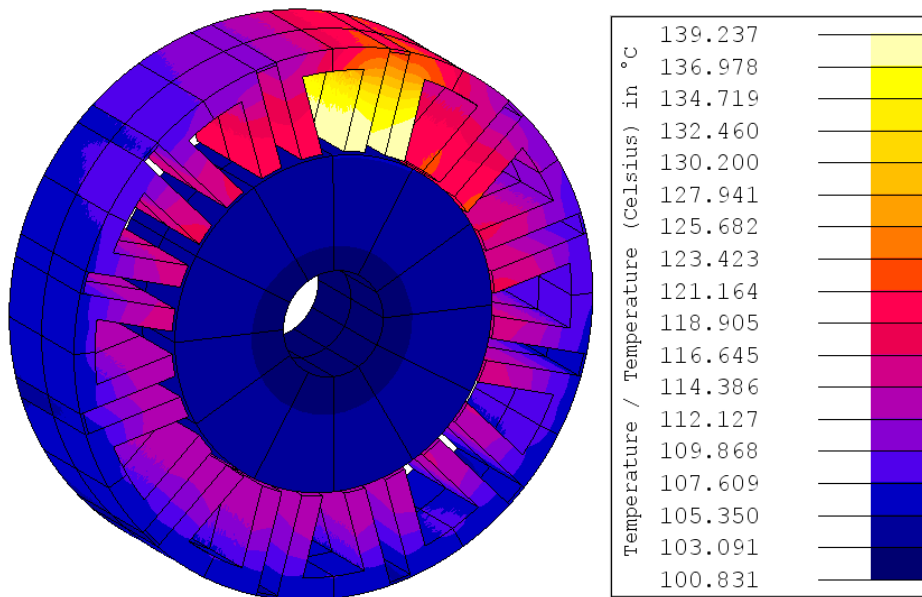


Fig. 5.7. Temperature distributions within the machine at 1000 rpm. (a) windings (healthy), $t = 1$ hour, (b) windings (faulty), $t = 2.5$ hours, (c) PMs (healthy), $t = 1$ hour, (d) PMs (faulty), $t = 2.5$ hours.

The lamination magnetic properties can also be affected by the temperature increase. Therefore the temperature distribution on both stator and rotor are shown next in Fig. 5.8. The temperature rises from 67°C after one hour in healthy mode up to almost 140°C . This not only affects the performance but could damage the insulation coating between the lamination sheets, especially if the coating layer's temperature class was chosen towards a lower rating. Also, the temperature in the rotor is uniformly distributed in a circumferential fashion which is consistent with the rotating motion, justifying the previous simplification of the rotor geometry.



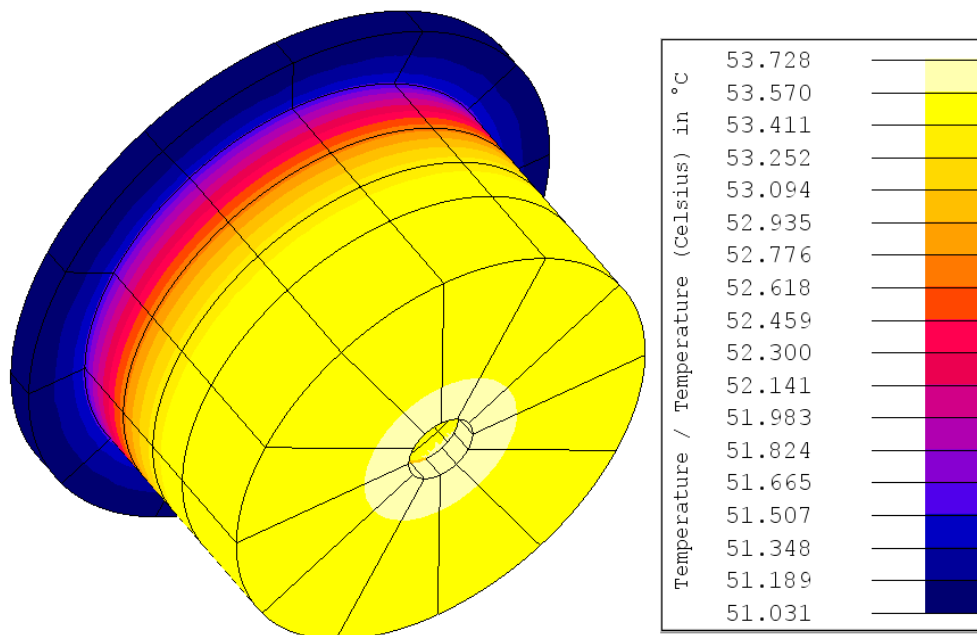
(a)



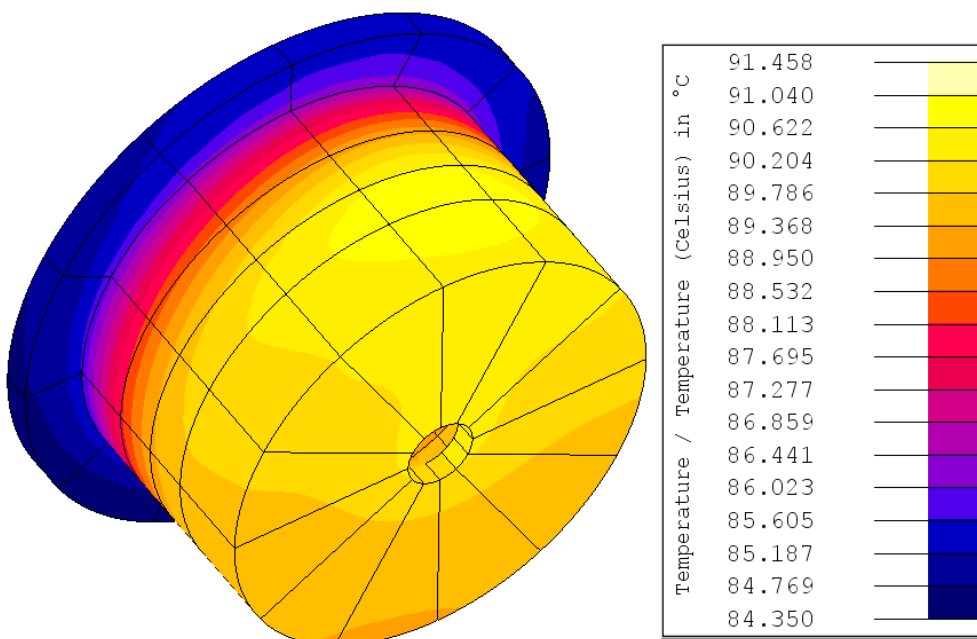
(b)

Fig. 5.8. Temperature distributions within laminations at 1000 rpm. (a) healthy case, $t = 1$ hour, (b) faulty case, $t = 2.5$ hours.

Finally, the temperature distribution for both healthy and faulty cases on the aluminium casing is given in Fig. 5.9. The housing's high thermal conductivity is helping with spreading the heat flux along its circumference and further dissipating it through the convection and radiation processes. Even at the end of the faulty regime, the difference between the temperature extremes is roughly 6°C .



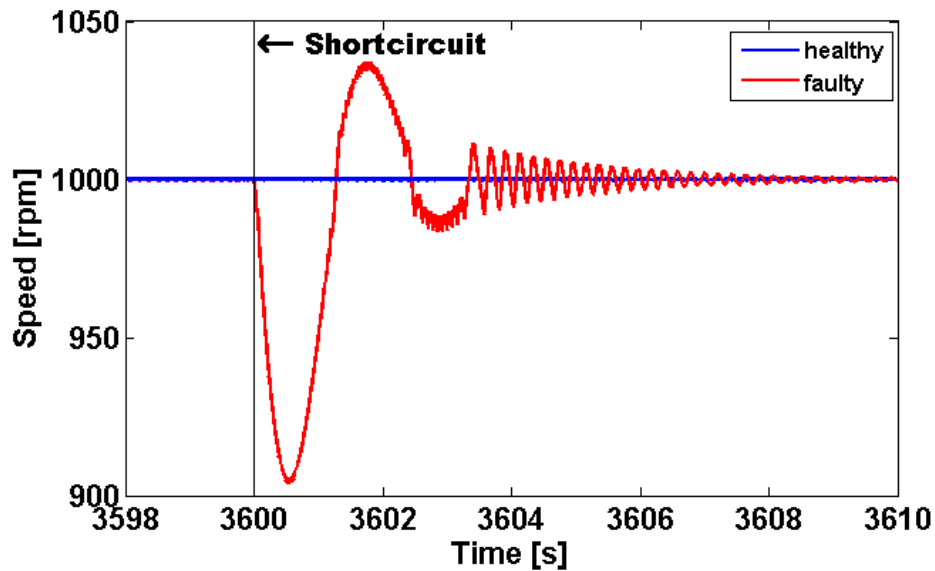
(a)



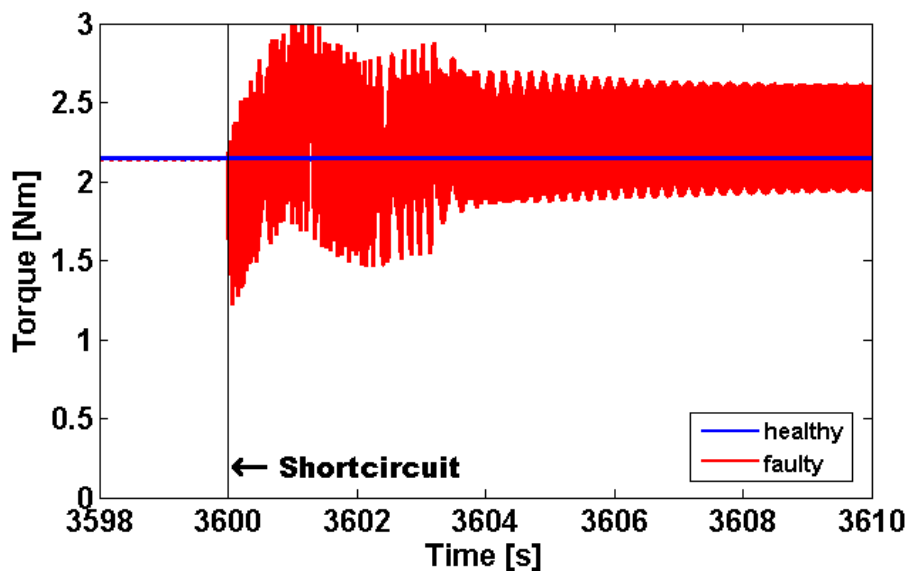
(b)

Fig. 5.9. Temperature distributions within the machine's housing at 1000 rpm. (a) healthy case, $t = 1$ hour, (b) faulty case, $t = 2.5$ hours.

The speed and torque resulting from the electromechanical model are shown in Fig. 5.10. The temperature has no visible influence over these quantities because the control strategy shown in Appendix section A.2 compensates them. The speed disturbance due to the inter-turn short-circuit is attenuated in around 10s. However, the torque ripple is high during the faulty mode, as expected.



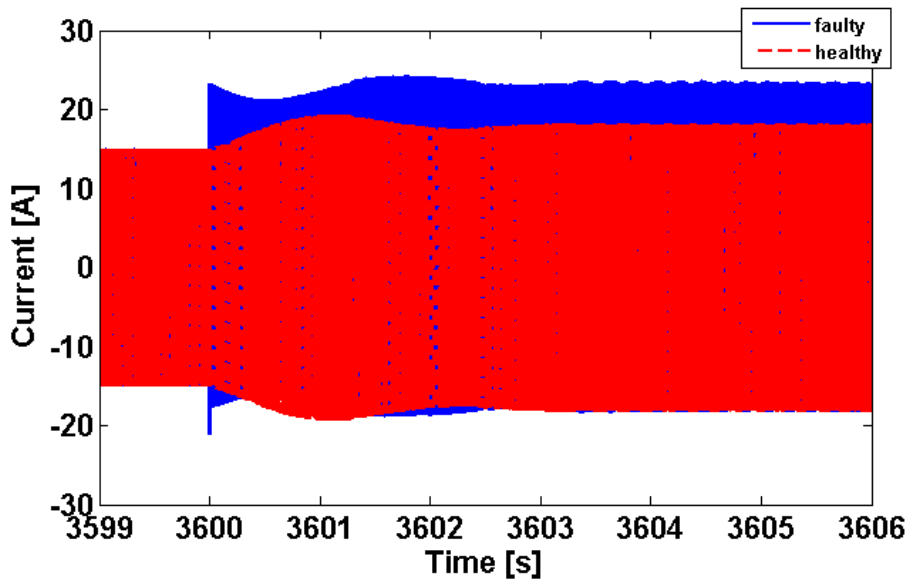
(a)



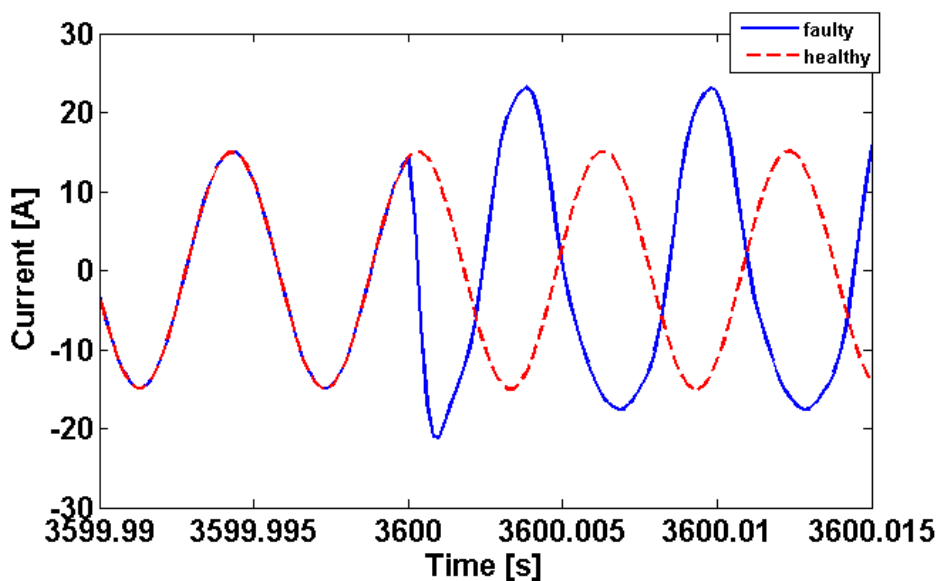
(b)

Fig. 5.10. Speed and torque (1000 rpm, faulty case).

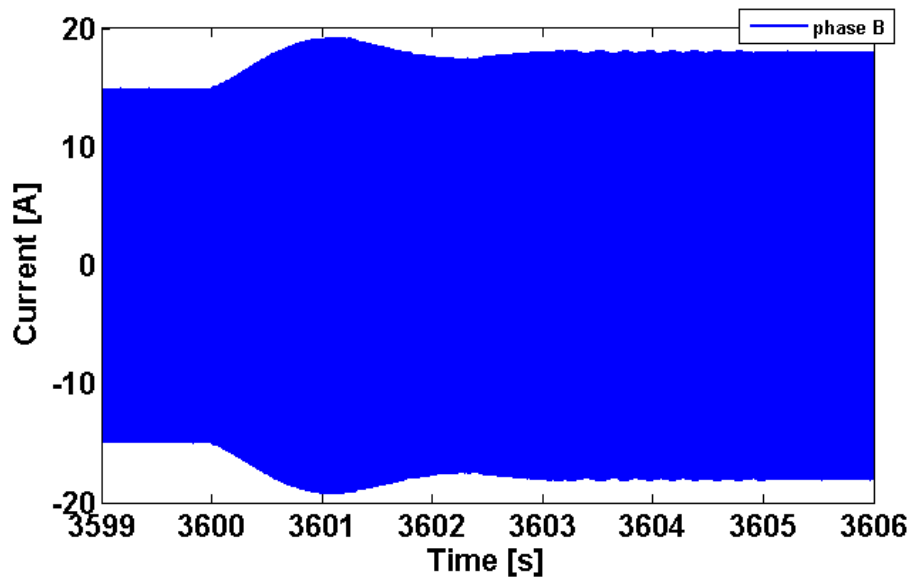
The current waveforms are given next for an interval of time around the occurrence of the short-circuit ($t = 3600$ s). It can be seen that the current is increased in the remaining phases, due to the control strategy, to compensate for the loss of torque. These increased currents also lead to increased copper losses which will be studied in the next section.



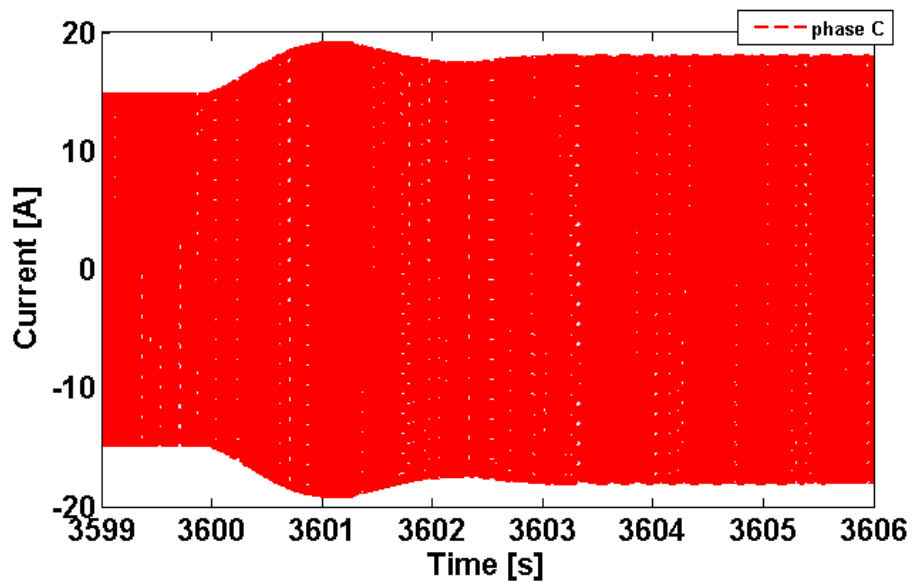
(a)



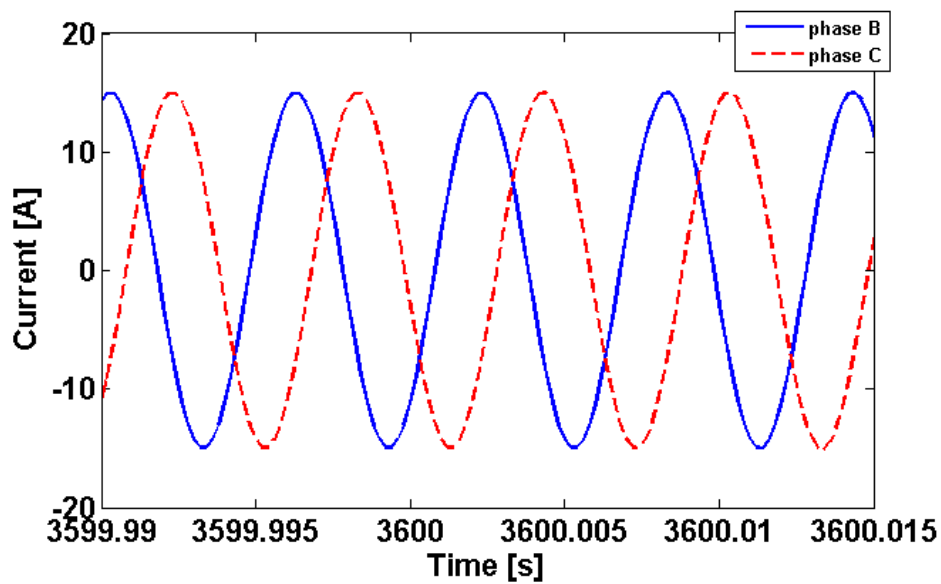
(b)



(c)



(d)



(e)

Fig. 5.11. The current waveforms of all phases (1000 rpm). (a) Healthy and faulty currents in phase A, (b) detail of the healthy and faulty current waveforms before and after short-circuit event, (c) Phase B current, (d) Phase C current, (e) details for phase B and C currents before and after short-circuit event.

5.3.2. DEMAGNETIZATION ANALYSIS

The models studied in the previous sections are analysed and compared further from the point of view of magnet demagnetization. The first quantities studied are the copper losses, as shown in Fig. 5.12, which justifies why thermal analysis is necessary. At low speed, the copper losses (only DC component is considered) in the affected coil have a modest increase of 37% due to the short-circuit fault. The copper losses in the remaining healthy coils (only one representative coil, e.g. B1, is shown) increases with a similar value due to the fact that the control strategy tries to compensate torque drop due to the fault by increasing the current in the healthy phases. When the fault occurs at a higher speed, e.g. 1000 rpm, the copper losses in the affected coil increase by about 861%, while again the control strategy is responsible for an additional increase of 70% in the healthy coils. This needs to be correlated with the Fig. 5.4 as the iron, PM and frame losses are also important and can be comparable with the copper losses at high speed. Given the significant copper losses increase during faulty operation, it is necessary to investigate the temperature evolution in the machine before and after the fault is introduced.

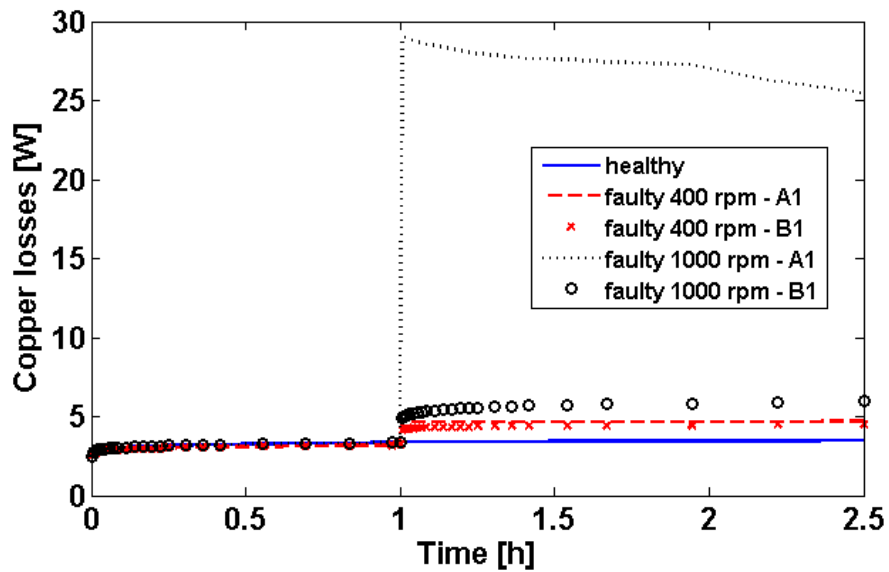


Fig. 5.12. Copper losses comparison.

The temperature increase in the PMs is studied further, as shown in Fig. 5.14. Although there are 12 PMs in the machine, only three representative PMs were chosen – the affected PM (A1), the adjacent PM (B1) as well as a third one (A4), located at 90° compared to A1. Fig. 5.13 shows the locations of the temperature measurement points and the selected PMs.

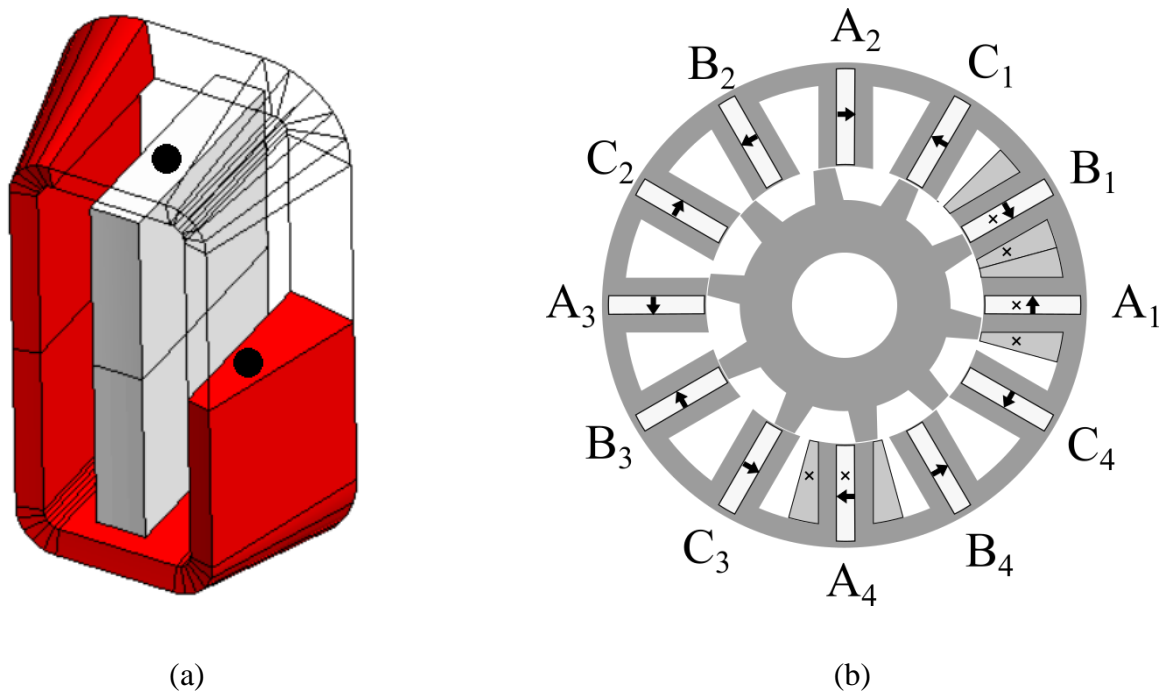


Fig. 5.13. Locations of thermocouples. (a) single coil and PM – 3D view, (b) all coils and PMs with thermocouples located at A1, B1 and A4.

For the considered PM grade (N35H), 100 °C is the threshold for irreversible demagnetization. It can be noticed that even during normal operation, there is a 7°C (about 10%) increase in temperature from 400 rpm to 1000 rpm due to higher PM losses. This might justify the necessity of magnet segmentation in order to reduce the PM losses. At rated speed, the temperature in the PMs is still below the irreversible demagnetization threshold. However, at 1000 rpm it can be noticed that all PMs are irreversibly demagnetized within about 30 minutes of the fault being introduced. However, the affected coil's PM demagnetizes in only a couple of minutes due to the close proximity and coupling to the short-circuited coil.

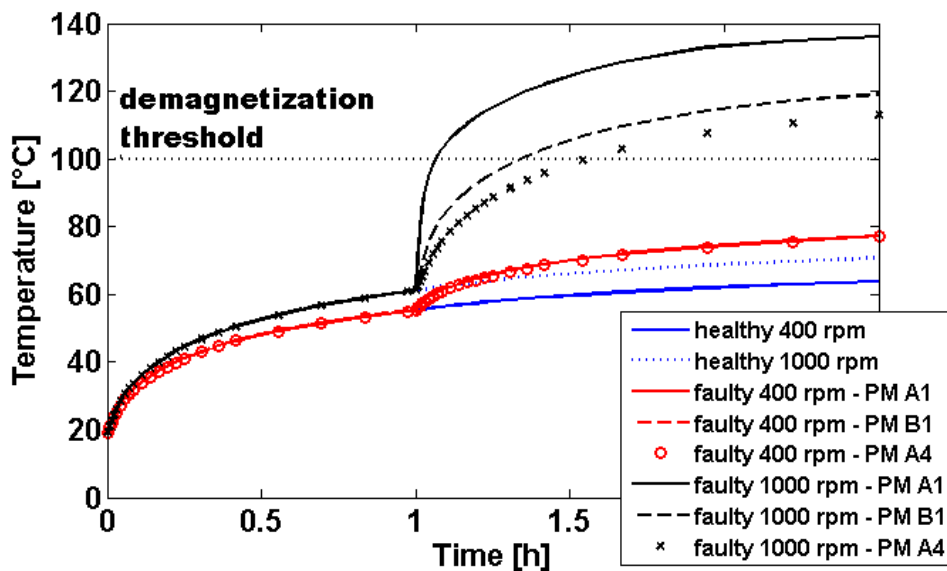


Fig. 5.14. PM temperature evolution before and after inter-turn short-circuit.

The previous results can be further analysed to assess the influence of the short-circuit current alone on the PM temperature rise. This can be done by applying the superposition principle, which is feasible because the coefficients (thermal conductivity and heat capacity) used in the thermal model are linear. The heat source effects can be then separated for regions of interest like the PMs. Two cases are possible considering the heating sources due to winding currents. The first case assumes all coils act as heating sources and are included in the thermal model, which is exactly the same as previous analyses. The second case, however, assumes that the heating source is only due to the short-circuit current in the short-circuited coil and the other coils are open-circuited. Similar to the previous section, the effects of both

low and high speeds are considered. The following relation is used to determine the relative temperature rise in PMs or windings during the faulty operation:

$$\Delta T[\%] = \frac{T_{faulty} - T_{healthy}}{T_{healthy} - T_{init}} \cdot 100 \quad (5.6)$$

where ΔT is the temperature rise (in %) due to fault mode. $T_{healthy}$ is the temperature achieved during the steady state (2.5 hours) in healthy mode. T_{faulty} is the the steady state temperature in faulty mode. Finally, T_{init} is the initial temperature. Table 5.3 summarizes the relative temperature increase during faulty mode based on (5.6) for the three representative PMs.

TABLE 5.3
TEMPERATURE RISE IN FAULTY MODE*

Region	all coils**	all coils**	coil A1***	coil A1***
	400 rpm	1000 rpm	400 rpm	1000 rpm
PM A1	29.9 %	127.2 %	24.4 %	104.7 %
PM B1	29.9 %	94.2 %	15.1 %	60.8 %
PM A4	29.9 %	82.1 %	11.8 %	45.2 %

*with respect to the healthy case. **all coils are included. ***only the short-circuited coil is included.

Taking PM A1 as an example, the results in Table 5.3 can be interpreted as following. When introducing the fault, the resulting copper losses will produce an increase in temperature by 29.9% (400 rpm) and 127.2% (1000 rpm) with respect to the healthy case. Furthermore, Table 5.3 shows the important contribution of the short-circuit current alone to the PM A1 heating. For 400 rpm, the short-circuit current contribute $24.4\%/29.9\% = 81.6\%$ of PM A1 overheating, and the remaining coils being responsible for less than 20%. This is plausible as the PM A1 is contained in the coil A1. Similar reasoning can be applied for higher speed, showing a contribution of $104.7\%/127.2\% = 82.3\%$ of the short-circuit current to total overheating of the PM A1. Extending the analysis to the PM B1 shows $15.1\%/29.9\% = 50.5\%$ (400 rpm) and $60.8\%/94.2\% = 64.5\%$ (1000 rpm) contributions due to the short-circuit current in the coil A1. Therefore, there is an important heat flow path from the affected coil (A1) to the adjacent ones during fault conditions.

Separating the heating sources and evaluating the temperature rise due to fault occurrence is possible

in the thermal model due to heat equation having constant coefficients with temperature. There is also the option of assessing the influence of the temperature on quantities from the electro-mechanical model. For example, in Fig. 5.15 the envelope of the current in the affected coil is represented over the entire duration of the study (1000 rpm case). For the healthy operation there is virtually no change with temperature, because the control strategy will compensate any reduction in performance due to temperature. After introducing the short-circuit at 1 hour mark, it can be seen for the rest of the study that the short-circuit current start decreasing (peak to peak value) albeit slowly. This can be explained based on several factors. First, the quantities in the electromechanical model are updated based on the average value of the temperature over a region of interest. For example, given the affected coil A1, its resistance in the Simulink model will be updated based on the averaged value of the temperature in the coil A1. At the time of the fault introduction, the machine has already operated for an hour and the temperature distribution is given in Fig. 5.7 (a) and (c). Second, given the high speed value (1000 rpm), the short-circuit current is still limited by the inductive reactance. Finally, there is still a magnetic coupling between the affected coil and the rest of the machine.

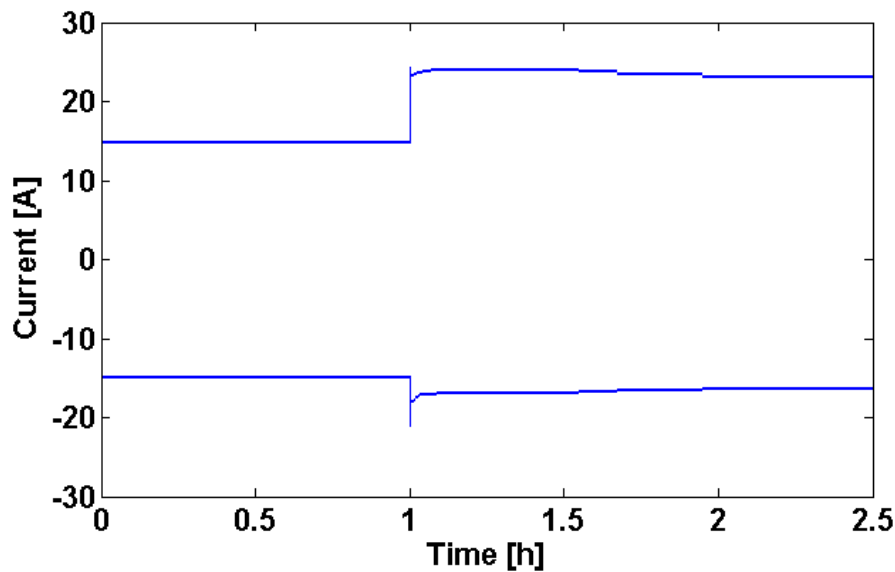


Fig. 5.15. Current envelope in the affected coil (A1) at 1000 rpm

5.4. EXPERIMENTAL VALIDATION OF THERMAL MODEL

The prototype machine from section 2.5 was used in order to validate the combined electromagnetic-faulty-thermal models. However, when winding the prototype it was not possible to achieve the filling

factor of 0.4 due to the difficulty of winding process (straight stator slots which make retaining the copper turns difficult)– instead a filling factor of 0.35 was used for the prototype machine. This means that in order to achieve the same rated torque, a higher current density is needed. Therefore, the prototype has a lower thermal load capability, which needs to be taken into account in the following analyses.

In addition, the influence of the test rig was found to be too significant. The SFPMM prototype housing front plate is in direct contact with the test rig. For this reason, initial models were predicting a low increase in temperature inside the windings despite compromises being made for the slot filling factor. In Fig. 5.16 it is shown the influence of the test rig on winding temperature hotspot, using 3D thermal FE models. There is a large temperature difference (50°C) in having attached the test rig as a large heat flux is flowing from the SFPMM to test rig. The test rig provides a much larger cooling surface area, which can lead to significant overestimation of the thermal performance of the investigated machine. Limiting the heat flux flowing between the SFPMM machine and test rig will provide results which will show more precisely the thermal response of the machine.

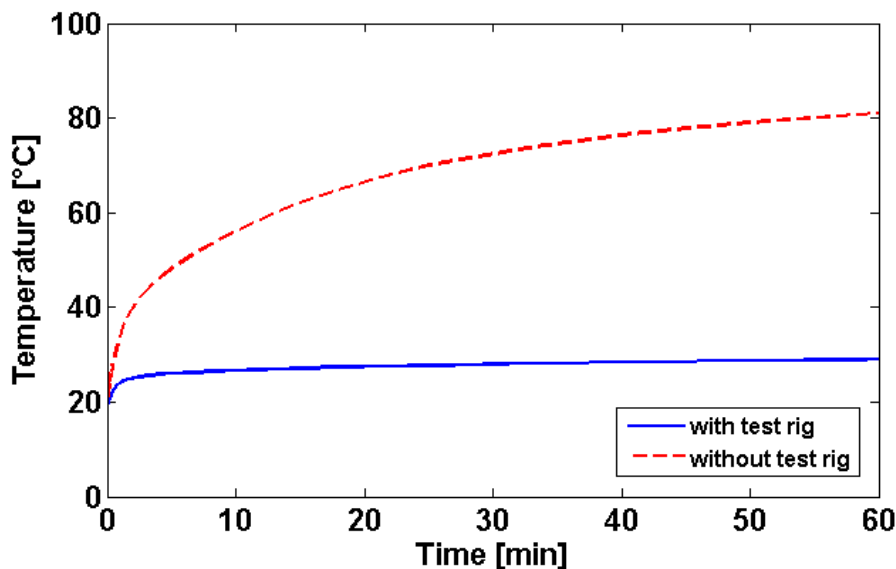


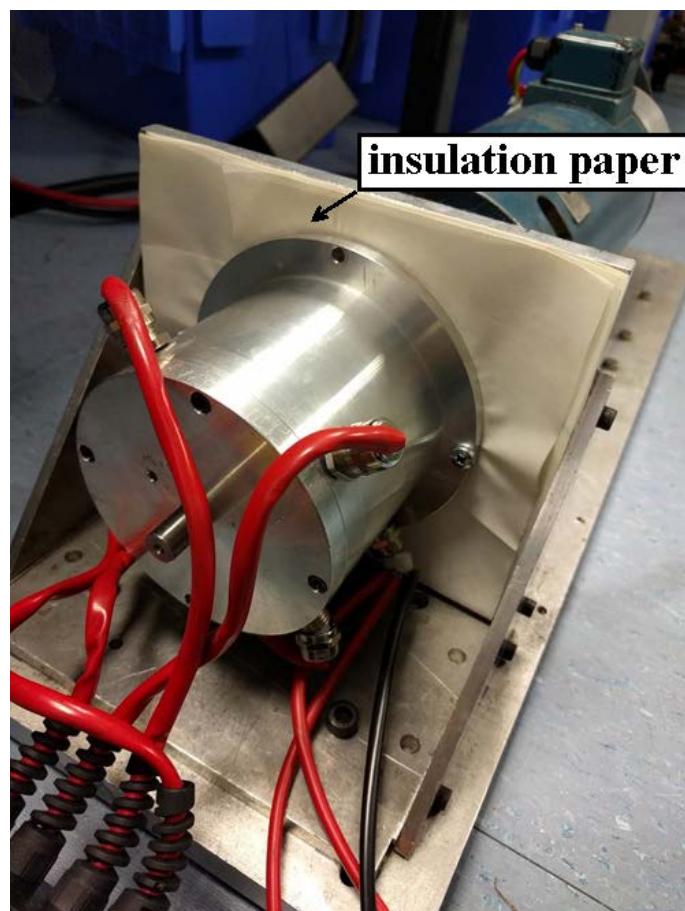
Fig. 5.16. Winding temperature with and without test rig influence (FE model, healthy case, 1000 rpm)

Therefore, several layers of insulation paper (totalling a 0.72 mm) were mounted between the prototype and the rig to limit the influence of the test rig (by reducing the heat flux flow between prototype and test rig). There are 7 thermocouples mounted in the machine (Fig. 5.13) – 3 on windings, 3 on PMs and one on the external surface of the housing. The machine works under speed control and the temperature is recorded during the dynamic operation. The control strategy is implemented using dSPACE. A DC

machine connected to a power resistor bank is used in generator mode as a mechanical load for the tested machine. After the machine is stopped, the temperature variation during the cooling down process is also recorded. In order to remove the noise induced in thermocouples due to the electromagnetic interference (EMI), a thermometer with low pass filter was used.



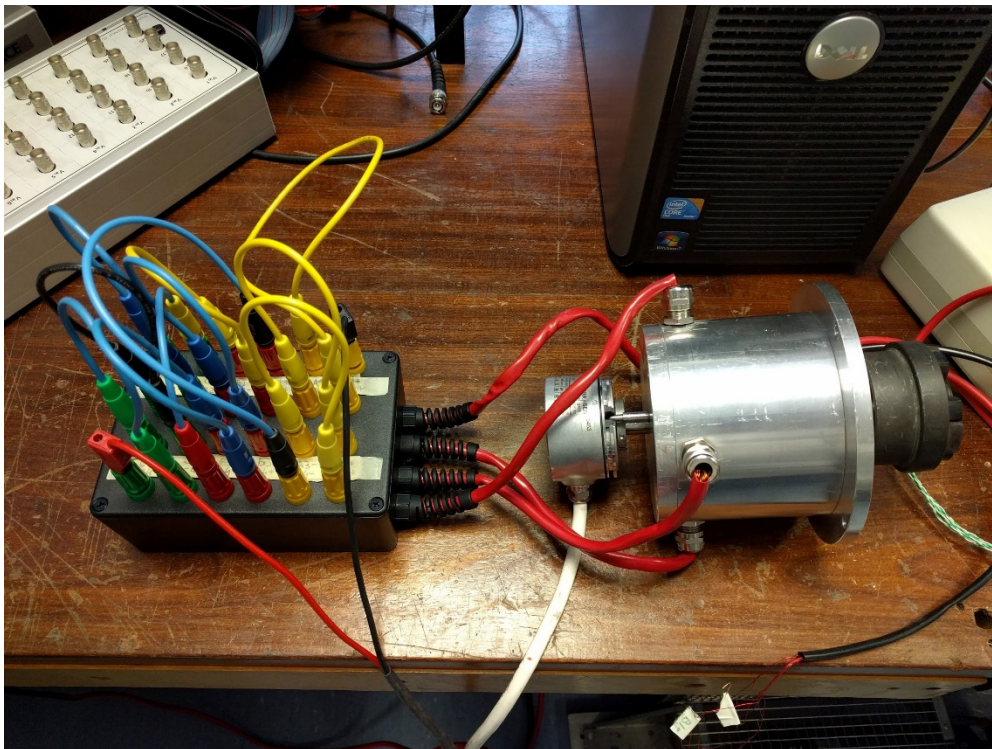
(a)



(b)



(c)



(d)

Fig. 5.17. Prototype of SFPMM with 12-slot/10-pole. (a) motor mounted on the test rig, (b) insulation paper detail, (c) power resistor bank, (d) assembled prototype with connection box, encoder and mechanical coupling.

The results for healthy case are given in Fig. 5.18. The test conditions are set at rated speed (400 rpm) and a mechanical load equal to 45% of the rated torque. This is necessary to prevent the potential damage due to overheating during the tests. Since the fault is not introduced, the imbalance does not exist, as expected. Therefore, only the temperature variations at three representative locations (coils A1, PM1 and the case) are shown. After two hours in the experiment, the machine operation is stopped. Since the heating sources are not present anymore, the cooling process begins. This is also recorded and compared against the predicted results. The predictions correlate well with the experiment measurements since the discrepancy between the predicted and measured results is within 5%.

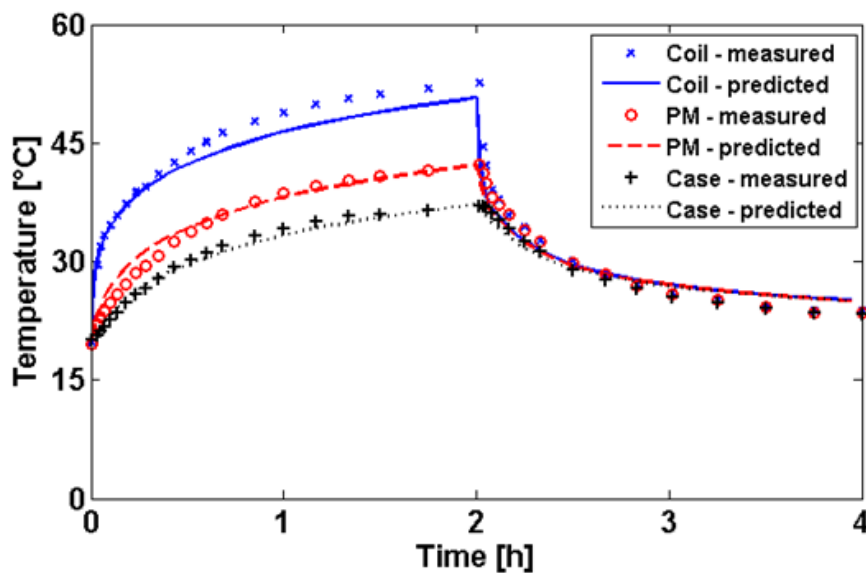
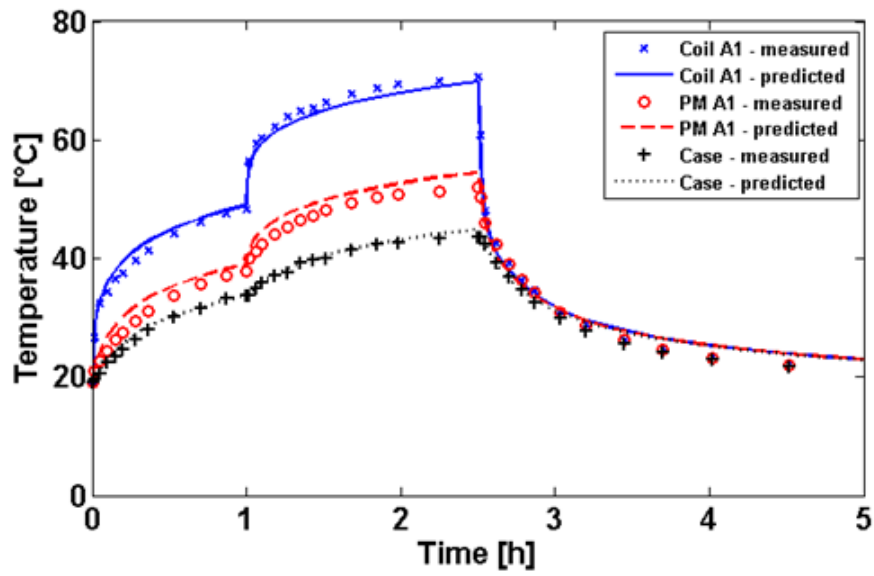
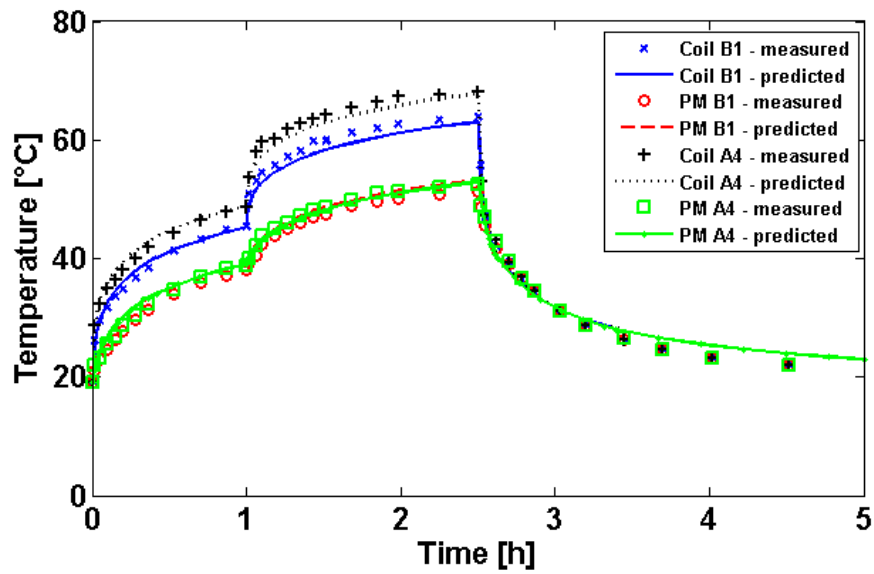


Fig. 5.18. Temperature variation in healthy case (400 rpm).

For the faulty case, the same conditions are maintained. The machine works under healthy conditions for one hour then the fault is introduced. The machine operates under fault conditions for about hour and a half afterwards. Between the interval 1 hour and 2 hours and a half from the beginning of the experiment, it can be seen a noticeable increase in the temperature. This is due to the short-circuit current but also due to the control strategy that increases the currents in the remaining healthy phases to compensate the influence of the short-circuit. Just like in the previous case, the cooling process is recorded and compared with predicted data.



(a)



(b)

Fig. 5.19. Temperature variation in faulty mode. (a) coil A1, PM1, Case, (b) Coils B1 and A4, PM inside B1 and A4.

5.5. CONCLUSIONS

A highly accurate multi-physics (electromechanical- thermal-faulty) model for a SFPMM is proposed in this chapter, which can take into account the temperature influence during dynamic operation in either healthy or faulty mode. It optimizes the required simulation time and computation resources by implementing the electromechanical part using less demanding Matlab/Simulink models coupled in a bidirectional manner with a 3D FE thermal model. It also allows to include temperature dependent characteristics of various parameters such as back-EMF, cogging torque and phase resistance.

The introduction of the fault such as inter-turn short-circuit affects all the PMs. The PM irreversible demagnetization happens due to the increase in temperature. In addition, since there is little thermal separation between the coils, the heat generated by the inter-turn short-circuit in one coil can easily spread to other phases causing them to be overheated. The influence of the short-circuit current on temperature rise is quantitatively analysed, based on the superposition principle. The time needed for the PM to be demagnetized under the inter-turn short-circuit can be assessed. Based on these conclusions, possible improvements such as the forced convection in the end-winding regions or better overall external cooling might need to be taken into account during design phase for the SFPMM. Further studies concern various fault severities and comparisons with modular SFPMM like C-Core and E-Core topologies are necessary. These modular machine topologies might provide extra fault tolerant capability due to physical, electromagnetic and thermal separation between phases.

The hotspots occur in the windings due to its poor radial heat flow. Possible improvements include impregnating the coils or achieving a better slot fill factor. The cooling process is predominantly radial since the heat flows from the inner part of the machine to the outside. Better materials (insulation) can be used to facilitate this, for example a slot liner with high thermal conductivity. A design strategy can be employed in which the heat removal paths are optimized with proper materials to reduce the hotspots value and efficiently cool the machine.

Chapter 6. Conclusions and Future Work

6.1. SUMMARY OF STUDIED CONFIGURATIONS

A summary of performance and fault tolerant capability for SFPMM, its derivatives as well as DSPMM and FRPMM is given in Table 6.1. All topologies have a 10 poles rotor with the exception of DSPMM which has 8 poles. The number of turns and coil area (and therefore copper losses) are also the same for all machines. The machines diameter as well as the lamination stack length are the same.

TABLE 6.1

COMPARISON OF INVESTIGATED TOPOLOGIES

	SFPMM	C-Core*	E-Core*	Modular*	DSPMM	FRPMM
Phase separation	no	no	yes	yes	no	no
Rated torque [Nm]	2.2	1.5	2.0	1.8	1.0	1.6
Torque/PM [kNm/mm ³]	0.12	0.16	0.22	0.20	0.267	0.275
PM volume [mm ³]	18360	9180	9180	9180	3750	5460
Demagnetization threshold [°C]	< 100	< 100	< 100	> 100	> 100	< 100

*Dimensions as given in Chapter 4.

6.2. CONCLUSIONS

In this investigation, the stator mounted PM machines have been studied under fault conditions. The fault conditions considered are inter-turn short-circuit and irreversible demagnetization. Conditions like high speed and temperature dependence have also been considered. Appropriate models have been developed to account for temperature dependence with various degrees of complexity.

It is found out that, in these topologies, the short-circuit current plays a negligible role in the irreversible demagnetization process. However, the magnetic circuit configuration and temperature rise are the main causes of demagnetization. Studies in chapters 2, 3 and 4 have used both low and high speed faults which lead to lower and higher peak short-circuit currents in the affected coil. In addition, frozen

permeability method has been employed to separate the effects of the current sources from the PM in the computation domain. The result is that for SFPMM and its derivatives, the demagnetizing MMF generated by short-circuit current is deflected by the two iron segments shielding the PM. For the FRPMM the demagnetizing MMF will simply be redirected towards the adjacent PM, the flux path of which is in series with the demagnetizing MMF. For the DSPMM, again the magnetic circuit structure provides alternative ways for the demagnetizing short-circuit MMF to be redirected. The conventional SFPMM stands out from this point of view due to the fact that it has the highest PM volume and it is the most affected by demagnetization. Because of this, the PMs are influencing each other, acting as demagnetizing forces and pushing the operating point down on the B(H) demagnetization curve. Other machines evolved from the SFPMM, such as the E-Core and Modular SFPMMs exhibit two features which makes them better fault tolerant alternatives. First, their stator volume is less occupied with PMs. As a result, the neighbouring PMs don't influence each other as much. Second, they have magnetic phase separation which again helps redirecting the demagnetizing MMF. The outcome of this is that at low temperature, even under high short-circuit currents (high speeds), the studied topologies will not suffer from demagnetization.

A hierarchy in terms of fault tolerant features between the conventional double layer SFPMM, the DSPMM and the FRPMM is established. The conventional double layer SFPMM is at the bottom, i.e. the easiest topology to be irreversibly demagnetized. The double layer configuration also generates a high short-circuit current and has no magnetic separation between the phases. However, the short-circuit current peak value is reduced for the other two double layer topologies in the study such as the DSPMM and the FRPMM. Albeit they also lack magnetic phase separation, they do have a lower PM volume as well as distinctive magnetic circuit configurations which allow them to have better fault tolerant capabilities. They also can withstand demagnetization better when compared with the conventional SFPMM.

Since the SFPMM has the lowest potential for a fault tolerant solution, a complex multi-physics model has been developed in Chapter 5 to accurately predict its thermal performance under different operation conditions including the fault operation. This is to assess the thermal state evolution in the critical parts like PMs or windings. The model is a coupling between a dynamic model implemented in Simulink (electro-mechanical) and a 3D finite element transient one (thermal). It overcomes the issues of lengthy solving process imposed by the required small time in the electromechanical domain. Using this model, it is found that, for 1000 rpm operating speed and under inter-turn short-circuit of one coil, both the PMs and windings can reach temperatures exceeding the demagnetization threshold and insulation temperature class, respectively.

When it comes to performance of the SFPMMs, the conventional double layer winding topology is the best since it has the largest PM volume. However, it would have the highest material cost of all studied machines as well. If a fault tolerant solution is required, with some acceptable penalty on the output torque, then the modular machine is a good candidate. If there are cost constraints, then the DSPMM exhibits a good potential due to its excellent torque/PM volume ratio, demagnetization capability and low short-circuit current.

6.3. FUTURE WORK

Potential directions for developing this work further are:

- Electromagnetic compatibility for SFPMM machines. This topologies have PMs extending to the edge of the machine and generating a strong leakage field. A strong magnetic field in its proximity can affect the equipment around. This raises issues like incompatibility with EMI (ElectroMagnetic Interference) standards in many applications. The presence of this leakage field has also potential to be used in a fault detection method;
- A future direction would be to optimize the heat flow path. The outcome can be lower hotspots in the windings. The current investigation focuses on thermal analysis and temperature rise in the machine. However, there is potential for optimal design, either by using more suitable materials or modifying the geometry to improve the machine thermal resilience. The model in Chapter 5 is a step forward in this direction as it allows both the electro-mechanical and thermal models to be simulated in the same time. Traditionally, the thermal design is performed after the electro-mechanical one;
- Studying the multi-physics model from Chapter 5 with forced radial cooling (water jacket). This would be relevant to follow due to particular structural features of the investigated machines. The PMs and windings are located in the stator and close to its outer diameter. This simplifies the cooling process and allows the volume reduction of the topologies involved;
- Applying the multi-physics model from Chapter 5 to E-Core, DSPMM and FRPMM. Currently, the model was only applied to conventional SFPMM. However, it would be interesting to evaluate for E-Core for example how the magnetless tooth affects the heat transfer from the affected coil to its adjacent ones. The DSPMM and FRPMM share similar challenges with the SFPMM but they also add some other challenges. The DSPMM's PM for example is also much closer to the windings (heat source), and hence might be more easily influenced by winding overheating;

- Comparing the current studied topologies with their multi-phase and also redundant versions. These machines open the door for several improvements including running on a single set of windings (3-phase) when fault occurred. Having more phases also helps with control during fault conditions since it provides more coils to control and compensate for fault effects;
- Comparing the current studied topologies with their hybrid excitation counterparts. The hybrid excitation machines add an extra DC winding to regulate (weaken or enhance) the flux. The flux weakening feature can also be utilized to reduce the short-circuit current in the armature windings, and hence prevent them from overheating. However, the extra DC current will generate heat as well, which could increase the overall machine temperature, leading to magnet irreversible demagnetization. All these phenomena will consist of our future research works.

Appendix

A.1. DYNAMIC ELECTRO-MECHANICAL MODEL

The dynamic electro-mechanical model implemented in Matlab/Simulink is based on [28], [124], [125], [126], [127], [148] and can be used for both the healthy and faulty operations:

$$[v] = [R] \cdot [i] + \frac{d([L] \cdot [i])}{dt} + [e_0] \quad (\text{A.1})$$

where $[v]$, $[i]$ and $[e_0]$ are the phase voltage, phase current and back-EMF vectors which can be further represented in their expanded form:

$$[v] = \begin{bmatrix} v_h \\ v_b \\ v_c \\ v_f \end{bmatrix}, [i] = \begin{bmatrix} i_h \\ i_b \\ i_c \\ i_f \end{bmatrix}, [e_0] = \begin{bmatrix} e_h \\ e_b \\ e_c \\ e_f \end{bmatrix} \quad (\text{A.2})$$

The h and f indices stands for healthy and faulty components of the affected phase A while b and c identify the remaining healthy phases B and C, respectively. The back-EMF $[e_0]$ is temperature dependent. Furthermore, introducing the ratio of affected turns $\alpha = N_f/N_{ph}$ the healthy and faulty components of back-EMF vector can be written as $e_h = (1 - \alpha)e_a$ and $e_f = \alpha e_a$.

The $[R]$ quantity is the matrix of the phase resistances, it is temperature dependent and it can be further expressed by:

$$[R] = \begin{bmatrix} R_h & 0 & 0 & 0 \\ 0 & R & 0 & 0 \\ 0 & 0 & R & 0 \\ 0 & 0 & 0 & R_f \end{bmatrix} \quad (\text{A.3})$$

The previously introduced ratio α can be used again in order to express the healthy and faulty components of the affected phase resistances, such as $R_h = (1 - \alpha)R$ and $R_f = \alpha R$ where R is the phase resistance.

The $[L]$ quantity contains the self- and mutual- inductances and is given by:

$$[L(\theta_e)] = \begin{bmatrix} L_h & M_{Bh} & M_{Ch} & M_{fh} \\ M_{hB} & L_B & M_{CB} & M_{fB} \\ M_{hC} & M_{BC} & L_C & M_{fC} \\ M_{hf} & M_{Bf} & M_{Cf} & L_f \end{bmatrix} \quad (\text{A.4})$$

where h and f are subscripts again referring to the phase A only. L_h is the self-inductance of the healthy part of the phase A and M_{Bh} is the mutual inductance resulting from the flux linkage through the phase B due to the current in the healthy part of phase A. The main diagonal of $[L]$ represent self-inductances characterizing each phase, as well as the faulty part, while the rest of the terms represent mutual inductances. The location and distribution of each term from the inductance matrix is given in Fig. A.. All terms are determined using finite element models as rotor position dependent. The derivative of the $[L][i]$ product in (A.1) is developed further in the Simulink model using the chain rule method as both the inductance and current are rotor position dependent.

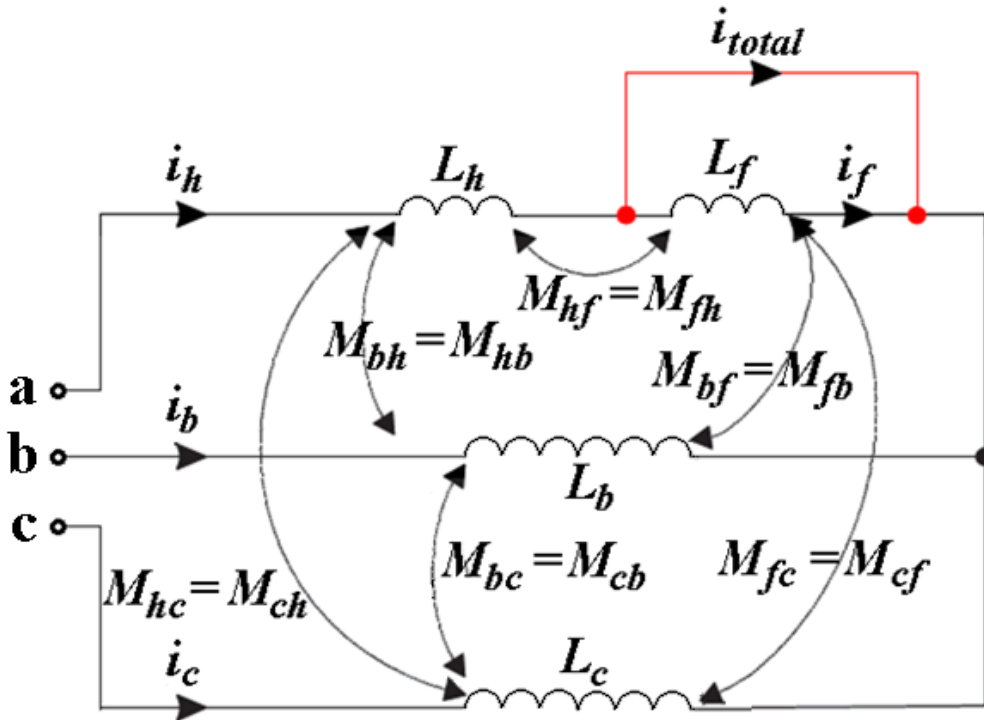


Fig. A.1. Self and mutual inductances between various phases when inter-turn short-circuit fault within one phase occurs [84]. i_h is the healthy current, i_f is the short-circuit current and i_{total} is the resultant current of the phase A.

The mechanical model is described by:

$$T_{em} + T_{cogg} + T_{reluct} = p \cdot [\Phi_0]^t \cdot [i] = J \cdot \frac{d\Omega}{dt} + f \cdot \Omega + T_{load} \quad (A.5)$$

where $p = 10$ is pole pair number, T_{em} is electromagnetic torque, T_{cogg} is the cogging torque and T_{reluct} is the reluctance torque. T_{load} is the torque imposed by the load. In the model, the cogging torque is considered as temperature dependent. The quantity $[\Phi_0]$ represents the open circuit flux linkages which can be obtained through derivation from the back-EMF $[e_0]$:

$$[e_0] = \frac{d[\Phi_0]}{dt} = p \cdot \Omega \cdot \frac{d\Phi_0}{d\theta_e} \quad (A.6)$$

For the SFPMMs, their average reluctance torques are negligible under healthy conditions but can play a non-negligible role during short-circuit operations [149]. The reluctance torque has been implemented in the Simulink model using the following relation:

$$T_{reluct} = \frac{1}{2} \cdot \sum_k^{h,f,b,c} \frac{dL_k}{d\theta} \cdot i_k^2 + \sum_{k,j;k \neq j}^{h,f,b,c} \frac{dM_{k,j}}{d\theta} \cdot i_k \cdot i_j \quad (A.7)$$

where θ represents the rotor position.

A.2. CONTROL DIAGRAM

The objective of the control strategy is to maintain the same speed and also the same average torque after the fault was introduced. The Maximum Torque per Ampere (MTPA) control is used and the simplified schematic of the model is depicted in Fig. A.2.

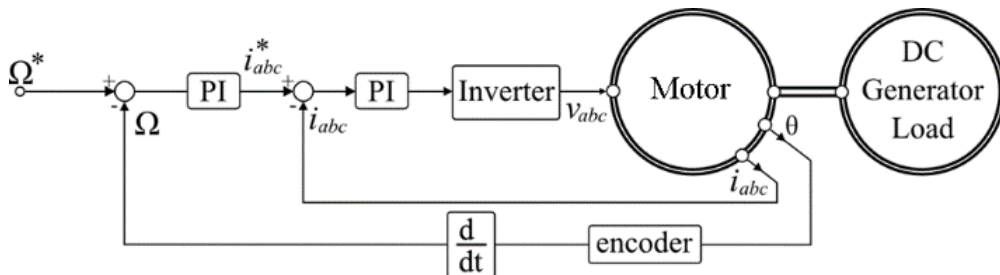


Fig. A.2 Simplified diagram of the Matlab/Simulink model.

A.3. IRON LOSSES AND PERMANENT MAGNET EDDY CURRENT LOSS

The iron losses and permanent magnet eddy current loss are calculated using 2D finite element models [150]. Their variation with speed is also considered. The iron losses are calculated on the stator and rotor regions as spatial power density distributions. They consist of hysteresis (p_h) and eddy current losses (p_{eddy}) and are given by the formula:

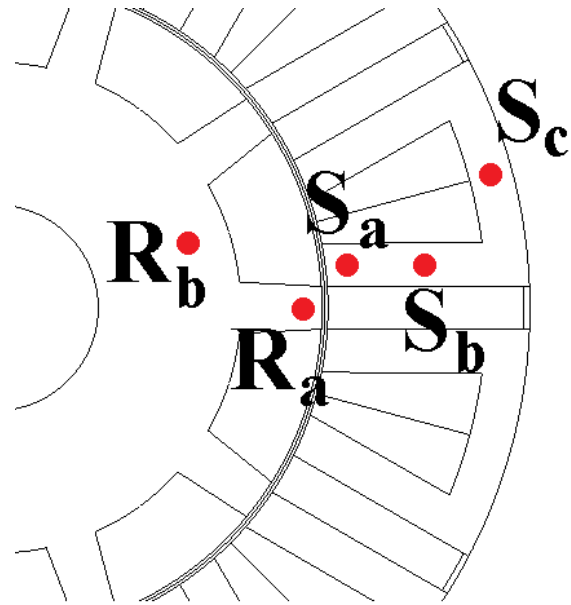
$$p_{iron} = p_{eddy} + p_h = f k_{eddy} \int_0^{\frac{1}{f}} \left(\frac{dB}{dt}(t) \right)^2 dt + f (k_{h1} \Delta B_{pp} + k_{h2} \Delta B_{pp}^2) \quad (\text{A.8})$$

which is an improvement on the Steinmetz's classic iron loss model. The losses are highly dependent on the flux density variation B (ΔB_{pp} is the local peak to peak value) and frequency f . The coefficients k_{h1} (= 5A/m) and k_{h2} (= 40A/m) are experimentally determined. The k_{eddy} coefficient has a 0.022 Am/V value and can be determined considering the expression:

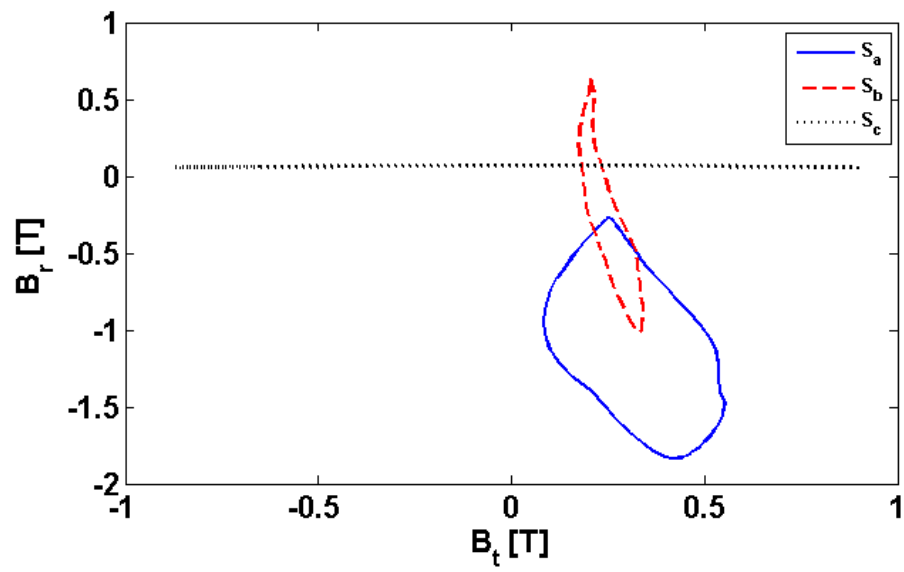
$$k_{eddy} = \frac{\sigma \cdot d^2}{12} \quad (\text{A.9})$$

where 2173900 S/m for the electrical conductivity σ and 0.35 mm for the lamination sheet thickness d are adopted.

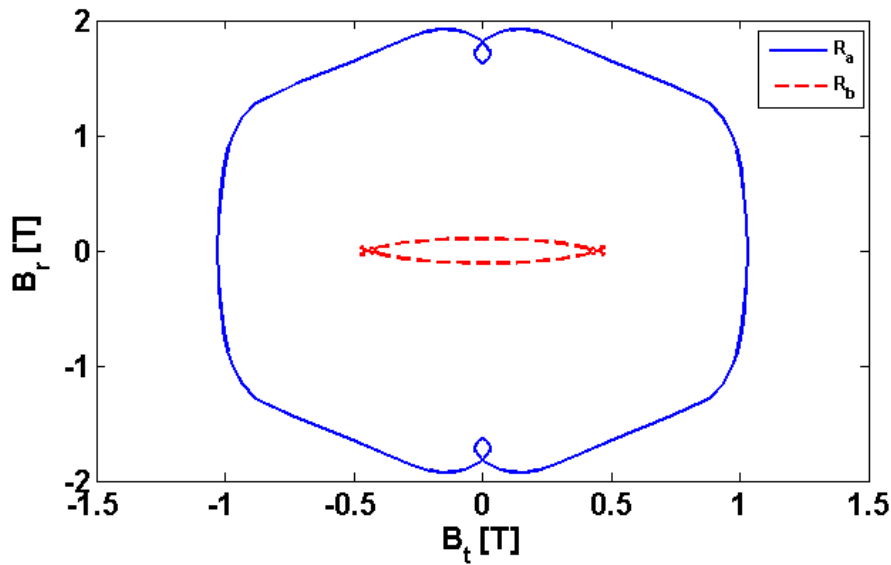
In order to correctly account for the frequency f , the flux density variation has been represented in both rotor and stator points, Fig. A.3 (a). It was found out that in the rotor the flux density variation frequency is 1.667 higher than in the stator and this was considered in the iron loss computation accordingly. In addition, the flux density loci was plotted for the considered points in the stator and rotor, Fig. A.3 (b) and (c). Based on this information, it can be seen that the highest value of the local iron losses occurs in rotor teeth due to both a large variation of the flux density (both radial and circumferential components) and higher frequency. In fact, this is validated according to Fig. 5.4. where the rotor losses are higher than the stator ones. The stator points, S_a , S_b and S_c show some interesting characteristics. In the point S_a for example, due to its close proximity to the magnet, the flux lines have an imposed direction consistent with the magnet orientation. This explains why both B_r and B_t do not change sign over an electric cycle. For S_b and S_c the flux switching effect can be noticed, especially for S_c for which only the circumferential component is present.



(a)



(b)



(c)

Fig. A.3 Flux density local variation in points in stator and rotor. (a) stator and rotor points location. (b) loci for stator flux density, (c) loci for rotor flux density.

For the permanent magnet the eddy losses are calculated as speed dependent. The magnet regions in the computation domain are set as solid conductor types with a resistivity of $1.8e-5 \Omega\text{m}$ [106].

A.4. THERMAL MODEL

The thermal model considerations and limitations as implemented by the finite element package (Flux 3D) is given next.

$$\gamma c_p \frac{\partial T}{\partial t} = k \nabla^2 T + p \quad (\text{A.10})$$

where γ is the mass density of the material, c_p is the specific heat capacity, k is the thermal conductivity and p is the heat source. For the thermal model γ , c_p and k are not temperature dependent. The heat source p however is considered as changing with the temperature as it depends on several factors. The heat source p is a power density distribution given by the sum:

$$p = p_{iron} + p_{PM} + p_{copper} \quad (A.11)$$

where p_{iron} , p_{PM} and p_{copper} are the iron, permanent magnet (eddy losses) and copper losses. The copper losses depend on temperature since the phase resistance changes with temperature. The iron and PM losses depend on speed only. This simplification is introduced because the copper losses are the dominant losses for the speed interval of study for both healthy and faulty cases. For healthy operation, the copper losses increase to 76W which is about 40% more than all the other heat sources combined even at the maximum speed in the study (3000 rpm Fig. 5.4). During the fault, the copper losses will increase by tenfold. This is due to the fact that the control strategy need to compensate any performance drop in the average torque. Therefore in order to maintain or increase the speed, the phase currents must increase and hence the temperature will rise accordingly.

(A.10) requires boundary and initial conditions which is equal to specifying the convection and radiation conditions on various boundary surfaces in the model. The boundary surfaces can be the outer surface of the housing, end windings' surfaces, etc.

$$p_{out} = \alpha_c \cdot (T - T_{amb}) + \epsilon \cdot \sigma \cdot (T^4 - T_{amb}^4) \quad (A.12)$$

with $T_{init} = constant$

where p_{out} is the heat flux exchanged through the surface on which the boundary condition is imposed, α_c is the convection coefficient, T_{amb} is the ambient temperature, ϵ is the surface emissivity and σ is the Stefan-Boltzmann constant ($5.67e-8 \text{ W/m}^2/\text{K}^4$). The first term in the p_{out} describes the heat flux exchanged through convection process while the second one is the heat flux exchanged due to radiation. T_{init} is the initial temperature.

References

- [1] B. Sarlioglu and C. T. Morris, "More Electric Aircraft: Review, Challenges, and Opportunities for Commercial Transport Aircraft," *IEEE Trans. Transport. Electrification*, vol. 1, no. 1, pp. 54 - 64, 2015.
- [2] S. E. Rauch and L. J. Johnson, "Design principles of flux-switch alternators," *Power apparatus and systems, part III, Transactions of the American Institute for Electrical Engineers*, vol. 74, no. 3, 1955.
- [3] Z. Q. Zhu, Y. Pang, D. Howe, S. Iwasaki, R. Deodhar and A. Pride, "Analysis of electromagnetic performance of flux-switching permanent-magnet machines by nonlinear adaptive lumped parameter magnetic circuit model," *IEEE Trans. Magn.*, vol. 41, no. 11, pp. 4277 - 4287, Nov. 2005.
- [4] W. Hua, M. Cheng and G. Zhang, "A novel hybrid excitation flux-switching motor for hybrid vehicles," *IEEE Trans. Magn.*, vol. 45, no. 10, pp. 4728-4731, 2009.
- [5] C. Ditmanson, P. Hein, S. Kolb, J. Molck and S. Bernet, "A new modular flux-switching permanent-magnet drive for large wind turbines".
- [6] C. Pollock and M. Wallace, "The flux switching motor, a DC Motor without magnets or brushes," in *IEEE Industry Applications Conference*, 1999.
- [7] Z. Q. Zhu, "Switched flux permanent magnet machines - innovation continues," in *Proc. ICEMS*, Beijing, China, 20 -23 August 2011.
- [8] E. Hoang, A. H. Ben-Ahmed and J. Lucidarme, "Switching flux permanent magnet polyphased synchronous machines," in *Proc. 7th Eur. Conf. Power Electronics and Applications*, 1997.
- [9] Y. Li, S. Li, Y. Yang and B. Sarlioglu, "Analysis of flux switching permanent magnet machine design for high-speed applications," in *ECCE 2014*, Pittsburgh, PA, 2014.
- [10] J. D. McFarland, T. M. Jahns and A. M. EL-Refaie, "Analysis of the torque production mechanism for flux-switching permanent magnet machines," in *Proc. ECCE*, Pittsburgh, USA, 14 - 18 September 2014.
- [11] F. Liao, F. Liang and T. A. Lipo, "A novel permanent magnet machine with doubly saliency structure," *IEEE Trans. Ind. Appl.*, pp. 1069-1078, 1995.
- [12] R. P. Deodhar, S. Andersson, I. Boldea and T. J. E. Miller, "The flux-reversal machine: a new brushless doubly-salient permanent-magnet machine," *IEEE Trans. Ind. Appl.*, vol. 33, no. 4, pp. 925-934, 1997.
- [13] T. H. Kim and J. Lee, "A study of design for the flux reversal machine," *IEEE Trans. on Magn.*, vol. 10, no. 4, pp. 2053-2055, 2004.
- [14] C. Wang, S. A. Nasar and I. Boldea, "Three-phase flux reversal machine (FRM)," *Electric Power Applications, IEE Proceedings*, vol. 146, no. 2, pp. 139-146, 1999.
- [15] H. K. Kim, J. Hur, B. W. Kim and G. H. Kang, "Characteristic analysis of IPM type BLDC motor considering the demagnetization of PM by stator turn fault," in *ECCE 2010*, Atlanta, SUA, 2010.
- [16] K. T. Kim, Y. S. Lee and J. Hur, "Transient analysis of irreversible demagnetization of permanent magnet brushless DC motor with stator turn fault under the operating state," *IEEE Trans. Ind. Appl.*, vol. 50, no. 5, pp. 3357-3364, Sept.-Oct. 2014.

- [17] Zhou P., D. Lin, Y. Xiao, N. Lambert and M. A. Rahman, "Temperature-Dependent Demagnetization Model of Permanent Magnets for Finite Element Analysis," *IEEE Trans. Magn.*, vol. 48, pp. 1031-1034, 2012.
- [18] S. Li, Y. Li and B. Sarlioglu, "Partial irreversible demagnetization assessment of flux switching permanent magnet machine using ferrite permanent magnet material," *IEEE Trans. Magn.*, vol. 51, no. 7, pp. 1-9, July 2015.
- [19] V. I. Patel, J. Wang and S. S. Nair, "Demagnetization assessment of fractional-slot and distributed wound 6-phase permanent magnet machines," *IEEE Trans. Magn.*, vol. 51, no. 6, 2015.
- [20] Z. Q. Zhu and D. Howe, "Electrical machines and drives for electric, hybrid, and fuel cell vehicles," *Proc. IEEE*, vol. 95, no. 4, pp. 746-765, April 2007.
- [21] W. Hua, M. Cheng, Z. Q. Zhu and D. Howe, "Analysis and optimization of back EMF waveform of a flux-switching permanent magnet motor," *IEEE Trans. Energy Convers.*, vol. 23, no. 3, pp. 727-733, 2008.
- [22] Z. Q. Zhu and J. T. Chen, "Advanced flux-switching permanent magnet brushless machines," *IEEE Trans. Magn.*, vol. 46, no. 6, pp. 1447-1453, June 2010.
- [23] J. Zhang, M. Cheng, Z. Chen and W. Hua, "Comparison of stator-mounted permanent-magnet machines based on a general power equation," *IEEE Trans. on Energy. Conv.*, vol. 24, no. 4, pp. 826-834, 2009.
- [24] W. Hua, M. Cheng, H. Jia and X. Fu, "Comparative Study of Flux-Switching and Doubly-Salient PM Machines Particularly on Torque Capability," in *Proc. of IAS08*, Edmonton, Canada, 2008.
- [25] M. Cheng, W. Hua, J. Zhang and W. Zhao, "Overview of Stator-Permanent Magnet brushless machines," *IEEE Trans. Ind. Electron.*, vol. 58, no. 11, pp. 5087-5101, Nov. 2011.
- [26] C.-C. Hwang, C.-M. Chang, S.-S. Hung and C.-T. Liu, "Design of High Performance Flux Switching PM Machines with Concentrated Windings," *IEEE Trans. Magn.*, vol. 50, no. 1, Jan. 2014.
- [27] J. T. Chen and Z. Q. Zhu, "Winding Configurations and Optimal Stator and Rotor Pole Combination of Flux-Switching PM Brushless AC Machines," *IEEE Trans. Energy. Convers.*, vol. 25, no. 2, pp. 293 - 302, June 2010.
- [28] G. J. Li, J. Ojeda, E. Hoang and M. Gabsi, "Double and single layers flux-switching permanent magnet motors: Fault tolerant model for critical applications," in *ICEMS*, Beijing, 2011.
- [29] J. T. Chen, Z. Q. Zhu, S. Iwasaki and R. Deodhar, "A novel E-core flux-switching PM brushless AC machine," in *IEEE Energy Conversion Congress and Exposition*, 2010.
- [30] W. Min, J. T. Chen, Z. Q. Zhu, Y. Zhu, M. Zhang and G. H. Duan, "Optimization and comparison of novel E-core and C-core linear switched flux PM machines," *IEEE Trans. Magn.*, vol. 47, no. 8, pp. 2134-2141, 2011.
- [31] Z. Q. Zhu, M. M. J. Al-Ani, X. Liu, M. Hasegawa, A. Pride and R. Deodhar, "Comparative study of torque-speed characteristics of alternate switched-flux permanent magnet machine topologies," in *PEMD 2012*, Bristol UK, 2012.
- [32] G. Li, S. Hloui, J. Ojeda, E. Hoang, M. Lecrivain, M. Gabsi and Z. Q. Zhu, "Excitation winding short-circuits in hybrid excitation permanent magnet motor," *IEEE Trans. Energy Convers.*, vol. X, 2014.
- [33] H. Pollock, C. Pollock, R. T. Walter and B. V. Gorti, "Low cost, high power density, flux-switching machines and drives for power tools," *IEEE Ind. Appl. Soc. Annu. Meeting*, vol. 3, pp. 1451-1457, 2003.
- [34] R. L. Owen, "Hybrid excited flux-switching permanent magnet machines," in *EPE 2009*,

- Barcelona, Spain, 2009.
- [35] W. Hua, G. Zhang and M. Cheng, "Flux-regulation theories and principles of hybrid-excited flux-switching machines," *IEEE Trans. on Ind. Electron.*, vol. PP, no. 99, 2015.
- [36] B. Zhang, R. Qu, X. Fan and J. Wang, "Thermal and Mechanical Optimization of Water Jacket of Permanent Magnet Synchronous Machines for EV Application," in *IEMDC 2015*, Coeur d'Alene, ID, USA, 2015.
- [37] B. Gaussens, E. Hoang, M. Lecrivain, P. Manfe and M. Gabsi, "A new hybrid-excited flux-switching machine with excitation coils in stator slots," in *ICEMS 2012*, Sapporo, 2012.
- [38] G. Zhang, M. Cheng, W. Hua and J. Dong, "Analysis of the oversaturated effect in hybrid excited flux-switching machines," *IEEE Trans. Magn.*, vol. 47, no. 10, pp. 2827-2830, 2011.
- [39] W. Hua, G. Zhang, M. Cheng and X. Sun, "Comparison of flux-regulation capability of a hybrid-excited flux-switching machine with different magnet materials," in *CEFC 2010*, Chicago, 2010.
- [40] J. T. Chen, Z. Q. Zhu, S. Iwasaki and R. P. Deodhar, "A Novel Hybrid-Excited Switched-Flux Brushless AC Machine for EV/HEV Applications," *IEEE Trans. Veh. Technol.*, vol. 60, no. 4, pp. 1365 - 1373, 2011.
- [41] G. Zhang, W. Hua, M. Cheng and J. Liao, "Design and comparison of two six-phase hybrid-excited flux-switching machines for EV/HEV applications," *IEEE Trans. Ind. Electron.*, vol. 63, no. 1, pp. 481-493, Jan. 2016.
- [42] Z. Q. Zhu, J. T. Chen, D. Howe, S. Iwasaki and R. Deodhar, "Analysis of a Novel Multi-Tooth Flux-Switching PM Brushless AC Machine for High Torque Direct-Drive Applications," *IEEE Trans. Magn.*, vol. 44, no. 11, pp. 4313-4316, 2008.
- [43] Y. J. Zhou and Z. Q. Zhu, "Torque Density and Magnet Usage Efficiency Enhancement of Sandwiched Switched Flux Permanent Magnet Machines Using V-Shaped Magnets," *IEEE Trans. Magn.*, vol. 49, no. 7, pp. 3834-3837, 2013.
- [44] A. S. Thomas, Z. Q. Zhu and L. J. Wu, "Novel modular-rotor switched-flux permanent magnet machines," *IEEE Trans. Ind. Appl.*, vol. 48, no. 6, pp. 2249-2258, 2012.
- [45] W. Fei, P. C. Kwong Luk, D. M. Miao and J. X. Shen, "Investigation of torque characteristics in a novel permanent flux switching machine with an outer-rotor configuration," *IEEE Trans. Magn.*, vol. 50, no. 4, 2014.
- [46] Z. Q. Zhu, M. M. J. Al-Ani, X. Liu and B. Lee, "A mechanical flux weakening method for switched flux permanent magnet machines," *IEEE Trans. Energy Convers.*, 2014.
- [47] Z. Q. Zhu, M. M. J. Al-Ani, X. Liu, M. Hasegawa, A. Pride and R. Deodhar, "Comparison of flux weakening capability in alternative switched flux permanent magnet machines by mechanical adjusters," in *ICEM 2012*, Marseille, 2012.
- [48] R. P. Deodhar, A. Pride, S. Iwasaki and J. J. Bremner, "Performance improvement in flux-switching PM machines using flux diverters," *IEEE Trans. Ind. Appl.*, vol. 50, no. 2, pp. 973 - 978, 2014.
- [49] W. Hua, P. Su, G. Zhang and M. Cheng, "A novel rotor-permanent magnet flux-switching machine," in *EVER 2015*, Monte Carlo, 2015.
- [50] P. Su, W. Hua, G. Zhang and M. Cheng, "Investigation of a novel rotor permanent magnet flux switching machine for EV and HEV applications," in *INTERMAG 2015*, Beijing, China, 2015.
- [51] W. Zhang, M. Lin, D. Xu, X. Fu and L. Hao, "Novel fault-tolerant design of axial field flux-switching permanent magnet machine," *IEEE Trans. Appl. Supercond.*, vol. 24, no. 3, 2014.
- [52] L. Hao, M. Lin, X. Zhao, X. Fu, Z. Q. Zhu and P. Jin, "Static characteristics analysis and experimental study of a novel axial field flux-switching permanent magnet generator," *IEEE*

- Trans. Magn.*, vol. 48, no. 11, pp. 4212-4215, 2012.
- [53] D. J. Evans and Z. Q. Zhu, "Novel Partitioned Stator Switched Flux Permanent Magnet Machines," *IEEE Trans. on Magn.*, vol. 51, no. 1, 2015.
- [54] Y. Pang, Z. Q. Zhu, D. Howe, S. Iwasaki, R. Deodhar and A. Pride, "Comparative study of flux-switching and interior permanent magnet machines," in *Proc. ICEMS*, Seoul, Korea, 8 - 11 October 2007.
- [55] R. Cao, C. Mi and M. Cheng, "Quantitative Comparison of Flux-Switching Permanent-Magnet Motors With Interior Permanent Magnet Motor for EV, HEV, and PHEV Applications," *IEEE Trans. Magn.*, vol. 48, no. 8, pp. 2374 - 2384 , 2012.
- [56] A. Fasolo, L. Alberti and N. Bianchi, "Performance Comparison Between Switching-Flux and IPM Machines With Rare-Earth and Ferrite PMs," *IEEE Trans. Ind. Appl.*, vol. 50, no. 6, pp. 3708 - 3716, 2014.
- [57] A. S. Thomas, Z. Q. Zhu and G. W. Jewell, "Comparison of flux switching and surface mounted permanent magnet generators for high-speed applications," *IET*, vol. 1, no. 3, pp. 111 - 116, Sep. 2011.
- [58] A. S. Thomas, Z. Q. Zhu and G. W. Jewell, "Comparison of flux switching and surface mounted permanent magnet generators for aerospace applications," in *PEMD 2010*, Brighton, UK, 2010.
- [59] W. Hua, M. Cheng, Z. Q. Zhu, W. Zhao and X. Kong, "Comparison of electromagnetic performance of brushless motors having magnets in stator and rotor," *Journal of Appl. Phys.*, no. 103, 2008.
- [60] W. Hua, Z. Q. Zhu, M. Cheng, Y. Pang and D. Howe, "Comparison of flux-switching and doubly-salient permanent magnet brushless machines," in *Proc. ICEMS 2005*, 2005.
- [61] D. G. Dorrell, I. Chindurza and F. Butt, "Operation, theory and comparison of the flux reversal machine - is it a viable proposition?," in *PEDS2003*, Singapore, 2003.
- [62] H. K. Shin, T. H. Kim and C. J. Kim, "A study on irreversible permanent magnet demagnetization in flux-reversal machines," in *Proc. of ICEMS2011*, Beijing, China, 2011.
- [63] W. Hua and M. Cheng, "A comprehensive comparison of flux-switching and flux-reversal brushless PM machines," in *Int. Magnetics Conf.*, Madrid, Spain, 2008.
- [64] S. L. Ho, S. X. Niu and W. N. Fu, "Design and Comparison of Vernier Permanent Magnet Machines," *IEEE Trans. Magn.*, vol. 47, no. 10, pp. 3820 - 3283, October 2011.
- [65] D. Li, R. Qu and J. Li, "Topologies and analysis of flux-modulation machines," in *Proc. of ECCE 2015*, Montreal, QC, Canada, 20-24 Sept. 2015 .
- [66] Z. Z. Wu and Z. Q. Zhu, "Analysis of Air-Gap Field Modulation and Magnetic Gearing Effects in Switched Flux Permanent Magnet Machines," *IEEE Trans. Magn.* , vol. 51, no. 5, pp. 1 - 12, May 2015.
- [67] S. Ruoho, J. Kolehmainen, J. Ikäheimo and A. Arkkio, "Interdependence of demagnetization, loading, and temperature rise in a permanent-magnet synchronous motor," *IEEE Trans. Magn.*, vol. 46, no. 3, pp. 949-953, Mar. 2010.
- [68] G. Zhao, L. Tian, Q. Shen and R. Tang, "Demagnetization analysis of permanent magnet synchronous machines under short circuit fault," in *Proc. of APPEEC 2010*, Chengdu, 2010.
- [69] S. Ruoho, E. Dlala and A. Arkkio, "Comparison of Demagnetization Models for Finite-Element Analysis of Permanent-Magnet Synchronous Machines," *IEEE Transactions on Magnetics*, vol. 43, no. 11, pp. 3964 - 3968, 2007.
- [70] J. D. McFarland, T. M. Jahns and A. M. EL-Refaie, "Demagnetization performance characteristics of flux switching permanent magnet machines," in *Proc. ICEM2014*, Berlin, Germany, 2-5 Sept.

- 2014.
- [71] J. D. McFarland and T. M. Jahns, "Influence of d- and q-axis currents on demagnetization in PM synchronous machines," in *ECCE*, Denver, SUA, 2013.
- [72] S. Zhu, M. Cheng, W. Hua and X. Cai, "Finite Element Analysis of Flux-switching PM Machine Considering Oversaturation and Irreversible Demagnetization," *IEEE Trans. Magn.*, 2015.
- [73] N. Bianchi and S. Bolognani, "Fault-tolerant PM motors in automotive applicatinos," in *Proc. of VPPC*, Chicago, IL, 2005.
- [74] W. Zhao, M. Cheng, W. Hua and H. Jia, "A redundant flux-switching permanent magnet motor drive for fault-tolerant applications," in *IEEE Vehicle Power and Propulsion Conference*, Harbin, China, 2008.
- [75] W. Zhao, M. Cheng, K. T. Chau and J. Ji, "A new modular flux-switching permanent-magnet machine using fault-tolerant teeth," in *Proc. CEFC*, Chicago, USA, 9-12 May 2010.
- [76] M. J. Jin, C. F. Wang, J. X. Shen and B. Xia, "A modular permanent-magnet flux-switching linear machine with fault-tolerant capability," *IEEE Trans. Magn.*, vol. 45, no. 8, pp. 3179-3186, August 2009.
- [77] X. Xue, W. Zhao, J. Zhu, G. Liu, X. Zhu and M. Cheng, "Design of five-phase modular flux-switching permanent-magnet machines for high reliability applications," *IEEE Trans. Magn.*, vol. 49, no. 7, pp. 3941 - 3944, July 2013.
- [78] T. Raminosoa and C. Gerada, "A comparative study of permanent magnet - synchronous and permanent magnet - flux switching machines for fault tolerant drive systems," in *Proc. ECCE*, Atlanta, USA, 12 - 16 September 2010.
- [79] H. Liu, W. Zhao, J. Ji, Y. Du, H. Zhou and D. Zhang, "Fault-tolerant control of modular linear flux-switching permanent-magnet motor," in *ICEMS*, Busan, Korea, 2013.
- [80] W. Zhao, M. Cheng, K. Chau, W. Hua, H. Jia, J. Ji and W. Li, "Stator-flux-oriented fault-tolerant control of flux-switching permanent-magnet motors," *IEEE Trans. Magn.*, vol. 47, no. 10, pp. 4191-4194, 2011.
- [81] W. Zhao, M. Cheng, W. Hua, L. Xu, R. Cao and Y. Du, "Post-fault operation of redundant flux-switching permanent-magnet motors using harmonic injected current," in *ICEMS*, 2010.
- [82] M. Khov, J. Regnier and J. Faucher, "Monitoring of turn short-circuit faults in stator of PMSM in closed loop by on-line parameter estimation," in *Proc. IEEE SDEMPED*, 2009.
- [83] N. Leboeuf, T. Boileau, B. Nahid-Mobarakeh, G. Clerc and F. Meibody-Tabar, "Real-Time Detection of Interturn Faults in PM Drives Using Back-EMF Estimation and Residual Analysis," *IEEE Trans. on Ind. Appl.*, vol. 47, no. 6, pp. 2402-2412, 2011.
- [84] G. J. Li, Contribution à la Conception des Machines Electriques à Rotor Passif pour des Applications Critiques: Modélisations Electromagnétiques et Thermiques sur Cycle de Fonctionnement, Etude du Fonctionnement en Mode Dégradé, PhD Thesis, 2011.
- [85] W. X. Zhao, M. Cheng, K. T. Chau and C. C. Chan, "Control and operation of fault-tolerant flux-switching permanent-magnet motor drive with second harmonic current injection," *IET*, vol. 6, no. 9, pp. 707 - 715, 2012.
- [86] J. Zhu, N. Ertugrul and W. L. Soong, "Minimum torque ripple current control strategy in a dual fault tolerant PM AC motor drive," in *Proc. of PESC 2008*, Rhodes, 2008.
- [87] W. Zhao, M. Cheng, R. Cao, G. Liu and J. Ji, "Minimum copper loss fault-tolerant control of redundant flux-switching permanent-magnet motors," in *ICEMS*, Beijing, China, 20 - 23 August 2011.
- [88] J. A. Haylock, B. C. Mecrow, A. G. Jack and D. J. Atkinson, "Operation of fault tolerant machines

- with winding failures,” *IEEE Trans. Energy Conv.*, vol. 14, no. 4, pp. 1490-1495, 1999.
- [89] N. Takorabet, J. P. Caron, B. Vaseghi, B. Nahid-Mobarakeh, F. Meibody-Tabar and G. Humbert, “Study of Different Architectures of Fault Tolerant Actuator Using a Double-Star PM Motor,” in *Proc. of IAS 2008*, Edmonton, Canada, 2008.
- [90] B. A. Welchko, T. M. Jahns, W. L. Soong and J. M. Nagashima, “IPM synchronous machine drive response to symmetrical and asymmetrical short circuit faults,” *IEEE Trans. Energy Conv.*, vol. 18, no. 2, pp. 291 - 298, 2003.
- [91] B. A. Welchko, T. A. Jahns and T. A. Lipo, “Short-circuit fault mitigation methods for interior PM synchronous machine drives using six-leg inverters,” in *Proc. of PESC 2004*, Aachen, Germany, 2004.
- [92] S. Dwari and L. Parsa, “Optimum Fault-Tolerant Control of Multi-phase Permanent Magnet Machines for Open-Circuit and Short-Circuit Faults,” in *APEC 2007*, Anaheim, CA, USA, 2007.
- [93] J. Wang, K. Atallah and D. Howe, “Optimal torque control of fault-tolerant permanent magnet brushless machines,” *IEEE Trans. Magn.*, vol. 39, no. 5, pp. 2962-2964, 2003.
- [94] “Cooling of Automotive Traction Motors: Schemes, Examples and Computation Methods - A Review,” *IEEE Trans. Ind. Electron.*, vol. Early Access, May 2018.
- [95] P. H. Mellor, D. Roberts and D. R. Turner, “Lumped parameter thermal model for electrical machines of TEFC design,” *IEE Proceedings B - Electric Power Applications*, vol. 138, no. 5, pp. 205 - 218, Sept. 1991.
- [96] J. Nerg, M. Rilla and J. Pyrhonen, “Thermal Analysis of Radial-Flux Electrical Machines With a High Power Density,” *IEEE Trans. Ind. Electron.* , vol. 55, no. 10, pp. 3543-3554, 2008.
- [97] R. Soderberg, “Steady flow of heat in large turbine-generators,” *Trans. AIEEE*, vol. 50, pp. 782-802, 1931.
- [98] M. D. Ltd, “MotorCad webpage,” [Online]. Available: www.motor-design.com. [Accessed 20 June 2018].
- [99] T. Jokinen and J. Saari, “Modelling of the coolant flow with heat flow controlled temperature sources in thermal networks (in induction motors),” *IEE Proceedings - Electric Power Applications*, vol. 144, no. 5, pp. 338 - 342, Sept. 1997.
- [100] M. Rosu, P. Zhou, D. Lin, D. M. Ionel, M. Popescu, F. Blaabjerg, V. Rallabandi and D. Staton, *Multiphysics Simulation by Design for Electrical Machines, Power Electronics and Drives*, Wiley-IEEE Press, 2018.
- [101] E. Hoang, M. Lecrivain and M. Gabsi, “A new structure of a switching flux synchronous polyphased machine with hybrid excitation,” in *2007 European Conference on Power Electronics and Applications*, 2007.
- [102] C. Pollock, H. Pollock, R. Barron, J. R. Coles, D. Moule, A. Court and R. Sutton, “Flux-switching motors for automotive applications,” *IEEE Trans. Ind. Appl.* , vol. 42, no. 5, pp. 1177-1184, 2006.
- [103] A. Fasolo, L. Alberti and N. Bianchi, “Performance comparison between switching-flux and IPM machine with rare earth and ferrite PMs,” in *Proc. ICEM*, Marseille, France, 2-5 Sept. 2012.
- [104] S. Li, Y. Li and B. Sarlioglu, “Partial irreversible demagnetization assessment of flux switching permanent magnet machines,” in *Proc. ICEM2014*, Berlin, Germany, 2014.
- [105] I. A. A. Afinowi, Z. Q. Zhu, Y. Guan, J. C. Mipo and P. Farah, “Performance analysis of switched-flux machines with hybrid NdFeB and ferrite magnets,” in *Proc. ICEMS 2014*, Hangzhou, China, 2014.
- [106] “NdFeB products datasheet - Arnold Magnetics,” Arnold Magnetics, [Online]. Available: www.arnoldmagnetics.com. [Accessed 27 April 2018].

- [107] W. Q. Chu and Z. Q. Zhu, "Average torque separation in permanent magnet synchronous machines using frozen permeability," *IEEE Trans. Magn.*, vol. 49, no. 3, pp. 1202-1210, Mar. 2013.
- [108] P. Taras, G. J. Li and Z. Q. Zhu, "Comparative study of fault tolerant switched flux permanent magnet machines," *IEEE Trans. Ind. Electron.*, vol. 64, no. 3, pp. 1939-1948, Mar. 2017.
- [109] J. T. Chen, Z. Q. Zhu, S. Iwasaki and R. P. Deodhar, "A novel E-core switched-flux PM brushless AC machine," *IEEE Trans Ind. Appl.*, vol. 47, no. 3, pp. 1273-1282, May - June 2011.
- [110] R. L. Owen, Z. Q. Zhu, A. S. Thomas, G. W. Jewell and D. Howe, "Alternate poles wound flux-switching PM brushless AC machines," *IEEE Trans. Ind. Appl.*, vol. 46, no. 2, pp. 790-797, March - April 2010.
- [111] G. J. Li, Z. Q. Zhu, W. Q. Chu, M. P. Foster and D. A. Stone, "Influence of Flux Gaps on Electromagnetic Performance of Novel Modular PM Machines," *IEEE Trans. Energy Convers.*, vol. 29, no. 3, pp. 716-726, September 2014.
- [112] A. M. EL-Refaie, "Fractional-slot concentrated windings synchronous permanent magnet machines: opportunities and challenges," *IEEE Trans. Ind. Electron.*, vol. 57, no. 1, pp. 107-121, January 2010.
- [113] G. Heins, D. Ionel and M. Thiele, "Winding factors and magnetic fields in permanent magnet brushless machines with concentrated windings and modular stator cores," in *Proc. ECCE*, 15 - 19 September 2013.
- [114] G. J. Li, Z. Q. Zhu, M. Foster and D. Stone, "Comparative studies of modular and unequal tooth PM machines either with or without tooth tips," *IEEE Trans. Magn.*, vol. 50, no. 7, July 2014.
- [115] T. J. E. Miller, *Brushless permanent-magnet and reluctance motor drives*, New York: Oxford University Press, 1989.
- [116] Z. Q. Zhu, "A simple method for measuring cogging torque in permanent magnet machines," in *Proc. IEEE Power Energy Soc. General Meeting*, July 2009.
- [117] G. J. Li and Z. Q. Zhu, "Demagnetization of modular surface mounted permanent magnet machines," in *2016 XXII International Conference on Electrical Machines (ICEM2016)*, Lausanne, Switzerland, 4-7 Sept. 2016.
- [118] P. Taras, G. J. Li and Z. Q. Zhu, "Comparative study of alternative modular switched flux permanent magnet machines," in *2015 IEEE International Conference on Industrial Technology*, Seville, 2015.
- [119] A. Bellini, F. Filippetti, C. Tassoni and G. A. Capolino, "Advances in diagnostic techniques for induction machines," *IEEE Trans. Ind. Electron.*, vol. 55, no. 12, pp. 4109-4126, Dec. 2008.
- [120] B. Sen, J. Wang and P. Lazari, "A high-fidelity computationally efficient transient model of interior permanent-magnet machine with stator turn fault," *IEEE Trans. Ind. Electron.*, vol. 63, no. 2, pp. 773-783, Feb. 2016.
- [121] A. Gandhi, T. Corrigan and L. Parsa, "Recent advances in modelling and online detection of stator interturn faults in electrical motors," *IEEE Trans. Ind. Electron.*, vol. 58, no. 5, pp. 1564-1575, 2011.
- [122] S. Nair, V. I. Patel and J. Wang, "Post-Demagnetization Performance Assessment for Interior Permanent Magnet AC Machines," *IEEE Trans. Magn.*, vol. 52, no. 4, pp. 1-10, April 2016.
- [123] P. Campbell, *Permanent Magnet Materials and their Application*, Cambridge University Press, 1996, pp. 93 - 96.
- [124] O. A. Mohammed, S. Liu and Z. Liu, "Physical modeling of PM synchronous motors for integrated coupling with machine drives," *IEEE Trans. Magn.*, vol. 41, no. 5, pp. 1628 - 1631,

May 2005.

- [125] B. Vaseghi, B. Nahid-Mobarakh, N. Takorabet and F. Meibody-Tabar, "Inductance Identification and Study of PM Motor with Winding Turn Short Circuit Fault," *IEEE Trans. Magn.*, vol. 47, no. 5, pp. 978-981, May 2011.
- [126] L. Romeral, J. C. Urresty, J. R. Riba Ruiz and A. Garcia Espinosa, "Modeling of surface-mounted permanent magnet synchronous motors with stator winding interturn faults," *IEEE Trans. Ind. Electron.*, vol. 58, no. 5, pp. 1576-1585, May 2011.
- [127] N. Leboeuf, T. Boileau, B. Nahid-Mobarakh, N. Takorabet, F. Meibody-Tabar and G. Clerc, "Effects of imperfect manufacturing process on electromagnetic performance and online interturn fault detection in PMSMs," *IEEE Trans. Ind. Electron.*, vol. 62, no. 6, pp. 3388-3398, June 2015.
- [128] A. Boglietti, A. Cavagnino, D. Staton, M. Shanel, M. Mueller and C. Mejuto, "Evolution and Modern Approaches for Thermal Analysis of Electrical Machine," *IEEE Trans. Ind. Electron.*, vol. 56, no. 3, pp. 871 - 882, 2009.
- [129] J. Bai, Y. Sui, C. Tong, Q. Zhao and J. Zhang, "Investigation of the Cooling and Thermal-Measuring System of a Compound-Structure Permanent-Magnet Synchronous Machine," *Energies*, pp. 1393 - 1426, 2014.
- [130] X. Chen, J. Wang and A. Griffo, "A high-fidelity and computationally efficient electrothermally coupled model for interior permanent-magnet machines in electric vehicle traction applications," *IEEE Trans. Transp. Electrific.*, vol. 1, no. 4, pp. 336-347, Dec. 2015.
- [131] R. Wrobel and P. Mellor, "A General Cuboidal Element for Three-Dimensional Thermal Modelling," *IEEE Trans. Magn.*, vol. 46, no. 8, pp. 3197-3200, Aug. 2010.
- [132] R. Zeinali, H. Bulent Ertan, C. Yamali and R. Tarvirdilu-Asl, "Magnetically Geared Direct Drive Wind Generator Thermal Analysis," in *OPTIM 2017/ACEMP 2017*, Brasov, Romania, 25-27 May 2017.
- [133] Y. K. Chin and D. Staton, "Transient thermal analysis using both lumped circuit approach and finite element method of a permanent magnet traction motor," in *AFRICON 2004*, 2004.
- [134] "3M's Scotchcast™ 5230N electrical dielectric coating resin," [Online]. Available: <http://multimedia.3m.com/mws/media/1949530/3mtm-scotchcasttm-electrical-resin-5230n.pdf>. [Accessed 25 April 2018].
- [135] G. J. Li, P. Taras, Z. Q. Zhu, J. Ojeda and M. Gabsi, "Investigation of irreversible demagnetisation in switched flux permanent magnet machines under short-circuit conditions," *IET Electric Power Applications*, vol. 11, no. 4, pp. 595 - 602, April 2017.
- [136] A. S. Thomas, Z. Q. Zhu and G. J. Li, "Thermal modelling of switched flux permanent magnet machines," in *Proc. ICEM*, Berlin, 2014.
- [137] X. Cai, M. Cheng, S. Zhu and J. Zhang, "Thermal modelling of flux-switching permanent-magnet machines considering anisotropic conductivity and thermal contact resistance," *IEEE Trans. Ind. Electron.*, vol. 63, no. 6, pp. 3355-3365, June 2016.
- [138] G. Zhang, W. Hua, M. Cheng, B. Zhang and X. Guo, "Coupled magnetic-thermal fields analysis of water cooling flux-switching permanent magnet motors by an axially segmented model," *IEEE Trans. Magn.*, vol. 53, no. 6, pp. 1-4, June 2017.
- [139] G. J. Li, J. Ojeda, E. Hoang and M. Gabsi, "Thermal-electromagnetic analysis of a fault-tolerant dual-star flux-switching permanent magnet motor for critical applications," *IET Electrical Power Applications*, vol. 5, no. 6, pp. 503-513, July 2011.
- [140] Cedrat, User Guide Flux 12 Volume 3, 22 January 2015.
- [141] D. M. Ionel, M. Popescu, M. I. McGilp, T. J. E. Miller, S. J. Dellinger and R. J. Heideman,

- “Computation of core losses in electrical machines using improved models for laminated steel,” *IEEE Trans. Ind. Appl.*, vol. 43, no. 6, pp. 1554 - 1564, Nov./Dec. 2007.
- [142] D. Staton, A. Boglietti and A. Cavagnino, “Solving the more difficult aspects of electric motor thermal analysis in small and medium size industrial induction motors,” *IEEE Trans. Energy Convers.*, vol. 20, no. 3, pp. 620-628, Sept. 2005.
- [143] “Aluminum Emisivity Coefficients for various surface conditions,” [Online]. Available: www.engineeringtoolbox.com. [Accessed October 2016].
- [144] “Engineering toolbox - Air thermal properties for a range of temperatures,” [Online]. Available: www.engineeringtoolbox.com. [Accessed October 2016].
- [145] G. J. Li, J. Ojeda, E. Hoang, M. Gabsi and M. Lecrivain, “Thermal–Electromagnetic Analysis for Driving Cycles of Embedded Flux-Switching Permanent-Magnet Motors,” *IEEE Trans. Veh. Technol.*, vol. 61, no. 1, pp. 140-151, Jan. 2012.
- [146] D. A. Staton and A. Cavagnino, “Convection heat transfer and flow calculations suitable for electric machines thermal models,” *IEEE Trans. Ind. Electron.*, vol. 55, no. 10, pp. 3509-3516, Oct. 2008.
- [147] J. H. Lienhard, A Heat Transfer Textbook, Cambridge, MA: Phlogiston Press, 2016.
- [148] B. Vaseghi, Contribution à l'Etude des Machines Electriques en Presence de Defaut entre-Spires Modelisation - Reduction de courant de defaut, PhD Thesis, Institut National Polytechnique de Lorraine - INPL, 2009.
- [149] E. Ben Sedrine, J. Ojeda, M. Gabsi and I. Slama-Belkhodja, “Fault-tolerant control using the GA optimization considering the reluctance torque of a five-phase flux switching machine,” *IEEE Trans. Energy Convers.*, vol. 30, no. 3, pp. 927-938, Sept. 2015.
- [150] J. T. Chen, Z. Q. Zhu, S. Iwasaki and R. Deodhar, “Comparison of losses and efficiency in alternate flux-switching permanent magnet machines,” in *Proc. ICEM*, Rome, Italy, 6 - 8 September 2010.
- [151] W. Hua, Z. Q. Zhu, M. Cheng and Y. Pang, “Comparison of flux-switching and doubly-salient permanent magnet brushless machines,” in *Proc. ICEMS*, Nanjing, China, 27 -29 September 2005.
- [152] W. Hua, M. Cheng, Z. Q. Zhu and W. X. Zhao, “Comparison of electromagnetic performance of brushless machiness having magnets in stator and rotor,” *J. Appl. Phys.*, vol. 103, no. 7, March 2008.
- [153] T. Raminosoa, G. Gerada and M. Galea, “Design considerations for a fault-tolerant flux-switching permanent-magnet machine,” *IEEE Trans. Ind. Electron.*, vol. 58, no. 7, pp. 2818-2825, July 2011.
- [154] Y. Shi, L. Jian, J. Wei, Z. Shao, W. Li and C. C. Chan, “A new perspective on the operating principle of flux-switching permanent-magnet machines,” *IEEE Trans. Ind. Electron.*, vol. 63, no. 3, pp. 1425-1437, March 2016.
- [155] P. E. Kakosimos, A. G. Sarigiannidis, M. E. Beniakar, A. G. Kladas and C. Gerada, “Induction motors versus permanent-magnet actuators for aerospace applications,” *IEEE Trans. Ind. Electron.*, vol. 61, no. 8, pp. 4315-4325, Aug. 2014.